Thèse présentée pour l'obtention du grade de Docteur de
l'Ecole Polytechnique

Réalisée au sein du Laboratoire de Mécanique des Solides
de l'Ecole Polytechnique
et du Laboratoire de BioMécanique et BioIngénierie
de l'Université de Technologie de Compiègne

Discipline : Mécanique

Biomécanique de capsules en écoulement

Par : **Claire Dupont**

Membres du jury:

M. Jean–Marc Allain	Ecole Polytechnique, Palaiseau	Examinateur
M^{me} Dominique Barthès-Biesel	Université de Technologie de Compiègne	Invitée
M. Dominique Chapelle	Inria Saclay	Président du Jury
M. Marc Jaeger	Ecole Centrale Marseille	Rapporteur
M. Patrick Le Tallec	Ecole Polytechnique, Palaiseau	Directeur de Thèse
M^{me} Anne–Virginie Salsac	Université de Technologie de Compiègne	Directrice de Thèse
M^{me} Annie Viallat	Université de la Méditerranée, Aix-Marseille	Rapporteur
M^{me} Marina Vidrascu	Inria Rocquencourt	Invitée

Date de soutenance : 18 décembre 2014

A mes parents
A mon 'petit' frère
A mes grands–parents

Remerciements

La thèse est un long chemin semé d'embûches avec des centaines de feuilles noircies d'équations, des réunions à se demander si on ne s'est pas trompé de destination (surtout au début). Mais c'est surtout des moments inoubliables et une expérience humaine extraordinaire. C'est pourquoi je tenais ici à remercier toutes les personnes qui m'ont accompagnée tout au long de cette fabuleuse aventure.

Cette aventure n'aurait certainement jamais été possible si un jour, ma candidature à un projet de recherche en laboratoire n'avait pas reçu de réponse. Merci Anne-Virginie d'avoir cru en moi et d'avoir accepté d'être ma tutrice de projet, ma suiveuse, ma directrice de stage, ma directrice de thèse et maintenant bien plus. Merci pour tout le chemin parcouru depuis notre première rencontre car, sans toi, je n'aurais pas vécu cette thèse de la même façon. J'aimerais également remercier Patrick Le Tallec, mon deuxième directeur de thèse. Merci Patrick d'avoir accepté de partir avec nous à la découverte des mystères des capsules et d'avoir pris le temps de répondre à mes questions sur les modèles de coques, sur le projet. Je tenais également à remercier Marina Vidrascu pour l'aide qu'elle a pu m'apporter pour la compréhension de shelddon et son couplage avec le solver fluide de l'UTC. Merci Marina d'avoir toujours répondu à mes SOS concernant le code avec toujours beaucoup de gentillesse. Merci beaucoup pour ton soutien dans ses moments de solitude. Enfin, je tenais également à remercier Dominique Barthès-Biesel d'avoir partagé avec moi sa passion pour les capsules, ses connaissances, ses idées et d'avoir accepté de se plonger dans les modèles de coques avec nous. Merci pour votre gentillesse, votre disponibilité et vos questions qui m'ont permis d'apprendre énormément.

J'ai été très honorée qu'Annie Viallat et Marc Jaeger acceptent d' être les rapporteurs de ma thèse. Je tiens à les remercier pour le temps et l'énergie qu'ils ont consacrés à la lecture de ce manuscrit. Leurs remarques et leurs corrections ont été extrêmement précieuses. Je tiens également à remercier Jean-Marc Allain d'avoir accepté d'être examinateur et Dominique Chapelle le Président du jury. Je tiens à remercier tous les membres de mon jury pour leurs questions durant la soutenance qui m'ont permis de prendre du recul sur mon travail.

Je tenais également à remercier l'Académie Française de m'avoir permis de partir trois mois à Munich au sein du Lehrtuhl für Numerische Mechanick. Viele Dank, Prof. W. A. Wall, für die Einladung. Merci à tous les étudiants du laboratoire pour leur accueil et de m'avoir fait découvrir les traditions allemandes. Un merci particulier à Aline de m'avoir prise sous son aile et de répondre toujours à mes questions. Aujourd'hui, j'espère qu'on trouvera d'autres occasions que les conférences pour se voir.

Etre affiliée à deux laboratoires peut parfois être difficile d'un point de vue administratif mais cela n'a pas été mon cas et c'est pourquoi je tenais à remercier particulièrement Alexandra, Anna, Valérie, Catherine, Valérie, Maryse, les secrétaires et gestionnaires du LMS, de BMBI et de l'Inria pour leur aide et leur efficacité pour régler les démarches administratives.

Je tiens également à remercier tous mes collègues du LMS et de BMBI. En particulier, je souhaite remercier Barbara, Dimitri, Armel, Jessica, Pierre pour leur accueil toujours souriant lors de mes journées au LMS et de m'avoir pleinement intégrée à la vie du LMS même si je n'étais là que de temps en temps. Merci également à Cristi, Dr. TChutchu (Xuan), Xu Qu, de m'avoir pris sous leur aile lors de mon arrivée au sein de l'équipe et pour leur bonne humeur. Merci également à Benjamin, Pierre-Yves, Nadège, Yixin, Océane (x2), Ulysse, Jean-Matthieu, Vittoria, Luihui, Muriel, Murielle, Patrick, Christophe, Cécile et tous ceux que j'oublie pour ces bons moments, leurs sourires et leurs bonjours dans les couloirs. Merci à Anne pour ses relectures, ses conseils et toutes ses discussions plus ou moins professionnelles. Merci également à Justine pour ses visites surprises dans mon bureau, d'avoir accepté mes défis sportifs et pour son soutien gastronomique cet été. Dommage qu'il se soit arrêté en septembre, parce que c'est tellement plus facile de rédiger avec un goûter qui sort du four. Je tiens également à remercier mon Bisounours préféré. Merci d'être devenu beaucoup plus que mon premier stagiaire. Merci d'avoir toujours pris le temps de me faire rire au bon moment. Je tiens à remercier particulièrement Iolanda, de m'avoir appris combien il était important d'avoir une vie à côté de la thèse. Merci pour toutes ces soirées découvertes, ces week-ends touristiques improvisés. C'est promis; maintenant, c'est à toi de me faire découvrir l'Italie. Merci pour ton amitié sans frontière.

Je tenais également à remercier Sophie Canella d'avoir pris le temps de m'écouter, de me rassurer le mardi matin. Merci pour votre sourire et tout ce que vous m'avez appris.

Merci à Laura, Rym, Pauline et Thibaut de m'avoir fait découvrir qu'il était possible de suer dans l'eau et de faire plein de choses sur un vélo. Merci à Brigitte, Caroline, Sophie, Corinne et toutes mes "collègues" d'aquabike pour toutes ses séances d'aquarigolade. J'adresse un merci tout particulier à Laura d'être devenue beaucoup plus que la 'prof d'aquabike'. Merci de m'avoir fait découvrir que le sport pouvait être un véritable ami dans les moments difficiles. Merci pour tous ces bons moments passés et ceux à venir. Merci d' être là tout simplement.

Je tiens également à remercier mes amis, Elodie, David, Anne-Lise, Alex, Anne-Sophie, Pierre, Ludivine, Philippe, Yannick, Cécile. Un merci tout particulier à Régine, Annick, Robert, Marie-Paule, Bernard, Christian, Fabienne, Corinne et Philippe d'être venus du grand nord pour m'apporter votre soutien lors de ma soutenance.

Mille mercis aux quatre plus belles fleurs cambraisiennes pour leur magnifique cadeau. Merci beaucoup pour ce magnifique moment inoubliable.

Je finirai ces remerciements avec un petit mot pour mes parents et mon « petit » frère pour leurs soutiens sans faille. Merci de m'avoir supporté même à distance ces derniers mois. Je me doute que cela n'a pas été facile pour vous aussi. Merci à mon "petit" frère d'avoir toujours trouvé les mots pour me faire rire quand cela paraissait impossible. Avant de terminer ces remerciements, j'ai une pensée toute particulière pour mes grands-parents.

Ainsi s'achève trois ans d'une fabuleuse aventure, merci tout simplement.

Contents

Abstract

Capsules are small liquid droplets enclosed by a thin hyperelastic membrane. The membrane allows the separation and the protection of the internal fluid from the environment and can control its liberation into the external media. Capsules are used as biomimetic model of red blood cells and have many applications in bioengineering and pharmaceutics such as drug targeting. Artificial capsules are classically produced by interfacial polymerization of emulsions: they tend to be quasi–spherical with a thin membrane, which facilitates transmembrane exchanges. Under hydrodynamic stress, the capsule membrane is subjected to buckling phenomena, which may persist at steady state depending on the flow conditions. The first objective of the thesis is to analyze the effect of the bending resistance on the dynamics of a capsule by modeling its wall as a thin shell with bending resistance. The membrane effects and the bending effects are decoupled in this new model. This allows to implement various hyperelastic constitutive law to model the softening or hardening behavior of the mid–surface in the median plane, combined with the generalized Hooke's law for the bending effects. For the first time, this problem is solved numerically by coupling a boundary integral method for the internal and external flows with a shell finite element method for the wall deformation. For an initially spherical capsule subjected to a simple shear flow or a planar hyperbolic flow, we show that the motion and the deformation of the capsule at steady state are identical to those observed for a 2D surface without bending resistance: the main deformation mode of the wall is thus essentially controlled by the stretching of the mid–surface (elastic deformation in the median plane). However, at low flow strength, wrinkles persist at steady state. To model rigorously buckling phenomena, we take into account the bending resistance of the wall. This allows us to determine the constitutive law that relates the wrinkle wavelength to the wall bending resistance. All these results were used to estimate the value of the bending modulus of artificial capsules subjected to a simple shear flow from experimental images published in the literature using an inverse analysis method.

The second objective of the thesis is to investigate the influence of a non–spherical shape on the dynamics of capsules subjected to a simple shear flow. We consider prolate as well as oblate capsules, the red blood cells having an oblate discoidal shape. We have determined the stable equilibrium configurations, modeling the capsule wall as a 2D surface devoid of bending resistance, and studied the influence of the viscosity ratio between the internal and the external fluids. We have shown that the stable regimes are not necessarily the ones traditionally observed when the capsule revolution axis is placed within the shear plane and that they only depend on the capsule aspect ratio, the viscosity ratio and the ratio between the viscous and the elastic forces. We have also determined the convergence time for an oblate capsule to reach its stable equilibrium configurations. One of the perspective of this thesis is to simulate ellipsoidal capsules with the thin shell model.

Keywords: Capsule, fluid–structure interaction, boundary integral method, finite element method, thin shell model, buckling and wrinkling, stable equilibrium configurations

Résumé

Les capsules sont des gouttes liquides entourées par une fine membrane hyperélastique, qui joue un rôle de protection et peut servir au contrôle de la libération du fluide interne dans le milieu environnant. Si les capsules constituent un modèle biomimétique pour les globules rouges, elles sont également très largement utilisées en bioingénierie et en pharmacologie pour véhiculer des principes actifs, par exemple. Les capsules artificielles, classiquement fabriquées par polymérisation interfaciale d'émulsions, ont une forme quasi–sphérique et une membrane très fine. Cette dernière facilite les échanges transmembranaires. Sous contrainte hydrodynamique, la membrane de la capsule est soumise à des phénomènes de flambage, qui peuvent subsister à l'état stationnaire suivant les conditions d'écoulement. Le premier objectif de la thèse a été d'analyser l'effet de la rigidité de flexion sur la dynamique d'une capsule en modélisant sa paroi comme une coque mince comprenant une rigidité de flexion. La nouveauté du modèle est de découpler les effets de membrane des effets de flexion. Cela permet de modéliser des comportements adoucissant ou durcissant de la surface moyenne située dans le plan médian tout en décrivant la déformation en flexion par la loi de Hooke généralisée. Ce problème d'interaction fluide–structure a été simulé numériquement en couplant pour la première fois la méthode des intégrales de frontière (résolution des écoulements interne et externe) avec la méthode des éléments finis de coque (résolution de la déformation de la paroi). Pour une capsule initialement sphérique soumise à un écoulement de cisaillement simple ou hyperbolique plan, nous avons montré qu'à l'état stable, le mouvement et la déformation de la capsule sont identiques à ceux observés pour une surface 2D sans rigidité de flexion: le mode principal de déformation de la paroi est donc essentiellement piloté par les effets de membrane (déformation élastique dans le plan médian). Néanmoins, à faible écoulement, des plis persistent à l'état stationnaire. La modélisation rigoureuse du phénomène de flambage, qui nécessite de prendre en compte la résistance à la flexion de la paroi, a permis de déterminer la loi de comportement reliant la longueur d'ondes des plis à la résistance à la flexion de la paroi. L'ensemble de ces résultats a été utilisé pour estimer la valeur du module de flexion de capsules artificielles sous cisaillement simple à partir d'images expérimentales de la littérature grâce à une méthode d'analyse inverse.

Le deuxième objectif de la thèse a été d'étudier l'influence d'une forme non–sphérique sur la dynamique de capsules soumises à un écoulement de cisaillement simple, que les capsules aient une forme allongée ou aplatie comme dans le cas du globule rouge. Nous avons déterminé les régimes mécaniquement stables pour une capsule ellipsoïdale, dont la paroi est modélisée comme une surface 2D sans rigidité de flexion, et étudié l'effet du rapport de viscosité entre les fluides interne et externe. Nous avons montré que les régimes stables ne correspondent pas forcément à ceux traditionnellement observés pour une capsule, dont l'axe de révolution est placé dans le plan de cisaillement et qu'ils sont uniquement fonction du rapport d'aspect de la capsule, du rapport de viscosité et du rapport entre force visqueuse et force élastique de la capsule. Nous avons également déterminé le temps necessaire pour qu'une capsule aplatie atteigne son état d'équilibre. Les perspectives de l'étude portent sur la simulation des capsules ellipsoïdales avec le modèle de coque.

Mots clés: Capsule, interaction fluide–structure, méthode des intégrales de frontière, méthode des éléments finis, modèle de coque mince, flambage et formation de plis, configurations d'équilibre stables

Principal notations

Latin symbols

$\underline{a}_1, \underline{a}_2, \underline{a}_3$	Covariant base vectors in the current configuration.
$\underline{A}_1, \underline{A}_2, \underline{A}_3$	Covariant base vectors in the reference configuration.
$\underline{\underline{C}}$	Green deformation tensor.
Ca_s	Surface capillary number.
Ca_v	Bulk capillary number (shell model).
D_{ij}	Taylor parameter computed from the length L_i and L_j of the axis of the ellipsoid of inertia.
$\underline{\underline{e}}$	Green-Lagrange strain tensor.
$\underline{e}_1, \underline{e}_2, \underline{e}_3$	Cartesian base.
$\underline{\underline{F}}$	Deformation gradient.
G	Shear modulus.
G_s	Surface shear modulus.
$\underline{g}_1, \underline{g}_2, \underline{g}_3$	Three–dimensional covariant base in the current configuration.
$\underline{G}_1, \underline{G}_2, \underline{G}_3$	Three–dimensional covariant base in the reference configuration.
I_{s1}, I_{s2}	Invariants of membrane strain tensor.
J	Jacobian.
K_s	Area dilatation modulus.
ℓ	Characteristic capsule size (Radius of the sphere with the same volume as the capsule).
L_i	Length of the ellipsoid axis.
M_b	Bending modulus.
$\underline{q}$	Viscous load exerted by the fluids on the wall.
Re	Reynolds number.
r, s, z	Intrinsic local Cartesian coordinates.
$\mathcal{S}_t$	Membrane surface (membrane model) or mid–surface (shell model).
t	Time.
$\underline{\underline{T}}$	Cauchy tension tensor.
$\underline{u}$	Displacement field.
$\underline{v}^{\infty}$	Undisturbed velocity.

w	Strain energy density.
$\underline{x}$	Position vector in the current configuration.
$\underline{X}$	Position vector in the reference configuration.

Greek symbols

α	Relative wall thickness = ratio between the capsule wall thickness and the characteristic size
$\underline{\underline{\chi}}$	Bending strain tensor.
δ^{α}_{β}	Kronecker symbol.
Δt	Time step.
Δx	Mesh size.
$\dot{\gamma}$	Shear rate (characteristic of the external flow).
$\underline{\underline{\gamma}}$	Membrane strain tensor.
λ	Viscosity ratio between the internal and external fluids.
$\lambda^{(i)}$	Shape functions.
$\lambda_{s1}, \lambda_{s2}$	Surface principal dilatation ratio.
μ	Viscosity of the external fluid.
ν	Poisson ratio.
$\underline{\underline{\pi}}$	Piola-Kirchhoff tension tensor.
$\underline{\underline{\sigma}}$	Cauchy stress tensor.
$\underline{\underline{\Sigma}}$	Piola-Kirchhoff stress tensor.
$\underline{\theta}$	Rotation vector.
$\underline{\varphi}$	Vector position of a point on the mid–surface.
ρ	Fluid density.
ξ^1, ξ^2, ξ^3	Curvilinear coordinates.
$\underline{\zeta}$	Shear strain tensor.
ζ_0	Initial angle between the capsule revolution axis and the vorticity axis.

Other symbols

$\mathbb{I}$	Identity tensor.
∇_s	Surface divergent operator.
$\cdot_s$	Subscript used to identify the quantities relative to the membrane model.

Chapter 1

Introduction

1.1 Encapsulation: definition and applications

Microencapsulation technology involves the immobilization of a fragile substance within a solid wall. The thin wall forms a physical barrier that protects the encapsulated substance against the external environment and controls its liberation. Depending on the wall mechanical properties, the internal substance can be liberated slowly by diffusion across the wall or rapidly if the wall ruptures or presents large pores as compared to the size of the encapsulated molecules.

The principle of microencapsulation is ubiquitous. Many instances may be found in nature. Seeds, eggs and cells can be considered as natural capsules since a wall separates the internal media from the external environment (Figures 1.1). Red blood cells are an example of "simple" natural capsules as they do not contain genetic material but are responsible for complex functions. Their wall is composed of two layers: a lipid bilayer (outer layer), which is incompressible and endows the wall with intrinsic viscosity and bending elasticity, and a cytoskeleton, which is composed of a network of highly extensible spectrin molecules and provides wall elastic properties. It protects the hemoglobin, which is the protein responsible for the transport of oxygen through the organism and the control of gas transfer to and from the tissues (Mohandas & Gallagher, 2008). With a diameter of 8 μm, red blood cells have the capability to squeeze through capillaries 3 μm in diameter during their life cycle of 120 days without breakup (Klöppel, 2012). They, hence, have remarkable mechanical properties that enable them to undergo large deformations.

One of the earliest industrial applications of capsules appeared in the 1930s in which

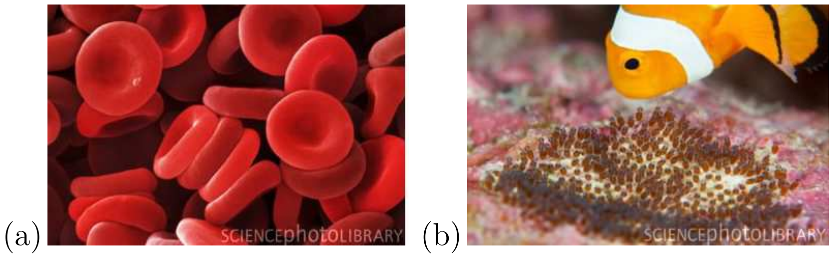

Figure 1.1: Examples of natural capsules: (*a*) red blood cells and (*b*) fish eggs (www.sciencephoto.com).

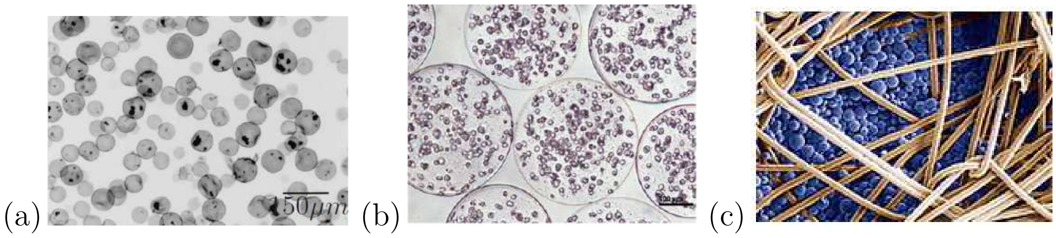

Figure 1.2: Examples of artificial capsules used (*a*) for drug delivery (Pariot *et al.*, 2002), (*b*) for cell encapsulation (Orive *et al.*, 2014) and (*c*) on textile (www.sciencephoto.com).

small capsules containing dye were used to copy typewritten material. The technique of encapsulation rapidly interested a large panel of manufacturers since it allowed to protect an internal substance from damage by environmental factors (acidity, alkalinity, evaporation, heat, oxidization, light, moisture, etc.) (Lam & Gambari, 2014). Microencapsulation became widely used in many industrial domains, such as agriculture (Gimeno, 1996), printing (She *et al.*, 2012), photography (T. Vandamme & Subra-Paternault, 2007) etc. We hereafter highlight a few examples of current use of capsules in the fields of biotechnology, pharmaceutics, food and textile industries.

In pharmaceutics, drugs are usually administrated orally or by injection. Orally administrated drugs have a limited efficacy and a low bioavailability since they are generally degraded by hepatic enzymes before reaching their target. Transdermal drug delivery is another possible technique of administration (Lam & Gambari, 2014; Bhujbal *et al.*, 2014), but the passage of the skin barrier leads to slow drug penetration rates and limited drug uptake. To deliver a sufficient amount of drug to a targeted area, a higher quantity must then be administrated, which can lead to systemic problem. Microencapsulation is a promising alternative since it provides a physical barrier to protect the active molecules, which increases their therapeutic efficiency, bioavailability and minimizes environmental damages (Ghirardi *et al.*, 1977) (Figure 1.2a). For example, insulin used to stabilize the glycemia level of patients with diabetes, is a protein–based drugs sensible to enzymatic degradation and thus has a poor oral bioavailability. Zheng *et al.* (2009) have developed insulin microcapsules, which improve glucose tolerance from 2 h in the case of free insulin to even 12 h in the case of insulin microcapsules. Microcapsules have also been used as carriers for anti–inflammatory (Valot *et al.*, 2009), antibiotic (Pandey *et al.*, 2003) and anti–tumor substances (Liu *et al.*, 2005). However, the complexity of preparation, the high manufacturing cost and the risk of allergic or immune reactions remain major drawbacks (Bhujbal *et al.*, 2014).

Cell encapsulation is another promising application of microencapsulation in biotechnology. It consists of the immobilization of cells within a microcapsule with a semipermeable polymeric wall (Figure 1.2b). The latter permits the passage of nutriments and oxygen from the external environment, which are necessary for cells to survive, and the exit of byproduct molecules produced by the cells. It also protects the cells from immune reactions. To guarantee the long–term functionality of the cells, one has to design capsules with suitable stability, biocompatibility, durability and diffusion properties. If so microcapsules with encapsulated cells have the potential to deliver drug over long periods of time. Microencapsulation of islets of Langerhans could offer a possible solution to the shortage of spleen donors and to the difficulties related to whole organ graft rejection (Clayton *et al.*, 1993; Ma & Su, 2013). Cell microencapsulation is also studied to treat neurological diseases, bone and cartilage defect and ischemic myocardial tissue (Ma & Su, 2013; Orive *et al.*, 2014).

Microencapsulation also has a high potential in food industry. It enables to protect sensitive components during the phase of food processing and passage through the gastrointestinal tract. It is otherwise used to create visible and textural effects, preserve the nutritional components and healthiness of ingredients, control their release and mask/preserve flavors (Yang *et al.*, 2014; Nazzaro *et al.*, 2012). However, microencapsulation results in additional costs, complicates the production process and may displease consumers in some cases (e.g. new textural effects). Encapsulation is thus not the first option when designing food formulations. Nevertheless, for the last few decades, the demand for encapsulation has been growing to render food products healthier and tastier (Zuidam & Shimoni, 2010).

Microencapsulation has found new applications in textile industry. It is used to produce biofunctional textiles, for which microcapsules are put onto the surface or incorporated into the fibers. Various substances can be encapsulated such as perfumes, dyes, antimicrobials, enzymes, flame retardants and insect repellents (Ocepek *et al.*, 2012). They can be liberated instantaneously by breakup when the textile touches the skin or over long period of times such as for perfumes. In this case, the challenge is to design capsules capable of withstanding harsh washing conditions (Li *et al.*, 2008).

These few examples show that microencapsulation is a promising technique, which could be used in a large panel of industrial domains in the future. However, industrial applications require encapsulation techniques, which are able to produce capsules with controlled size and mechanical properties adapted to their applications at stake. Encapsulation techniques developed to produce liquid–filled microcapsules will be presented in section 1.2. We will then describe methods to characterize the wall mechanical properties in section 1.3. As in most applications, capsules flow in an external flow, it is also necessary to characterize their dynamics when they are subjected to an external flow. A review of experimental and numerical studies of capsules in flow will be detailed in sections 1.4 and 1.5, respectively.

1.2 Fabrication of liquid–filled capsules

The fabrication of artificial capsules is typically composed of two steps. The first step consists of the generation of a liquid droplet with the required size and the second of the creation of the wall around the droplet. In this section, we will briefly summarize some classical as more recent techniques used to fabricate artificial capsules.

1.2.1 Classical techniques

Droplet formation

One of the most common methods to produce droplets is the emulsification process illustrated in Figure 1.3a (Edwards-Lévy *et al.*, 1994; Chu *et al.*, 2011). It is based on the use of two immiscible fluids. A dispersed phase is poured into a continuous phase subjected to a mechanical agitation. Due to the emulsification effect, a large number of droplets are generated. The average size of the fabricated droplets is controlled by the process parameters, i.e. the agitation velocity, emulsification time and fluids properties etc. It, however, produces droplets with a large size dispersion (up to 40%) (Chu, 2011). The inhomogeneity of the fabricated droplets also constitutes a limitation.

To generate droplets with more homogeneous size, an extrusion method can be used. It consists in extruding the dispersed phase through an orifice or a syringe needle under a controlled pressure (Gautier *et al.*, 2011; Zhang & Salsac, 2012) (Figure 1.3b). Under the effect of surface tension, droplets are formed one by one, which limits the number of fabricated droplets. The advantage of this technique is the homogeneity of the droplet size, which is controlled by the orifice/needle size and applied pressure.

Wall formation

The membrane around the droplets is generally formed by interfacial polycondensation (Bouchemal *et al.*, 2004; Janssen & Nijenhuis, 1992) or interfacial cross–linking polymerization (Chu *et al.*, 2011; Edwards-Lévy *et al.*, 1994). A solution of monomers is used as dispersed phase to form droplets. A cross–linking agent is then poured in the continuous phase which contains the droplets. The cross–linking agent induces a reaction between the monomers to form the wall. The reaction is typically stopped through rinsing. It may also stop naturally if the reaction is no longer possible across the increasingly thicker wall. The size of the fabricated capsules depends on the size of the droplets and on the capacity of the two monomers to react together.

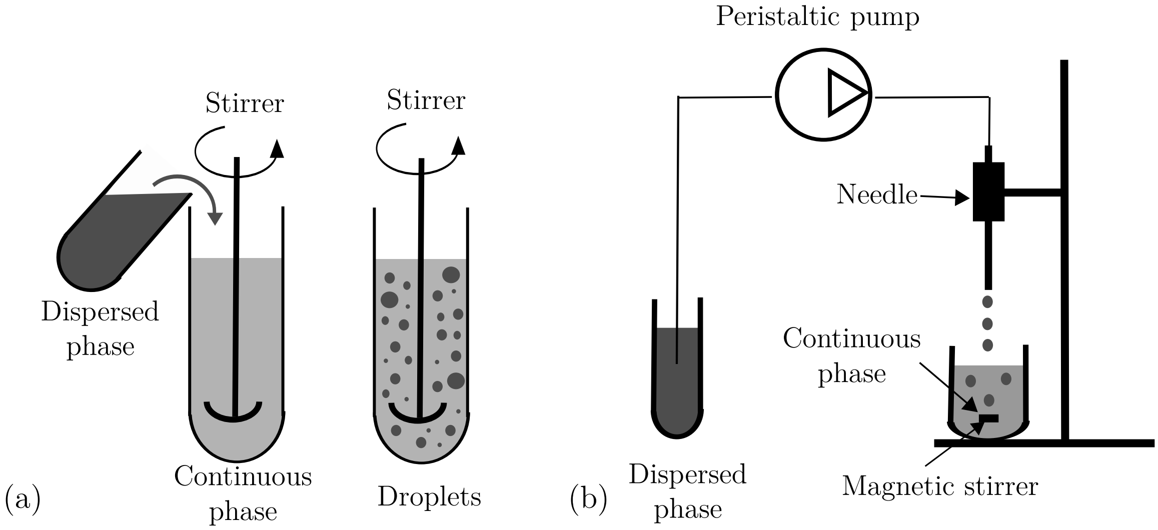

Figure 1.3: Fabrication of droplets (*a*) from the emulsification process produced by a mechanical agitation and (*b*) from an extrusion process.

1.2.2 Microfluidic techniques

The fabrication of microcapsules with a homogeneous and controlled size is important in many applications. Over the past few years, several microfluidic techniques have been developed to produce capsules.

A simple method to generate droplets with a microfluidic device is based on the control of the flow of non–mixing phases through bifurcating microchannels. The two most common channel geometries used to generate droplets are:

- the **cross–flowing** or **T–junction** (Garstecki *et al.*, 2006; Koleva & Rehage, 2012). Introduced by Thorsen *et al.* (2001), this geometry is composed of a main channel, where the continuous phase flows and a channel perpendicular to it, where the dispersed phase is injected (Figure 1.4a).

- the **flow focusing** or **Y–junction** (Ganán-Calvo & Gordillo, 2001; Anna *et al.*, 2003; Chu *et al.*, 2013). This system is composed of a central channel and two lateral channels. The dispersed phase is injected in the central channel and the continuous phase in the lateral channels (Figure 1.4b).

At the junction, a droplet forms when the flow of the dispersed phase penetrates into the main channel and is split by the continuous phase flow: the shearing forces applied by the continuous phase draws the interface between the two fluids into the direction of the flow of the continuous phase and forms a neck. Due to the continuous phase flow, the neck breaks and a droplet is generated. The droplet size is controlled by the geometry (channel size, angle between the main and lateral channels), fluids properties (viscosity, wetting

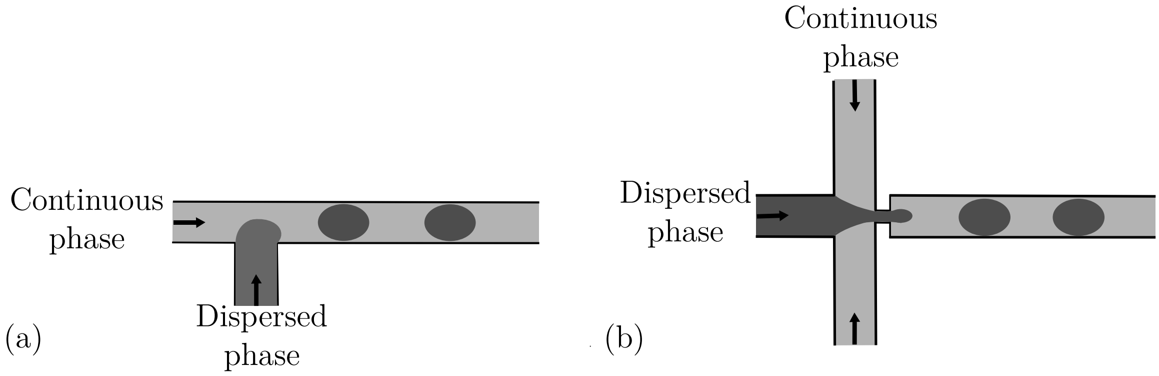

Figure 1.4: Schematic of the droplet formation processes (a) in a cross–flowing (or T–junction) geometry or in (b) in a flow focusing geometry.

properties) and experimental parameters (temperature, flow rate). This technique allows to produce easily droplets with a strong control of their size and a high monodispersity.

Like in bulk methods, the wall around the droplets is generally formed by interfacial reaction. After their production in the microfluidic device, droplets can be collected in a reservoir containing a cross–linking agent to generate microcapsules by interfacial polymerization (Huang *et al.*, 2007; Yeh *et al.*, 2009). One issue is that the wall mechanical properties are generally not homogeneous over the entire batch since the reaction time depends on the moment when the droplet is produced: the first droplet will be in contact with the cross–linking agent for a longer time than the last one.

In order to control the reaction time, and consequently the wall mechanical properties, microfluidic systems have been developed to generate droplets and then form the membrane within the same microsystem (Zhang *et al.*, 2006; Chu *et al.*, 2013). A schema of the microsystem developed by Chu *et al.* (2013) is represented in Figure 1.5. The microsystem is composed of two parts: a first junction to fabricate the droplets and a second junction to inject the cross–linking agent. The time of cross–linking is then controlled by the length of a wavy channel located downstream of the second channel. Between the end of the wavy channel and the reservoir to collect the fabricated microcapsules, Chu *et al.* (2013) have added a cylindrical microchannel to characterize the wall mechanical properties by inverse analysis as described in the following section.

1.3 Characterization of the capsule wall mechanical properties

Different techniques exist to characterize the physical (porosity) and mechanical properties of capsules. In this section, we will highlight three of them, which have been developed to

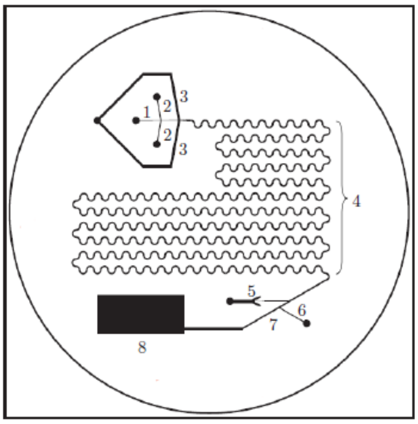

1: Dispersed phase flow
2: Continuous phase injection
3: Cross–linking agent injection
4: Wavy channel to control the reaction time
5: Channel to remove cross–linking agent
6: Injection of a continuous phase to dilute the residual of cross–linking agent
7: Cylindrical channel to characterize the wall mechanical properties
8: Reservoir

Figure 1.5: Schematic representation of a microfluidic system to fabricate and characterize microcapsules in situ (Chu *et al.*, 2013).

determine the mechanical properties of the capsule wall. All the developed methods are based on the same idea. The capsule is deformed under a controlled stress, whether it is induced by compression, aspiration or under an external flow. A picture of the deformed capsule profile is visualized to compute the deformation and a mechanical model is then applied to deduce the wall mechanical properties.

1.3.1 Technique of compression

One possible method to determine the mechanical properties of spherical millimetric capsules is to compress them between two solid parallel plates at a constant velocity (Carin *et al.*, 2003; Rachik *et al.*, 2006). During the experiment, the distance $d(t)$ between the two plates and the resultant force on the capsule are recorded. Knowing the initial diameter of the capsule (denoted $2\,r_0$ on Figure 1.6) and the time evolution of the distance $d(t)$ between the two plates, the capsule deformation can be computed as a function of time. A mechanical model is then used to estimate the intrinsic mechanical properties of the capsule wall, such as the apparent elastic modulus from the capsule deformation and the resultant force.

Rachik *et al.* (2006) have used this method to determine the influence of the thickness of serum albumin–alginate capsule membranes on the Young modulus. They have shown that the Young modulus does not increase linearly with the thickness. The fabrication of thicker wall results in stiffer capsules.

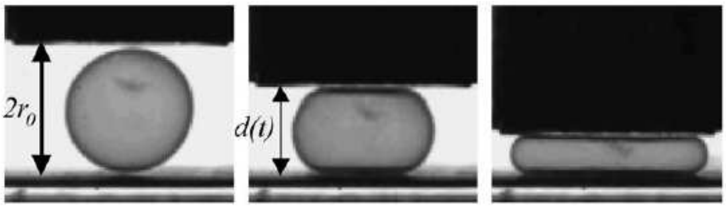

Figure 1.6: Compression of an initially spherical capsule between two parallel plates (Rachik *et al.*, 2006).

1.3.2 Micropipette aspiration technique

In the case of microcapsules, the mechanical characterization of the wall properties is a challenging task due to the small size of the objects. The micropipette aspiration technique has been successfully used to study the deformability of vesicles (liquid droplets enclosed by a fluid membrane) (Kwok & Evans, 1981; Evans & Rawicz, 1990), cells such as red blood cells (Hochmuth, 2000) and artificial capsules (Heinrich & Rawicz, 2005).

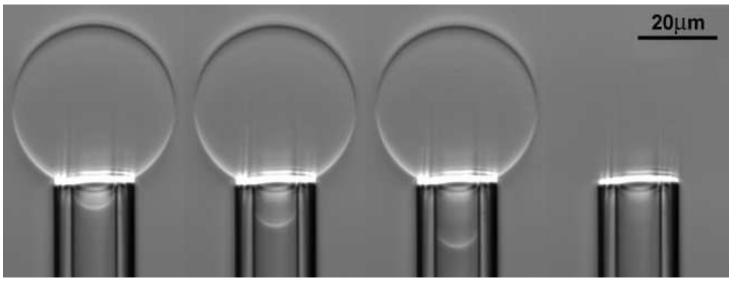

Figure 1.7: Aspiration of a phospholipid vesicle by a micropipette under a linear pressure until its rupture (Heinrich & Rawicz, 2005).

As illustrated in Figure 1.7, a capsule is aspirated through a micropipette with an inner diameter of several micrometers under a controlled pressure. The capsule deformation into the micropipette depends on the applied pressure and is monitored by microscopy as a function of the applied pressure. A mechanical model, which depends on the material to characterize, is then used to determine the membrane elastic properties. For example, Aoki *et al.* (1997) and Alexopoulos *et al.* (2003) have developed a model to interpret the results obtained with biological incompressible membrane.

This technique is able to deform a capsule wall under a controlled pressure. However, a limited number of capsules can be characterized with this technique since it requires to manipulate skillfully capsules one by one.

1.3.3 Microfluidic technique

In order to characterize the wall mechanical properties of a capsule population, microfluidic techniques have been developed. The principle of the microfluidic techniques is illustrated in Figure 1.8. They consist of flowing a capsule suspension into a microfluidic channel with cross dimension of the same order as the capsule size. Capsules undergo large deformation due to hydrodynamic forces and boundary confinement. Capsules can take either a parachute shape (Figure 1.8) or a slug shape. The wall mechanical properties are then deduced by comparing the experimental recorded capsule profiles with the one obtained with numerical model of the set–up.

Lefebvre *et al.* (2008) and Chu *et al.* (2011) have deformed the capsule into a cylindrical glass capillary tube to determine the mechanical properties of ovalbumin membrane using an axisymmetric model. One limitation of the technique comes from the difficulty to connect the small cylindrical capillary tube to the pumping device. Microfluidic technologies may offer easier solutions to connect the capillary tube but the tubes thus produced usually have a square or rectangular cross–section owing to fabrication constraint. Experiments can no longer be analyzed with an axisymmetric model and require a specific model of the flow of a capsule in a square or a rectangular pore. Hu *et al.* (2013) have recently proven that the identification technique can be transposed to the case of a square–section channel, if one simulates the three–dimensional fluid–structure interactions of the capsule flowing in a square–section channel (Hu *et al.*, 2012).

1.4 Capsules in an external flow: experimental observations

Capsules are generally subjected to an external flow in most their applications. They undergo large deformations because of the strong fluid–structure viscous coupling of the wall with the internal and suspending fluid flows. A good understanding of the capsule motion and deformation is essential but few experimental studies have so far been conducted owing to the difficulty to measure the deformation of a small–size particle flowing in a controlled flow environment. In this section, we are interested specifically in the dynamics of a liquid–filled capsule in an unbounded external flow and not in the collective behavior of suspensions.

Two types of flow are generally considered to study capsule deformation: a planar hyperbolic flow and a simple shear flow. These flows were first used by Taylor (1934) to study the behavior of droplets in Stokes flow. Experiments of artificial capsules suspended in a planar hyperbolic flow can either be generated at the center of a four–roller device or at the center of a cross–like channel as it has been done more recently (Figure 1.9a) (de Loubens *et al.*, 2014). They show that an initially spherical capsule is elongated in the elongational direction and compressed in the perpendicular direction until it reaches a steady state (Figures 1.9 b, c) (Akchiche, 1987; Barthès-Biesel, 1991; Chang & Olbricht,

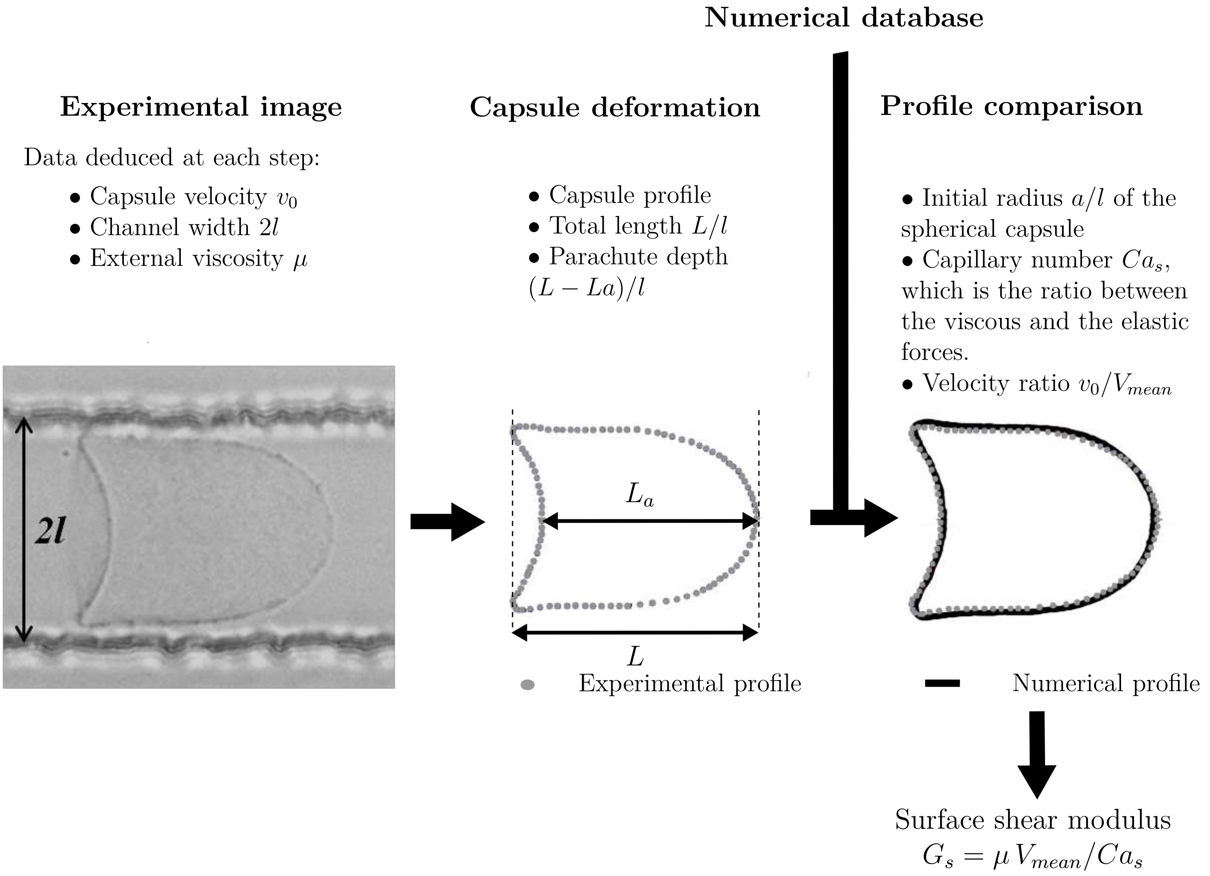

Figure 1.8: Principe of the inverse analysis used to deduce the wall mechanical properties of a capsule flowing in a square–section channel (Hu *et al.*, 2013).

1993*a*; de Loubens *et al.*, 2014). At steady state, the capsule wall and the internal fluid are fixed, irrespectively of the internal viscosity.

The deformation of an artificial microcapsule subjected to a simple shear flow has relied on the use of a Couette apparatus with distant walls to neglect their influence on the capsule. It was observed by Chang & Olbricht (1993*b*), Walter *et al.* (2000, 2001) and Koleva & Rehage (2012) (Figure 1.10a). The capsule is elongated in the straining direction by the external flow. At steady state, the capsule wall rotates around the deformed shape because of the flow vorticity. This motion is called *tank–treading.* An interesting point revealed by Walter *et al.* (2001) and Koleva & Rehage (2012) is the membrane folding at low flow strength (Figure 1.10b).

Some small shape oscillations about the straining direction have been observed at steady state additionally to the tank–treaking (Koleva & Rehage, 2012; Walter *et al.*, 2001). This motion, called *swinging*, is due to the fact that artificial capsules are never perfectly spherical. The artificial capsules fabricated by Koleva & Rehage (2012) for instance had an aspect ratio of 0.97 - 0.99. A small deviation from sphericity is enough to

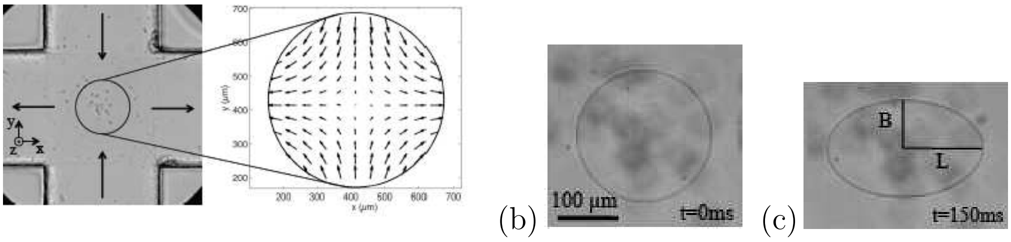

(a) (b) (c)

Figure 1.9: (*a*) Microfluidic system used to created a planar hyperbolic flow along with the velocity field observed by particle tracking velocimetry. (*b*) Initial capsule shape. (*c*) Capsule shape at steady state (de Loubens *et al.*, 2014).

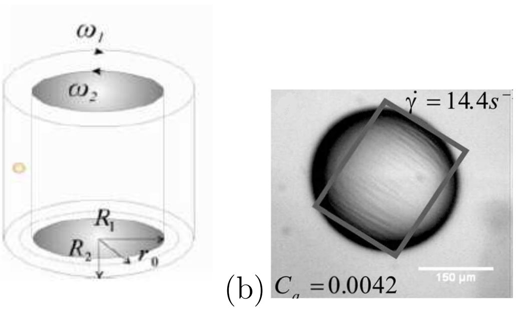

(a) (b)

Figure 1.10: (*a*) Couette apparatus used to created a simple shear flow. (*b*) Membrane folding of an initially spherical capsule at steady state (Koleva & Rehage, 2012).

induce motions, which are typically observed on red blood cells in shear flow depending on the shear rate, viscosity ratio between the internal and the external media, mechanical properties etc (Skotheim & Secomb, 2007). At low shear stress, a red blood cell exhibits a *tumbling* motion, which is a solid–like motion in which the cell axis of symmetry rotates in the shear plane (Figure 1.11a). If the viscosity of the surrounding fluid decreases, the cell membrane experiences a tank–treading motion as the one described previously for artificial capsules (Abkarian & Viallat, 2008). When the shear stress increases above a critical value, the cells follow a swinging motion, in which the cell orientation oscillates periodically on either side of the flow direction but stays in the shear plane (Abkarian *et al.*, 2007) (Figure 1.11b). Nevertheless, Dupire *et al.* (2012) have recently observed that a red blood cell in tumbling exhibits a *rolling* motion when the shear stress increases, if the revolution axis does not lie in the shear plane. In rolling, the axis of symmetry of the cell is perpendicular to the shear plane and the cell rotates like a wheel (Figure 1.11c). Even if most of the experimental observations of the motion of an ellipsoidal capsule in shear flow were conducted on red blood cells, artificial ellipsoidal capsules are interesting to use since they have a higher surface–to–volume ratio than spherical ones (for the same internal volume). This characteristic is particularly interesting for capsule applications since the mass transfer between the internal and external media is enhanced (Schneeweiss & Rehage, 2005). Thereby, some researchers have developed microfluidic devices to produce prolate

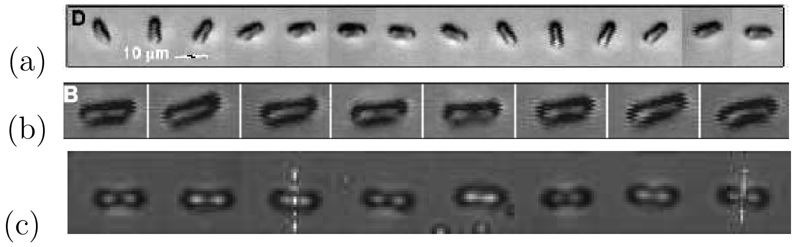

Figure 1.11: Dynamics of a red blood cell in shear flow: (*a*) tumbling, (*b*) swinging (Abkarian & Viallat, 2008) and (*c*) rolling (Dupire *et al.*, 2012). (*a*) and (*b*) are top views of the shear plane, whereas (*c*) is a side view.

or oblate microcapsules with arbitrary aspect ratio (Xiang *et al.*, 2008; Liu *et al.*, 2009). Sometimes, ellipsoidal artificial capsules are fabricated unintentionally when two droplets merge before adding the polymerizing agent to form the membrane (Chu, 2011).

1.5 Capsules in an external flow: numerical simulations

As we have seen on the previous section, the dynamics of a capsule in an external flow is a complex fluid–structure interaction problem. In order to understand the influence of capsule shape, wall mechanical properties and flow strength on the capsule dynamics, theoretical and numerical models have been developed. A good understanding of their influence is essential to design artificial capsules with the adequate properties for the targeted applications. In this section, we will highlight some strategies adopted to solve the fluid–structure interaction problem.

1.5.1 Theoretical studies

Barthès-Biesel (1980) studied for the first time the mechanism of deformation of a microcapsule subjected to a simple shear flow. She established the principal assumptions of the problem, which are always used nowadays: internal and external flows governed by Stokes equations, two–dimensional elastic membrane, large deformation. Inspired by the work done on droplets, she considered the influence of three parameters, the viscosity ratio between the two fluids, a non–dimensional number hereafter called surface capillary number, which compares the membrane elastic forces to the viscous forces and the membrane constitutive law, on the capsule deformation in the shear plane and orientation relative to the shear direction. She showed that the orientation of an initially spherical capsule in shear flow depends on the ratio between the internal and external viscosity: the more viscous the capsule, the more tilted it is towards the streamline. However, this theoretical study considers small deviation from the initial spherical shape and is limited to steady state configurations.

Barthès-Biesel & Rallison (1981) improved the model by studying the time deformation of an initially spherical capsule with a two–dimensional elastic membrane under an arbitrary Stokes flow. Transient phenomena could thus be studied with this method. However, theoretical studies are limited to small deformation. When a capsule undergoes large deformation, the problem becomes non–linear and numerical models are needed.

1.5.2 Axisymmetric models

Li *et al.* (1988) have studied numerically the dynamics of a capsule in an elongational flow. They introduce the coupling strategy, which is always used nowadays to solve this fluid–interaction problem. At each time step, the solid problem is solved to find the load exerted by the fluids on the membrane. The fluid problem is then solved to deduce the velocity of the membrane. The capsule deformation can then be updated. In this study, as the flow is assumed to be axisymmetric, the problem is integrated in the orthoradial direction and only half of the capsule contour is discretized with 48 collocation points. A boundary integral method is used to solve for the Stokes flows inside and outside the capsule. The capsule membrane equilibrium is expressed locally at each grid point of the capsule wall. The method is reasonably accurate and stable in large deformation, even if some numerical smoothing is necessary. This method has been used by Pozrikidis (1990) to investigate the dynamics of a red blood cell in a straining flow. Diaz *et al.* (2000) have improved the precision of the numerical method using B–spline functions to interpolate the position of the membrane points.

Lefebvre & Barthès-Biesel (2007) have used an axisymmetric method to simulate numerically the dynamics of a capsule in a cylindrical channel. As their numerical results are in agreement with experimental observations, their numerical model has been used to determine the mechanical properties of artificial capsule flowing in a cylindrical channel (Lefebvre *et al.*, 2008; Chu *et al.*, 2011). However, Lefebvre *et al.* (2008) and Chu *et al.* (2013) have observed experimentally membrane wrinkling due to compressive stresses in the orthoradial direction (Figure 1.12). The assumption of invariance in the orthoradial direction is thus not satisfied even if the base flow is axisymmetric.

1.5.3 Two–dimensional models

The capsule dynamics in an external flow has also been studied with two–dimensional models. The capsule membrane that encloses the internal medium is represented by an elastic line in motion in a plane and the internal volume conservation is replaced by the

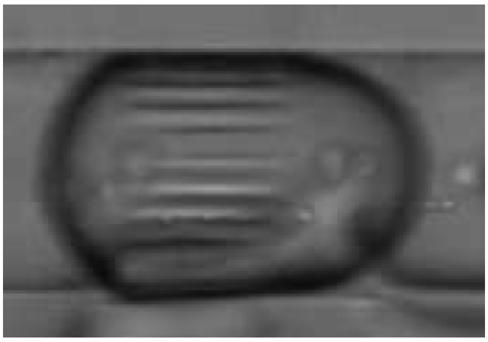

Figure 1.12: Wrinkling of the membrane of a cross–linked serum albumin capsule flowing in a cylindrical channel (Chu *et al.*, 2013).

invariance of the internal surface area.

Two–dimensional models allow to study non–axisymmetric problem, while maintaining reasonable time computations. For example, they have been used to simulate the migration of vesicles (Coupier *et al.*, 2008) or red blood cells (Secomb *et al.*, 2007) in a bounded flow and to study red blood cell dynamics in suspension (Bagchi, 2007).

It is, however, questionable whether these simplified two–dimensional models can provide quantitative accurate results, since capsules are three–dimensional objects. It seems for instance difficult for a two–dimensional model to simulate properly the post–buckling behavior of a capsule in shear flow since it is a three–dimensional phenomenon.

1.5.4 Three–dimensional membrane models

Pozrikidis (1995) studied, for the first time, the dynamics of a capsule in a simple shear flow with a three–dimensional numerical method. Other numerical methods have then been developed to simulate the capsule behavior in an external flow. They are based on the coupling strategy introduced by Li *et al.* (1988) but the manner to discretize and to resolve the solid and fluid problems differ.

Most of the three–dimensional models consider the capsule wall as a two–dimensional hyperelastic surface devoid of bending resistance. Two approaches have been adopted to solve the capsule membrane mechanics:

- The **strong form** is widely used to simulate the capsule dynamics. It consists in writing the equilibrium locally at each point of the capsule wall. Different approaches are then used to find the viscous load exerted on the membrane by the internal and external fluids: Pozrikidis (1995), Ramanujan & Pozrikidis (1998) and Li & Sarkar (2008) computed the membrane load as a piecewise constant function, Lac *et al.* (2004) and Lac & Barthès-Biesel (2005) used bi–cubic B–splines instead of interpolation functions to compute the loads with high accuracy, whereas

Dodson & Dimitrakopoulos (2008) used a spectral discretization of the problem.

- The **weak form**: the membrane equilibrium is written in its weak form to be converted into a variational problem. A finite element method is then used to find the viscous load exerted by the fluids on the membrane. This method is generally coupled with an immersed boundary method (Eggleton & Popel, 1998; Doddi & Bagchi, 2008*a*,*b*) or a boundary integral method (Walter *et al.*, 2010) to solve the fluid problem.

When a capsule is suspended in an external flow, its membrane and consequently the two fluid domains undergo large displacements. In order to avoid remeshing the fluid domains, three principal methods are applied:

- The **boundary integral method** (Ramanujan & Pozrikidis, 1998; Lac *et al.*, 2004; Dodson & Dimitrakopoulos, 2008; Walter *et al.*, 2010, 2011; Foessel *et al.*, 2011; Hu *et al.*, 2012). Introduced by Ladyzhenskaya (1969), this method allows, in Stokes flow, to discretize only the membrane which avoids meshing the fluid domains. The velocity of the membrane points is indeed expressed as a function of an integral on the problem boundary. Generally, the same mesh is used to solve the solid problem and compute the integral on the capsule wall.

- The **immersed boundary method**, developed by Peskin (2002). In this method, the internal and external fluids are discretized with a fixed Eulerian grid whereas the interface is discretized with a two–dimensional Lagrangian deformable mesh. This method is less accurate than the boundary integral method since the velocity and the load are exchanged between the solid and the fluids using approached Dirac functions. This method allows to consider large Reynolds numbers and non–Newtonian fluids.

- The **Lattice–Boltzmann method** used, for example, by Sui *et al.* (2010). Contrary to the more traditional methods, the fluid domains consist of fictive particles. The fluid particles can collide with each other as they move under applied forces. The rules governing the collisions are defined such that the time average motion of the particles follows the Navier–Stokes equation. This method allows treating complex boundaries, incorporating microscopic interactions and parallelizing the algorithm easily.

The numerical simulations of an initially spherical capsule in shear flow have recovered the tank–treading motion observed experimentally (Ramanujan & Pozrikidis, 1998; Lac *et al.*, 2004; Li & Sarkar, 2008; Walter *et al.*, 2010; Foessel *et al.*, 2011). The capsule motion and deformation depend on two main parameters: the surface capillary number and viscosity ratio between the external and the internal fluids. Wrinkle formation has been observed at low surface capillary number since the capsule is compressed in the equatorial region. When an initially spherical capsule is subjected to a planar hyperbolic flow, the phenomena of stretching in the elongational direction and compression in the perpendicular direction have also been studied numerically with a membrane model (Dodson & Dimitrakopoulos, 2008; Lac *et al.*, 2004; Walter *et al.*, 2010; Dimitrakopoulos, 2014; Dodson & Dimitrakopoulos, 2014). It was observed that the membrane also tends to buckle at low surface capillary number similarly to the simple shear flow case.

Motivated by the experimental observations on red blood cells and the interesting properties of the ellipsoidal capsules, the dynamics of non–spherical capsule have been also studied numerically using a membrane model (Ramanujan & Pozrikidis, 1998; Sui *et al.*, 2008; Walter *et al.*, 2011). Previous studies focused on the case when the capsule revolution axis is initially in the shear plane. They recovered the tumbling and the swinging motion observed on red blood cells. Walter *et al.* (2011) showed that the capsule motion depends on the flow strength but not on the capsule aspect ratio.

1.5.5 Three–dimensional models with bending resistance

Finken & Seifert (2006) showed that buckling and wrinkle formation, which are due to compressive stresses, are controlled by the wall bending resistance. In order to study the capsule post–buckling behavior, some numerical models were developed to take into account the capsule wall bending resistance. Pozrikidis (2001) studied, for the first time, the influence of bending resistance on the capsule deformation by computing the bending moments from the element curvature. However, inadequate spatial resolution leads to significant inaccuracies and numerical instability at large deformation.

Other studies have been inspired by the studies carried out on vesicles, for which the bending resistance is an important parameter (Kessler *et al.*, 2008; Le *et al.*, 2009; Hang *et al.*, 2012). They considered the capsule wall as a two–dimensional surface and decomposed the wall strain energy into the sum of a membrane elastic energy and of a bending energy computed from the local curvature. Le *et al.* (2009) and Hang *et al.* (2012) observed a significant influence of the bending resistance on the deformation of an initially spherical capsule when capsules have the same surface shear modulus. However, extremely high values of bending modulus are used: for a spherical capsule with a homogeneous wall, it would correspond to a wall thickness of more than half of the capsule radius. The value of bending modulus, which are considered, do not have any link with the bulk shear modulus of the wall and are thus unrealistic.

Only Le & Tan (2010) considered the capsule wall as a three–dimensional material and modeled it as a thin shell. They investigated the capsule behavior in large deformation but restricted the analysis to a Kirchhoff–Love kinematic assumption (i.e. no transverse shear) and only considered one value of bending resistance. The influence of the bending resistance on the capsule deformation is thus still an open question.

Contrary to most capsule models, the ones that are specifically developed to simulate red blood cells typically take into account the cell bending resistance. Many models of the mechanics of red blood cells are available in the literature but we have chosen to highlight two of them, which consider the mechanical behavior of the cytoskeleton and phospholipid bilayer. Recently, Klöppel & Wall (2011) developed a numerical model, where the cytoskeleton and the lipid bilayer are represented by two distinct layers of shell elements. The lipid bilayer behavior is described by an anisotropic viscoelastic constitutive model, which is associated with a incompressible shell elements, whereas the cytoskeleton is modeled as an isotropic hyperelastic third–order material. This model can be used to study the effects of defects or disease on the red blood cell dynamics. Peng *et al.* (2011) modeled also the lipid bilayer and the cytoskeleton as two distinct layers of continuum shells. A molecular-based constitutive model is used to obtain the mechanical properties of the cytoskeleton. This multiscale approach to model the red blood cell membrane allows to understand the correlation between the molecular structure.

At low flow strength, the capsule membrane buckling, previously observed by Walter *et al.* (2001), Koleva & Rehage (2012) and Chu *et al.* (2013) (Figures 1.10b, 1.12) is due to the hydrodynamic stresses exerted by the flows of the internal and suspending fluids. Wrinkling formation has also been observed in other fluid–structure interaction problems like in downwind yacht sails (Trimarchi, 2012). In order to capture the structural behavior and wrinkle formation, Trimarchi *et al.* (2013) used shell finite elements of the Mixed Interpolation of Tensorial Components (MITC) family. These elements allow to avoid locking phenomena of thin structures as sails.

1.6 Objectives

The dynamics of a capsule in an external flow is a complex fluid–structure interaction problem, for which some questions are still open. The first one is related to the membrane wrinkling, which is observed experimentally at low flow strength in an unbounded shear flow (Figure 1.10b) or in a channel (Figure 1.12). As we have seen in section 1.5.5, there are no existing numerical models to study the influence of realistic bending modulus on the capsule deformation and the wrinkle formation. It is important to study the capsule post–buckling behavior since wrinkling may weaken the capsule wall and the internal fluid could be liberated before reaching the desirable place. Our first objective is thus to develop a new numerical method to investigate the influence of the bending resistance on the capsule dynamics by modeling its wall as a thin shell with bending resistance. Based on the numerical method developed by Walter *et al.* (2010) in the Biomechanics and Bioingineering Laboratory (Université de Technologie de Compiègne, France), we couple a boundary integral method for the internal and external flows with a shell finite element method for the wall deformation to solve this fluid–structure interaction problem. The problem is presented in chapter 2. The new numerical model is outlined in chapter 3 and validated in chapter 4. The influence of the bending resistance on the dynamics of an initially spherical capsule in a simple shear flow or a planar hyperbolic flow is investigated in chapter 5 for various constitutive laws.

Since Dupire *et al.* (2012) has observed that red blood cell can exhibit a rolling motion in shear flow, the stability of the tumbling and the swinging motion of ellipsoidal capsules is a second open question. The second objective of this thesis is thus to determine the stable equilibrium configurations of a non–spherical capsule subjected to a simple shear flow, when capsule wall is modeled as a 2D surface devoid of bending resistance. We use the numerical method developed by Walter *et al.* (2010) and Foessel *et al.* (2011). The problem statement is briefly reminded in chapter 2. The stable equilibrium configurations of a prolate capsule in shear flow are identified in chapter 6. We determine the stable equilibrium configurations of an oblate capsule in shear flow and the time required for it to reach equilibrium in chapter 7. In this last chapter, we also determine the influence of the viscosity ratio between the internal and the external fluids on the stable equilibrium configurations of an oblate capsule.

Chapter 2

Capsule in Stokes flow

In this chapter, we will present the three–dimensional mechanical models for a capsule flowing in an infinite Stokes flow. After the presentation of the problem assumptions, we will briefly summarize the membrane BI–FE model introduced by Walter *et al.* (2010) to simulate the motion of a capsule made of an infinitely thin wall devoid of bending stiffness. The BI–FE model was generalized by Foessel *et al.* (2011) to account for any viscosity ratio between the internal and external media. The membrane model will be considered as our reference model when the wall thickness tends towards zero. We will then present the thin shell model used to investigate the influence of bending resistance on the capsule dynamics. Finally, the equations governing the fluid problem and the boundary integral method, which is used to solve them, will be introduced in the last section.

2.1 Problem assumptions

A microcapsule, consisting of a liquid droplet enclosed by a thin hyperelastic wall, is initially freely suspended in an external liquid. The internal and external fluids are both incompressible and Newtonian with viscosity $\lambda\mu$ and μ respectively, and have the same density ρ. The gravitational effect can be neglected at the microscopic scale.

As the capsule wall is assumed to be impermeable, the mass conservation of the internal flow is satisfied and the volume does not change over time. The capsule is thus characterized by the length scale ℓ defined as the radius of the sphere with the same volume V as the capsule:

$$\ell = \left(\frac{3V}{4\pi}\right)^{1/3}. \tag{2.1}$$

The capsule wall consists of a three–dimensional incompressible homogeneous material characterized by a bulk shear modulus G, a bending modulus M_b, a Poisson ratio $\nu = 0.5$ and a thickness $\alpha\ell$ with α the ratio between the wall thickness and the length scale ℓ. For a homogeneous material, the bending modulus M_b is given by

$$M_b = \frac{G}{6(1-\nu)}(\alpha\ell)^3. \tag{2.2}$$

Assuming that the capsule wall thickness is very small compared to the length scale, the wall will be modeled as:

- a **membrane**, i.e. a purely two–dimensional elastic surface $\mathcal{S}_t$ of surface shear modulus $G_s = \alpha \ell G$. The bending resistance is neglected compared to the elastic forces in the membrane.

- a **thin shell** defined by a mid–surface $\mathcal{S}_t$ at time t and the wall thickness $\alpha \ell$. In the case of a spherical capsule, ℓ represents the length between the capsule center and the mid–surface. In order to compare the bending and shear elastic forces, we introduce the bending number:

  $$K_b = \frac{M_b}{\alpha G \ell^3} = \frac{M_b}{G_s \ell^2} \tag{2.3}$$

  In the case of an incompressible homogeneous material, the bending number is simply written $K_b = \alpha^2/3$ from Eq. 2.2.

In this thesis, the capsule will be suspended in a simple shear flow with undisturbed velocity

$$\underline{v}^\infty = \dot{\gamma} y \underline{e}_x \tag{2.4}$$

or in a planar hyperbolic flow with undisturbed velocity

$$\underline{v}^\infty = \dot{\gamma}(x\underline{e}_x - y\underline{e}_y) \tag{2.5}$$

in the laboratory reference frame $\mathcal{F}(\mathrm{O}, \underline{e}_x, \underline{e}_y, \underline{e}_z)$ with O the center of mass of the capsule. The shear rate $\dot{\gamma}$ characterizes the external flow and is the time scale of the problem.

In order to characterize the interactions between the capsule and the internal and external flows, we introduce two capillary numbers:

- the bulk capillary number

  $$Ca_v = \frac{\mu \dot{\gamma}}{G}, \tag{2.6}$$

  which compares the viscous to the elastic forces in the case of the thin shell model.

- the surface capillary number

  $$Ca_s = \frac{\mu \dot{\gamma} \ell}{G_s} = \frac{Ca_v}{\alpha}, \tag{2.7}$$

which compares the viscous to the surface elastic forces. This surface capillary number is classically denoted Ca when the capsule is modeled as a membrane.

We denote the vectors in the reference and deformed configurations with uppercase and lowercase letters respectively. The surface tensor components will be designed with

Greek subscripts and the three–dimensional tensor components with Latin indices. The quantities relative to the membrane model are denoted with the subscript "s". We adopt the Einstein summation convention on repeated indices.

2.2 Membrane model

2.2.1 Membrane mechanics

In the membrane model, the thickness of the capsule wall is assumed to be small compared to the capsule dimensions and typical radius of curvature. The capsule is then modeled as a two–dimensional isotropic hyperelastic surface $\mathcal{S}_t$ at time t with shear modulus G_s and area dilatation modulus K_s. It is assumed to be devoid of bending resistance. In this section, we will briefly describe the membrane mechanics. More details can be found in Walter *et al.* (2010) and Barthès-Biesel *et al.* (2010).

A membrane material point, identified by its position $\underline{X}_s$ in the reference state, is displaced to the position $\underline{x}_s(\underline{X}_s, t)$ in the deformed state through the displacement $\underline{u}_s$

$$\underline{x}_s(\underline{X}_s, t) = \underline{X}_s + \underline{u}_s(\underline{X}_s, t). \tag{2.8}$$

At each time t, the position $\underline{x}_s$ is found by solving the fluid problem. As we neglect the wall bending resistance, the deformation occurs only in the plane of the membrane and the normal vector remains normal to the surface during the deformation. The Green deformation tensor is

$$\underline{\underline{C}}_s = \underline{\underline{F}}_s^T \cdot \underline{\underline{F}}_s, \tag{2.9}$$

where $\underline{\underline{F}}_s$ represents the transformation gradient defined as $\underline{\underline{F}}_s = \partial \underline{x}_s / \partial \underline{X}_s$. The local deformation of the surface is measured by the surface Green–Lagrange strain tensor

$$\underline{\underline{e}}_s = \frac{1}{2}(\underline{\underline{F}}_s^T \cdot \underline{\underline{F}}_s - \mathbb{I}) \tag{2.10}$$

with $\mathbb{I}$ the identity tensor. The membrane deformation can also be quantified by the principal dilation ratios λ_{s1} and λ_{s2} in the membrane plane, which correspond to the eigenvalues of $\underline{\underline{e}}_s$. The two invariants of the transformation I_{s1} and I_{s2} can be defined by

$$\begin{aligned} I_{s1} &= \operatorname{tr} \underline{\underline{C}}_s - 2 = \lambda_{s1}^2 + \lambda_{s2}^2 - 2, \\ I_{s2} &= \det \underline{\underline{C}}_s - 1 = \lambda_{s1}^2 \lambda_{s2}^2 - 1. \end{aligned} \tag{2.11}$$

The ratio of the deformed membrane area to the reference area is measured by the Jabobian $J_s = \det \underline{\underline{F}}_s = \lambda_{s1} \lambda_{s2}$.

The material mechanical properties are given by the strain energy function $w_s(I_{s1}, I_{s2})$ per unit area of undeformed membrane. Since the capsule wall is modeled as a two–dimensional material, the elastic stresses are replaced by elastic tension tensors, which correspond to forces per unit arc length measured in the plane of deformation. The Piola–Kirchhoff tension tensor is defined as

$$\underline{\underline{\pi}} = \frac{\partial w_s}{\partial \underline{\underline{e}}_s}. \tag{2.12}$$

The Cauchy tension tensor $\underline{\underline{T}}$ is related to the Piola–Kirchhoff tension tensor by

$$\underline{\underline{T}} = \frac{1}{J_s} \underline{\underline{F}}_s \cdot \underline{\underline{\pi}} \cdot \underline{\underline{F}}_s^T. \tag{2.13}$$

2.2.2 Constitutive laws

In large deformation, thin hyperelastic membrane can have a *strain–softening* behavior as gelled membranes exhibiting rubber–like elasticity or a *strain–hardening* behavior as membranes made of a polymerized network with strong covalent links. A number of constitutive laws were introduced to describe these different behaviors. However in this thesis, we will consider only three laws with constant material coefficients.

Generalized Hooke's law

The Hooke's law, which describes the mechanical behavior of homogeneous isotropic linear material, is the first–order linearization of any hyperelastic material Law. It assumes that the Piola–Kirchoff tension tensor depends linearly on the Green–Lagrange strain tensor such as

$$\underline{\underline{\pi}} = \underline{\underline{\mathcal{H}}}_s : \underline{\underline{e}}_s. \tag{2.14}$$

However, in many cases, the assumption of homogeneity and isotropy is not fulfilled and a more general formulation is required. This law is called generalized Hooke's law. It keeps the linear proportionality between the stress and strain tensors but the non–linear expression of the strain tensor is used.

For a two–dimensional material, the strain energy function is

$$w_s = \frac{G_s^{HG}}{4}\left(2I_{s1} - 2I_{s2} + \frac{1}{1-\nu_s} I_{s1}^2\right) \tag{2.15}$$

with ν_s the surface Poisson ratio. The surface Poisson ratio ν_s, the surface shear modulus G_s and the area dilatation modulus K_s are linked by $K_s = G_s(1+\nu_s)/(1-\nu_s)$ with $\nu_s \,]{-1}, 1[$.

Neo–Hookean law

Appropriate to model the behavior of protein–reticulated membrane (Carin *et al.*, 2003; Chu *et al.*, 2011), the neo–Hookean law (NH) describes the behavior of an infinitely thin sheet of a three–dimensional isotropic and incompressible material. For a two–dimensional material, the strain energy function of the neo–Hookean law is given by

$$w_s^{NH} = \frac{G_s^{NH}}{2}\left(I_{s1} - 1 + \frac{1}{I_{s2}+1}\right). \tag{2.16}$$

The area dilatation is balanced by membrane thinning because of the volume incompressibility. The link between the area dilatation modulus and the surface shear modulus is $K_s^{NH} = 3G_s^{NH}$ when $\nu_s = 0.5$.

Skalak law

Introduced by Skalak *et al.* (1973) to model the large deformation of biological membranes such as red blood cells, the Skalak law (SK) is written

$$w_s^{Sk} = \frac{G_s^{Sk}}{2}\left(I_{s1}^2 + 2I_{s1} - 2I_{s2} + CI_{s2}^2\right), \qquad C > -1/2. \tag{2.17}$$

The parameter C relates the area dilatation modulus K_s to surface shear modulus G_s such that $K_s = (1+2C)G_s$. The law is used to describe biological membranes that are nearly incompressible, by imposing large values of the parameter C. However, this law is general and can describe the behavior of membranes, such as albumin–alginate membrane, for which the area dilatation modulus K_s and the surface shear modulus G_s are of the same order of magnitude (Carin *et al.*, 2003).

Comparison of laws

In the limit of small deformation, these three laws reduce to the two–dimensional Hooke's law with surface shear elastic modulus G_s, if the surface Poisson ratio equals $\nu_s = 0.5$ and the parameter of the Skalak law $C = 1$. However, large differences occur under large deformation. Under an uniaxial stretching ($T_{11} \neq 0$ and $T_{22} = 0$), Figure 2.1 shows that the Generalized Hooke's law and the Skalak law ($C = 1$) are strain–hardening, whereas the neo–Hookean is strain–softening.

2.2.3 Membrane equilibrium

Owing to the negligible inertia of a membrane with small thickness, the Cauchy tension tensor $\underline{\underline{T}}$ and the external load $\underline{q}$ exerted by the fluids on the membrane are in equilibrium.

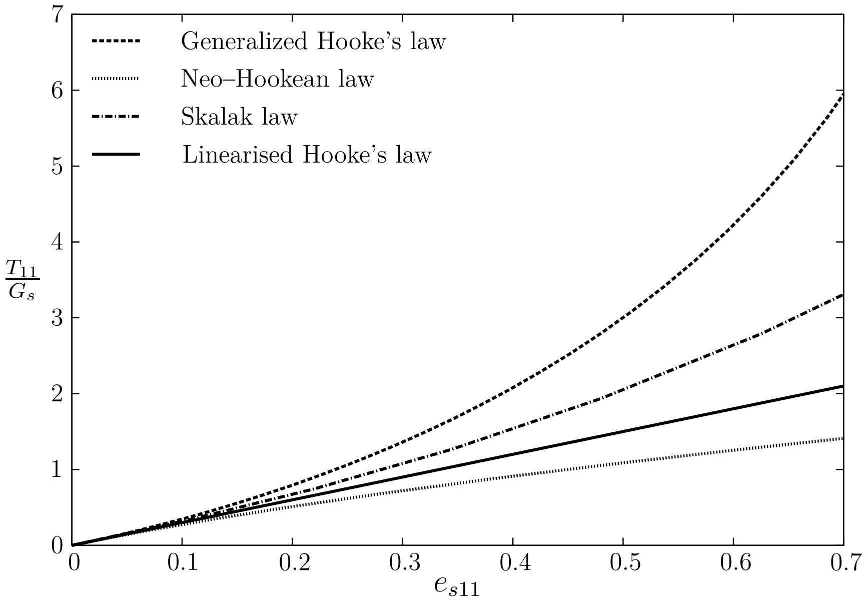

Figure 2.1: Evolution of the principal tension T_{11}/G_s as a function of the deformation e_{S11} during an uniaxial test.

The membrane motion is thus governed by the local equilibrium equation

$$\underline{\nabla}_s \cdot \underline{\underline{T}} + \underline{q} = \underline{0}, \tag{2.18}$$

where $\underline{\nabla}_s$ represents the surface divergence operator in the deformed configuration.

The principal of virtual work is then applied to deduce the weak form of the equation (2.18), on which the finite element method is based. Let $\mathcal{V}$ be the Sobolev space $H^1(\mathcal{S}_t, \mathbb{R}^3)$. For any virtual displacement field $\hat{\underline{u}}_s \in \mathcal{V}$, the virtual work of the external fluid forces balances the virtual work of the membrane elastic forces. The solid problem is written

$$\forall \hat{\underline{u}}_s \in H^1(\mathcal{S}_t, \mathbb{R}^3), \text{ find } \underline{q} \text{ such as}$$

$$\int_{\mathcal{S}_t} \hat{\underline{u}}_s \cdot \underline{q} \, dS = \int_{\mathcal{S}_t} \hat{\underline{\underline{\epsilon}}}_s(\hat{\underline{u}}_s) : \underline{\underline{T}} \, dS, \tag{2.19}$$

where $\hat{\underline{\underline{\epsilon}}}_s(\hat{\underline{u}}_s) = \frac{1}{2}(\underline{\nabla}_s \, \hat{\underline{u}}_s + \underline{\nabla}_s \, \hat{\underline{u}}_s^T)$ denotes the virtual deformation tensor and is computed from $\underline{x}_s$ found by solving the fluid problem.

2.3 Thin shell model

The thin shell model assumes that the capsule wall is thin enough to be modeled as a shell defined by its mid–surface $\mathcal{S}_t$ at time t and wall thickness $\alpha\ell$. The principle of the thin shell consists of evaluating all the quantities of interest on the mid—surface. In practice, it is commonly accepted that the thin shell approximation is valid for $\alpha < 10\%$. When the wall is devoid of bending resistance, the mid–surface corresponds to the two–dimensional surface of the membrane model.

2.3.1 Shell geometric definition

In the laboratory reference frame $\mathcal{F}(O, \underline{e}_x, \underline{e}_y, \underline{e}_z)$, it is convenient to introduce the independent curvilinear coordinates (ξ^1, ξ^2, ξ^3) to describe the curved mid–surface. In the reference configuration, the position of a point M of the mid–surface is given by

$$\underline{OM} = \underline{\varphi}(\xi^1, \xi^2). \tag{2.20}$$

The local covariant base ($\underline{A}_1$,$\underline{A}_2$,$\underline{A}_3$) is then defined such as

$$\underline{A}_\alpha = \frac{d\underline{\varphi}(\xi^1, \xi^2)}{d\xi^\alpha} = \underline{\varphi}_{,\alpha} \qquad \text{and} \qquad \underline{A}_3 = \frac{\underline{A}_1 \times \underline{A}_2}{\| \underline{A}_1 \times \underline{A}_2 \|} \tag{2.21}$$

to study easily the mid–surface deformation. $\underline{A}_3$ represents the unit normal vector. The contravariant base $(\underline{A}^1, \underline{A}^2, \underline{A}^3)$ is then deduced using $A^\alpha \cdot A_\beta = \delta^\alpha_\beta$, with δ^α_β the Kronecker tensor and $\underline{A}^3 = \underline{A}_3$.

In the reference configuration, the three–dimensional position of a point $\underline{X}$ within the capsule wall is denoted

$$\underline{X}(\xi^1, \xi^2, \xi^3) = \underline{\varphi}(\xi^1, \xi^2) + \xi^3 \underline{A}_3 \tag{2.22}$$

with $|\xi^3| < \alpha\ell/2$.

In the reference configuration, the three–dimensional covariant base $(\underline{G}_1, \underline{G}_2, \underline{G}_3)$ is defined as

$$\underline{G}_\alpha = \underline{X}_{,\alpha} = \underline{A}_\alpha + \xi^3 \underline{A}_{3,\alpha} \qquad \text{and} \qquad \underline{G}_3 = \underline{A}_3. \tag{2.23}$$

The volumemetric tensor is $G_{ij} = \underline{G}_i \times \underline{G}_j$ such that

$$\begin{cases} G_{\alpha\beta} = \underline{G}_\alpha \cdot \underline{G}_\beta \\ G_{\alpha 3} = \underline{G}_\alpha \cdot \underline{G}_3 = 0 \\ G_{33} = \underline{G}_3 \cdot \underline{G}_3 = 1. \end{cases}$$

The contravariant base $(\underline{G}^1, \underline{G}^2, \underline{G}^3)$ is defined by $G^\alpha \cdot G_\beta = \delta^\alpha_\beta$.

The local three–dimensional covariant and contravariant bases are also defined in the deformed state using lowercase letters: they are respectively denoted $(\underline{a}_1, \underline{a}_2, \underline{a}_3)$ and $(\underline{a}^1, \underline{a}^2, \underline{a}^3)$ for the base defined according to the position of a point in the mid–surface, $(\underline{g}_1, \underline{g}_2, \underline{g}_3)$ and $(\underline{g}^1, \underline{g}^2, \underline{g}^3)$ for the base defined according to the three–dimensional position of the same point.

Some essential symmetric tensors are now introduced for the shell analysis in the deformed configuration. The metric tensors defined according to the local covariant base $(\underline{a}^1, \underline{a}^2, \underline{a}^3)$ and contravariant vectors $(\underline{a}_1, \underline{a}_2, \underline{a}_3)$ are called *first fundamental form* of the surface. In the deformed configuration, they are given by

$$a_{\alpha\beta} = \underline{a}_\alpha \cdot \underline{a}_\beta, \qquad a^{\alpha\beta} = \underline{a}^\alpha \cdot \underline{a}^\beta, \tag{2.24}$$

and represent the restriction of the three–dimensional metric tensor to the tangent plane.

The curvature tensor $\underline{\underline{b}}$, called *second fundamental form* of the surface, is another important second–order tensor, since it contains all the information concerning the surface curvature. It is defined by

$$b_{\alpha\beta} = \underline{a}_3 \cdot \underline{a}_{\alpha,\beta}. \tag{2.25}$$

Its covariant–contravariant components are given by

$$b^\alpha_\beta = a^{\alpha\lambda} b_{\lambda\beta} = -\underline{a}_{3,\beta} \cdot \underline{a}^\alpha = \underline{a}^\alpha_{,\beta} \cdot \underline{a}_3 \tag{2.26}$$

The mean and the Gaussian curvatures of the surface respectively are

$$C_m = \frac{1}{2}\left(b^1_1 + b^2_2\right) = \frac{1}{2}\mathrm{tr}\,\underline{\underline{b}} \qquad \text{and} \qquad C_G = b^1_1 b^2_2 - b^1_2 b^2_1 = \det \underline{\underline{b}}. \tag{2.27}$$

2.3.2 Shell kinematics

In the deformed configuration, the new position $\underline{x}$ of a material point differs from its initial position $\underline{X}$ through the unknown displacement $\underline{u}$:

$$\underline{x}(\underline{X}, t) = \underline{X} + \underline{u}(\underline{X}, t), \tag{2.28}$$

where the vector $\underline{u}$ represents the displacement between the initial and deformed configurations. In the shell model, we assume that the displacement $\underline{u}$ satisfies the Reissner–Mindlin kinematical assumption (Chapelle & Bathe, 2011), i.e. a material line initially orthogonal to the mid–surface remains straight and unstretched during deformation but does not remain orthogonal to the deformed mid–surface. All the terms depending on $(\xi^3)^2$ are thus neglected in the expression of the displacement $\underline{u}$, which can then be written as

$$\underline{u}(\xi^1, \xi^2, \xi^3, t) = \underline{u}_s(\xi^1, \xi^2, t) + \xi^3\, \theta_\lambda(\xi^1, \xi^2, t)\, \underline{a}^\lambda(\xi^1, \xi^2). \tag{2.29}$$

In this expression, the first term represents the displacement of a line perpendicular to the mid–surface at coordinates (ξ^1, ξ^2). The angles θ_1 and θ_2 represent the rotations of the line around the tangential vectors $\underline{a}^1$ and $\underline{a}^2$, respectively. In the case of the Reissner–

Mindlin kinematical assumption, the rotation vector is not defined along $\underline{a}^3$. To simplify the notation, we introduce the rotation vector $\underline{\theta}(\xi^1, \xi^2, t) = \theta_\lambda\,(\xi^1, \xi^2, t)\underline{a}^\lambda(\xi^1, \xi^2, t)$ and equation (2.29) then reads

$$\underline{u}(\xi^1, \xi^2, \xi^3, t) = \underline{u}_s(\xi^1, \xi^2, t) + \xi^3\,\underline{\theta}(\xi^1, \xi^2, t). \tag{2.30}$$

In this equation, the displacement $\underline{u}_s$ is deduced from the fluid problem and the rotational term $\underline{\theta}$ is an unknown.

The deformation gradient $\underline{\underline{F}}$ links the covariant base vectors in the reference and current configurations

$$\underline{g}_i = \underline{\underline{F}} \cdot \underline{G}_i. \tag{2.31}$$

It is generally a non–symmetric second–order tensor. Its determinant, the Jacobian $J = \det(\underline{\underline{F}})$, has to be non–zero.

The Green–Lagrange strain tensor is defined by

$$\underline{\underline{e}} = \frac{1}{2}\left(\underline{\underline{F}}^T \cdot \underline{\underline{F}} - \mathbb{I}\right). \tag{2.32}$$

In the contravariant base, this expression becomes

$$\begin{aligned} \underline{\underline{e}} &= \frac{1}{2}\left(\underline{\underline{F}}^T \cdot \underline{\underline{F}} - \underline{\underline{G}}\right) \\ &= e_{ij}\;\underline{G}^i \otimes \underline{G}^j \end{aligned} \tag{2.33}$$

with

$$\begin{aligned} e_{ij} &= \frac{1}{2}\left(g_{ij} - G_{ij}\right) \\ &= \frac{1}{2}\left(\underline{u}_{,i} \cdot \underline{G}_j + \underline{u}_{,j} \cdot \underline{G}_i + \underline{u}_{,i} \cdot \underline{u}_{,j}\right) \end{aligned} \tag{2.34}$$

using the definition of the covariant base vectors $\underline{g}_i$ in the current configuration.

The Reissner–Mindlin kinematical assumption implies that $e_{33} = 0$. However, using the definitions of the displacement field (Eq. 2.30) and the covariant base vectors, we find that e_{13} and e_{23} are non–zero and both involve the rotation θ_λ. Under the Reissner–Mindlin kinematical assumption, the expression of the non–linear Green–Lagrange strain tensor is

$$\begin{cases} e_{\alpha\beta} = \gamma_{\alpha\beta}(\underline{u}_s) + \xi^3\chi_{\alpha\beta}(\underline{u}_s, \underline{\theta}) + (\xi^3)^2\kappa_{\alpha\beta}(\underline{\theta}), \\ e_{\alpha 3} = \zeta_\alpha(\underline{u}_s, \underline{\theta}), \\ e_{33} = 0. \end{cases} \tag{2.35}$$

The tensors $\underline{\underline{\gamma}}$, $\underline{\underline{\chi}}$ and $\underline{\underline{\kappa}}$ represent, respectively, the membrane, bending and curvature strain tensors, and $\underline{\zeta}$ the shear strain vector. They are defined by

$$\begin{cases} \gamma_{\alpha\beta} = \dfrac{1}{2}[\underline{A}_\alpha \cdot \underline{u}_{s,\beta} + \underline{A}_\beta \cdot \underline{u}_{s,\alpha} + \underline{u}_{s,\alpha} \cdot \underline{u}_{s,\beta}], \\ \chi_{\alpha\beta} = \dfrac{1}{2}[\underline{A}_\alpha \cdot \underline{\theta}_{,\beta} + \underline{A}_{3,\alpha} \cdot \underline{u}_{s,\beta} + \underline{A}_\beta \cdot \underline{\theta}_{,\alpha} + \underline{A}_{3,\beta} \cdot \underline{u}_{s,\alpha} + \underline{u}_{s,\beta} \cdot \underline{\theta}_{,\alpha} + \underline{u}_{s,\alpha} \cdot \underline{\theta}_{,\beta}], \\ \kappa_{\alpha\beta} = \dfrac{1}{2}[\underline{A}_{3,\alpha} \cdot \underline{\theta}_{,\beta} + \underline{A}_{3,\beta} \cdot \underline{\theta}_{,\alpha} + \underline{\theta}_{,\alpha} \cdot \underline{\theta}_{,\beta}, \\ \zeta_\alpha = \dfrac{1}{2}[\underline{A}_\alpha \cdot \underline{\theta} + \underline{A}_3 \cdot \underline{u}_{s,\alpha} + \underline{\theta} \cdot \underline{u}_{s,\alpha}], \end{cases} \tag{2.36}$$

in which the components of the shear strain vector $\underline{\zeta}$ depending on ξ^3 are neglected since the zero–order term can itself be proved to be of the order of the thickness at solution.

2.3.3 Shell equilibrium

Similarly to the membrane model, the Cauchy stress tensor $\underline{\underline{\sigma}}$, which corresponds to forces per unit area of deformed material, can be related to the Piola–Kirchhoff stress tensor $\underline{\underline{\Sigma}}$ by

$$\underline{\underline{\sigma}} = \frac{1}{J} \underline{\underline{F}} \cdot \underline{\underline{\Sigma}} \cdot \underline{\underline{F}}^T. \tag{2.37}$$

It follows that $\underline{\underline{\sigma}}$ is a non–linear function of strain in large deformation.

The wall equilibrium satisfies the following conditions

$$\begin{cases} \nabla \cdot \underline{\underline{\sigma}} = \underline{0} \text{ inside the wall,} \\ \underline{\underline{\sigma}} \cdot \underline{a}_3 = \underline{q}^+ \text{ on the external wall surface } \mathcal{S}_t^+, \\ \underline{\underline{\sigma}} \cdot \underline{a}_3 = -\underline{q}^- \text{ on the internal wall surface } \mathcal{S}_t^-, \end{cases} \tag{2.38}$$

where $\underline{q}^+$ (respectively $\underline{q}^-$) represents the viscous load per unit deformed area exerted by the external (respectively internal) fluid on the wall. Let $\mathcal{V}$ be the Sobolev space $H^1(\mathcal{S}_t, \mathbb{R}^3)$. For any virtual displacement $\underline{\hat{u}}_s \in H^1(\mathcal{S}_t, \mathbb{R}^3)$ and virtual rotation $\underline{\hat{\theta}} \in H^1(\mathcal{S}_t, \mathbb{R}^2)$, the wall equilibrium (Eq. 2.38) can be rewritten using the principle of virtual work as

$$\int_{\mathcal{S}_t^+} \underline{\hat{u}}\,(\underline{\hat{u}}_s, \underline{\hat{\theta}}) \cdot \underline{q}^+ \, dS - \int_{\mathcal{S}_t^-} \underline{\hat{u}}\,(\underline{\hat{u}}_s, \underline{\hat{\theta}}) \cdot \underline{q}^- \, dS = \int_V \underline{\underline{\hat{e}}}\,(\underline{\hat{u}}_s, \underline{\hat{\theta}}) : \underline{\underline{\sigma}} \, dV, \tag{2.39}$$

where V is the shell wall volume in the deformed state, $\underline{\hat{u}}$ an arbitrary kinematically admissible virtual displacement, which satisfies the Reissner–Mindlin assumption (Eq. 2.29) (Chapelle & Bathe, 2011) and $\underline{\underline{\hat{e}}}$ the corresponding virtual strain tensor. This equation means that the work done by the external loads acting on a deformable body equals to the virtual change in internal strain energy.

On $\mathcal{S}_t^+$, the virtual displacement reads

$$\underline{\hat{u}}\,(\xi^1,\xi^2,t) = \underline{\hat{u}}_s(\xi^1,\xi^2,t) + \frac{\alpha\ell}{2}\,\underline{\hat{\theta}}\,(\xi^1,\xi^2,t), \tag{2.40}$$

$+\alpha\ell/2$ being replaced by $-\alpha\ell/2$ on $\mathcal{S}_t^-$.

Since the capsule wall is treated as a thin shell for both the real and virtual displacement fields, the virtual work of the external load can be expressed in terms of the jump of viscous traction forces $\underline{q}$ exerted by the fluids on the wall evaluated on the mid–surface. The weak form of the wall equilibrium equations (Eq. 2.38) can thus be written as

$$\forall\,\underline{\hat{u}}_s,\underline{\hat{\theta}} \in H^1(\mathcal{S}_t,\mathbb{R}^3)\otimes H^1(\mathcal{S}_t,\mathbb{R}^2),$$
$$\int_{\mathcal{S}_t}\underline{\hat{u}}\,(\underline{\hat{u}}_s,\underline{\hat{\theta}})\cdot\underline{q}\,dS = \int_V \underline{\underline{\hat{e}}}\,(\underline{\hat{u}}_s,\underline{\hat{\theta}}) : \underline{\underline{\sigma}}\,dV, \tag{2.41}$$

on the deformed configuration.

It must be noted that the deformation are measured with respect to the reference configuration and the constitutive law generally links the Green–Lagrange strain tensor and the second Piola–Kirchhoff stress tensor (Chamoret, 2002; Le Tallec, 2009). To change the constitutive law easily, it is useful to write the right–hand side term of the principle of virtual work (Eq. 2.41) on the reference configuration

$$\forall\,\underline{\hat{u}}_s,\underline{\hat{\theta}} \in H^1(\mathcal{S}_t,\mathbb{R}^3)\otimes H^1(\mathcal{S}_t,\mathbb{R}^2),$$

$$\begin{aligned}\int_V \underline{\underline{\hat{e}}}\,(\underline{\hat{u}}_s,\underline{\hat{\theta}}) : \underline{\underline{\sigma}}\,dV &= \int_{V_0} \underline{\underline{\hat{e}}}\,(\underline{\hat{u}}_s,\underline{\hat{\theta}}) : J\,(\underline{\underline{\sigma}}\,\underline{F}^{-1})\;dV \\ &= \int_{V_0} \underline{\underline{\hat{e}}}\,(\underline{\hat{u}}_s,\underline{\hat{\theta}}) : \underline{F}\,\underline{\underline{\Sigma}}\,dV.\end{aligned} \tag{2.42}$$

In the case of the thin shell model, the solid problem is written

$$\forall\,\underline{\hat{u}}_s,\underline{\hat{\theta}} \in H^1(\mathcal{S}_t,\mathbb{R}^3)\otimes H^1(\mathcal{S}_t,\mathbb{R}^3),\ \text{find } \underline{q} \text{ such as}$$
$$\int_{\mathcal{S}_t}\underline{\hat{u}}\,(\underline{\hat{u}}_s,\underline{\hat{\theta}})\cdot\underline{q}\,dS = \int_{V_0} \underline{\underline{\hat{e}}}\,(\underline{\hat{u}}_s,\underline{\hat{\theta}}) : \underline{F}\,\underline{\underline{\Sigma}}\,dV. \tag{2.43}$$

2.3.4 Shell mathematical models

In order to take into account the bending resistance of the capsule wall, we want to replace the membrane model by a thin shell model in the numerical algorithm developed by Walter *et al.* (2010) in the Biomechanics and Bioingineering Laboratory (Université de Technologie de Compiègne). However, instead of rewriting entirely the shell model, we use the shell finite element library Shelddon designed by Inria. The first shell finite element used was based on the mathematical formulation of the *basic shell model*. However, the mathematical formulation of this model in the library is based only on the generalized Hooke's law. In order to consider the constitutive laws, which are traditionally used to describe the capsule membrane behavior (see section 2.2.2) , we introduce a new shell finite element based on the mathematical formulation of a *shear–membrane–bending model.* Chapelle & Bathe (2011) have described the mathematical formulation of this model in the case of a linear strain tensor. The shear, membrane and bending deformation are separated in the formulation. It enables to choose a strain–hardening or strain–softening constitutive law to describe the membrane effects combined with the generalized Hooke's law for the bending and shear effects. The mathematical formulation of the basic and shear–membrane–bending shell models are presented in the following subsection. More details on shell models may be found in Chapelle & Bathe (2011), Suarez (2006) and Lee (2004).

The basic shell model

The basic shell model is important to understand the essential characteristics of most classical shell models. In this model, an asymptotic analysis (Chapelle & Bathe, 2011) shows that the shell is undergoing plane stress at first order ($\Sigma_{33} = 0$ at the first order). This information is then used to eliminate the terms, which depend on e_{33} in the constitutive law. The combination of this assumption with the one of the Reissner–Mindlin kinematical assumption ($e_{33} = 0$) is in apparent contradiction. However, the value of the component e_{33} is not present in the variational formulation. It thus has no impact on the problem. More details are available in Chapelle & Bathe (2011).

The finite element of the Shelddon library based on the basic shell model describes only the behavior of an isotropic linear elastic material using the generalized Hooke's law, sometimes called St Venant–Kirchhoff law. As we have seen in two–dimension in the section 2.2.2, this law assumes a linear relationship between the Green–Lagrange strain tensor $\underline{\underline{e}}$ and the second Piola–Kirchhoff stress tensor

$$\Sigma^{ij} = \mathcal{H}^{ijkl}\, e_{kl}, \tag{2.44}$$

with the elasticity tensor

$$\mathcal{H}^{ijkl} = \frac{\nu E}{(1+\nu)(1-2\nu)}\, G^{ij}\, G^{kl} + \frac{E}{2(1+\nu)}\, (G^{ik}\, G^{jl} + G^{il}\, G^{jk}), \tag{2.45}$$

where ν is the Poisson ratio and E the Young's modulus, which is related to the shear modulus by $G = \dfrac{E}{2(1+\nu)}$.

Using the properties of the metric tensor G^{ij} (Eq. 2.24), the assumption of plane stress and the properties of symmetry owing to the isotropy of the material, the second Piola–Kirchhoff stress tensor becomes

$$\begin{cases} \Sigma^{\alpha\beta} = C^{\alpha\beta\lambda\mu}\, e_{\lambda\mu}, \\ \Sigma^{\alpha 3} = \dfrac{1}{2} D^{\alpha\lambda}\, e_{\lambda 3}, \end{cases}$$

with

$$\begin{aligned} C^{\alpha\beta\lambda\mu} &= G\left(G^{\alpha\lambda}\, G^{\beta\mu} + G^{\alpha\mu}\, G^{\beta\lambda} + \frac{2\nu}{1-\nu}\, G^{\alpha\beta}\, G^{\lambda\nu}\right), \\ D^{\alpha\lambda} &= 4G\, G^{\alpha\lambda}. \end{aligned} \tag{2.46}$$

The solid problem (Eq. 2.43) becomes

$$\forall\, \underline{\hat{u}}_s, \underline{\hat{\theta}} \in H^1(\mathcal{S}_t, \mathbb{R}^3) \otimes H^1(\mathcal{S}_t, \mathbb{R}^2), \text{ find } \underline{q} \text{ such as}$$

$$\int_{V_0} F_{\alpha\beta} \left[C^{\alpha\beta\lambda\mu}\, e_{\alpha\beta}\, \hat{e}_{\lambda\mu} + D^{\alpha\lambda}\, e_{\alpha 3}\, \hat{e}_{\lambda 3}\right] dV = \int_{\mathcal{S}_t} \underline{\hat{u}} \cdot \underline{q}\, dS. \tag{2.47}$$

The shear–membrane–bending model

In order to describe the stretching of the mid–surface with a Skalak or a neo–Hookean law, we introduce the mathematical formulation of a new shear–membrane–bending model. It is deduced directly from the basic shell model. The principle of this model is to separate the work done by the shear, membrane and bending effects in the weak form of the wall equilibrium.

Due to the small size of the wall thickness, we neglect the high–order terms of the transverse coordinate ξ^3 in the expressions of the Green–Lagrange strain tensor (Eq. 2.35) and the contravariant metric tensors. Namely, the components of the Green–Lagrange strain tensor (Eq. 2.35) become

$$\begin{cases} e_{\alpha\beta} = \gamma_{\alpha\beta}(\underline{u}_s) + \xi^3 \chi_{\alpha\beta}(\underline{u}_s, \underline{\theta}), \\ e_{\alpha 3} = \zeta_\alpha(\underline{u}_s, \underline{\theta}), \\ e_{33} = 0. \end{cases} \tag{2.48}$$

The terms $G^{\alpha\beta}$ are replaced by $A^{\alpha\beta}$ in the expressions of $C^{\alpha\beta\lambda\mu}$ and $D^{\alpha\lambda}$ (Eq. 2.46). $C^{\alpha\beta\lambda\mu}$ and $D^{\alpha\lambda}$ are now written as

$$\begin{aligned} C_0^{\alpha\beta\lambda\mu} &= G\left(A^{\alpha\lambda}\, A^{\beta\mu} + A^{\alpha\mu}\, A^{\beta\lambda} + \frac{2\nu}{1-\nu}\, A^{\alpha\beta}\, A^{\lambda\nu}\right), \\ D_0^{\alpha\lambda} &= 4G\, A^{\alpha\lambda}. \end{aligned} \tag{2.49}$$

The weak form of the wall equilibrium (Eq. 2.47) becomes

$$\forall\, \underline{\hat{u}}_s, \underline{\hat{\theta}} \in H^1(\mathcal{S}_t, \mathbb{R}^3) \otimes H^1(\mathcal{S}_t, \mathbb{R}^2),$$

$$\begin{aligned} \int_{\mathcal{S}_t} \underline{\hat{u}} \cdot \underline{q}\, d\mathcal{S}_t &= \int_{V_0} F_{\alpha\beta} \left[C_0^{\alpha\beta\lambda\mu} \left(\gamma_{\alpha\beta} + \xi^3 \chi_{\alpha\beta} \right) \left(\hat{\gamma}_{\lambda\mu} + \xi^3 \hat{\chi}_{\lambda\mu} \right) \right] dV \\ &+ \int_{V_0} F_{\alpha\beta}\, D_0^{\alpha\lambda}\, \zeta_{\alpha 3}\, \hat{\zeta}_{\lambda 3}\, dV. \end{aligned} \tag{2.50}$$

We further assume that the thickness depends only on ξ^1 and ξ^2 and that the term coupling the bending and membrane deformations is negligible. The weak form (Eq. 2.51) is now written

$$\forall\, \underline{\hat{u}}_s, \underline{\hat{\theta}} \in H^1(\mathcal{S}_t, \mathbb{R}^3) \otimes H^1(\mathcal{S}_t, \mathbb{R}^2),$$

$$\int_{\mathcal{S}_t} \underline{\hat{u}} \cdot \underline{q}\, dS = \int_{\mathcal{S}_0} F_{\alpha\beta}\, C_0^{\alpha\beta\lambda\mu} \left[(\alpha\ell)\, \gamma_{\alpha\beta}\, \hat{\gamma}_{\lambda\mu} + \frac{(\alpha\ell)^3}{12}\, \chi_{\alpha\beta}\, \hat{\chi}_{\lambda\mu} \right] dS \tag{2.51}$$

$$+ \int_{\mathcal{S}_0} (\alpha\ell)\, F_{\alpha\beta}\, D_0^{\alpha\lambda}\, \zeta_{\alpha 3}\, \hat{\zeta}_{\alpha 3}\, dS. \tag{2.52}$$

In the previous equation, we can notice that $(\alpha\ell) C_0^{\alpha\beta\lambda\mu} = \frac{\partial^2 w_s}{\partial \underline{\underline{e}}_s^2}$ for the generalized Hooke's law. The formulation of the solid problem can thus be generalized to consider other constitutive laws to describe the mechanical behavior of the mid–surface in the median plane. It becomes

$$\forall\, \underline{\hat{u}}_s, \underline{\hat{\theta}} \in H^1(\mathcal{S}_t, \mathbb{R}^3) \otimes H^1(\mathcal{S}_t, \mathbb{R}^2),$$

$$\int_{\mathcal{S}_t} \underline{\hat{u}} \cdot \underline{q}\, d\mathcal{S}_t = \int_{\mathcal{S}_0} F_{\alpha\beta}\, \frac{\partial^2 w_s}{\partial \underline{\underline{\gamma}}^2}\, \gamma_{\alpha\beta}\, \hat{\gamma}_{\lambda\mu}\, dS \tag{2.53}$$

$$\begin{aligned} &+ \int_{\mathcal{S}_0} F_{\alpha\beta}\, C_0^{\alpha\beta\lambda\mu} \frac{(\alpha\ell)^3}{12}\, \chi_{\alpha\beta}\, \hat{\chi}_{\lambda\mu} dS \\ &+ \int_{\mathcal{S}_0} (\alpha\ell)\, F_{\alpha\beta}\, D_0^{\alpha\lambda}\, \zeta_{\alpha 3}\, \hat{\zeta}_{\alpha 3}\, dS \end{aligned} \tag{2.54}$$

where w_s represents the strain energy function defined in section 2.2.2. A strain–hardening or softening constitutive law can be thus used to model the behavior of the mid–surface in the median plane, combined with the generalized Hooke's law for the bending effects.

2.4 Fluids problem

2.4.1 Stokes flow

The capsule is subjected to a viscous flow that follows the constitutive law

$$\underline{\underline{\sigma}} = 2\mu \underline{\underline{d}} - p\mathbb{I}. \tag{2.55}$$

For any velocity field $\underline{v}$, this constitutive law assumes that the strain rate tensor

$$\underline{\underline{d}} = \frac{1}{2}\left(\frac{\partial \underline{v}}{\partial \underline{x}_s} + \left(\frac{\partial \underline{v}}{\partial \underline{x}_s}\right)^T\right) \tag{2.56}$$

is proportional to the imposed stress tensor $\underline{\underline{\sigma}}$ (after subtracting the pressure term p).

The characteristic length ℓ is assumed to be sufficiently small, so that the Reynolds number

$$Re = \frac{\rho\dot{\gamma}\ell^2}{\mu} \ll 1, \tag{2.57}$$

which indicates that the viscous effects are dominant compared to the inertial effects. In addition to the incompressibility condition

$$\underline{\nabla} \cdot \underline{v}_{int} = 0, \qquad \text{and} \qquad \underline{\nabla} \cdot \underline{v}_{ext} = 0, \tag{2.58}$$

the internal and external flows are governed by the Stokes flow equations

$$\underline{\nabla} \cdot \underline{\underline{\sigma}}_{int} = \underline{0} \qquad \text{and} \qquad \underline{\nabla} \cdot \underline{\underline{\sigma}}_{ext} = \underline{0} \tag{2.59}$$

where $\underline{v}$ and $\underline{\underline{\sigma}}$ represent the velocity and the stress fields of the internal and external flows.

2.4.2 Boundary conditions

Equations (2.58, 2.59) are solved on the capsule wall $\mathcal{S}_t$ by assuming the following problem boundary conditions:

- Far away of the capsule, the external flow is not disturbed by the presence of the capsule:

$$\underline{v}_{ext} \to \underline{v}^{\infty}. \tag{2.60}$$

- There is no slip on the capsule deformed wall $\mathcal{S}_t$

$$\underline{v}_{int}\left(\underline{x}_s, t\right) = \underline{v}_{ext}\left(\underline{x}_s, t\right) = \underline{v}(\underline{x}_s, t) = \frac{\partial}{\partial t}\,\underline{x}_s\left(\underline{X}_s, t\right), \qquad \underline{x}_s \in \mathcal{S}_t. \tag{2.61}$$

- The load $\underline{q}$ per unit area on the wall is due to viscous traction jump on $\mathcal{S}_t$

$$[\underline{\underline{\sigma}}]\cdot\underline{a}_3 = (\underline{\underline{\sigma}}_{ext}-\underline{\underline{\sigma}}_{int})\cdot\underline{a}_3=\underline{q}, \qquad \underline{x}_s\in\mathcal{S}_t. \tag{2.62}$$

2.4.3 Boundary Integral formulation

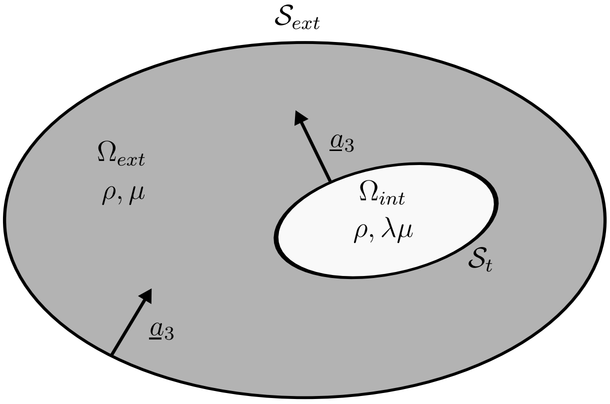

Figure 2.2: Capsule freely suspended in a Stokes flow.

The boundary integral method, introduced by Ladyzhenskaya (1969), is based on the fact that the instantaneous flow is independent of the motion history. This method only depends on the present configuration due to the linearity of the Stokes equation. In this section, we will present only the results that are relevant for a capsule flowing in a suspending fluid. More details are available in Pozrikidis (1992), Walter (2009) and Walter *et al.* (2010).

We consider a droplet of viscosity $\lambda\mu$ modeled by the volume domain Ω_{int} and suspended in an external fluid of viscosity μ contained in the volume Ω_{ext} (Figure 2.2). We assume that the internal and external fluids have the same density ρ. A surface $\mathcal{S}_t$ separates the internal droplet and the surrounding fluid. The whole suspending fluid domain is enclosed by an imaginary boundary $\mathcal{S}_{ext}$. The normal vector $\underline{a}_3$ of the interface $\mathcal{S}_{ext}$ points inwards, whereas the normal vector $\underline{a}_3$ of the surface $\mathcal{S}_t$ points into the external flow domain.

Using the boundary integral formulation for the three–dimensional motion of the internal and external fluids on each interface, the velocity of the membrane or mid–surface point located at $\underline{x}_s$ can be written

$$\begin{aligned} \forall \underline{x}_s \in \mathcal{S}_t, \qquad \frac{1+\lambda}{2}\,\underline{v}(\underline{x}_s) &= -\frac{1}{8\pi\mu}\int_{\mathcal{S}_t} \underline{\underline{J}}(\underline{r})\cdot[\underline{\underline{\sigma}}]\cdot\underline{a}_3(\underline{y}_s)\,dS \\ &+ \frac{1-\lambda}{8\pi\mu}\int_{\mathcal{S}_t}^{PV} \underline{v}(\underline{y}_s)\cdot\underline{\underline{\underline{K}}}(\underline{r})\cdot\underline{a}_3(\underline{y}_s)\,dS \\ &- \frac{1}{8\pi\mu}\int_{\mathcal{S}_{ext}} \underline{\underline{J}}(\underline{r})\cdot\underline{\underline{\sigma}}_{ext}\cdot\underline{a}_3(\underline{y}_s)\,dS \\ &+ \frac{1}{8\pi}\int_{\mathcal{S}_{ext}}^{PV} \underline{v}(\underline{y}_s)\cdot\underline{\underline{\underline{K}}}(\underline{r})\cdot\underline{n}(\underline{y}_s)\,dS, \end{aligned} \tag{2.63}$$

where $\underline{r} = \underline{y}_s - \underline{x}_s$ represents the distance vector between the point $\underline{x}_s$, where the velocity vector is calculated, and a point $\underline{y}_s$ on the surface $\mathcal{S}_t$. $\underline{\underline{J}}$ and $\underline{\underline{\underline{K}}}$ denote the Green kernels defined by

$$\underline{\underline{J}}(\underline{r}) = \frac{1}{r}\mathbb{I} + \frac{\underline{r}\otimes\underline{r}}{r^3}, \qquad \underline{\underline{\underline{K}}}(\underline{r}) = -6\,\frac{\underline{r}\otimes\underline{r}\otimes\underline{r}}{r^5} \tag{2.64}$$

with $r = \|\underline{r}\|$. The notation PV means that the integral calculation is defined by Cauchy principal value.

When a capsule is subjected to a unbounded flow, we assume that $\mathcal{S}_{ext} = \mathcal{S}_\infty$, i.e. the surface $\mathcal{S}_{ext}$ is located such as the velocity is undisturbed on it. If $\underline{v}^\infty$ denotes the undisturbed velocity and $\underline{\underline{\sigma}}^\infty$ the corresponding stress tensor, the equation (2.63) becomes

$$\begin{aligned} \forall \underline{x}_s \in \mathcal{S}_t, \qquad \frac{1+\lambda}{2}\,\underline{v}(\underline{x}_s) &= -\frac{1}{8\pi\mu}\int_{\mathcal{S}_t} \underline{\underline{J}}(\underline{r})\cdot[\underline{\underline{\sigma}}]\cdot\underline{a}_3(\underline{y}_s)\,dS \\ &+ \frac{1-\lambda}{8\pi\mu}\int_{\mathcal{S}_t}^{PV} \underline{v}(\underline{y}_s)\cdot\underline{\underline{\underline{K}}}(\underline{r})\cdot\underline{a}_3(\underline{y}_s)\,dS \\ &- \frac{1}{8\pi\mu}\int_{\mathcal{S}_\infty} \underline{\underline{J}}(\underline{r})\cdot\underline{\underline{\sigma}}^\infty\cdot\underline{a}_3(\underline{y}_s)\,dS \\ &+ \frac{1}{8\pi}\int_{\mathcal{S}_\infty}^{PV} \underline{v}^\infty(\underline{y}_s)\cdot\underline{\underline{\underline{K}}}(\underline{r})\cdot\underline{n}(\underline{y}_s)\,dS. \end{aligned} \tag{2.65}$$

In the absence of capsule, the undisturbed velocity on a fluid domain Ω' surrounded by the surface $\mathcal{S}_\infty$ is written

$$\begin{aligned} \forall \underline{x}_s \in \Omega', \qquad \underline{v}^\infty(\underline{x}_s) &= -\frac{1}{8\pi\mu}\int_{\mathcal{S}_\infty} \underline{\underline{J}}(\underline{r})\cdot\underline{\underline{\sigma}}^\infty\cdot\underline{a}_3(\underline{y}_s)\,dS \\ &+ \frac{1}{8\pi}\int_{\mathcal{S}_\infty}^{PV} \underline{v}^\infty(\underline{y}_s)\cdot\underline{\underline{\underline{K}}}(\underline{r})\cdot\underline{n}(\underline{y}_s)\,dS. \end{aligned} \tag{2.66}$$

According to this equation and the boundary condition (Eq. 2.62), the velocity of the membrane or mid–surface point located at $\underline{x}_s$ is written

$$\begin{aligned} \forall \underline{x}_s \in \mathcal{S}_t, \qquad \frac{1+\lambda}{2}\underline{v}(\underline{x}_s) &= \underline{v}^{\infty}(\underline{x}_s) - \frac{1}{8\pi\mu}\int_{\mathcal{S}_t} \underline{\underline{J}}(\underline{r})\cdot\underline{q}\,dS \\ &+ \frac{1-\lambda}{8\pi}\int_{\mathcal{S}_t}^{PV} \underline{v}(\underline{y}_s)\cdot\underline{\underline{K}}(\underline{r})\cdot\underline{a}_3(\underline{y}_s)\,dS. \end{aligned} \tag{2.67}$$

In order to eliminate the singularities in the Green kernels, the integral of the expression (2.67) is rewritten under an integral, which is easier to compute numerically. The equation (2.67) can be written

$$\begin{aligned} \forall \underline{x}_s \in \mathcal{S}_t, \qquad \frac{1+\lambda}{2}\underline{v}(\underline{x}_s) &= \underline{v}^{\infty}(\underline{x}_s) - \frac{1}{8\pi\mu}\int_{\mathcal{S}_t} \underline{\underline{J}}(\underline{r})\cdot\underline{q}\,dS \\ &+ \frac{1-\lambda}{8\pi}\int_{\mathcal{S}_t}^{PV} \Big(\underline{v}(\underline{y}_s)-\underline{v}(\underline{x}_s)\Big)\cdot\underline{\underline{K}}(\underline{r})\cdot\underline{a}_3(\underline{y}_s)\,dS \\ &+ \frac{1-\lambda}{8\pi}\int_{\mathcal{S}_t}^{PV} \underline{v}(\underline{x}_s)\cdot\underline{\underline{K}}(\underline{r})\cdot\underline{a}_3(\underline{y}_s)\,dS. \end{aligned} \tag{2.68}$$

On the closed surface $\mathcal{S}_t$, we have

$$-\frac{1}{4\pi}\int_{\mathcal{S}_t}^{PV} \underline{\underline{K}}(\underline{r})\cdot\underline{a}_3(\underline{y}_s)\,dS = \mathbb{I}. \tag{2.69}$$

Finally, the solution of the fluid problem is given by

$$\begin{aligned} \forall \underline{x}_s \in \mathcal{S}_t, \qquad \underline{v}(\underline{x}_s) &= \underline{v}^{\infty}(\underline{x}_s) - \frac{1}{8\pi\mu}\int_{\mathcal{S}_t} \underline{\underline{J}}(\underline{r})\cdot\underline{q}\,dS \\ &+ \frac{1-\lambda}{8\pi}\int_{\mathcal{S}_t}^{PV} \Big(\underline{v}(\underline{y}_s)-\underline{v}(\underline{x}_s)\Big)\cdot\underline{\underline{K}}(\underline{r})\cdot\underline{a}_3(\underline{y}_s)\,dS. \end{aligned} \tag{2.70}$$

2.5 Problem summary

In summary, a capsule, which is subjected to an external unbounded Stokes flow, is a fluid–structure interaction problem. Knowing the position $\underline{x}_s$, we solve the wall equilibrium given by

$$\forall \underline{\hat{u}}_s \in H^1(\mathcal{S}_t,\mathbb{R}^3), \int_{\mathcal{S}_t} \underline{\hat{u}}_s\cdot\underline{q}\,dS = \int_{\mathcal{S}_t} \underline{\underline{\hat{\epsilon}}}_s(\underline{\hat{u}}_s) : \underline{\underline{T}}\,dS, \tag{2.71}$$

when the capsule wall is modeled as a two–dimensional surface devoid of bending resistance or

$$\forall\, \underline{\hat{u}}_s, \underline{\hat{\theta}} \in H^1(\mathcal{S}_t,\mathbb{R}^3) \otimes H^1(\mathcal{S}_t,\mathbb{R}^2),$$

$$\int_{\mathcal{S}_t} \underline{\hat{u}} \cdot \underline{q} \, dS = \int_{\mathcal{S}_0} F_{\alpha\beta} \, \frac{\partial^2 w_s}{\partial \underline{\underline{\gamma}}^2} \, \gamma_{\alpha\beta} \, \hat{\gamma}_{\lambda\mu} \, dS \tag{2.72}$$

$$\begin{aligned} &+ \int_{\mathcal{S}_0} F_{\alpha\beta} \, C_0^{\alpha\beta\lambda\mu} \, \frac{(\alpha\ell)^3}{12} \, \chi_{\alpha\beta} \, \hat{\chi}_{\lambda\mu} dS \\ &+ \int_{\mathcal{S}_0} (\alpha\ell) \, F_{\alpha\beta} \, D_0^{\alpha\lambda} \, \zeta_{\alpha 3} \, \hat{\zeta}_{\alpha 3} \, dS \end{aligned} \tag{2.73}$$

when the capsule wall is modeled as a thin shell, to find the viscous load $\underline{q}$. According to these two equations, the viscous load $\underline{q}$ is a function of the displacement $\underline{u}_s$ and consequently a function of the position $\underline{x}_s$.

Knowing the viscous load $\underline{q}$, the velocity of the points is computed from the following equation

$$\begin{aligned} \forall \underline{x}_s \in \mathcal{S}_t, \qquad \underline{v}(\underline{x}_s) &= \underline{v}^{\infty}(\underline{x}_s) - \frac{1}{8\pi\mu} \int_{\mathcal{S}_t} \underline{\underline{J}}(\underline{r}) \cdot \underline{q} \, dS \\ &+ \frac{1-\lambda}{8\pi} \int_{\mathcal{S}_t}^{PV} \Big(\underline{v}(\underline{y}_s) - \underline{v}(\underline{x}_s) \Big) \cdot \underline{\underline{\underline{K}}}(\underline{r}) \cdot \underline{a}_3(\underline{y}_s) \, dS. \end{aligned} \tag{2.74}$$

According to these equations and the boundary conditions, which are presented in the section 2.4.2, the whole problem can be thus viewed as a first–order differential equation in time

$$\boxed{\forall \underline{x}_s \in \mathcal{S}_t, \quad \underline{v}\,(\underline{x}_s) = \frac{\partial}{\partial t} \, \underline{u}_s.} \tag{2.75}$$

Chapter 3

Numerical method

When the capsule wall is modeled as a two–dimensional surface (membrane model), the fluid–structure interaction problem is solved by the method introduced by Walter *et al.* (2010) by coupling a finite element method to solve the capsule membrane deformation with a boundary integral method for the internal and external flows. This method was adapted in this thesis to implement a thin shell model for the capsule wall to take into account the wall bending resistance.

In this section, we present firstly the temporal scheme used to solve the fluid–structure interaction problem. We then introduce the mesh discretization before formulating the procedure to solve this problem with the thin shell model.

3.1 Temporal scheme

The dynamics of a capsule in an external flow is solved coupling a boundary integral method for the Stokes equations with a finite element method to solve wall equilibrium (Walter *et al.*, 2010). Firstly, the capsule is deformed and oriented in space to get its desired reference state. The external flow is then started. At each time step, the finite element method is used to solve the wall deformation (Eq. 2.18 or 2.54 depending on the wall model) knowing the mid–surface displacement $\underline{u}_s$ and deduce the viscous load $\underline{q}$ exerted by the fluids on the wall at each node. Knowing $\underline{q}$, the velocity of the capsule nodes is then computed using the boundary integral method (Eq. 2.74). To update the position of the nodes $\underline{u}_s$ at the following time step, the velocity, given by the Eq. 2.75 is integrated using an explicit second–order Runge–Kutta method in case of the membrane model and an explicit Euler integration scheme in case of the thin shell model. The numerical method is illustrated in Figure 3.1. Thereafter, we will present only the numerical algorithm for the thin shell model, as the finite element formulation used for the membrane model are presented in details in Walter (2009).

As the numerical method is explicit in time when integrating the evolution equation (2.75), it is stable only for sufficiently small time steps Δt that respect the stability criterion

$$\dot{\gamma}\Delta t < \mathcal{O}\left(\frac{\Delta x \, Ca_s}{\ell}\right) \tag{3.1}$$

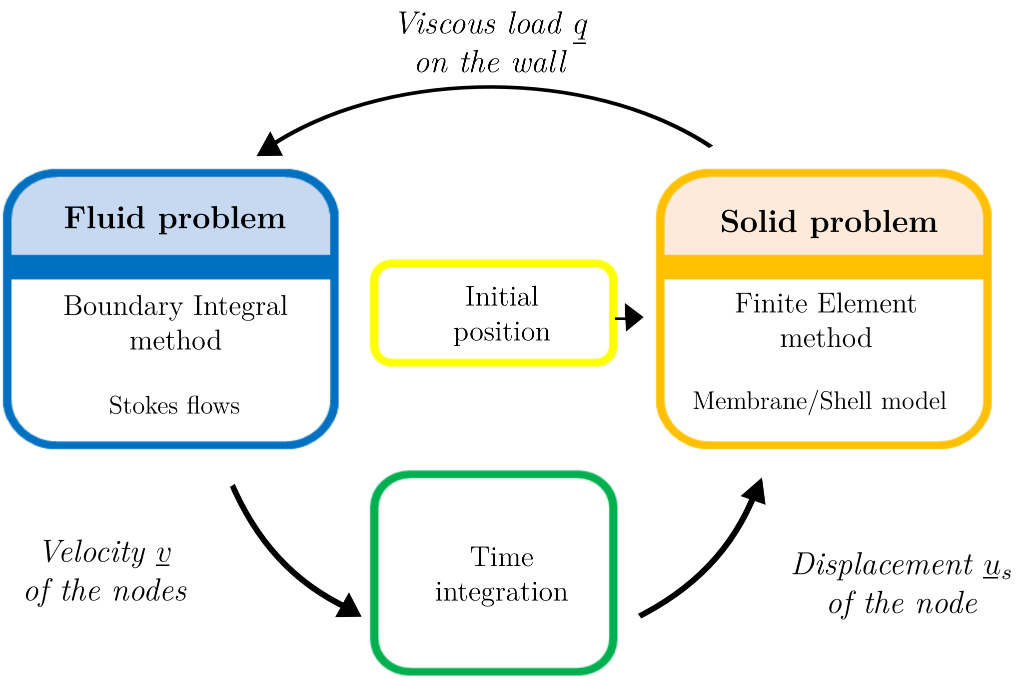

Figure 3.1: Numerical method coupling a boundary integral method with a finite element method (Walter, 2009).

with Δx the mesh size (Walter *et al.*, 2011). When the capsule is modeled with the thin shell model, the introduction of bending does not modify the stability analysis because the bending terms are imposed to be in equilibrium when solving the wall equilibrium problem (see Appendix A).

3.2 Mesh discretization

Depending on the shell geometry and boundary conditions, the behavior of a shell structure is different, when the thickness becomes small. It can be classified in three asymptotic categories: membrane–dominated, bending–dominated, or mixed shell problems. Regardless of the shell geometry, asymptotic category and thickness, the shell finite element formulation should converge uniformly towards the exact solution of the mathematical model. Otherwise, the phenomenon of numerical locking occurs. However, displacement–based shell finite elements are too stiff for bending–dominated shell structures of small thickness. In order to avoid the locking problems of thin structures, we use the MITC (Mixed Interpolation of Tensorial Component) triangular shell finite elements based on a mixed formulation, that were introduced by Lee & Bathe (2004). In this case, an additional interpolation is performed for the out–of–plane components of the strains (the $e_{\alpha 3}$ components). As a continuous function can be represented as the sum of the contributions calculated in a finite number of locations, the idea of the MITC technique is to interpolate the out–of–plane components of strain and displacement separately and connect these interpolations at specific tying points. The MITC shell finite elements have shown to behave well both in bending and membrane dominated problems and to satisfy the following conditions:

- The finite element discretization can be solved for and no spurious zero energy mode is encountered. This condition is called *ellipticity*.
- The finite element solutions converge to the solution of the mathematical model, when the mesh size $\Delta x/\ell$ tends to zero. The element thus respects the *consistency* condition.
- The shell is free from shear and membrane locking. The solution accuracy is independent of the shell thickness. These two points are called *Inf–sup condition*.
- The matrices do not depend on the element orientation. It is the *spatial isotropy*.

More details on the MITC can be found in Lee & Bathe (2004) and Suarez (2006).

Several MITC shell finite elements have been developed with square or triangular shape, with one node at each vertex or a node at each vertex and one at the middle of each side (Dvorkin & Bathe, 1984; Bathe & Dvorkin, 1986; Bucalem & Bathe, 1993; Lee & Bathe, 2004). In the case of the thin shell model, we have chosen to discretize the mid–surface using triangular elements, called MITC3, which have one node at each vertex (Figure 3.2a). MITC6 triangular elements, which have six nodes, one at each vertex and one at the middle of each side, exist and could be used to discretize the mid–surface, but large differences on the load computed at a point and its neighbors have been observed. As this problem has not been yet solved, we have used linear triangular elements and refined the mesh to obtain the same mesh size than with the mesh used in the case of the membrane model. In this case, the surface of the capsule is discretized using triangular curved P_2 elements, which have six nodes, one at each vertex and one at the middle of each side (Figure 3.2b). The surface and the mid–surface are discretized using isoparametric interpolations. All the unknowns (e.g. the point position, the velocity and the load) are interpolated with the same shape functions.

In order to locate the position of a node on a element of the surface $\mathcal{S}_t$, we use the local Cartesian coordinates (r, s, z), where (r, s) are the intrinsic coordinates in the plane element (defined such that r, s and $1 - r - s \in [0, 1]$) and z is the coordinate along $\underline{a}_3$ $(z \in [-1, 1])$. If we consider a vector $\underline{f}$, the value of the interpolated quantity is calculated from the nodal values $\underline{f}^{(p)}$. We note $f_{X_j}^{(p)}$ the j^{th} Cartesian component of $\underline{f}$ at node p, where $p \in \{1, ..., nn\}$ with nn the number of nodes of the element. The array of size $3N_N$

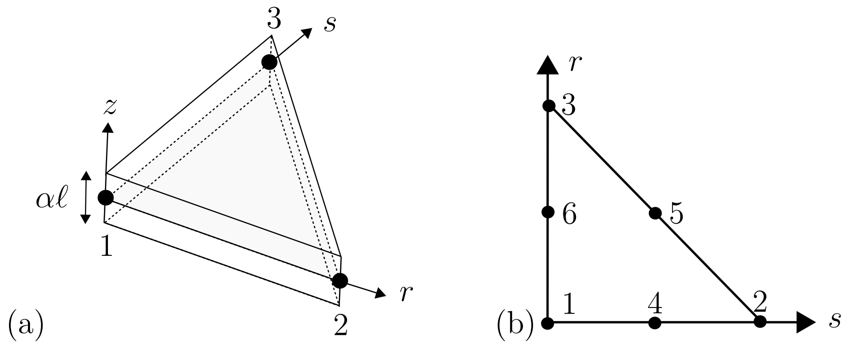

Figure 3.2: Capsule wall discretization: (*a*) MITC3 element (thin shell model), (*b*) P_2 element (membrane model).

containing the Cartesian components of the vector nodal values is denoted by $\{f\}$. An interpolated formulation for the vector $\underline{f}$ is then expressed as

$$\underline{f}(r,s) = \sum_{p=1}^{nn} \lambda^{(p)}(r,s)\, \underline{f}^{(p)}, \tag{3.2}$$

where $\lambda^{(p)}(r,s)$ represent the standard shape functions and depend on the element type. For MITC3 elements, the shape functions are

$$\lambda^{(1)}(r,s) = 1 - r - s\,, \tag{3.3a}$$

$$\lambda^{(2)}(r,s) = r\,, \tag{3.3b}$$

$$\lambda^{(3)}(r,s) = s\,. \tag{3.3c}$$

and for P_2 elements

$$\lambda^{(1)}(r,s) = (1-r-s)(1-2r-2s)\,, \tag{3.4a}$$

$$\lambda^{(2)}(r,s) = r(2r-1)\,, \tag{3.4b}$$

$$\lambda^{(3)}(r,s) = s(2s-1)\,, \tag{3.4c}$$

$$\lambda^{(4)}(r,s) = 4r(1-r-s)\,, \tag{3.4d}$$

$$\lambda^{(5)}(r,s) = 4rs\,, \tag{3.4e}$$

$$\lambda^{(6)}(r,s) = 4s(1-r-s)\,. \tag{3.4f}$$

The position vector $\underline{x}$ at node p inside an element MITC3 can thus be written

$$\underline{x}(t) = \sum_{p=1}^{3} \lambda^{(p)}(r,s) \left(\underline{x}_s^{(p)}(t) + z\,\frac{\alpha\ell}{2}\,\underline{a}_3^{(p)}(t) \right), \tag{3.5}$$

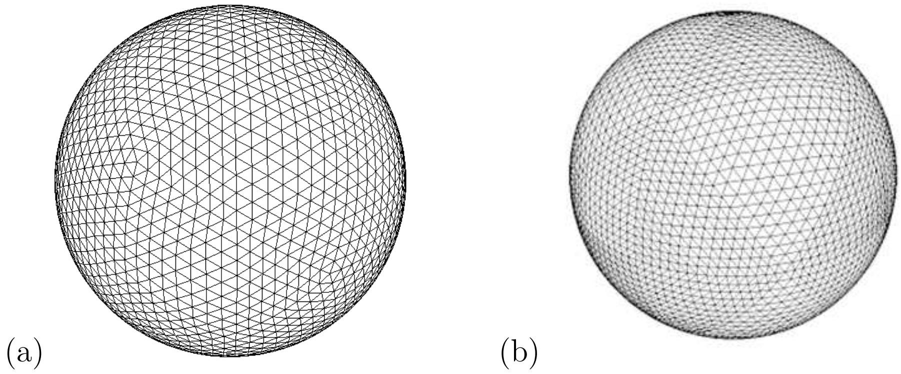

Figure 3.3: Typical capsule mesh with flat triangles (MITC3 elements) obtained (*a*) from an icosahedron ($N_E = 5120$, $N_N = 2562$) and (*b*) from an octahedron ($N_E = 8192$, $N_N = 642$).

and the corresponding virtual displacement

$$\underline{\hat{u}} = \sum_{p=1}^{3} \lambda^{(p)}(r,s) \left(\underline{\hat{u}}_s^{(p)} + z \, \frac{\alpha \ell}{2} \, \underline{\hat{\theta}}^{(p)} \right). \tag{3.6}$$

Initially, the capsule mid–surface (or surface) $\mathcal{S}_t$ is spherical. It is meshed with triangular elements. The triangular mesh is obtained by inscribing an icosahedron (regular polyhedron with 20 triangular faces) or an octahedron (regular polyhedron with 8 triangular faces) in a sphere. Each triangular face is then divided into 4 triangular sub–elements by placing a new node in the middle of each side and projecting the new nodes radially onto the sphere until reaching the desired number of elements. To obtain P_2 elements from a P_1 element, which has one node at each vertex, a node is positioned at the middle of each edge and is projected onto the sphere. We denote N_E and N_N the total number of elements and nodes. Typical meshes obtained from an icosahedron and an octahedron are represented in Figure 3.3. This figure shows that the mesh obtained from an icosahedron is more homogeneous than the one generated from an octahedron, which is symmetrical about two meridians. Table 3.1 gives the numbers of nodes and the average mesh size Δx used in this dissertation as a function of the number of MITC3 elements. In the case of ellipsoidal capsule, the meshed sphere is deformed into an ellipsoid corresponding to the capsule reference shape, before the computation is run.

N_E	N_N	$\Delta x/\ell$
320	162	0.3
512	**258**	**0.23**
1280	642	0.15
2048	**1026**	**0.12**
5120	2562	0.075
8192	**4098**	**0.06**

Table 3.1: Number of nodes N_N and mesh size $\Delta x/\ell$ as a function of the number of MITC3 elements. The meshes obtained from an octahedron are written in boldface.

3.3 Finite element formulation for shell model

Instead of rewriting entirely the MITC method, we use the shell finite element library Shelddon designed by Inria[1]. The Shelddon library is coupled with the fluid solver developed in the Biomechanics and Bioingineering Laboratory (Walter *et al.*, 2010, 2011; Foessel *et al.*, 2011) using a Parallel Virtual Machine protocol.

For a given deformed configuration, the weak form of the wall equilibrium equation (2.43)[2] is solved to determine the unknown viscous load $\underline{q}$ exerted by the fluids on the wall. The objective of this section is to express Eq. (2.43) as a linear algebraic equations at the mid–surface nodes. The integral over the shell volume can be decomposed as a sum over all individual elements. The left–hand side of Eq. (2.43) can be expressed on the deformed state as

$$\begin{aligned} \int_{\mathcal{S}_t} \underline{\hat{u}} \cdot \underline{q} \, dS &= \sum_{el} \hat{u}_{X_j}^{(p)} \left(\int_{S_{el}} \lambda^{(p)} \lambda^{(q)} dS \right) q_{X_j}^{(q)}, \\ &= \sum_{el} \{\hat{u}_{el}\}^T \left[M_{el} \right] \{q_{el}\} \end{aligned} \tag{3.7}$$

where $\{\hat{u}_{el}\}$ and $\{q_{el}\}$ of size N_N represent the Cartesian components of the discrete virtual displacement and of the load, respectively, at the element nodes:

$$\begin{aligned} \{q_{el}\} &= \left\{ q_1^{(1)}, q_2^{(1)}, q_3^{(1)}, \ \ldots, \ q_1^{(nn)}, q_2^{(nn)}, q_3^{(nn)} \right\}, \\ \{\hat{u}_{el}\} &= \left\{ \hat{u}_1^{(1)}, \hat{u}_2^{(1)}, \hat{u}_3^{(1)}, \ \ldots, \ \hat{u}_1^{(nn)}, \hat{u}_2^{(nn)}, \hat{u}_3^{(nn)} \right\}. \end{aligned} \tag{3.8}$$

The vectors $\{\hat{u}_{el}\}$ and $\{q_{el}\}$ are then assembled into their global counterparts $\{q\}$ and $\{\hat{u}\}$ of size $3N_N$. The same is done for the matrix $[M_{el}]$, which is assembled into $[M]$ of size

---

[1] The library is registered at the *Agence pour la Protection des Programmes* under ref: IDDN.FR.001.030018.000.S.P.2010.000.20600. The base of the program is open source and available online: www-rocq.inria.fr/modulef

[2] To explain easily the finite element formulation, we consider only the general formulation of the weak form of the wall equilibrium.

$3N_N \times 3N_N$. The left–hand side of equation (2.43) becomes

$$\int_{\mathcal{S}_t} \underline{\hat{u}} \cdot \underline{q}\, dS = \{\hat{u}\}^T [M] \{q\}. \tag{3.9}$$

Similarly, the right–hand side of equation (2.43) can be written over all individual elements. First, we note that in the case of the generalized Hooke's law, the constitutive law is written

$$\underline{\underline{\sigma}} = \underline{\underline{\underline{\underline{H}}}} : \underline{\underline{e}}(\underline{u}). \tag{3.10}$$

The right–hand side of equation (2.43) becomes

$$\int_V \underline{\underline{\hat{e}}}\left(\underline{\hat{u}}_s, \underline{\hat{\theta}}\right) : \underline{\underline{\sigma}}\, dV = \sum_{el} \int_V \left[e_{el}\left(\{\hat{u}_{el}\}\right)\right]^T [H_{el}] \left[e_{el}\left(\{u_{el}\}\right)\right] dV \tag{3.11}$$

According to the definition (Eq. 2.34), the Green–Lagrangean strain tensor is non linear and can be written

$$\left[e_{el}\left(\{u_{el}\}\right)\right] = [B_{el}] \{u_{el}\} \tag{3.12}$$

where $[B_{el}]$ is the element matrix, which contains the partial derivative. See Batoz & Dhatt (1992) (p. 324 - 325) and Bonnet *et al.* (2014) for more details.

The right–hand side of equation (2.43) can be expressed as

$$\begin{aligned} \int_V \underline{\underline{\hat{e}}}\left(\underline{\hat{u}}_s, \underline{\hat{\theta}}\right) : \underline{\underline{\sigma}}\, dV &= \sum_{el} \int_V \{\hat{u}_{el}\}^T [B_{el}]^T [H_{el}] [B_{el}] \{u_{el}\}\, dV \\ &= \sum_{el} \{\hat{u}_{el}\}^T [K_{el}] \{u_{el}\} \end{aligned} \tag{3.13}$$

where $[K_{el}]$ the element stiffness matrix equals

$$\int_V [B_{el}]^T [H_{el}] [B_{el}]\, dV. \tag{3.14}$$

Finally, the right–hand side of equation (2.43) becomes

$$\int_V \underline{\underline{\hat{e}}}\left(\underline{\hat{u}}_s, \underline{\hat{\theta}}\right) : \underline{\underline{\sigma}}\, dV = \sum_{el} \{\hat{u_{el}}\}^T \{R_{el}\} \tag{3.15}$$

$$= \{\hat{u}\}^T \{R\} \tag{3.16}$$

after assembling the vectors $\{\hat{u}_{el}\}$ and $\{R_{el}\}$ into their global counterparts.

The discretized form of equation (2.43) becomes

$$\{\hat{u}\}^T [M] \{q\} = \{\hat{u}\} \{R\} \left(\{u_s\}, \{\theta\}\right). \tag{3.17}$$

As the equation must be satisfied for any virtual displacement, it can be simplified as

$$[M]\,\{q\} = \{R\}\,(\{u_s\},\{\theta\})\,.$$

The membrane degrees of freedom and the rotational degrees of freedom can be separated. Eq. 3.3 finally becomes

$$\begin{cases} \{R\}_s\,(\{u_s\},\{\theta\}) - [M]_s\,\{q_s\} = \{0\}_s, & (3.18a)\\ \{R\}_\theta\,(\{u_s\},\{\theta\}) = \{0\}_\theta. & (3.18b) \end{cases}$$

In this system, the mid–surface displacement degrees of freedom $\{u_s\}$ is known at time $t+\Delta t$: it is found by integrating the node velocity given by the fluid solver at the previous time step t. The viscous loads $\{q_s\}$ and the rotations $\{\theta\}$ are unknown. To solve this system, we first solve the nonlinear equation (3.18b) in $\{\theta\}$ by a Newton's method. Numerically, we define the residual of equation (3.18b) as

$$\mathcal{R}(\{\theta\}) = \{R\}_\theta\,(\{u_s\},\{\theta\})\,. \tag{3.19}$$

We search for the rotations $\{\theta\}$ such that $\mathcal{R}=0$. The equation is solved by subiterations setting the convergence criterion at 1×10^{-7}. Let $\{\theta^t\}$ be the rotation vector that satisfied the zero–residual condition at time t and $\{\theta^{t+\Delta t}\}$ the solution we are looking for at time $t+\Delta t$. As rotation initial guess $\{\theta_0^{t+\Delta t}\}$, we use the rotation found at the previous time step.

Using a first–order Taylor series, one can express the residual at the subiteration $i+1$ as

$$\mathcal{R}(\{\theta_{i+1}^{t+\Delta t}\}) = \mathcal{R}(\{\theta_i^{t+\Delta t}\}) + \frac{\partial\mathcal{R}(\{\theta_i^{t+\Delta t}\})}{\partial\{\theta\}}\left(\{\theta_{i+1}^{t+\Delta t}\} - \{\theta_i^{t+\Delta t}\}\right). \tag{3.20}$$

Let us search for $\{\theta_{i+1}^{t+\Delta t}\}$, such that $\mathcal{R}(\{\theta_{i+1}^{t+\Delta t}\})=0$. From equation (3.20), it reads

$$\begin{aligned} \{\theta_{i+1}^{t+\Delta t}\} &= \{\theta_i^{t+\Delta t}\} - \left[\frac{\partial\mathcal{R}(\{\theta_i^{t+\Delta t}\})}{\partial\{\theta\}}\right]^{-1}\mathcal{R}(\{\theta_i^{t+\Delta t}\})\\ &= \{\theta_i^{t+\Delta t}\} - \left[K(\{\theta_i^{t+\Delta t}\})\right]^{-1}\mathcal{R}(\{\theta_i^{t+\Delta t}\}), \end{aligned} \tag{3.21}$$

where $[K]$ represents the stiffness matrix. Equation (3.21) is solved for explicitly since $[K(\theta_i^{t+\Delta t})]$ and $\mathcal{R}(\theta_i^{t+\Delta t})$ are known from subiteration i. If the new solution respects the convergence criterion

$$|\{\theta_{i+1}^{t+\Delta t}\} - \{\theta_i^{t+\Delta t}\}| < 10^{-7}, \tag{3.22}$$

the properly value of the rotation is found. Otherwise, one has to move on to the next subiteration and iterate until convergence.

When the value of the rotation is found, the load $\{q_s\}$ exerted by the fluids on the wall is then obtain by a direct inversion of equation (3.18a).

3.4 Fluid solver

When the viscous load $\underline{q}$ is known from the solid solver, the velocity field at the nodes is obtained explicitly from the boundary integral equation (2.74), which is discretized on the same triangular mesh as for the solid problem. The equation (2.74) can be decomposed as a sum of integrals on the N_E elements and 12 Hammer points are then used for the integration.

The kernels $\underline{\underline{J}}$ and $\underline{\underline{K}}$ vary respectively as $1/r$ and $1/r^5$. When $\underline{y}_s \rightarrow \underline{x}_s$, they become very large and can lead to numerical errors. In order to eliminate these singularies, polar coordinates centered on $\underline{x}_s$ are used, when $\underline{y}_s$ and $\underline{x}_s$ belong to the same element. This change of coordinates introduces a Jacobian which goes to 0 as fast as r. In this case, 6 Gauss points are used for integration along each of the polar coordinates.

When the internal and external fluids do not have the same viscosity ($\lambda \neq 1$), the procedure faces problem of convergence. One technique to circumvent this issue is to solve the fluid problem (Eq. 2.74) by subiterations using a simple relaxation method. At the subiteration n, we write

$$\underline{v}^{n+1} = \omega\, \underline{v}_s^{n+1} + (1-\omega)\, \underline{v}^n \tag{3.23}$$

with

$$\begin{aligned} \underline{v}_s^{n+1} \quad &= \quad \underline{v}^{\infty}(\underline{x}_s) - \frac{1}{8\pi\mu} \int_{\mathcal{S}_t} \underline{\underline{J}}(\underline{r}) \cdot \underline{q}\, dS \\ &+ \quad \frac{1-\lambda}{8\pi} \int_{\mathcal{S}_t}^{PV} \Big(\underline{v}^n(\underline{y}_s) - \underline{v}^n(\underline{x}_s) \Big) \cdot \underline{\underline{K}}(\underline{r}) \cdot \underline{a}_3(\underline{y}_s)\, dS. \end{aligned} \tag{3.24}$$

and ω the relaxation factor, which equals to $\omega = 1.8/(1+\lambda)$ (Foessel *et al.*, 2011). This equation is solved setting the convergence criterion at

$$\|\underline{v}^{n+1} - \underline{v}^n\| < \omega \times 10^{-6}. \tag{3.25}$$

Chapter 4

Numerical method validation

The validation of our numerical method coupling a boundary integral method with a shell finite element is presented in this section. We first validate the mechanical behavior of the shell finite elements in large deformation by simulating the inflation of an initially spherical capsule. To validate the fluid–structure coupling, we then consider the case of an initially spherical capsule with a small thickness subjected to a simple shear flow and compare the results with the ones obtained with the membrane model. Finally, we investigate the convergence of the numerical method in time and space.

4.1 Large isotropic deformation

Before coupling the shell finite element method to the boundary integral method, we verify if the shell finite elements behave properly in large deformation by inflating a spherical capsule with a relative wall thickness $\alpha \leq 0.01$. Its initial radius ℓ, defined as the length between the capsule center and the mid–surface, increases to the radius $\ell_p = (1+a)$ under an internal pressure p, where a is the inflation ratio. Numerically, a constant displacement

$$\underline{u}_s = a\,\underline{x}_s \tag{4.1}$$

perpendicular to the mid–surface is imposed. The capsule wall is then subjected to an isotropic traction characterized by the stretch ratio $\lambda_p = 1 + a$. Using the definition of the membrane and bending deformation tensors as well as the shear vector (Eq. 2.36), we find that the deformations due to bending and shear are nil. Bending resistance and transverse shear play no role in this test case. The corresponding analytical model is thus the one of the inflation of a two–dimensional surface devoid of bending resistance. The relation between the isotropic principal tensions T and the stretch ratio λ_p is obtained by computing analytically the tension from the strain energy functions (Eq. 2.15, 2.16 and 2.17). The tensions are easily derived for a two–dimensional isotropic material and read:

- for the generalized Hooke's law

$$T^{HG} = G_s(\lambda_p^2 - 1)\frac{1+\nu_s}{1-\nu_s}, \tag{4.2}$$

- for the neo–Hookean law

$$T^{NH} = G_s \left(1 - \frac{1}{\lambda_p^6}\right), \tag{4.3}$$

- for the Skalak law

$$T^{Sk} = G_s \left(\lambda_p^2 - 1 + C\lambda_p^2 \left(\lambda_p^4 - 1\right)\right). \tag{4.4}$$

The different parameters are chosen to have the same mechanical behavior in small deformation ($\nu_s = 0.5$ for the generalized Hooke's law and $C = 1$ for the Skalak law).

The analytical relation between the internal pressure and the inflation ratio a deduced from the Laplace's law is

$$p = \frac{2T}{\ell_p} = \frac{2T}{(1+a)\ell}. \tag{4.5}$$

Figure 4.1 shows the evolution of the non–dimensional pressure $p\ell/G_s$ obtained numerically as a function of the inflation factor a for the three constitutive laws. It is computed in the case of two thickness ratio α for a capsule modeled with 5120 MITC3 elements. The numerical results are in good agreement with the analytical solution (Figure 4.1). The maximum relative error with respect to the analytical solution of 0.001% with the generalized Hooke's law, of 0.04% with the neo–Hookean law and of 0.2% with the Skalak law.

It is interesting to note that the generalized Hooke's law is linear under an isotropic traction, whereas it is strain–hardening under an uniaxial stretching (Figure 2.1).

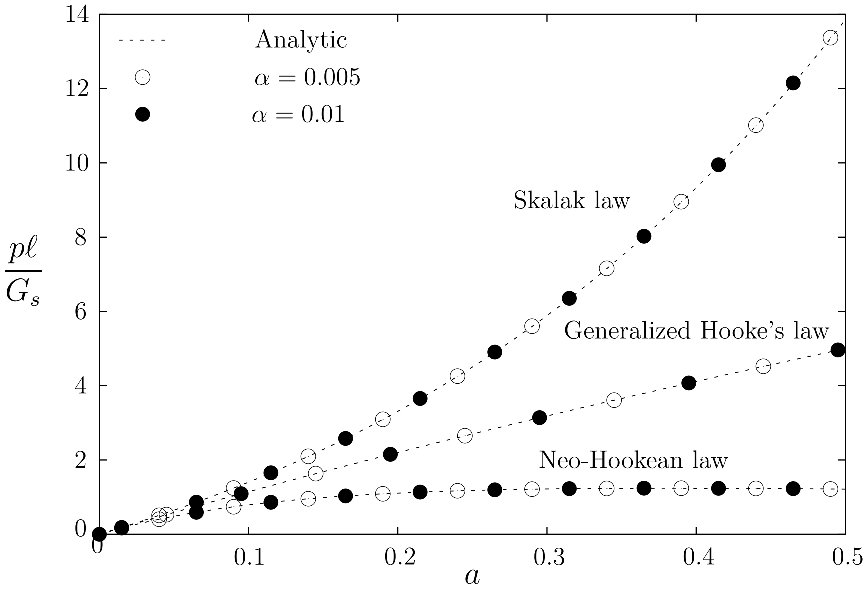

Figure 4.1: Evolution of the non–dimensional pressure as a function of the inflation factor a for thickness ratio $\alpha = 0.005$ and 0.01

As we use the MITC3 shell finite elements from the Shelddon library developed by Inria, we assume that the mechanical behavior of these elements under a bending force has already been validated. As we have only modified the numerical algorithm relative to the in–plane deformation, we validate only the in–plane deformation of the shell finite elements with the inflation of an initially spherical capsule.

4.2 Spherical capsule in shear flow

To validate the fluid–structure interaction coupling, we consider a classical test case: the motion of an initially spherical capsule of thickness ratio $\alpha = 0.01$ subjected to a simple shear flow at $Ca_s = 0.6$ with the same viscosity for the inner and outer fluids. The thickness ratio is voluntarily small in order to minimize the influence of the bending resistance and compare the results obtained with the shell model with the ones obtained with the membrane model, which have been already validated by Walter *et al.* (2010).

Regardless of the in–plane constitutive law, we recover the tank–treading motion, observed previously when a capsule is modeled as a two–dimensional surface devoid of bending resistance (Ramanujan & Pozrikidis, 1998; Lac *et al.*, 2004; Walter *et al.*, 2010). At steady state, the capsule has a quasi–ellipsoidal shape, which can be approximated by the ellipsoid of inertia of the mid–surface $\mathcal{S}_t$. If we call L_1 and L_2 the lengths of the two principal axes of the ellipsoid of inertia in the shear plane, the Taylor parameter D_{12} defined by

$$D_{12} = \frac{L_1 - L_2}{L_1 + L_2}. \tag{4.6}$$

provides an estimate of the capsule overall deformation.

Figure 4.2 shows the temporal evolution of the Taylor parameter D_{12} obtained with the membrane model ($\alpha = 0$) and with the shell model when we impose a thickness ratio $\alpha = 0.01$. 5120 MITC elements and 1280 P_2 elements are used to discretize the capsule wall in the shell and membrane models respectively. We recover the same temporal evolution for the Taylor parameter when the mid–surface deformation in the median plane is governed by the generalized Hooke's law, the neo–Hookean law or the Skalak law. The numerical coupling is thus validated.

4.3 Convergence test

To verify the temporal and spatial convergence of the coupling method, we consider the motion of an initially spherical capsule of thickness ratio $\alpha = 0.01$ subjected to a simple shear flow at $Ca_s = 0.6$, when the mid–surface deformation in the median plane

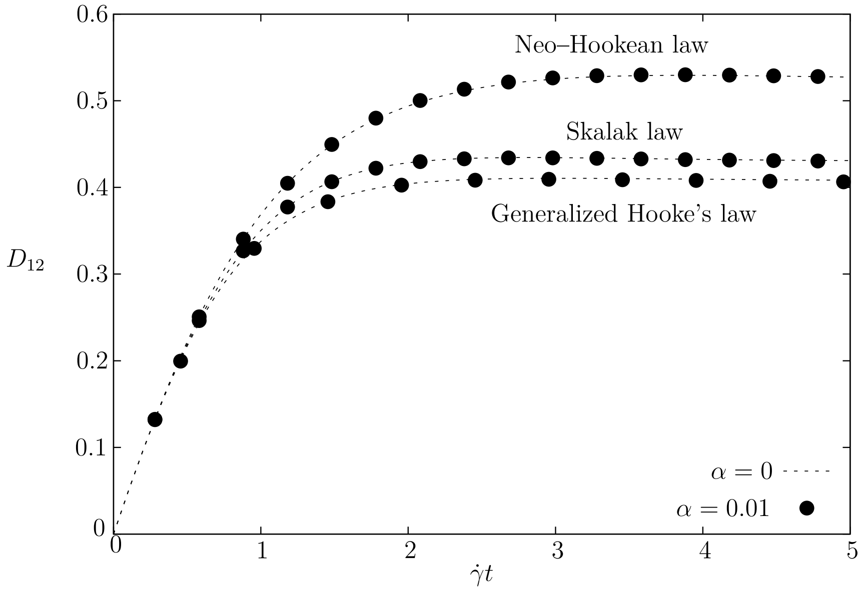

Figure 4.2: Initially spherical capsule subjected to a shear flow at $Ca_s = 0.6$: comparison of the temporal evolution of the Taylor parameter D_{12} obtained with the shell model ($\alpha = 0.01$) and the membrane model ($\alpha = 0$).

is described by the generalized Hooke's law.

No analytical solution of a spherical capsule in a shear flow exists. We take as reference solution the one obtained with a small time step and a small mesh size. We then compare the value of the Taylor parameter at steady state D_{12}^{∞} found for different mesh sizes and time steps to the one of the reference solution $D_{12}^{\infty,ref}$. We define the relative numerical error as the difference between the D_{12}^{∞} and the reference value $D_{12}^{\infty,ref}$:

$$\epsilon_{D_{12}} = \frac{|D_{12}^{\infty} - D_{12}^{\infty,ref}|}{D_{12}^{\infty,ref}}. \tag{4.7}$$

To study the spatial convergence of the numerical method, we take as reference value $D_{12}^{\infty,ref}$ the value of D_{12}^{∞} obtained with the time step $\dot{\gamma}\Delta t = 1 \times 10^{-4}$ and the mesh size corresponding to $N_E = 8192$. The evolution of the relative error as a function of the mesh size is shown in Figure 4.3a. The coupled numerical procedure appears to converge as $(\Delta x/\ell)^2$. As the difference between $N_E = 5120$ and $N_E = 8192$ is less than 3×10^{-4}, the results reported here will be obtained using 5120 MITC3 elements, except when specified otherwise.

The temporal convergence is then verified using as reference $D_{12}^{\infty,ref}$ the value of D_{12}^{∞} obtained with a time step $\dot{\gamma}\Delta t = 1 \times 10^{-4}$ and $N_E = 5120$ elements. The evolution of the relative error as a function of the dimensionless time step is shown in Figure 4.3b. We find that the relative error remains small ($\epsilon_{D_{12}} < 3 \times 10^{-3}$) and that the numerical procedure converges linearly in time.

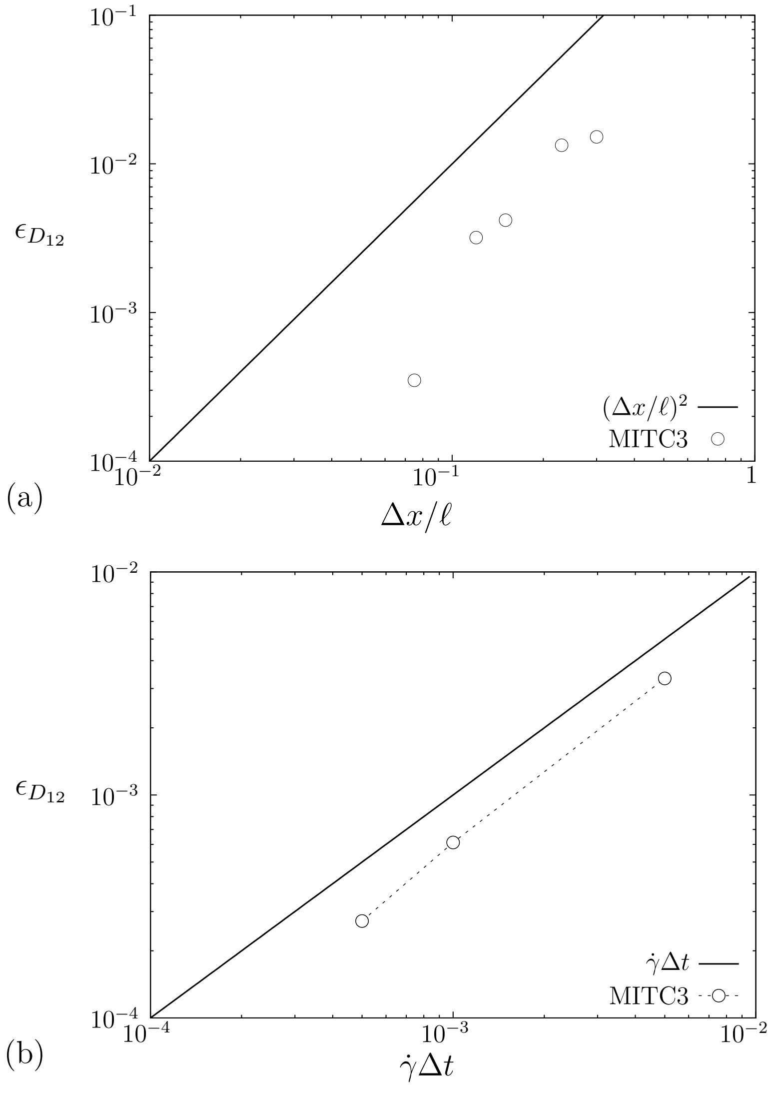

Figure 4.3: Relative numerical error $\epsilon_{D_{12}}$ on the Taylor parameter D_{12}^{∞} for $Ca_s = 0.6, \alpha = 0.01$. (*a*) Spatial convergence (reference corresponding to $\dot{\gamma}\Delta t = 1 \times 10^{-4}$, $N_E = 8192$); (*b*) Time convergence (reference corresponding to $\dot{\gamma}\Delta t = 1 \times 10^{-4}$, $N_E = 5120$).

Chapter 5

Influence of bending resistance on the capsule dynamics

In this chapter, we investigate the effect of the wall bending resistance on the dynamics of an initially spherical capsule subjected to a shear flow. The study was accepted for publication in the journal "*Physics of Fluids*" with the title "Influence of bending resistance on the dynamics of a spherical capsule in shear flow". This study was carried out with A.-V. Salsac, D. Barthès-Biesel, M. Vidrascu and P. Le Tallec. Additional results on the influence of the wall constitutive law are presented in section 5.6 when a capsule is subjected to a simple shear flow or a planar hyperbolic flow.

5.1 Introduction

Capsules, which consist of an internal liquid droplet enclosed by a membrane, have numerous applications in bioengineering, cosmetics and pharmaceutics: they are designed to protect fragile or volatile substances and to control their liberation in the external media. They are also used as biomimetic models of cells such as red blood cells. One classical technique to produce deformable capsules relies on interfacial polymerization of an emulsion. The fabricated capsules are typically quasi–spherical at rest. The membrane thickness and mechanical properties depend on the fabrication process (Edwards-Lévy *et al.*, 1994; Xiang *et al.*, 2008; Chu *et al.*, 2011; Koleva & Rehage, 2012). For many processes such as interfacial cross-linking, the capsule wall thickness results to be small as compared to the radius. But determining its exact value remains technically challenging, as it tends to be sub-micronic.

The dynamics of an initially spherical capsule subjected to a shear flow are of practical interest and have thus been studied extensively over the past years (see the review (Barthès-Biesel, 2011)). It has been observed experimentally (Chang & Olbricht, 1993*b*; Walter *et al.*, 2000, 2001; Koleva & Rehage, 2012) that at steady state, a spherical capsule is elongated in the straining direction by the hydrodynamic stresses exerted by the external flows, while the membrane rotates around the deformed shape because of the flow vorticity. However, for low flow strength, the capsule membrane is compressed in the equatorial region and thus becomes wrinkled (Walter *et al.*, 2001; Koleva & Rehage, 2012). Membrane wrinkling and buckling weaken the capsule membrane and may lead to fatigue breakup. It is thus important to predict these phenomena in order to avoid/provoke the membrane rupture depending on the application.

In order to understand the complex behavior of a spherical capsule in an external flow, numerical models of the fluid–structure interaction have been developed where the membrane is treated as a zero thickness elastic surface devoid of bending resistance (Barthès-Biesel, 2011). The observed experimental phenomena of elongation along the viscous strain direction, membrane rotation and tendency towards buckling at low shear rates are recovered by the numerical models. The models show clearly how the capsule motion and deformation depend on the flow strength relative to the elastic forces and on the viscosity ratio between the external and internal fluids (Ramanujan & Pozrikidis, 1998; Lac *et al.*, 2004; Li & Sarkar, 2008; Walter *et al.*, 2010; Foessel *et al.*, 2011).

In order to study the buckling and wrinkling phenomena in a rigorous way, the capsule wall bending stiffness must be accounted for in the model. Most numerical models that include bending effects have decomposed the wall strain energy into the sum of a membrane elastic energy and of a bending energy computed from the local curvature (Hang *et al.*, 2012; Kessler *et al.*, 2008). The bending modulus values, which have been used, are extremely high and have no relation with the bulk shear modulus of the wall. Such a decoupled energy-based model is likely to be relevant for objects like the red blood cells, which have a composite membrane consisting of a lipid bilayer lined by a protein network. Its relevance can, however, be questioned for artificial capsules with a thin homogeneous membrane, especially when irrealistic values of bending modulus are modeled.

Another approach has been to consider the membrane wall as a three–dimensional homogeneous material and to use the thin shell approximation. Le & Tan (2010) have developed such a thin shell model, but they have restricted the analysis to a Kirchhoff–Love kinematical assumption (i.e. no transverse shear) and only considered one small value of wall thickness. The effect of the wall bending resistance on the dynamics of a capsule suspended in an external flow is thus still an open question.

The objective of the study is to analyze the deformation of an initially spherical capsule in a simple shear flow, assuming that the wall is thin and made of a three–dimensional homogeneous elastic material with uniform thickness that resists both membrane and bending deformations. The equations governing the problem are solved numerically coupling a boundary integral method to compute the flow of the internal and external liquids with a shell finite element method to compute the deformation of the capsule wall, as outlined in sections 5.2 and 5.3. We show how, for a given wall material, the thickness influences the deformation under a given flow strength in section 5.4 and analyze which physical phenomena govern the capsule global deformation. We finally discuss the formation of wrinkles on the membrane and show how their wavelength is related to the bending resistance and correlatively to the wall thickness.

5.2 Problem formulation

We consider an initially spherical capsule enclosed by a three–dimensional homogeneous incompressible wall of thickness $\alpha\ell$ ($\alpha < 1$). The capsule radius ℓ is measured from the capsule mid–surface $\mathcal{S}_t$, which is located at the middle of the wall thickness. The wall is made of a material, which is supposed to be hyperelastic at moderate deformation with bulk shear modulus G and Poisson ratio $\nu = 1/2$. The capsule is suspended in a simple shear flow in the xy–plane with undisturbed velocity field

$$\underline{v}^{\infty} = \dot{\gamma} y \, \underline{e}_x, \tag{5.1}$$

where $\dot{\gamma}$ is the shear rate. The inner and outer fluids have the same viscosity μ and density.

By convention, all quantities are denoted by capital letters in the reference state and by lowercase letters in the deformed state. The surface tensor components are denoted with Greek indices and the 3D tensor components with Latin indices. We adopt the Einstein summation convention on repeated indices.

5.2.1 Wall mechanics

Due to the small mass of the capsule wall, all inertia effects are neglected when solving for the wall deformation. We assume the wall to be sufficiently thin to be modeled as a thin shell with mid–surface $\mathcal{S}_t$, as described, among others, by Chapelle & Bathe (2011) and briefly reviewed thereafter. The principle of the thin shell consists of evaluating all the quantities of interest on the mid–surface.

The position of a material point in the shell is defined by the independent curvilinear coordinates (ξ^1, ξ^2, ξ^3). In the reference non–deformed state (time $t = 0$), the position of a point M of the mid–surface is given by

$$\underline{OM} = \underline{\varphi}(\xi^1, \xi^2) \tag{5.2}$$

with O the chosen origin. It is convenient to introduce the local covariant base $(\underline{A}_1, \underline{A}_2, \underline{A}_3)$ defined as

$$\underline{A}_\alpha = \frac{d\underline{\varphi}(\xi^1, \xi^2)}{d\xi^\alpha} = \underline{\varphi}_{,\alpha} \qquad \text{and} \qquad \underline{A}_3 = \frac{\underline{A}_1 \times \underline{A}_2}{\| \, \underline{A}_1 \times \underline{A}_2 \, \|}, \tag{5.3}$$

where $\underline{A}_3$ is the unit normal vector. The contravariant base $(\underline{A}^1, \underline{A}^2, \underline{A}^3)$ is defined by $A^\alpha \cdot A_\beta = \delta^\alpha_\beta$ with δ^α_β the Kronecker tensor and $\underline{A}^3 = \underline{A}_3$. The same quantities are defined in the deformed state using lowercase letters: the local covariant and contravariant bases are respectively denoted $(\underline{a}_1, \underline{a}_2, \underline{a}_3)$ and $(\underline{a}^1, \underline{a}^2, \underline{a}^3)$. In the reference configuration, the three–dimensional position $\underline{X}$ of a material point within the capsule wall is then

$$\underline{X}(\xi^1, \xi^2, \xi^3) = \underline{\varphi}(\xi^1, \xi^2) + \xi^3 \underline{A}_3, \tag{5.4}$$

where $|\xi^3| \leq \alpha\ell/2$. In the deformed configuration, the new position $\underline{x}$ of a material point differs from the original position $\underline{X}$ through an unknown displacement field $\underline{u}$:

$$\underline{x}(\underline{X}, t) = \underline{X} + \underline{u}(\underline{X}, t). \tag{5.5}$$

The thin shell theory (Chapelle & Bathe, 2011) assumes that the displacement field satisfies the Reissner–Mindlin kinematic assumption, i.e. a material line initially orthogonal to the mid–surface remains straight and unstretched during deformation but does not remain orthogonal to the deformed mid–surface. All the terms depending on $(\xi^3)^2$ are thus neglected in the expression of the displacement $\underline{u}$, which can then be written as

$$\underline{u}(\xi^1, \xi^2, \xi^3, t) = \underline{u}_s(\xi^1, \xi^2, t) + \xi^3\, \theta_\lambda(\xi^1, \xi^2, t)\, \underline{a}^\lambda(\xi^1, \xi^2, t). \tag{5.6}$$

The first term represents the displacement of the mid–surface at coordinates (ξ^1, ξ^2). In the second term, the angles θ_1 and θ_2 are the rotation angles of the line passing by the point (ξ^1, ξ^2) of the mid–surface and perpendicular to the latter around the tangential vectors $\underline{a}^2$ and $\underline{a}^1$, respectively. To simplify the notations in the following, we introduce the rotational surface vector $\underline{\theta}(\xi^1, \xi^2, t) = \theta_\lambda(\xi^1, \xi^2, t)\, \underline{a}^\lambda(\xi^1, \xi^2, t)$.

The deformation gradient $\underline{\underline{F}} = \dfrac{\partial \underline{x}}{\partial \underline{X}}$ and the Green–Lagrange strain tensor $\underline{\underline{e}} = \dfrac{1}{2}\,(\underline{\underline{F}}^T \cdot \underline{\underline{F}} - \mathbb{I})$ induced by this displacement field are then deduced from Eq. (5.5-5.6) (see Eq. 2.35). The same asymptotic analysis (Chapelle & Bathe, 2011) also shows that the shell is undergoing plane stress at first order.

We assume that the wall material is hyperelastic: the second Piola–Kirchhoff stress tensor $\underline{\underline{\Sigma}}$ inside the wall is a given function of the Green–Lagrange strain tensor through the strain energy density function. For a linear isotropic material, the stress-strain relationship reduces to the generalized Hooke's law

$$\underline{\underline{\Sigma}} = 2\, G \left(\underline{\underline{e}} + \frac{\nu}{1-\nu}\, \mathrm{tr}\, \underline{\underline{e}} \right) . \tag{5.7}$$

The Cauchy stress tensor $\underline{\underline{\sigma}}$, which contains forces per unit area of deformed material, is related to the Piola–Kirchhoff stress tensor by

$$\underline{\underline{\sigma}} = \frac{1}{\det \underline{\underline{F}}}\, \underline{\underline{F}} \cdot \underline{\underline{\Sigma}} \cdot \underline{\underline{F}}^T. \tag{5.8}$$

It follows that, even for a linear material, $\underline{\underline{\sigma}}$ is a non–linear function of strain.

The wall equilibrium equations are then

$$\begin{cases} \nabla \cdot \underline{\underline{\sigma}} = \underline{0} \text{ inside the wall,} \\ \underline{\underline{\sigma}} \cdot \underline{a}_3 = \underline{q}^+ \text{ on the external wall surface } \mathcal{S}_t^+, \\ \underline{\underline{\sigma}} \cdot \underline{a}_3 = -\underline{q}^- \text{ on the internal wall surface } \mathcal{S}_t^-, \end{cases} \tag{5.9}$$

where $\underline{q}^+$ (respectively $\underline{q}^-$) is the viscous load per unit deformed area exerted by the external (respectively internal) fluid flow. They can be rewritten using the principle of virtual work, which dictates that the work done by the external loads acting on a deformable body are equal to the virtual change in internal strain energy. Let $\mathcal{V}$ be the Sobolev space $H^1(\mathcal{S}_t, \mathbb{R}^3)$. For any virtual displacement $\hat{\underline{u}}_s \in H^1(\mathcal{S}_t, \mathbb{R}^3)$ satisfying the Reissner–Mindlin assumption (Eq. 5.6) and any virtual rotation $\hat{\underline{\theta}} \in H^1(\mathcal{S}_t, \mathbb{R}^2)$, we have from Eq. (5.9)

$$\int_{\mathcal{S}_t^+} \hat{\underline{u}}\,(\hat{\underline{u}}_s, \hat{\underline{\theta}}) \cdot \underline{q}^+ \, dS - \int_{\mathcal{S}_t^-} \hat{\underline{u}}\,(\hat{\underline{u}}_s, \hat{\underline{\theta}}) \cdot \underline{q}^- \, dS = \int_V \hat{\underline{\underline{e}}}\,(\hat{\underline{u}}_s, \hat{\underline{\theta}}) : \underline{\underline{\sigma}} \, dV, \tag{5.10}$$

where V is the shell wall volume in the deformed state, $\hat{\underline{u}}$ an arbitrary kinematically admissible virtual displacement and $\hat{\underline{\underline{e}}}$ the corresponding virtual strain tensor. On $\mathcal{S}_t^+$, the virtual displacement reads

$$\hat{\underline{u}}\,(\xi^1, \xi^2, t) = \hat{\underline{u}}_s(\xi^1, \xi^2, t) + \frac{\alpha \ell}{2}\, \hat{\underline{\theta}}\,(\xi^1, \xi^2, t), \tag{5.11}$$

$+\alpha\ell/2$ being replaced by $-\alpha\ell/2$ on $\mathcal{S}_t^-$.

Since the capsule wall is treated as a thin shell for both the real and virtual displacement fields, the virtual work of the external load can be expressed in terms of a load $\underline{q}$ evaluated on the mid–surface

$$\int_{\mathcal{S}_t} \hat{\underline{u}}\,(\hat{\underline{u}}_s, \hat{\underline{\theta}}) \cdot \underline{q} \, dS = \int_V \hat{\underline{\underline{e}}}\,(\hat{\underline{u}}_s, \hat{\underline{\theta}}) : \underline{\underline{\sigma}} \, dV, \tag{5.12}$$

where $\underline{q}$ is the jump of viscous traction forces exerted by the fluids. The difference between the membrane and shell models is that, in the membrane model, all the terms which are $O(\alpha)$ are ignored, so that the membrane displacement is only given by $\underline{u}_s(\xi^1, \xi^2, t)$. In the shell model, the rotational and three–dimensional effects across the wall thickness are taken into account in the displacement (Eq. 5.6). These effects are included in the right–

hand side term of Eq. (5.12) and lead to a resistance to bending, which is quantified by a bending modulus M_b. For a homogeneous material that follows the generalized Hooke's law (Eq. 5.7), M_b is given by

$$M_b = \frac{G}{6\,(1-\nu)}\,(\alpha\ell)^3. \tag{5.13}$$

It follows that for the same deformation of the mid–surface, the expression of the load $\underline{q}$ is different for the membrane and shell models.

5.2.2 Internal and external flows

Owing to the small capsule size, the Reynolds number $Re = \rho\ell^2\dot{\gamma}/\mu$ is very small. The internal and external flows are thus governed by the Stokes equations. For thin walls, when the inner and outer fluids are of equal viscosity, the local velocity of the mid–surface points is then equal to the following integral of the viscous traction jump over the deformed capsule surface $\mathcal{S}_t$

$$\forall \underline{x}_s \in \mathcal{S}_t, \quad \underline{v}(\underline{x}_s) = \underline{v}^\infty(\underline{x}_s) - \frac{1}{8\pi\mu}\int_{S_t}\left(\frac{\mathbb{I}}{\parallel \underline{r} \parallel} + \frac{\underline{r}\otimes\underline{r}}{\parallel \underline{r} \parallel^3}\right)\cdot \underline{q}(\underline{y}_s)\,dS, \tag{5.14}$$

where $\underline{v}^\infty$ is the undisturbed flow velocity. The vector $\underline{r} = \underline{x}_s - \underline{y}_s$ is the distance vector between the point $\underline{x}_s$, where the velocity vector is calculated, and the point of integration $\underline{y}_s$ located on the surface $\mathcal{S}_t$. The wall and fluid mechanics are coupled through $\underline{q}$ and through the kinematic condition, which relates the wall velocity to the time derivative of the displacement field at the capsule mid–surface:

$$\forall \underline{x}_s \in \mathcal{S}_t, \quad \underline{v}\left(\underline{x}_s(\xi^1,\xi^2,t)\right) = \frac{\partial}{\partial t}\,\underline{u}_s(\xi^1,\xi^2,t). \tag{5.15}$$

Note that the velocities of the inner and outer fluids must be equal in order to keep the membrane shear finite.

5.2.3 Problem parameters

The capsule dynamics are governed by the relative wall thickness α and by the bulk capillary number

$$Ca_v = \frac{\mu\dot{\gamma}}{G}, \tag{5.16}$$

which compares the viscous to the elastic forces. When the wall is infinitely thin ($\alpha \ll 1$), it is customary to introduce a surface shear modulus $G_s = G\alpha\ell$, to which corresponds a surface capillary number

$$Ca_s = \frac{\mu\dot{\gamma}\ell}{G_s} = \frac{Ca_v}{\alpha}. \tag{5.17}$$

This surface capillary number is classically used to study the dynamics of capsules without bending resistance. When the bending resistance of the wall is accounted for, a bending number K_b can be introduced to measure the relative importance of bending and shearing effects:

$$K_b = \frac{M_b}{\alpha G \ell^3} = \frac{M_b}{G_s \ell^2}. \tag{5.18}$$

When we consider the capsule wall to be composed of a homogeneous incompressible material, the bending number is simply $K_b = \alpha^2/3$ as predicted from Eq. (5.13).

5.3 Numerical method

To solve the fluid–structure interaction problem (Eq. 5.7, 5.8, 5.12, 5.14, 5.15), we iteratively couple (*i*) a shell finite element method to solve the solid problem (i.e. Eq. 5.7, 5.8, 5.12) for the capsule deformation knowing the mid–surface displacement $\underline{u}_s$ to find the viscous load $\underline{q}$ acting on the capsule wall, and (*ii*) a boundary integral method to compute the local velocity of the mid–surface points using Eq. (5.14) for a given deformed capsule geometry and the viscous load transferred by the solid solver. We then update the position $\underline{u}_s$ of the mid–surface by integrating in time Eq. (5.15) using a first–order explicit Euler scheme. The underlying philosophy of the method is similar to the one designed by Walter *et al.* (2010) to simulate the dynamics of a capsule devoid of bending resistance. But, when the wall is modeled as a thin shell with finite thickness and bending resistance, the three-dimensional displacement field $\underline{u}$ is no longer known at the beginning of each iteration (only $\underline{u}_s$ is): the rotation vector $\underline{\theta}$ first needs to be solved for.

Since the evolution equation (Eq. 5.15) is integrated in time with an explicit scheme, the numerical method is stable only for sufficiently small time steps Δt. The stability criterion

$$\dot{\gamma}\Delta t < \mathcal{O}\left(\frac{\Delta x \, Ca_s}{\ell}\right), \tag{5.19}$$

previously defined by Walter *et al.* (2011) for a capsule without bending resistance remains valid, Δx denoting the mesh size. The introduction of bending does not modify the stability analysis, since the bending terms are imposed to be in equilibrium when solving the equilibrium of the microcapsule wall.

N_E	320	**512**	1280	**2048**	5120	**8192**
N_N	162	**258**	642	**1026**	2562	**4098**
$\Delta x/\ell$	0.3	**0.23**	0.15	**0.12**	0.075	**0.06**

Table 5.1: Number of nodes N_N and characteristic mesh size $\Delta x/\ell$ as a function of the number of elements N_E. The meshes obtained from an octahedron are written in boldface.

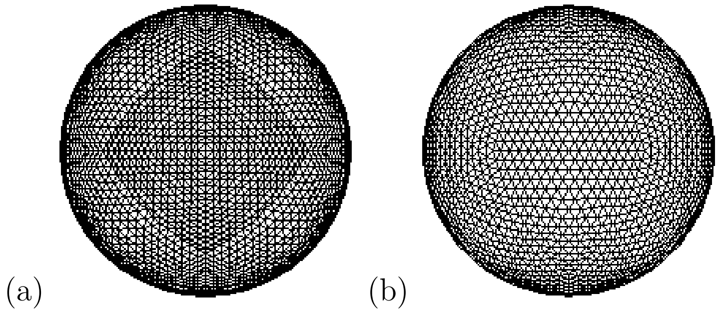

Figure 5.1: Typical meshes, respectively with 8192 and 5120 elements, obtained from the initial inscription of (*a*) an octahedron or of (*b*) an icosahedron in a sphere.

5.3.1 Discretization of the capsule wall

At time $t = 0$, the undeformed mid–surface of the capsule wall is discretized with linear triangular shell elements obtained by inscribing either an icosahedron (regular polyhedron with 20 triangular faces) or an octahedron (regular polyhedron with 8 triangular faces) in a sphere, and sequentially subdividing the triangular elements and projecting the resulting nodes on the spherical mid–surface. We denote N_E and N_N the number of elements and nodes respectively and $\Delta x/\ell$ the characteristic mesh size. The numbers of nodes and the average mesh size used in this study are given in Table 5.1 as a function of the number of elements. The mesh obtained from an octahedron is symmetrical about two meridians, while the mesh obtained from an icosahedron is more homogeneous (Figure 5.1).

5.3.2 Shell finite element procedure

The wall mid–surface equilibrium problem (Eq. 5.7, 5.8, 5.12) is treated with the shell finite element library Shelddon designed by Inria[1]. The shell finite element solver is coupled with the fluid solver (Walter *et al.*, 2010, 2011; Foessel *et al.*, 2011) by means of a Parallel Virtual Machine protocol.

The wall mid–surface is discretized with triangular shell elements of the MITC family (Mixed Interpolation Tensorial Components) with three nodes (one at each vertex), which

---

[1] The library is registered at the *Agence pour la Protection des Programmes* under ref: IDDN.FR.001.030018.000.S.P.2010.000.20600. The base of the program is open source and available online: www-rocq.inria.fr/modulef

are typically referred to as MITC3. Their formulation is based on standard linear shape functions $\lambda^{(p)}$ ($p \in \{1,2,3\}$) interpolating both the mid–surface displacement $\underline{u}_s$ and the rotations θ_λ. The unit normal vector $\underline{a}_3^{(p)}$ is calculated at each node p. The position of a point of the wall is determined by the local Cartesian coordinates (r,s,z), where (r,s) are the intrinsic coordinates in the plane element (defined such that r, s and $1-r-s \in [0,1]$) and z is the coordinate along $\underline{a}_3$ ($z \in [-1,1]$). The position vector $\underline{x}$ a node p inside an element thus reads

$$\underline{x}(t) = \sum_{p=1}^{3} \lambda^{(p)}(r,s) \left(\underline{x}_s^{(p)}(t) + z \, \frac{\alpha \ell}{2} \, \underline{a}_3^{(p)}(t) \right), \tag{5.20}$$

and the corresponding virtual displacement

$$\underline{\hat{u}} = \sum_{p=1}^{3} \lambda^{(p)}(r,s) \left(\underline{\hat{u}}_s^{(p)} + z \, \frac{\alpha \ell}{2} \, \underline{\hat{\theta}}^{(p)} \right). \tag{5.21}$$

The MITC technique is based on separate interpolations of the in–plane and out–of–plane components (e.g. $e_{\alpha 3}$ components) of the strain tensor, which are then connected at specific tying points. The MITC shell finite elements are shown to behave properly both for bending and for membrane dominated problems and satisfy the following properties:

- The finite element discretization leads to no spurious zero energy mode when solving the problem.
- The finite element solutions converge to the solution of the mathematical model, when the mesh size $\Delta x/\ell$ tends to zero.
- The shell is free of shear and membrane locking.
- The solution accuracy is independent of the shell thickness parameter.
- The matrices do not depend on the element orientation.

Details on the MITC technique can be found in Lee & Bathe (2004) and on the discretization of the equations in Chapelle & Bathe (2011).

Let $v_{X_j}^{(p)}$ denote the value of the j^{th} Cartesian component of any vector $\underline{v}$ at node p and $\{v\}$ the array of size $3N_N$ containing the Cartesian components of the vector nodal values. The wall equilibrium equation (Eq. 5.12) can be discretized element–wise as:

$$\sum_{el} \hat{u}_{X_j}^{(p)} \left(\int_{S_{el}} \lambda^{(p)} \lambda^{(q)} dS \right) q_{X_j}^{(q)} = \sum_{el} \int_{V_{el}} \hat{e}_{\alpha\beta} \sigma^{\alpha\beta} dV. \tag{5.22}$$

The discretization of the right–hand–side of Eq. (5.12) is more complex than in the case of the left–hand–side, since the Green-Lagrange strain tensor and the second Piola-Kirchhoff stress tensor have to be expressed according to the nodal displacements. More details can be found in Batoz & Dhatt (1992) (p. 324 - 325).

After assembling the arrays and matrices across the mesh elements, the discretized form of Eq. (5.12) becomes

$$\{\hat{u}\}^T [M] \{q\} = \{\hat{u}\}\{R\} (\{u_s\}, \{\theta\}), \tag{5.23}$$

where $[M]$ is the so-called mass matrix and the vector $\{R\}$ contains the elastic coefficients of the wall material.

As the equation must be satisfied for any virtual displacement, it can be simplified as

$$[M] \{q\} = \{R\} (\{u_s\}, \{\theta\}),$$

or more precisely, by separating the membrane degrees of freedom from the rotational degrees of freedom,

$$\begin{cases} \{R\}_s (\{u_s\}, \{\theta\}) - [M]_s \{q\} = \{0\}_s, & \text{(5.24a)} \\ \{R\}_\theta (\{u_s\}, \{\theta\}) = \{0\}_\theta. & \text{(5.24b)} \end{cases}$$

In this system, the mid–surface displacement degrees of freedom $\{u_s\}$ are known from the solution $\underline{x}_s$ of the fluid problem and the integration of Eq. (5.15), while the viscous loads $\{q\}$ and the rotations $\{\theta\}$ are unknown. To solve this system, we first solve the nonlinear equation (5.24b) in $\{\theta\}$ by a Newton's method and then obtain the load exerted by the fluids on the membrane by a direct inversion of Eq. (5.24a).

5.3.3 Numerical accuracy and convergence

To verify the temporal and spatial convergence of the coupling method, we consider the motion of an initially spherical capsule of thickness ratio $\alpha = 0.01$, subjected to a simple shear flow at $Ca_s = 0.6$. At steady state, the capsule mid–surface takes a quasi–ellipsoidal shape, which can be approximated by its ellipsoid of inertia. If we call L_1 and L_2 the lengths of the two principal axes of the ellipsoid of inertia in the shear plane (Figure 5.2), the capsule deformation at steady state can be measured by the Taylor parameter D_{12}^∞

$$D_{12}^\infty = \frac{L_1 - L_2}{L_1 + L_2}. \tag{5.25}$$

There is no analytical solution for the large deformation of a spherical capsule in a shear flow. To study the spatial convergence of the numerical method, we thus take as reference value $D_{12}^{\infty,ref}$ the value of D_{12}^∞ obtained with the smallest time step ($\dot{\gamma}\Delta t = 1 \times 10^{-4}$) and

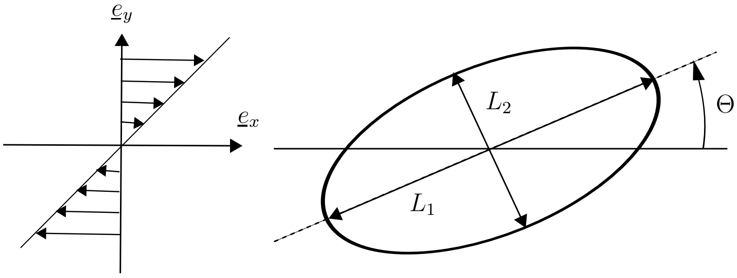

Figure 5.2: Representation in the shear plane $(\underline{e}_x, \underline{e}_y)$ of the ellipsoid of inertia of the deformed mid–surface of an initially spherical capsule. L_1 and L_2 are the lengths of the two principal axes in the shear plane. The angle Θ gives the inclination of the deformed capsule.

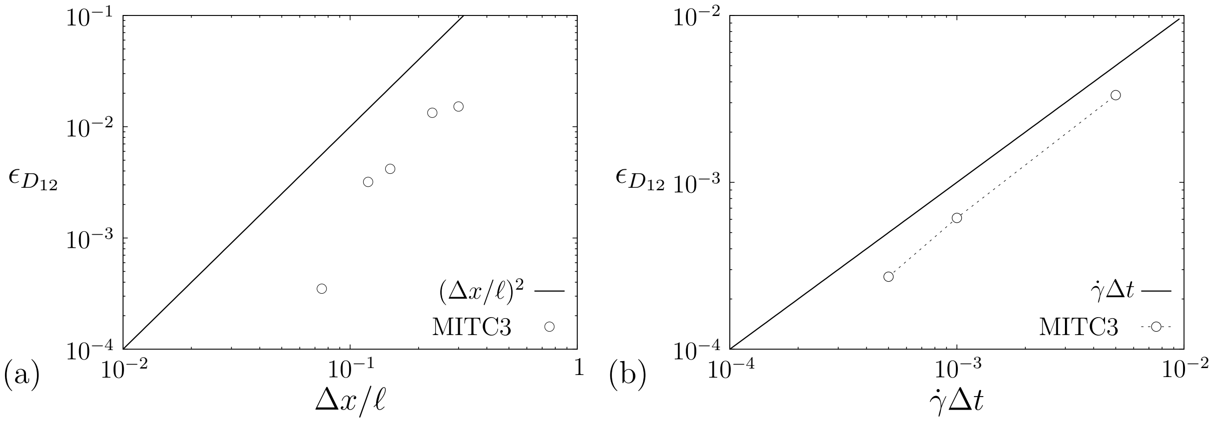

Figure 5.3: Relative numerical error $\epsilon_{D_{12}}$ based on the Taylor parameter D_{12}^{∞} for $Ca_s = 0.6, \alpha = 0.01$. (*a*) Spatial convergence (reference corresponding to $\dot\gamma\Delta t = 1 \times 10^{-4}$, $N_E = 8192$); (*b*) Time convergence (reference corresponding to $\dot\gamma\Delta t = 1 \times 10^{-4}$, $N_E = 5120$).

the most refined mesh size ($N_E = 8192$) at $\dot\gamma\Delta t = 4$, at which the steady state is reached. We define the relative numerical error as

$$\epsilon_{D_{12}} = \frac{|D_{12}^{\infty} - D_{12}^{\infty,ref}|}{D_{12}^{\infty,ref}}. \tag{5.26}$$

The evolution of the relative error as a function of the mesh size is shown in Figure 5.3a. The coupled numerical procedure appears to converge as $(\Delta x/\ell)^2$. We note that the difference between $N_E = 5120$ and $N_E = 8192$ is less than 3×10^{-4}. This justifies using only 5120 elements in the results reported here (except when specified otherwise).

The temporal convergence is then verified using as reference $D_{12}^{\infty,ref}$ the value of D_{12}^{∞} obtained for $\dot\gamma\Delta t = 1 \times 10^{-4}$ and $N_E = 5120$. The evolution of the relative error as a function of the dimensionless time step is shown in Figure 5.3b. We find that the relative error remains small ($\epsilon_{D_{12}} < 3 \times 10^{-3}$) and that the numerical procedure converges linearly in time.

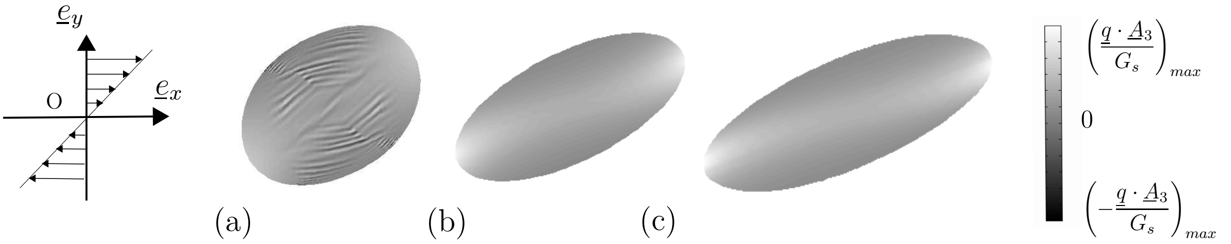

Figure 5.4: Steady shape of an initially spherical capsule with $\alpha = 0$ subjected to a simple shear flow ($N_E = 8192$): (*a*) $Ca_s = 0.1$; (*b*) $Ca_s = 0.6$; (*c*) $Ca_s = 1.2$. The grey level represents the repartition of the normal load, where the maximum value $\left(\underline{q} \cdot \underline{A}_3/G_s\right)_{max}$ is equal to (*a*) 0.5, (*b*) 3 and (*c*) 4.5.

5.4 Effect of wall bending resistance on the deformation of a capsule

We investigate the influence of two parameters on the dynamics of an initially spherical capsule subjected to a simple shear flow: the capillary number and the wall thickness (or equivalently the bending number). In the following, all the results (capsule profiles, deformation, etc.) pertain to the deformed capsule mid–surface.

5.4.1 Deformation of a capsule with no bending resistance

An initially spherical capsule with no bending resistance ($\alpha = 0$) subjected to a simple shear flow is elongated in the straining direction (Ramanujan & Pozrikidis, 1998; Lac *et al.*, 2004; Li & Sarkar, 2008; Walter *et al.*, 2010). This is illustrated in Figure 5.4 for a capsule with a membrane satisfying the generalized Hooke's law. At low flow strength, compressive tensions (forces per unit curved length in the capsule surface) arise in the central region during the transient phase and persist at steady state. They lead to membrane buckling and to the formation of wrinkles with a half–wavelength that is a function of the grid spacing (Figure 5.4a). The wrinkles are purely numerical, as no wall bending resistance is contained in the model, but the location where they occur is physical: it correlates with regions where the membrane is undergoing compression. When the surface capillary number increases above the critical value $Ca_{sL} \sim 0.4 - 0.45$ (irrespective of the wall constitutive law, because the deformation is still small), the capsule is more elongated: the tensions in the membrane increase and become all positive, so that wrinkles no longer appear at steady state (Figures 5.4b-c).

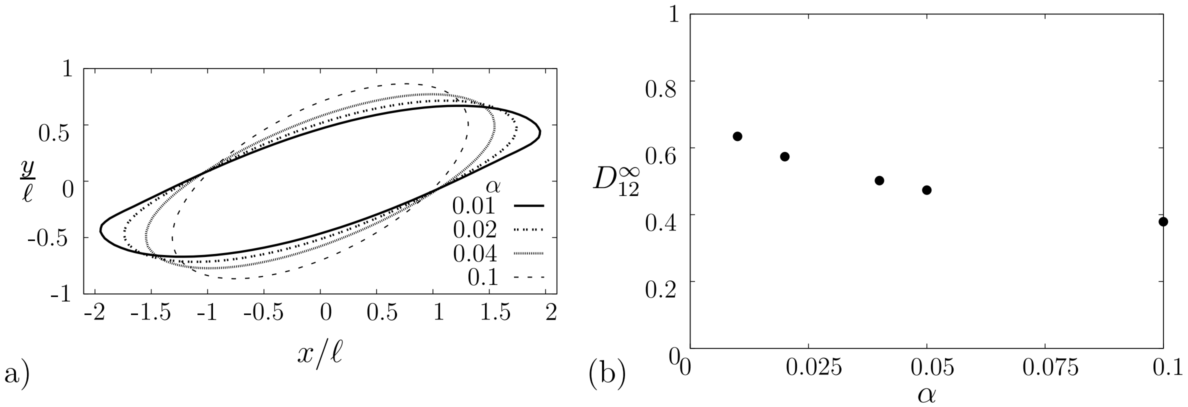

Figure 5.5: Capsule with wall material defined by $Ca_v = 0.05$: influence of wall thickness (a) on the mid–surface profile in the shear plane and (b) on the mid–surface deformation at steady-state D_{12}^{∞}.

5.4.2 Effect of wall thickness

In order to study the influence of the wall thickness on the capsule deformability, we simulate capsules made of the same homogeneous 3D material but with different wall thicknesses, subjected to a linear shear flow corresponding to $Ca_v = 0.05$. The profile of the capsule mid–surface in the shear plane is shown in Figure 5.5a. It shows that the thinner the wall, the more elongated the capsule becomes under the influence of the external flow. The capsule deformation decreases with the wall thickness. The tip curvature also decreases, so that the capsule has a more rounded shape. The steady–state deformation D_{12}^{∞} of the capsule mid–surface was computed from the corresponding ellipsoid of inertia. Figure 5.5b indicates that, for a given value of Ca_v, i.e. for a given wall material, the deformation decreases as the thickness increases.

We now study the combined effects of Ca_v and α. For a given wall thickness, the deformation increases when Ca_v increases, since the capsule is more elongated by the external flow (Figure 5.6a). If the wall thickness is now increased, we find again that the deformation decreases. Increasing the wall thickness thus has the drastic effect of preventing the capsule from deforming. It is interesting, however, that, if one plots the deformation as a function of the *surface* capillary number Ca_s, all the results fall onto one curve, which is the one obtained for a membrane wall devoid of bending resistance (Figure 5.6b). This means that even under large deformation, the bending resistance has a negligible effect on the overall capsule deformed profile and that the main mode of deformation results from the stretching of the mid–surface $\mathcal{S}_t$ in its plane (membrane mode).

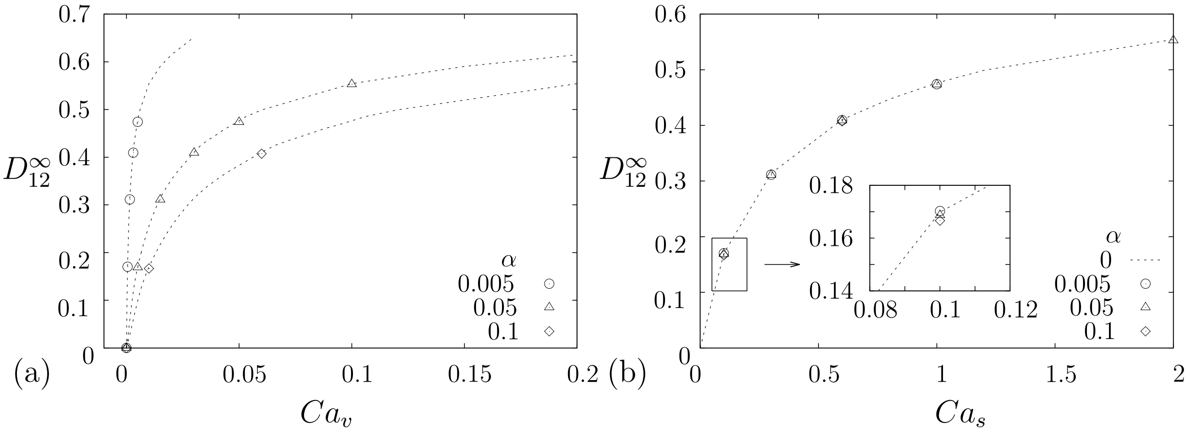

Figure 5.6: Mid–surface deformation at steady state D_{12}^{∞} as a function of (a) Ca_v and of (b) Ca_s for different thicknesses.

5.4.3 Membrane buckling at low flow strength

We now study the effect of bending resistance (or equivalently of shell thickness) on the behavior of a capsule for a constant Ca_s. We consider the case $Ca_s = 0.1$, which is below the critical value Ca_{sL}, in order to be in the regime where buckling is known to occur for zero–thickness capsules. The wall thickness is varied between $\alpha = 0.005$ and 0.02. The corresponding bulk capillary number Ca_v is small and varies between 5×10^{-4} and 2×10^{-3}.

When the capsule wall is treated as a thin shell, it is still subjected to compressive tensions in the central region as it was observed in the membrane model. As a consequence, buckling may occur at steady state depending on the bending resistance of the capsule wall (Figure 5.7). For very small thicknesses (e.g. $\alpha = 0.003$), the wrinkles that can be observed in Figure 5.7a appear at the same location and with the same pattern as those in Figure 5.4a, which correspond to a capsule devoid of bending stiffness. When the wall thickness is increased, the bending resistance increases and fewer wrinkles are formed (Figure 5.7b-d). For $\alpha \geq 0.02$, the wall is too thick for wrinkles to form (Figures 5.7e, 5.7j), even if it is subjected to compressive tensions. It is thus possible to prevent buckling by increasing the wall thickness (or equivalently the bending resistance).

5.4.4 Wrinkle analysis

It is not very easy to study the geometric characteristics of the wrinkles (amplitude, wavelength), as the capsule is a three–dimensional closed object. We first consider the same case as in the previous subsection of a capsule subjected to a surface capillary number $Ca_s = 0.1$. The capsule has a thickness ratio $\alpha = 0.01$. The most reproducible technique is to study the wrinkles in the yz–plane. Their characteristics are found from

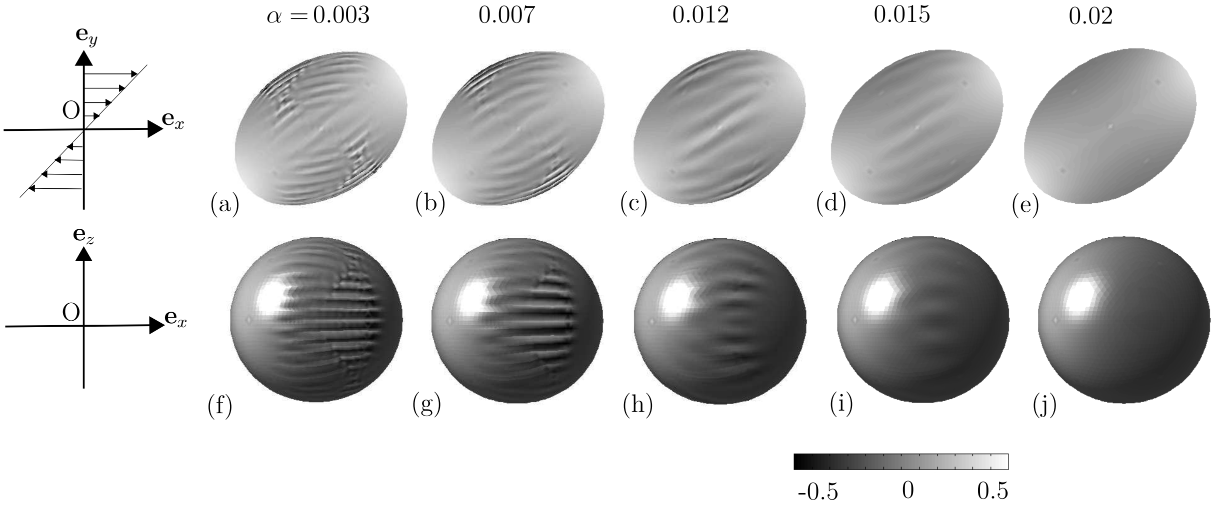

Figure 5.7: Steady profiles of an initially spherical capsule subjected to a simple shear flow at $Ca_s = 0.1$ for different wall thicknesses α ($N_E = 8192$). (*a*) to (*e*): projection in the shear xy–plane; (*f*) to (*j*): projection in the shear xz–plane. The grey levels represent the repartition of the normal load, the white spots on views (*f*) to (*j*) are a lighting artefact.

the capsule cross–section $\mathcal{S}_{yz}$ within the plane: we subtract from the in–plane capsule profile the profile of the ellipsoid of inertia in the same plane. The capsule profile is shown in Figure 5.8a in terms of the polar coordinates (ρ, θ), such that the shear plane is located at $\pi = 0, -1$. The radius difference $\Delta\rho/\ell$ between the two curves is shown in Figure 5.8b as a function of the arc length s/ℓ along $\mathcal{S}_{yz}$, where $s = 0$ when $\theta = 0$.

One must note that the profile oscillations $\Delta\rho/\ell$ are determined from the profile intersection with the yz–plane, which cuts through the surface grid and intersects the elements randomly. It follows that the $\Delta\rho/\ell$ versus s/ℓ curve has an uneven spatial discretization with mean value $\Delta x/2\ell$. In particular for the case shown in Figure 5.8b, we have between 9 and 12 points per oscillation, which is enough to determine a wavelength.

To determine a characteristic wrinkle wavelength at a given time $\dot{\gamma}t$, we measure the distance between two successive extrema for the wrinkles located near the shear plane ($s/\ell \in [-1.28, +1.28]$ - see the box in Figure 5.8b), which is the zone where the wrinkles are the most apparent, and compute the wrinkle mean wavelength λ_w/ℓ. The wrinkle wavelength λ_e in the equatorial plane of the capsule is then $\lambda_w \cos\Theta$, where Θ is the angle between the capsule long axis in the shear plane and the x–axis at steady state (Figure 5.2). A characteristic wrinkle amplitude A/ℓ is determined from the wrinkle located at $s = 0$ (wrinkle with the maximum amplitude).

Prior to studying the wrinkle characteristics, we first need to find the mesh refinement for which the wrinkle wavelength no longer depends on the mesh size. To do so, we determine the various wavelengthes of the wrinkles in the region of interest (boxed region shown in Figure 5.8b) and repeat the procedure at four instants of time ($\dot{\gamma}t$ = 3, 3.5, 4,

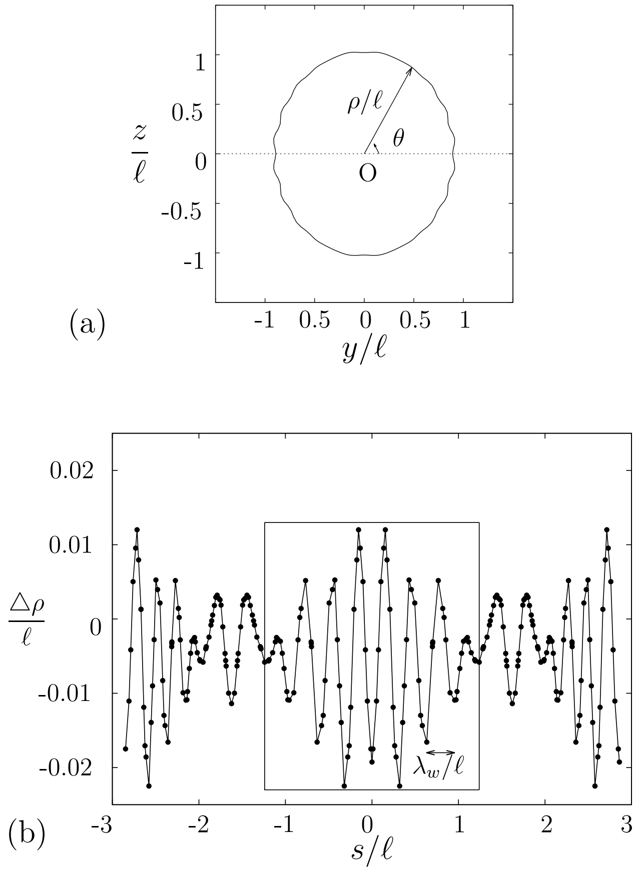

Figure 5.8: Membrane wrinkles for $Ca_s = 0.1$, $\alpha = 0.01$, $N_E = 8192$, $\Delta x/\ell = 0.06$. (*a*) Capsule mid–surface profile in the yz–plane (the dotted line represents the shear plane); (*b*) radius difference between the ellipsoid of inertia and the mid–surface in the yz–plane. The arc length is measured along the profile with $s = 0$ when $\theta = 0$, the points represent intersections with the grid.

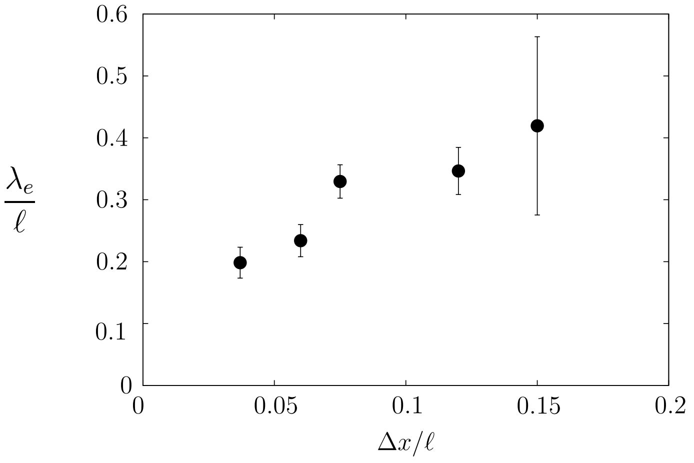

Figure 5.9: Influence of the mesh size $\Delta x/\ell$ on the space- and time-average wrinkle wavelength ($Ca_s = 0.1$, $\alpha = 0.01$).

4.5) to cover a quarter of the tank-treading period. Figure 5.9 shows the evolution of the space- and time-average value of the wrinkle wavelengthes as a function of the mesh size. The error bars correspond to the value of standard deviation, which is about 10% for $\Delta x/\ell \leq 0.12$ ($N_E \geq 2048$) and 30% for $\Delta x/\ell = 0.15$ ($N_E = 1280$). We have added a very fine mesh ($N_E = 20480$, $N_N = 10242$, $\Delta x/\ell = 0.037$) for the sake of completeness. For a coarse mesh (e.g. $\Delta x/\ell = 0.15$, $N_E = 1280$), the rigidity due to the surface elements is dominant, so that the wrinkle wavelength ($\lambda_e/\ell \sim 0.36$) is difficult to determine with great precision, but is approximately equal to twice the element spacing. When the number of elements increases, the mean wrinkle wavelength decreases and tends towards a limiting value $\lambda_e/\ell \sim 0.2$. Note that this plateau value becomes roughly independent of the mesh size when $\Delta x/\ell \leq 0.06$ ($N_E \geq 8192$) and that it is much larger than the grid point spacing. The difference between the mean wavelength values computed with $\Delta x/\ell = 0.06$ ($N_E = 8192$) and $\Delta x/\ell = 0.037$ ($N_E = 20480$) is less than 3.6×10^{-2}, which is of the same order of magnitude as the standard deviation. In the following, the results will therefore be obtained by considering a mesh with $N_E = 8192$ elements. The most refined mesh ($N_E = 20480$) indeed requires several weeks of computation to reach the steady state. One can finally note that Figure 5.9 indicates that $\lambda_e/\ell \sim 0.2$ is the physical buckling wavelength of a shell of thickness ratio $\alpha = 0.01$.

The influence of the thickness ratio on λ_e is shown in Figure 5.10a at $\dot{\gamma}t = 4.5$ for $Ca_s = 0.1$. We find that λ_e increases with α. The wall equilibrium is thus unstable and buckling occurs at the nodes where small numerical errors create a disturbance. If one increases the thickness (i.e. bending resistance), the wrinkles have a higher wavelength. Their amplitude remains about constant for low values of bending resistance (Figure 5.10b); it, however, strongly decreases hereafter when the bending resistance is increased, until being nil when the wrinkling phenomenon stops ($\alpha \geq 0.02$ for $Ca_s = 0.1$).

In order to determine whether the surface capillary number Ca_s influences the wrinkle wavelength, we have also considered the cases ($Ca_s = 0.07, \alpha = 0.005, 0.01, 0.015$) and ($Ca_s = 0.2, \alpha = 0.004$). As shown in Figure 5.10a, the corresponding wrinkle wavelength follows the same trend for all the values of Ca_s, and only depends on the relative wall thickness α. This result is not unexpected, as the buckling behavior of the wall depends on its bending resistance. The wall thickness above which wrinkles no longer form, however, decreases when the surface capillary number Ca_s increases. The amplitude is indeed nil for $\alpha \geq 0.02$ at $Ca_s = 0.1$ (Figure 5.10b) and for $\alpha \geq 0.005$ at $Ca_s = 0.2$. This is due to the fact that, as Ca_s increases, the wall deformation increases and the amplitude of the compressive tensions decreases (recall that for a flow strength larger than Ca_{sL}, there is no more compression and all tensions are positive). Consequently, as Ca_s is increased, the compression on the wall decreases, so that less thickness is needed to withstand buckling.

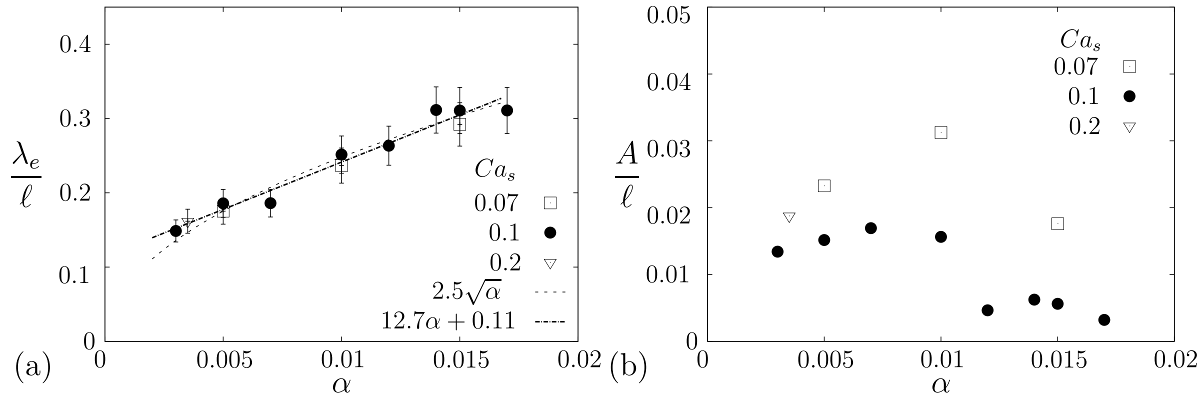

Figure 5.10: Influence of the shell thickness on (*a*) the wrinkle mean wavelength and (*b*) amplitude for different values of Ca_s.

5.5 Discussion and conclusion

The dynamics of an initially spherical capsule subjected to a linear shear flow has been studied numerically by coupling a shell finite element method with a boundary integral method to account for three–dimensional homogeneous wall properties and model the wall bending resistance. This method allows to study the influence of small thickness on the capsule deformation. It is numerically stable and free of locking.

We observe that, for a given wall material, the capsule deformability decreases when the wall thickness increases. However, if we consider only the dynamics of the shell mid–surface, we find that the overall deformation of the capsule depends only on the surface capillary number with no influence of the bending resistance. This means that the stretching of the mid–surface is the prevailing phenomenon. This is an important result, because it validates the use of a simple membrane model to compute the deformation of a capsule: such a model is indeed much faster and easier to run than a full shell model. Note that, if we use Ca_s as the main parameter for given flow strength and capsule size, the bulk elastic modulus G implicitly decreases when α is increased. This means that the larger α, the softer the material. This is probably the reason why we see no effect of thickness on the deformation curve in Figure 5.6b.

The sole dependence on Ca_s may also well be an effect of the facts that the capsule is initially spherical and that its core is entirely filled with an incompressible liquid. It can thus only deform by increasing its surface area, as its volume is constant. The capsule deformation thus results from elastic stretching of the wall. It follows that a simple membrane model is adequate to model the elastic behavior of spherical capsules, unless one is specifically interested in the post–buckling behavior. However, this may not be true for capsules which are initially non–spherical: such particles have an excess surface area compared to the enclosed volume and can change their geometry at small energy cost. In this case, bending effects may become preponderant compared to surface stretching.

Other authors such as Pozrikidis (2001), Le (2010) and Hang *et al.* (2012) have observed that the bending resistance reduces the capsule deformability at a given Ca_s. But they have all considered very large values of bending resistance that presently correspond to a wall thickness ratio α of 0.3 in the lowest case and up to 0.9: they, hence, do not respect the hypothesis of thin shell. It is difficult to imagine an existing homogeneous (or even composite) material that has both a very low shear elastic modulus and a very high bending modulus. The case of the red blood cell membrane is the exception, but its wall can hardly be considered as being homogeneous.

Even if a membrane model can be used to predict the post–buckling overall shape of a thin spherical capsule, a shell model is needed to analyze the formation of the wrinkles, which appear at low Ca_s. We have found that the wrinkle wavelength depends only on the wall thickness ratio α (or equivalently the bending number K_b) and increases with it. The wavelength can be correlated to the bending stiffness either linearly:

$$\lambda_e/\ell = 12.7\alpha + 0.11 \tag{5.27}$$

or by a power function:

$$\lambda_e/\ell = 2.5\sqrt{\alpha} = 3.3\,(K_b)^{1/4} \tag{5.28}$$

with a correlation coefficient $R^2 = 0.98$ in both cases. It is difficult to decide numerically between the two correlations, as it takes very long computational times to go below $\lambda_e/\ell = 0.2$. Indeed, this requires to impose very small wall thickness ($\alpha\ell < 0.003$) and to use an extremely fine mesh with a correspondingly small time step (Eq. 5.19). However in principle, the wrinkle wavelength should decrease to the asymptotic value of zero for $\alpha = 0$, which corresponds to a membrane with no resistance to bending. So it would seem that the correlation (Eq. 5.28) is physically more realistic than (Eq. 5.27). It is interesting to note that Cerda & Mahadevan (2003), who studied a thin homogeneous membrane stretched between two clamped ends, have predicted that the wavelength λ_e/ℓ of the wrinkles forming on the sheet is a function of the square root of the thickness ratio and have found the correlation law $\sqrt{\frac{8\pi}{3}}\sqrt{\alpha} = 2.9\sqrt{\alpha} = 3.8\,(K_b)^{1/4}$. The small difference between the factors of proportionality between Cerda and Mahadevan's correlation law and ours (Eq. 5.28) is due to the difference in geometry and boundary conditions. It seems to indicate that the wavelength of the wrinkles forming along the capsule can be predicted from a simple energy balance between bending and stretching under the constraint of the constitutive law of the wall material. However, if this balance is relatively simple to establish analytically for a flat membrane, it is much harder to find for a spherical membrane subjected to viscous shear forces. A numerical model is thus necessary in the

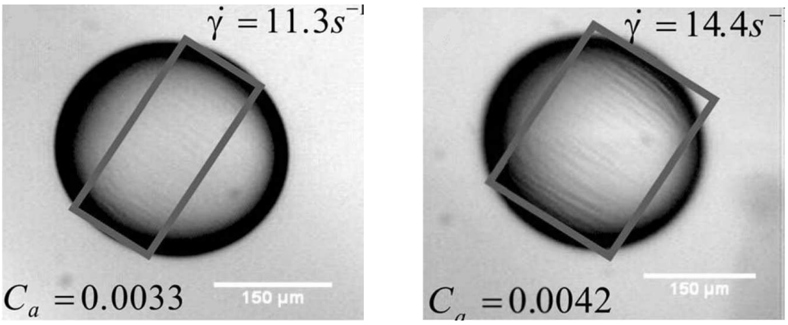

Figure 5.11: Polysiloxane capsule subjected to a simple shear flow. Wrinkles (inside the rectangle) appear in the central region due to compressive tensions. Images from Koleva & Rehage (2012), reproduced with the permission of The Royal Society of Chemistry. The capillary number C_a denoted on the pictures corresponds to the surface capillary number Ca_s.

latter case.

This result is essential from both a fundamental and an applied point of view. It can be used in practice to determine the capsule wall properties (thickness, surface shear modulus and bending modulus) from experiments, in which an initially spherical capsule is subjected to a linear shear flow with $Ca_s < Ca_{sL}$. The idea is to first compute the Taylor parameter D_{12} from an image of the deformed capsule shape acquired in the shear plane. The capillary number is deduced from the curve giving D_{12} as a function of the surface capillary number (Figure 5.6b). Its value is independent of the material behavior, as the deformation is small at low flow strength. The surface shear modulus is then deduced from the definition of the surface capillary number Ca_s (Eq. 5.17) and the experimental values of $\dot{\gamma}$ and μ. The second part of the procedure consists in measuring the wavelength of the wrinkles on the experimental image of the capsule. Knowing the wavelength λ_e, the wall thickness ratio can be estimated from Figure 5.10a or Eq. (5.28) and the bending modulus deduced from Eq. (5.13).

Using this method, we have analyzed the wrinkling processes of the polysiloxane capsules studied by Koleva & Rehage (2012), which have a radius equal to $\ell = 163\,\mu$m (Figure 5.11). The capsule surface shear modulus is estimated from the small deformation asymptotic relation (Barthès-Biesel, 2011)

$$D_{12} = \frac{25}{12}\frac{\mu\dot{\gamma}\ell}{G_s}. \tag{5.29}$$

and found to be equal to 2.19×10^{-1} N.m^{-1}. The wavelength of the folds can be measured to be roughly 10.4 - 12.9 μm. We find a value of wall thickness equal to $\alpha\ell \sim (107 - 163) \times 10^{-9}$m, and a bending modulus $M_b \approx 0.8 - 1.9 \times 10^{-3}$ N.m. The present analysis thus offers an interesting technique to characterize the mechanical properties of capsules of micrometric size and to provide an estimation of an apparent mean thickness of the wall.

In principle, the results of this paper are restricted to thin capsules. In the previous paragraph, we have just shown that the wall thickness of interface cross-linked capsules is about a thousand times smaller than the radius, which confirms the validity of the thin-shell approximation to study such artificial capsules If we want to model thicker capsules, one should probably switch to a three–dimensional model for the capsule wall, an endeavor which is outside the scope of this paper.

5.6 Additional results: influence of constitutive law

5.6.1 Capsule in shear flow

The constitutive law governing the behavior of the mid–surface in the median plane has been modified to study its influence on the dynamics of a spherical capsule with bending resistance in shear flow. A Skalak or a neo-Hookean law is used to model the membrane effects, combined with the generalized Hooke's law for the bending effects. For the sake of brevity, we denote the type of wall only by the constitutive law, which describes the behavior of the mid–surface in the median plane.

When capsules are made of the same homogeneous three–dimensional material but have different thicknesses at $Ca_v = 0.01$, we observe again that the thinner the wall, the more elongated the capsule becomes under the influence of the external flow (Figure 5.12). We observe, however, an influence of the constitutive law on the mid–surface deformation of the capsule mid–surface: at $\alpha = 0.01$, the capsule is more elongated with a neo–Hookean wall than with a Skalak law. As the neo–Hookean law is strain–softening and the Skalak law strain–hardening, for the same imposed stress, the deformation of the capsule with the neo–Hookean wall is higher than the one with a Skalak wall. The decrease of the capsule mid–surface deformation D_{12}^{∞} at steady state is represented in Figures 5.13 for different Ca_v and it is not surprising to observe that for a given wall thickness, the capsule mid–surface deformation increases with Ca_v, since the capsule is more elongated by the external flow.

The steady–state capsule mid–surface deformation is shown in Figure 5.14 as a function of Ca_s for the three constitutive laws. We recover that for a given constitutive law, the wall thickness has no significant influence on the deformation. This result confirms that the main deformation mode of a spherical capsule is governed by the elastic stretching of the mid–surface. Figure 5.14 shows that a little difference between the deformation curve obtained for the Skalak law and generalized Hooke's wall, since both constitutive laws are strain–hardening under uniaxial stretching. The fact that the neo–Hookean law is

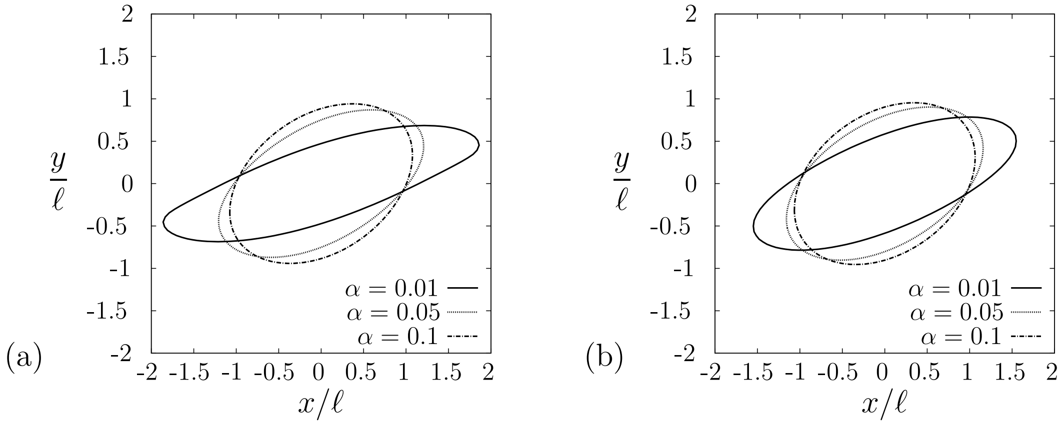

Figure 5.12: Spherical capsule in shear flow: influence of wall thickness on the profile of the capsule mid–surface within the shear plane for $Ca_v = 0.01$. (a) Neo-Hookean law, (b) Skalak law.

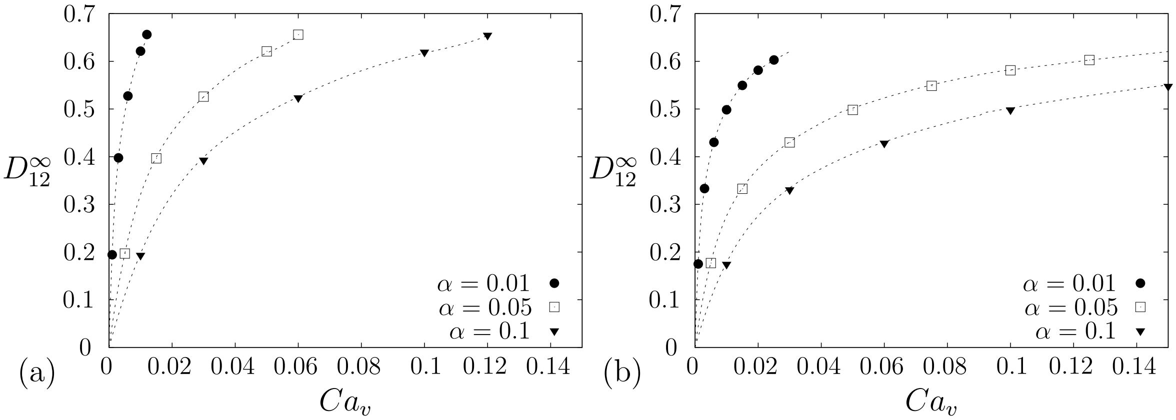

Figure 5.13: Spherical capsule in shear flow: steady–state deformation D_{12}^{∞} as a function of Ca_v. (a) Neo-Hookean law, (b) Skalak law.

strain–softening bears two consequences: (i) for the same Ca_s, the deformation is larger than the one with a Skalak or generalized Hooke's wall; (ii) the capsule does not reach a steady state at large Ca_s, contrary to the two other cases.

Similarly to the generalized Hooke's law, wrinkles appear in the equatorial region of a capsule with a neo–Hookean or Skalak wall at low Ca_s. As buckling occurs at low Ca_s, the capsule is under small deformation, which explains why the constitutive law hardly influence the capsule mid–surface deformation in this case. The capsule behavior is then in the linear part of curve shown in Figure 5.14. We thus do not expect the constitutive law to have a significant influence on the wrinkle wavelength and on its dependence on the bending rigidity.

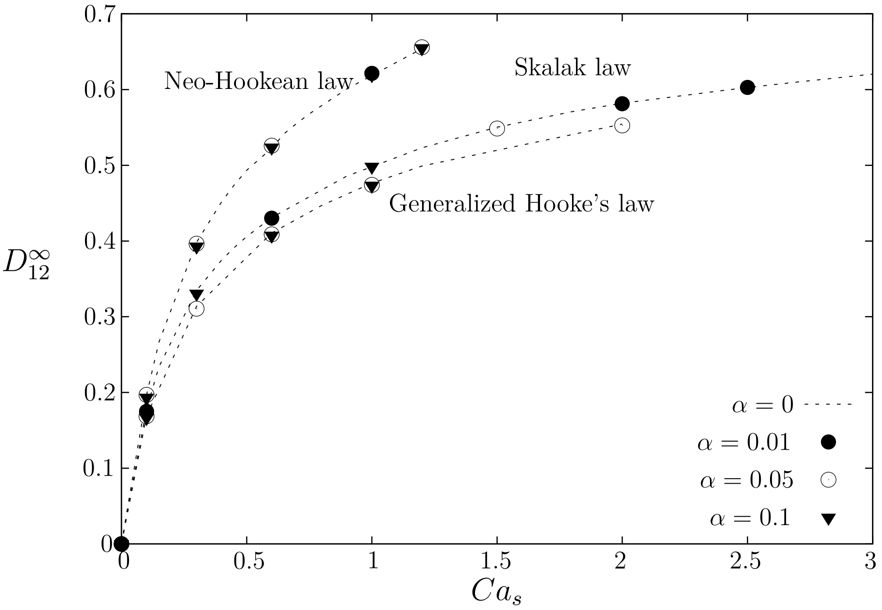

Figure 5.14: Spherical capsule in shear flow: steady–state deformation D_{12}^{∞} as a function of Ca_s for various constitutive laws.

5.6.2 Capsule subjected to a planar hyperbolic flow

We are now interested on the influence of the bending resistance on the dynamics of an initially spherical capsule subjected to a planar hyperbolic flow. We investigate the influence of the non–dimensional governing parameters on the deformation and study the influence of the bending resistance on the formation of the wrinkles, which appears at low Ca_s.

Effect of wall bending resistance on capsule deformation

We first consider an initially spherical capsule with constant bulk shear modulus G at $Ca_V = 0.005$ and vary the wall thickness. Figure 5.15 shows that the capsule with a generalized Hooke's wall is elongated in the flow direction and compressed in the perpendicular direction at steady state. More importantly, it qualitatively indicates that the thicker the wall, the less deformed the capsule is at steady state. The capsule deformation thus decreases with the bending resistance. The evolution of the steady–state Taylor parameter D_{12}^{∞} as a function of Ca_v and α is shown in Figures 5.16 for the three constitutive laws.

For a given wall thickness, the capsule elongates under the influence of the external flow, so that D_{12}^{∞} increases with the bulk capillary number Ca_v. The Figures 5.16 also prove what was observed qualitatively in Figure 5.15 with a generalized Hooke's wall, that increasing the wall thickness decreases the global capsule deformation.

If we now plot the Taylor parameter as a function of the surface capillary number Ca_s

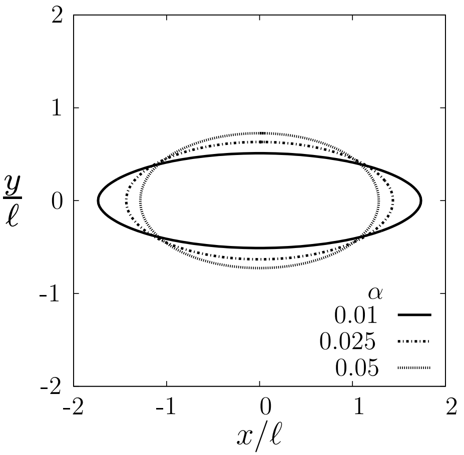

Figure 5.15: Spherical capsule in planar hyperbolic flow: influence of wall thickness on the profile of the capsule mid–surface (with a generalized Hooke's wall) within the shear plane for $Ca_v = 0.05$.

(Figure 5.17), we observe again that all the results fall onto the curve found for a capsule without bending resistance. We recover that the main deformation mode of a spherical capsule is thus governed by the elastic stretching of the mid–surface.

Effect of wall bending resistance on buckling

If stretching effects control the global capsule shape and deformation, bending effects may still play a role locally, whenever buckling occurs, as we have seen when a spherical capsule is subjected in shear flow. Results obtained on capsules without bending resistance in planar hyperbolic flow have shown that wrinkling occurs for Ca_s smaller than the critical value $Ca_{sL} = 0.14 - 0.15$. The latter is independent of the constitutive law, as the capsule deformation is then still in the small-deformation regime. The following results are obtained with a generalized Hooke's wall.

In order to investigate how the bending resistance influences the formation of wrinkles, let us consider a capsule such that $Ca_s = 0.1$, which is below Ca_{sL}. The corresponding capsule thickness is varied between $\alpha = 0.003$ and 0.02, while Ca_s is kept constant, so that Ca_v is varied between 3×10^{-4} and 2×10^{-2}.

When the capsule wall is modeled as a thin shell, buckling occurs in the central region of the capsule due to compressive tensions (Figures 5.18b-c). Wrinkles appear at the same location as those observed when the capsule is devoid of bending resistance (Figure 5.18a). As it was noted previously, the membrane model can thus be used to predict the location of the formation of wrinkles. But a thin shell model is needed to obtain information on the wrinkle wavelength, as it depends on the bending resistance. When the wall thickness increases, the bending resistance increases and fewer wrinkles are formed (Figures 5.18b-c). For $\alpha \geq 0.02$, wrinkles no longer form. Like in shear flow, it is thus possible to prevent

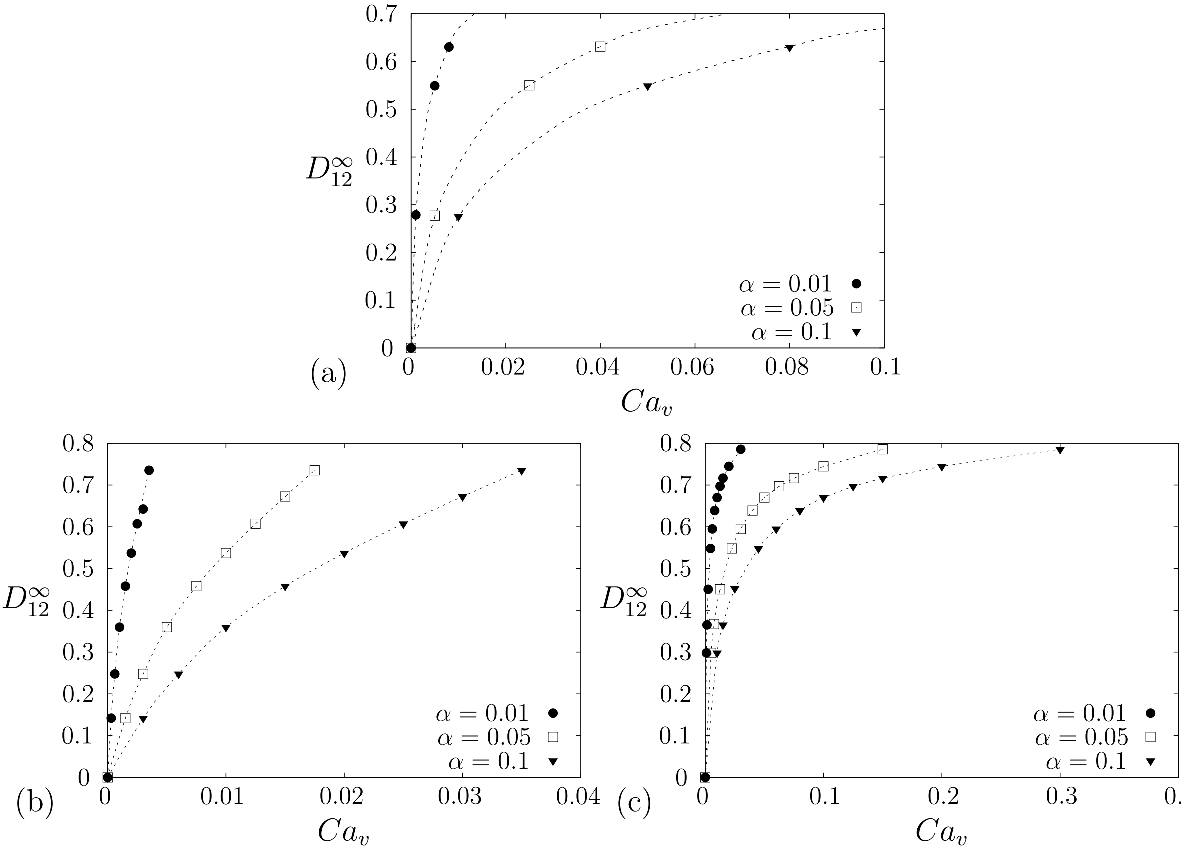

Figure 5.16: Spherical capsule in planar hyperbolic flow: steady–state deformation D_{12}^{∞} as a function of Ca_v. (*a*) Generalized Hooke's law, (*b*) Neo-Hookean law and (*c*) Skalak law.

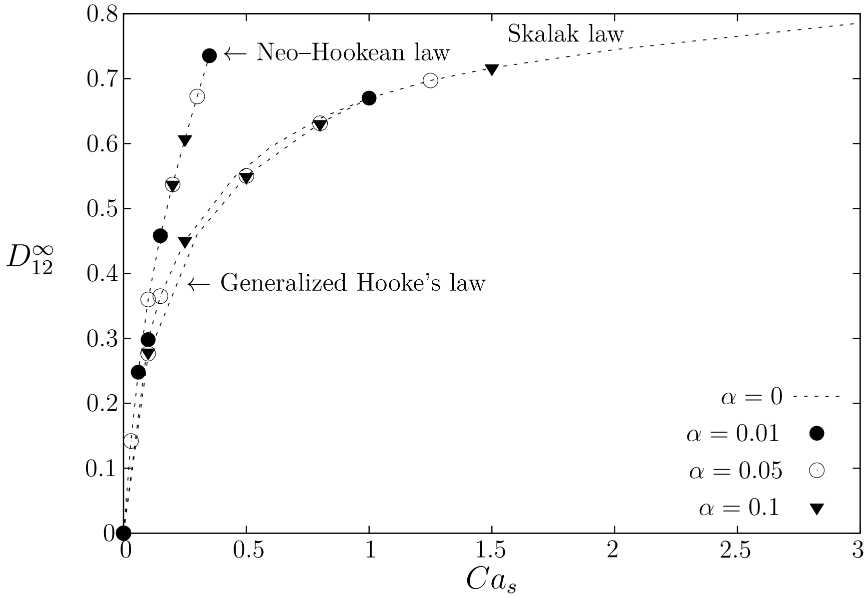

Figure 5.17: Spherical capsule in planar hyperbolic flow: steady–state deformation D_{12}^{∞} as a function of Ca_s for various constitutive laws.

buckling by increasing the wall thickness (Figure 5.18d).

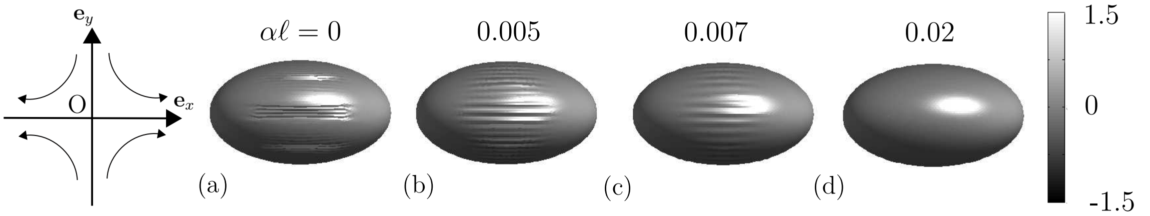

Figure 5.18: Shape evolution of a capsule with a generalized Hooke's wall at steady state for an initially spherical capsule subjected to a planar hyperbolic flow at $Ca_s = 0.1$ with (a) $\alpha = 0$; (b) 0.005; (c) 0.007; (d) 0.01. The grey levels represent the repartition of the normal load. The white spots are a lighting artefact.

We adopt the same method as in the shear flow, except that the wrinkle wavelength is directly found in the yz-plane. Before analyzing any further the wrinkle characteristics, we verify again that the wavelength is independent of the mesh used. Figure 5.19 shows the mean wrinkle wavelength λ_e/ℓ for a capsule with $\alpha = 0.01$ and $Ca_s = 0.1$ as a function of the number of elements. The wavelength reaches the constant value $\lambda_e/\ell = 0.25$ for meshes with at least 8000 elements. Thus, we choose to run all the simulations with 20480 elements.

The influence of the bending resistance on the wrinkle wavelength and amplitude is studied by increasing the relative wall thickness (Figure 5.20). Figure 5.20a shows that the wavelength monotonously increases with α, until wrinkles no longer form ($\alpha > 0.02$ for $Ca_s = 0.1$). Figure 5.20b indicates that the wrinkle amplitude A/ℓ is maximum for small values of α and then decreases until being nil for $\alpha > 0.02$.

To investigate whether the surface capillary number affects the wrinkle wavelength, we have considered the case of a capsule with a thickness $\alpha = 0.005$ and 0.007 at $Ca_s = 0.07$. The two points, added in Figure 5.20, are superimposed on the ones found for $Ca_s = 0.1$. Like in shear flow, the wrinkle wavelength is thus not a function of Ca_s and only depends on the bending number. As shown in Figure 5.20a, the wrinkle wavelength is a function of the square-root of the thickness ratio α. A correlation $\lambda_e/\ell = 2.6\sqrt{\alpha} = 3.4\, K_B^{1/4}$ is found with correlation coefficient $R^2 = 0.97$. We recover the same constitutive law than the one found in shear flow and it is similar to the one predicted by Cerda & Mahadevan (2003) for a thin homogeneous membrane is stretched between two clamps. The same inverse analysis as the one that we have explained in simple shear flow, can be used to characterize the mechanical properties of capsules.

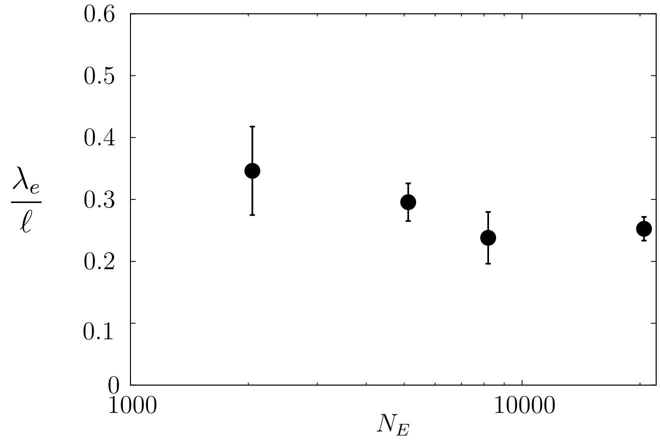

Figure 5.19: Capsule with a generalized Hooke's wall in a planar hyperbolic flow: influence of the number of elements N_E on the mean wrinkle wavelength for $Ca_s = 0.1$ and $\alpha = 0.01$.

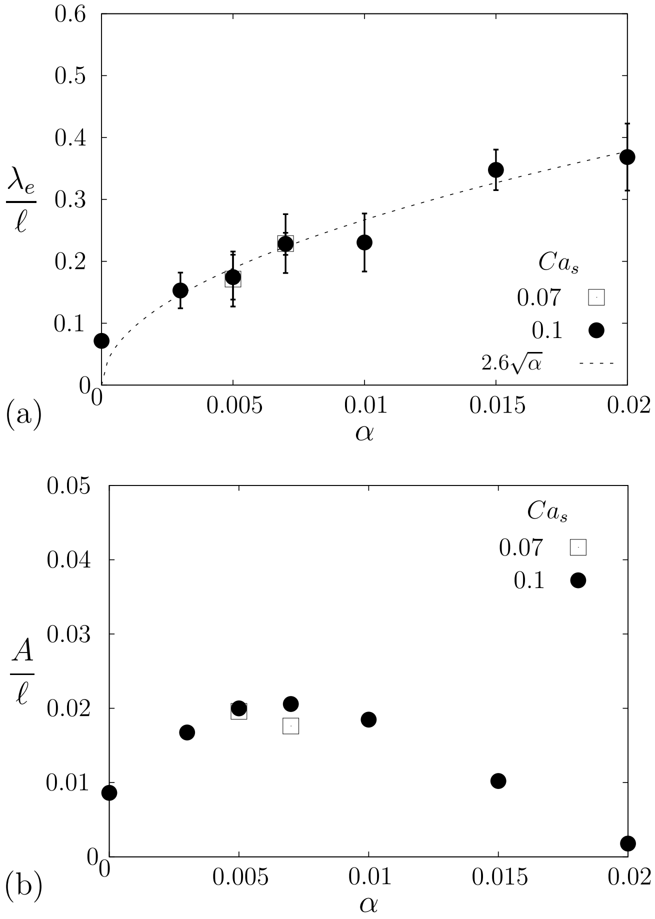

Figure 5.20: Capsule with a generalized Hooke's wall in a planar hyperbolic flow: Influence of the shell thickness on (a) the mean wrinkle wavelength and (b) amplitude. The dashed line is the $2.6\sqrt{\alpha}$ correlation curve.

Chapter 6

Off–plane motion of a prolate capsule

As we have seen in the introduction, the dynamics of a non–spherical capsule in shear flow is more complex than the one of an initially spherical capsule. Furthermore, the dynamics of an ellipsoidal capsule, which is observed when its revolution axis, seems not to correspond to a stable equilibrium state. In order to answer this question, we first determine the stable equilibrium configurations of a prolate capsule with a wall devoid of bending resistance. This study was published in the "*Journal of Fluid Mechanics* in 2013 with the title "Off–plane motion of a prolate capsule" (Dupont *et al.*, 2013). This study was carried out with A.-V. Salsac and D. Barthès-Biesel.

6.1 Introduction

Capsules are small liquid droplets enclosed by a thin deformable elastic membrane. They are used to protect and transport the particle internal content. Many occurrences may be found in nature (cells, eggs, seeds), but capsules have also numerous applications in bioengineering, pharmaceutics and cosmetics.

Nowadays artificial capsules can be produced in large quantities by first creating an emulsion and then adding a cross–linking agent to form a membrane around the droplets (Chang *et al.*, 1966; Lévy *et al.*, 1991, 1994, 1995; Edwards-Lévy *et al.*, 1993, 1994; Andry *et al.*, 1996). This results in the fabrication of capsules that are approximately spherical in shape. However, non–spherical capsules have a higher surface–to–volume ratio than spherical ones (for the same internal volume) and could therefore be interesting to use in order to enhance mass transfer between the internal and external media (Schneeweiss & Rehage, 2005). Nature has taken this course with red blood cells, which are small biconcave disks. Microfluidic systems have been developed recently to produce non–spherical artificial capsules. In particular Liu *et al.* (2009) and Xiang *et al.* (2008) have fabricated oblate and prolate microcapsules with arbitrary aspect ratio. More recently, Koleva & Rehage (2012) have fabricated slightly oblate polysiloxane capsules with an aspect ratio of 0.97–0.99.

When an initially spherical capsule is suspended in a simple shear flow, it elongates in the straining direction, while the vorticity of the flow induces a *tank–treading* rotation of the membrane around a steady deformed shape (Barthès-Biesel & Rallison, 1981;

Ramanujan & Pozrikidis, 1998; Lac *et al.*, 2004; Li & Sarkar, 2008). In the case of a slightly non–spherical capsule, Chang & Olbricht (1993*b*) and Walter *et al.* (2001) have observed experimentally a more complex behavior (the capsules used by Walter *et al.* have an aspect ratio of approximately 0.97). The capsule appears to have a *tank–treading* motion in the shear plane but undergoes small oscillations about the straining direction. This regime was also observed by Abkarian *et al.* (2007) for red blood cells and is now called *swinging*. As the shear rate increases, the swinging regime evolves towards a tank–treading regime where the cell orientation is steady. At low shear rates, red blood cells have a solid–like *tumbling* motion, where they rotate as a solid body about the vorticity axis (Abkarian & Viallat, 2008). Furthermore, Dupire *et al.* (2012) observed that the orbit of the red blood cell is unstable near the transition between the tumbling and the swinging regimes. Such an intermittent regime was also observed by Koleva & Rehage (2012).

Motivated by the experimental observations on red blood cells, numerical simulations have been carried out to understand the behavior of non–spherical capsules in shear flow (Ramanujan & Pozrikidis, 1998; Sui *et al.*, 2008; Walter *et al.*, 2011). These studies have considered the motion of an oblate capsule in a simple shear flow, in view of their relevance to red blood cells. Only Walter *et al.* (2011) have additionally studied the behaviour of a prolate capsule. In all of these numerical studies, the revolution axis of the capsule is initially positioned in the shear plane. Since the fluid inertia is either neglected or very small, Stokes flow conditions prevail and by symmetry the capsule axis must remain in the shear plane where it reaches an equilibrium periodic motion. These numerical models show that at low shear rate, the capsule rotates (‘tumbles’) about the vorticity axis as a quasi–solid body. As the shear rate increases, the capsule elongates in the maximum strain rate direction and the membrane rotates. However, since the initial geometry is not isotropic, the capsule elongation and orientation oscillate about mean values as observed experimentally in the swinging regime. The behaviour of prolate and oblate capsules is qualitatively the same, but the transition between tumbling and swinging occurs at lower shear rates for the oblate capsules (Walter *et al.*, 2011).

For spheroidal capsules, there is another obvious equilibrium configuration, which occurs when the capsule revolution axis is perpendicular to the shear plane. From symmetry considerations, it is clear that in Stokes flow, the capsule axis must then remain parallel to the vorticity axis. The sections of the capsule parallel to the shear plane lose their initial circular shape and are elongated in the strain direction, while the membrane tank–treads about the steady deformed shape. We will call this motion mode *rolling*, with reference to Abkarian *et al.* (2001) and Dupire *et al.* (2012). Of course in experiments, the capsule revolution axis is rarely aligned with either the shear flow or the vorticity axis. This raises the question of the *mechanical stability* of the motion of a capsule initially positioned with its axis in the shear plane or perpendicular to it.

The objective of this paper is thus to study the motion of a capsule in a simple shear flow when its revolution axis is initially positioned *off* the shear plane. We will consider prolate capsules and thus complement the work of Walter *et al.* (2011). The advantage of working with this geometry is that the tumbling–to–swinging transition occurs at higher shear rates for prolate than for oblate capsules, which facilitates the computations. In particular we will demonstrate that the capsule typically deviates from the tumbling and swinging motions, when the revolution axis is initially placed outside the shear plane.

The motion of a capsule in a flow is a classical fluid–structure interaction problem. We use the numerical method developed by Walter *et al.* (2010) to treat this problem. This method, based on the coupling of a membrane finite element method for the capsule deformation with a boundary integral method for the internal and external flows, has been shown to be very precise and to remain numerically stable. The problem and the numerical method are briefly outlined in section 6.2. The behavior of a prolate capsule initially positioned off the shear plane is presented in section 6.3 as a function of the shear rate. The effect of membrane law and aspect ratio on the capsule motion is shown in section 6.4. The results are then discussed in section 6.5.

6.2 Problem statement and numerical method

6.2.1 Problem statement

We consider an initially spheroidal capsule and denote by $2a$ the length of the revolution axis and by $2b$ the length of the two orthogonal axes. The capsule is prolate with aspect ratio a/b. We define a length scale $\ell = (ab^2)^{1/3}$ as the radius of the sphere with the same volume as the capsule. We shall consider two capsule shapes corresponding to $a/b = 2$ ($a/\ell = 1.587, b/\ell = 0.794$) and $a/b = 3$ ($a/\ell = 2.08, b/\ell = 0.693$) respectively. The reference frame based on the undeformed capsule principal axes is denoted $\mathcal{F}'$ (O, $\underline{e}'_x$, $\underline{e}'_y$, $\underline{e}'_z$), where O is the centre of mass of the capsule. Assuming that the revolution axis is along $\underline{e}'_z$, the capsule surface is given by

$$\left(\frac{x'_s}{b}\right)^2 + \left(\frac{y'_s}{b}\right)^2 + \left(\frac{z'_s}{a}\right)^2 = 1, \tag{6.1}$$

where (x'_s, y'_s, z'_s) is the position of a membrane material point.

The capsule is filled with a Newtonian incompressible fluid with viscosity μ. It is freely suspended in an unbounded Newtonian incompressible fluid with the same viscosity μ.

The external fluid is subjected to a simple shear flow with shear rate $\dot{\gamma}$ and undisturbed velocity

$$\underline{v}^{\infty} = \dot{\gamma}\, y\, \underline{e}_x \tag{6.2}$$

in the laboratory reference frame $\mathcal{F}$ $(\mathrm{O}, \underline{e}_x, \underline{e}_y, \underline{e}_z)$. The Reynolds number of the flow is assumed to be very small. Thus, the internal and external flows are governed by the Stokes equations. The symmetry of the problem and of the governing equations implies that, when the revolution axis of a capsule is initially in the shear plane or perpendicular to it, it remains as such.

At time $\dot{\gamma}t = 0$, the position of the capsule in space is defined by the angles between the basis vectors of frames $\mathcal{F}'$ and $\mathcal{F}$. As shown in Figure 6.1, we chose $(\underline{e}_x, \underline{e}'_x) = 0$ and $(\underline{e}_z, \underline{e}'_z) = (\underline{e}_y, \underline{e}'_y) = \zeta_0$. This means that the capsule revolution axis initially makes an angle ζ_0 with the vorticity axis and an angle $\pi/2 - \zeta_0$ with the shear plane.

The capsule membrane is modeled as an isotropic hyperelastic surface with shear modulus G_s and area dilatation modulus K_s. Two types of membrane constitutive laws can be considered, where the material is either strain–softening or hardening (Barthès-Biesel *et al.*, 2002). A strain–softening membrane can be described by the neo–Hookean law (NH). The principal elastic tensions T_1 and T_2 are then given in terms of the in–plane principal stretch ratios λ_{s1} and λ_{s2} by

$$T_1 = \frac{G_s}{\lambda_{s1}\lambda_{s2}} \left[\lambda_{s1}^2 - \frac{1}{(\lambda_{s1}\lambda_{s2})^2}\right] \qquad \text{(likewise for } T_2\text{).} \tag{6.3}$$

The surface shear and area dilatation moduli are related by $K_s/G_s = 3$. Conversely, a strain–hardening membrane can be described by the Skalak law (SK), initially proposed by Skalak *et al.* (1973) to model the red blood cell membrane

$$T_1 = \frac{G_s}{\lambda_{s1}\lambda_{s2}} \left[\lambda_{s1}^2(\lambda_{s1}^2 - 1) + C(\lambda_{s1}\lambda_{s2})^2 \Big((\lambda_{s1}\lambda_{s2})^2 - 1\Big)\right] \qquad \text{(likewise for } T_2\text{).} \tag{6.4}$$

The surface shear and area dilatation moduli are then related by $K_s = G_s(1+2C)$, where C is a constant such that $C > -1/2$. For $C = 1$ $(K_s/G_s = 3)$, the two laws NH and SK lead to the same small deformation behavior. Note that the Skalak membrane material can undergo surface–area changes while being strain–hardening.

The capsule motion and deformation are thus governed by the membrane constitutive law, the ratio of the area dilatation and shear moduli K_s/G_s, the particle initial aspect ratio a/b and initial orientation ζ_0, and by the capillary number $Ca_s = \mu\dot{\gamma}\ell/G_s$, which measures the ratio between the viscous and the elastic forces.

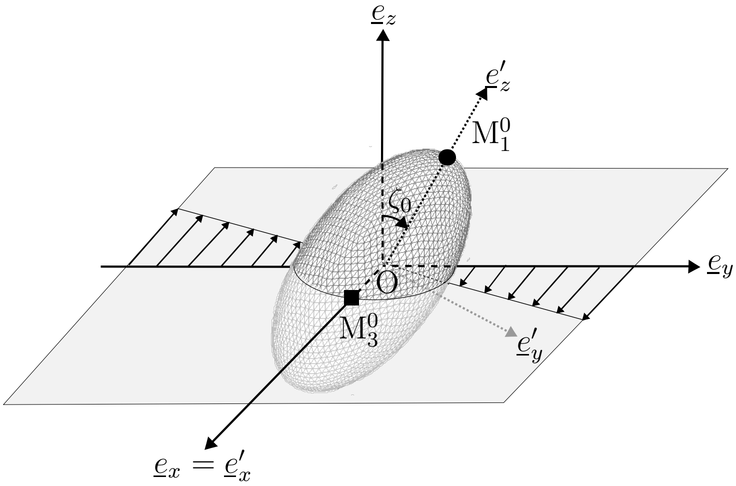

Figure 6.1: Reference configuration of the prolate capsule at $\dot{\gamma}t = 0$. The capsule inclination ζ_0 is the initial angle between the flow vorticity axis $\underline{e}_z$ and the capsule revolution axis $\underline{e}'_z$. During the capsule deformation, we will follow the motion of two specific points of the capsule membrane: the point M_3^0 is initially on the short axis $\underline{e}'_x$ (■) and the point M_1^0 on the long axis $\underline{e}'_z$ (●).

6.2.2 Numerical method

The motion and deformation of the capsule are solved by means of the numerical technique developed by Walter *et al.* (2010). This method couples a membrane finite element method (for the mechanics of the capsule wall) with a boundary integral method (for the internal and external flows). The method is briefly described in this subsection. More details on the procedure may be found in Walter *et al.* (2010) or in the book chapter (Barthès-Biesel *et al.*, 2010).

At time $\dot{\gamma}t = 0$, the capsule is in its reference ellipsoidal shape, when we start the flow. We then perform a Lagrangian tracking of the position of the membrane material points over time. At a given time, the position of the material points is known and we may thus compute the stretch ratios λ_{s1} and λ_{s2} and the elastic tension tensor $\underline{\underline{T}}$ from equation (6.3 or 6.4). The load $\underline{q}$ exerted by the fluids on the membrane is found by using the finite element method to solve the membrane equilibrium equation

$$\underline{\nabla}_s \cdot \underline{\underline{T}} + \underline{q} = \underline{0}, \tag{6.5}$$

where $\underline{\nabla}_s$ represents a surface gradient. The fluid velocity may be written as a boundary integral on the deformed surface $\mathcal{S}_t$ of the capsule

$$\underline{v}(\underline{x}_s) = \underline{v}^\infty(\underline{x}_s) - \frac{1}{8\pi\mu}\int_{\mathcal{S}_t}\left(\frac{\mathbb{I}}{\parallel \underline{r} \parallel} + \frac{\underline{r}\otimes\underline{r}}{\parallel \underline{r} \parallel^3}\right)\cdot \underline{q}(\underline{y}_s)dS(\underline{y}_s), \tag{6.6}$$

where $\underline{v}(\underline{x}_s)$ is the velocity of the membrane point located at $\underline{x}_s$, $\underline{r} = \underline{x}_s - \underline{y}_s$ and $\mathbb{I}$ is the identity tensor. An explicit second–order Runge–Kutta method is then used to integrate the velocity and obtain the new position of the membrane points at the following time step.

6.2.3 Discretization, stability and convergence

The surface of the capsule is discretized with triangular curved P_2 elements (Figure 6.1). The mesh is initially generated for a spherical capsule by inscribing an icosahedron (regular polyhedron with 20 triangular faces) in a sphere. The elements are subdivided sequentially until the desired number of elements is reached (Ramanujan & Pozrikidis, 1998; Walter *et al.*, 2010). At the last step, nodes are added at the middle of all the element edges and projected onto the sphere in order to generate the P_2 elements. The mesh is then deformed into an ellipsoid following equation 6.1. In the study, the capsule mesh has 2562 nodes and 1280 elements.

The numerical method is stable, when the time step satisfies the condition $\dot{\gamma} \bigtriangleup t < O(\Delta x \, Ca_s/\ell)$, where $\Delta x/\ell$ is the typical non–dimensional mesh size (Walter *et al.*, 2010). We use $\dot{\gamma} \bigtriangleup t = 5 \times 10^{-3}$ for $Ca_s \geq 0.5$ and decrease the time step proportionally for lower Ca_s.

A capsule initially placed off the shear plane takes a very long time to reach the equilibrium state. Computational times of the order of $\dot{\gamma}t = 10^2 - 10^3$ are therefore needed to capture the dynamics. With such long computational times, the numerical error may no longer be negligible. We thus monitor the relative error $\varepsilon_V = |V - V_0|/V_0$ on the capsule volume V, where V_0 is the capsule initial volume. For off–plane capsules, the error at $\dot{\gamma}t = 100$ is $\sim \mathcal{O}(10^{-2})$ for $Ca_s \leq 0.9$ and $\mathcal{O}(10^{-3})$ for $Ca_s > 0.9$.

6.2.4 Result analysis

Depending on the parameters, the capsule motion and deformation become complex and difficult to analyze. The global geometry of the capsule is evaluated by means of the ellipsoid of inertia of the deformed shape. We denote by L_i the half–lengths of the principal axes of the ellipsoid of inertia ($L_1 > L_2 > L_3$) and $\underline{v}_i$ the corresponding unit vectors in $\mathcal{F}$ ($\underline{v}_1 = \underline{e}'_z$ at time $\dot{\gamma}t = 0$ for a prolate capsule). The membrane rotation is measured from the motion of two points (Figure 6.1):

- the point M_3^0 is the Lagrangian position at time $\dot{\gamma}t$ of the membrane point that was initially located on the capsule short axis $\underline{e}'_x$.
- the point M_1^0 is the Lagrangian position at time $\dot{\gamma}t$ of the membrane point that was initially located on the capsule long axis $\underline{e}'_z$.

The capsule global motion is measured from the position of the capsule tip M_1^t, which corresponds to the Eulerian position in $\mathcal{F}$ of the intersection between the $\underline{v}_1$ axis and the membrane. At time $\dot{\gamma}t = 0$, the points M_1^0 and M_1^t are superimposed. The projections of M_1^t in the shear $xy-$plane or in the $xz-$plane are denoted $\mathrm{M}_{1,xy}^t$ and $\mathrm{M}_{1,xz}^t$, respectively.

The capsule deformation can be analyzed using the Taylor parameters

$$D_{ij} = \frac{L_i - L_j}{L_i + L_j} \;\; (i, j = 1, 2, 3 \;\text{ and }\; i \neq j). \tag{6.7}$$

Owing to the capsule initial ellipsoidal shape, the initial values of the Taylor parameters are $D_{23}^0 = 0$ and $D_{12}^0 = D_{13}^0 = (a - b)/(a + b) = 1/3$ for an aspect ratio $a/b = 2$ or $1/2$ for $a/b = 3$. The overall deformation can also be measured by the elastic energy E stored in the capsule wall

$$E(t) = \int_{\mathcal{S}_0} w_s(\lambda_{s1}, \lambda_{s2}, t) dS, \tag{6.8}$$

where w_s is the strain energy function per unit area of undeformed membrane and $\mathcal{S}_0$ is the initial surface of the capsule.

In most cases, the capsule has a kind of gyroscopic motion, where it rotates and reorients itself. Correspondingly, the coordinates of any point, the membrane energy, the capsule deformation, etc. have pseudo–periodic oscillations with amplitude changing over time. We have used a centered moving average method (Hay & Bull, 2009) to smooth the data and to visualize the time evolution of the parameters (Figure 6.2). This method replaces a value $x_s(t)$ by its average over a period T centered around the time value t. Here, we define the period of the motion as the time required for a point initially at $(x_s, 0, 0)$ to return on the $\underline{e}_x$ axis. Unless otherwise mentioned, all results pertain to quantities that are averaged over one period.

To simplify notation, we call C2SK and C3SK the capsules with a SK membrane of aspect ratios 2 and 3, respectively, and C2NH the capsules with a NH membrane of aspect ratio 2.

6.3 Results

We first consider a prolate capsule $a/b = 2$ enclosed by a SK ($C = 1$) membrane, and study in detail the effect of the initial orientation ζ_0 and of the flow strength measured by Ca_s. The influence of the membrane law and of the aspect ratio will be briefly discussed in section 6.4.

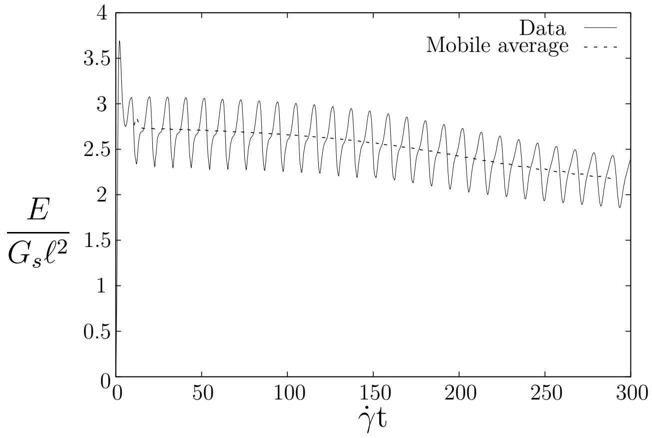

Figure 6.2: Time evolution of the elastic energy $E/G_s\ell^2$ stored in the membrane (solid line) for a C2SK capsule with $\zeta_0 = 85°$ and $Ca_s = 0.9$. The mobile average (dotted line) is obtained with a non–dimensional period $\dot{\gamma}T = 21.55$.

6.3.1 Motion of a capsule with $\zeta_0 = 90°$

Before studying the motion of a capsule initially placed off the shear plane with an arbitrary angle, we will first summarize the dynamics of a capsule when its revolution axis is initially positioned in the shear plane ($\zeta_0 = 90°$). Walter *et al.* (2011) have shown that the long axis remains in the shear plane. They have also shown that the capsule motion is a function of the capillary number Ca_s. At low capillary numbers ($Ca_s < 0.25$), the capsule rotates about the vorticity axis like a quasi–solid particle; its cross–section with the shear plane exhibits small deformations (Figure 6.3a). This regime is referred to as *tumbling*.

For $Ca_s > 0.35$, the capsule has a quasi–fluid behaviour. The angle of the capsule long axis with the streamlines and the capsule deformation oscillate about mean values (Figure 6.3b), because of the geometrical anisotropy of the initial shape. This is the so–called *swinging* regime. As Ca_s increases, the membrane deformation increases and the long axis is tilted towards the streamlines. Furthermore, the oscillation amplitudes of the deformation and orientation also decrease with increasing Ca_s. Asymptotically, the capsule tends towards the pure tank–treading regime, where the membrane rotates around a steady deformed profile.

6.3.2 Motion of a capsule with $\zeta_0 = 0°$

There is no available study of the case where the revolution axis of the capsule is initially perpendicular to the shear plane and thus parallel to the vorticity axis ($\zeta_0 = 0°$). In this situation, the capsule long axis remains parallel to the vorticity for symmetry reasons. The shear flow exerts a viscous torque on the membrane and thus the capsule cross–sections parallel to the shear plane that were initially circular become elongated in the

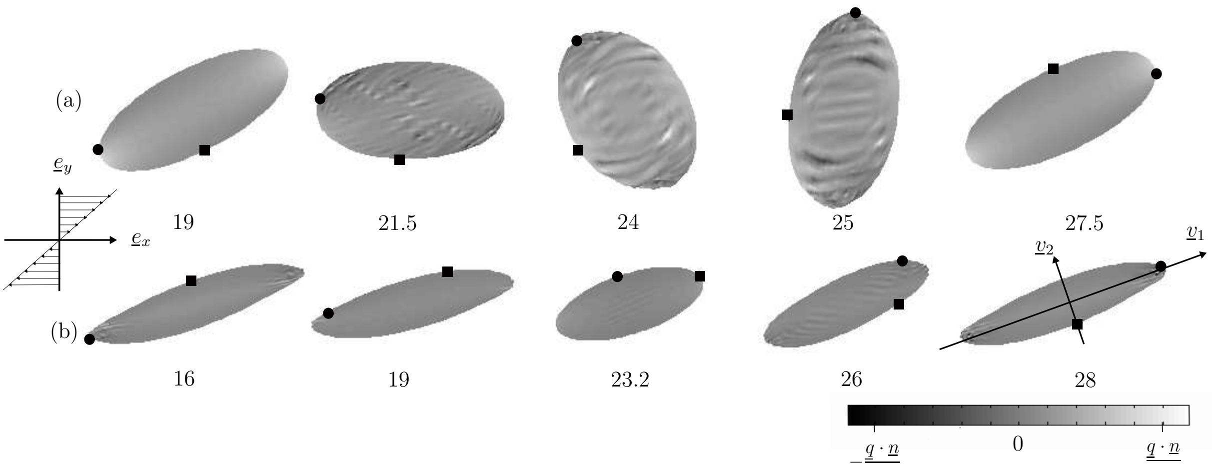

Figure 6.3: Capsule C2SK shape when $\zeta_0 = 90°$: shape evolution over one half period at steady state for (*a*) $Ca_s = 0.1$ and (*b*) $Ca_s = 2$. The grey scale corresponds to the normal component of the load $\underline{q} \cdot \underline{n}$ on the membrane. The maximum values of the normal load are (*a*) $\underline{q} \cdot \underline{n}/G_s = 0.9$ and (*b*) 25. The value of the non–dimensional time $\dot{\gamma}t$ is given below each shape. The points M_3^0 (■) and M_1^0 (●) were initially on the short and long axis respectively (Figure 6.1).

strain direction. The membrane then rotates around the steady capsule shape as shown in Figure 6.4. This capsule motion is the same for all the values of the capillary number and is called the *rolling* regime.

In order to further investigate the evolution of the capsule deformation, we have plotted the Taylor parameters calculated at steady state in Figure 6.5a. For low flow strength the principal direction $\underline{v}_1$ is along the vorticity axis. The deformation within the shear plane is thus measured by D_{23}, which sharply increases from zero (initially circular cross–section) to a plateau value a little above 0.5 (of the same order as the maximum deformation for a spherical capsule in simple shear flow). The deformation in planes perpendicular to the shear plane are measured by D_{12} and D_{13}. The decrease of D_{12} with Ca_s is due to the pinching of the capsule by the straining effect of the shear flow. For $Ca_s \geq 1.5$, the capsule reaches a shape that is hardly influenced by the flow strength.

The maximum value T_{max} of the principal elastic tensions within the membrane is shown in Figure 6.5b. We find that the elastic tension level and correlatively the risk of rupture increase quasi–linearly with Ca_s. The maximum is along the $\underline{v}_1$ principal direction; it is located in the shear plane at the intersection of the capsule edge with the $\underline{v}_3$ principal direction. This is where the rupture will most likely occur when the failure criterion of the membrane material is exceeded. The minimum of the principal tensions T_{min} is found to be about zero for all the values of Ca_s (data not shown). It is slightly negative until $Ca_s = 0.4$ ($T_{min}/G_s \in [-0.04, 0]$), so that the membrane undergoes moderate compression locally. This explains why wrinkles appear at the capsule apices

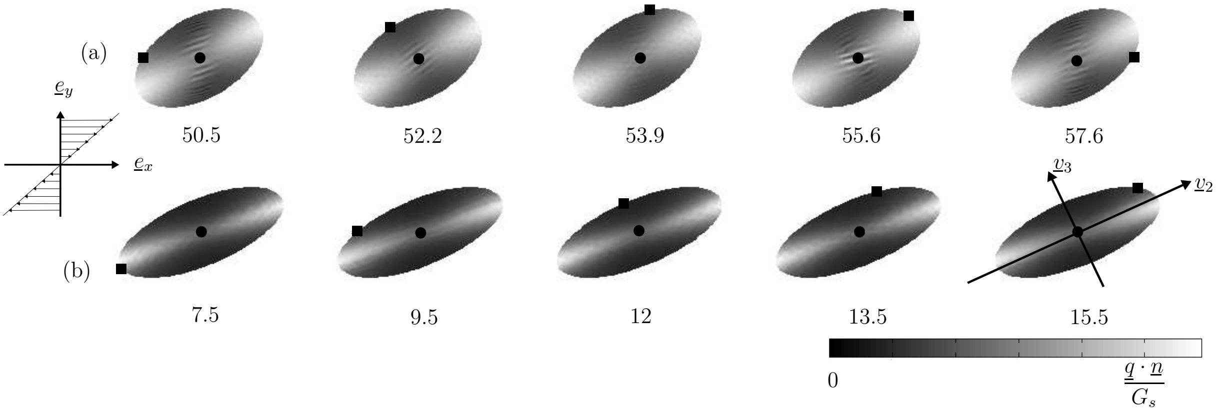

Figure 6.4: Capsule C2SK shape when $\zeta_0 = 0°$: shape evolution over one half period at steady state for (*a*) $Ca_s = 0.1$ and (*b*) $Ca_s = 0.6$. Same legend as in figure 6.3. The maximum values of the normal load are (*a*) $\underline{q}\cdot\underline{n}/G_s = 0.5$ and (*b*) 2.5.

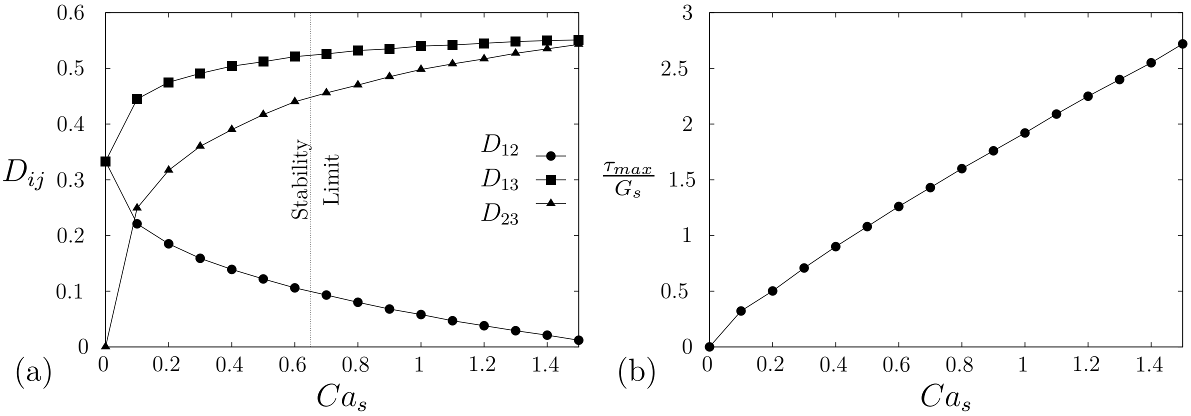

Figure 6.5: Capsule C2SK. Influence of the capillary number Ca_s on the rolling regime at $\zeta_0 = 0°$. (*a*) Capsule deformation estimated by the Taylor parameters D_{ij}, where the dotted line represents the stability limit; (*b*) maximum membrane tension T_{max}.

along the long axis (i.e. $\underline{v}_1$) in Figure 6.4 for $Ca_s = 0.1$ and not for $Ca_s = 0.6$.

Although we have shown results for large values of Ca_s, we will see in the following that for $Ca_s > 0.6$, the rolling configuration is no longer mechanically stable.

6.3.3 Off–plane capsule at low flow strength ($Ca_s \leq 0.6$)

When the capsule axis is displaced from the shear plane by a small angle of 5° ($\zeta_0 = 85°$), the capsule long axis does not go back to the shear plane. As shown in Figure 6.6a for $Ca_s = 0.1$, the projection $\mathrm{M}^t_{1,xy}$ of the capsule tip in the shear plane moves away from the fixed trajectory reached for $\zeta_0 = 90°$. It spirals around the flow vorticity axis $\underline{e}_z$ and eventually converges towards it. This is also apparent from Figure 6.6b, which shows the evolution of the projection $M^t_{1,xz}$ of point M^t_1 in the xz–plane. The stable equilibrium position is thus the rolling regime. It is the converging position for any

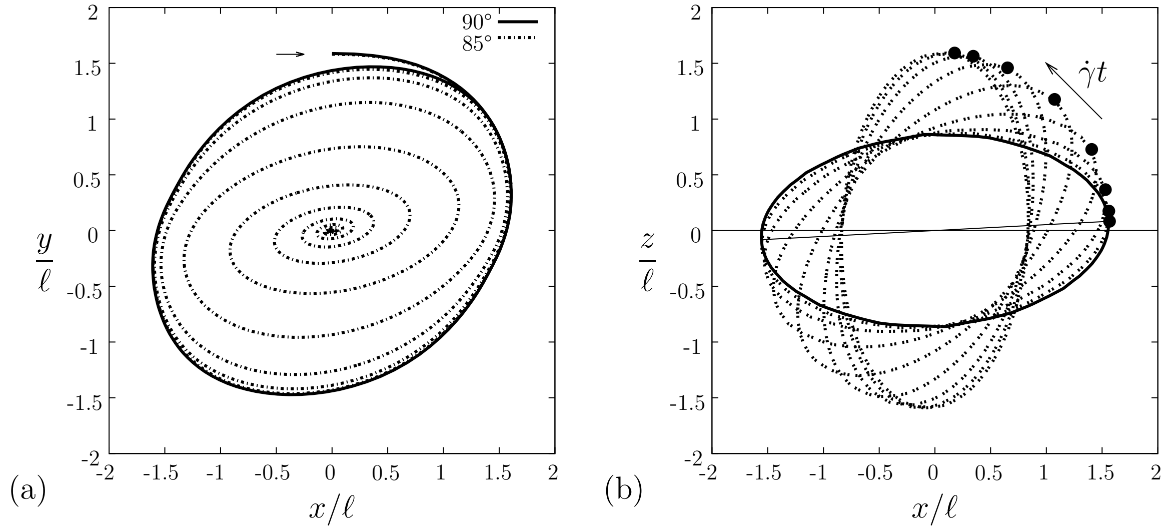

Figure 6.6: Motion of a C2SK capsule with $\zeta_0 = 85°$ at $Ca_s = 0.1$: (*a*) Comparison of the trajectory of point $\mathrm{M}^t_{1,xy}$ in the shear $xy-$plane with the case $\zeta_0 = 90°$. The arrow indicates the initial position of $\mathrm{M}^t_{1,xy}$. (*b*) Evolution of the capsule shape in the xz-plane at the beginning of each period (solid line: capsule shape at $\dot{\gamma}t = 0$). The black point indicates the position of point $\mathrm{M}^t_{1,xz}$ at $\dot{\gamma}t = 5$, 22, 38, 55, 721, 89, 106, 123.

off–plane orientation $\zeta_0 < 90°$ (not shown). At equilibrium the capsule deformation and tank–treading motion are identical to those of the same capsule initially positioned at $\zeta_0 = 0°$ (Figures 6.4 and 6.5), i.e. with its revolution axis initially along the vorticity axis.

As shown in Figure 6.7, when the capsule is not constrained in the shear plane by symmetry, the elastic energy stored in the membrane decreases during the transient motion until it reaches the value for a rolling capsule. The equilibrium configuration is thus the one for which the mean deformation (as measured by the energy) is the smallest. We also note in Figure 6.7 that the initial orientation angle ζ_0 influences the time the capsule needs to reach its equilibrium position. Indeed, the smaller the initial angle ζ_0, the smaller the time. The transient time until equilibrium also increases with the capillary number (not shown).

In conclusion we find that, for Ca_s up to 0.6, the *mechanically stable* situation corresponds to the *rolling* regime, a configuration where the capsule long axis is normal to the shear plane and the membrane tank–treads around it. Since the deformation is small at low capillary number, the capsule behaves almost as a solid ellipsoid and takes the position that dissipates the less energy (Jeffery, 1922). Consequently, the tumbling motion found when the capsule axis is in the shear plane ($\zeta_0 = 90°$) is an *unstable* equilibrium state. Over long times, the accumulation of numerical errors is enough to slowly destabilize it. Considering the fact that in a suspension, the initial capsule orientation is usually random, we can expect that most of the capsules align their long axis with the

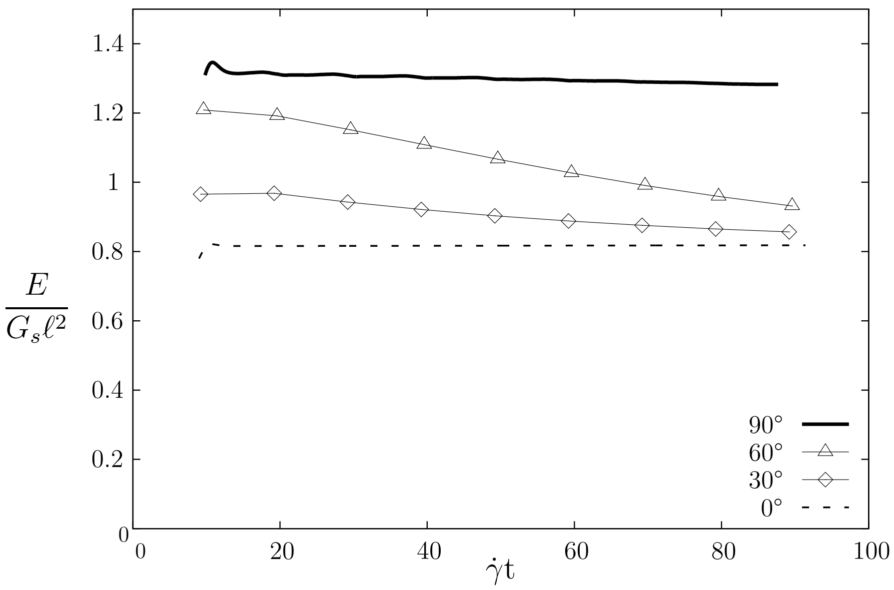

Figure 6.7: Capsule C2SK: time evolution of the elastic energy stored in the membrane $E/G_s\ell^2$, for various initial inclinations of the capsule with the shear plane ($Ca_s = 0.5$). The case $\zeta_0 = 90°$ represents the mechanically unstable tumbling motion.

flow vorticity and are eventually all in the rolling regime.

6.3.4 Transition at moderate flow strength ($0.6 < Ca_s < 1$)

For $Ca_s \geq 0.7$, the capsule no longer tends towards the rolling motion observed for lower values of Ca_s. Its motion is now a function of Ca_s.

For example, for $Ca_s = 0.9$ and different initial orientations $\zeta_0 \in \,]0°, 90°[$, the time evolution of the mean elastic membrane energy $E/G_s\ell^2$ shows that it converges towards a common equilibrium value (Figure 6.8). For $Ca_s = 0.9$, this equilibrium state corresponds more or less to the motion that the capsule takes almost immediately (i.e. after a short transient) for an initial angle $\zeta_0 = 15 - 30°$.

We choose, therefore, to examine in detail the motion of a capsule with $\zeta_0 = 15°$ for $Ca_s = 0.9$. The capsule rotates as a whole around the vorticity axis, while its tip M_1^t has a *wobbling* motion as shown in Figure 6.9. Indeed, the projection $\mathrm{M}_{1,xy}^t$ of M_1^t in the shear plane follows a roughly elliptical trajectory (Figure 6.9a), while the height of M_1^t above the shear plane oscillates (Figure 6.9b). This is of course different from the swinging motion obtained for $\zeta_0 = 90°$, where the tip of the capsule oscillates in the shear plane as shown in Figure 6.9a. We quantify this motion by means of ζ_{max}, which corresponds to the maximum angle between the capsule longest principal axis $\underline{v}_1$ and the vorticity axis (in Figure 6.9b, one can see the projection of the angle ζ_{max} in the $xz-$plane). The value of ζ_{max} depends on Ca_s as shown in Figure 6.10a. We retrieve the fact that for

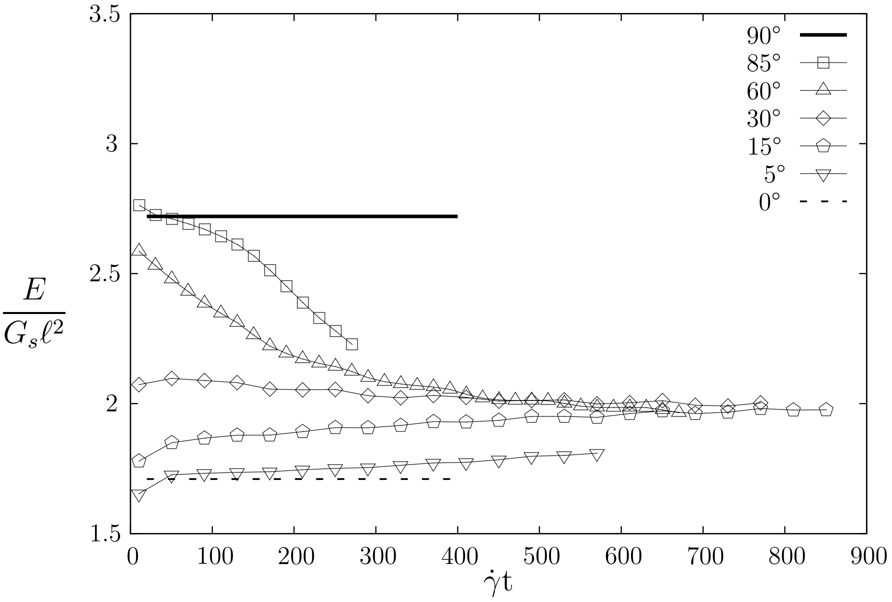

Figure 6.8: Capsule C2SK at $Ca_s = 0.9$: effect of the initial orientation on the time evolution of the elastic energy stored in the membrane $E/G_s\ell^2$

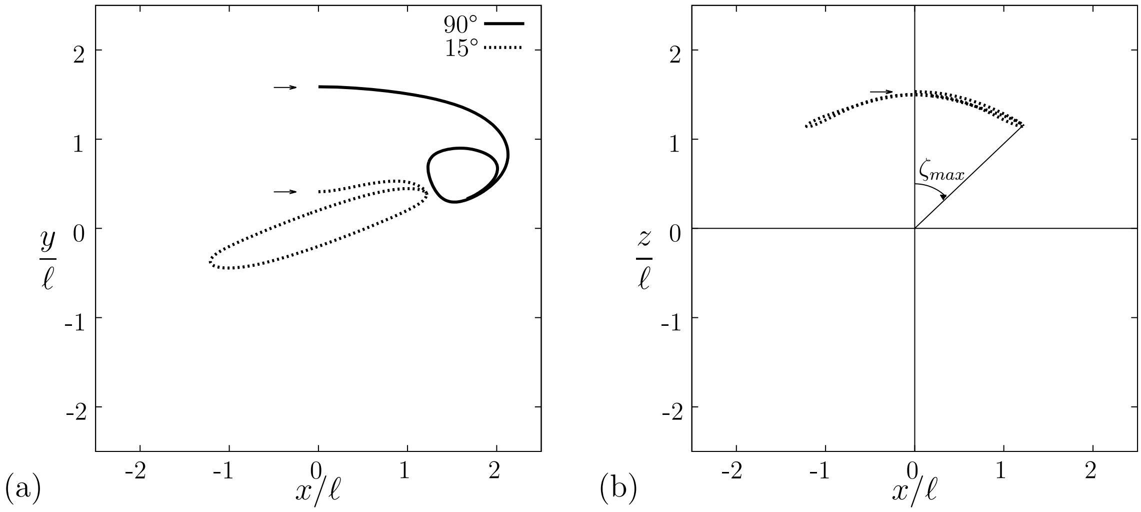

Figure 6.9: Motion of a C2SK capsule with $\zeta_0 = 15°$ at $Ca_s = 0.9$ up to the end of the first pseudo–period ($0 < \dot{\gamma}t < 26$): (*a*) trajectory of point $\mathrm{M}^t_{1,xy}$ in the shear plane (comparison with $\zeta_0 = 90°$); (*b*) trajectory of point $\mathrm{M}^t_{1,xz}$ in the xz–plane for $\zeta_0 = 15°$. The arrows indicate the initial position at $\dot{\gamma}t = 0$. The horizontal line at $z = 0$ represents the shear plane.

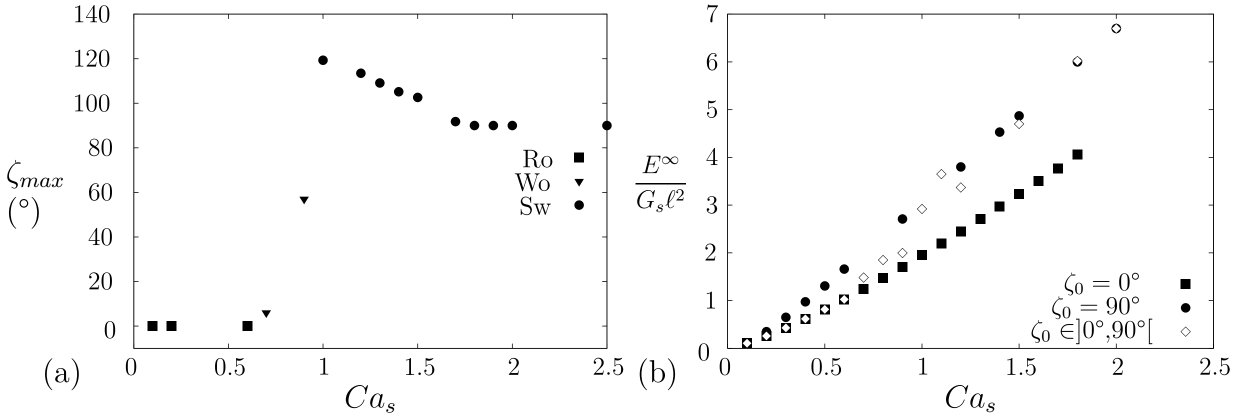

Figure 6.10: C2SK capsule. (*a*) Evolution of the maximum inclination ζ_{max} of the capsule longest axis with the vorticity axis at equilibrium as a function of Ca_s: Ro: rolling, Wo: wobbling, Sw: oscillating–swinging tending to pure swinging. (*b*) Evolution of the mean elastic energy E^∞ stored in the membrane at equilibrium as a function of Ca_s for initially off–plane capsules (diamond). Comparison with the cases $\zeta_0 = 0°$ (square) and 90° (circle).

$Ca_s \leq 0.6$, $\zeta_{max} = 0°$, which corresponds to the rolling motion. As the capillary number is increased above 0.6, the capsule starts to precess around the vorticity axis with a maximum amplitude ζ_{max}, which increases sharply with Ca_s.

The evolution of the mean elastic energy stored in the membrane at equilibrium E^∞ (Figure 6.10b) also indicates clearly that the capsule bifurcates from the rolling regime ($\zeta_0 = 0°$ curve) for $Ca_s \geq 0.7$. In the wobbling regime, the capsule deformation is still moderate but the energy of deformation is a little larger than the one that would be found in the rolling regime for the same Ca_s.

6.3.5 Off–plane motion at high flow strength ($Ca_s \geq 1$)

For a capillary number larger than 1, we find another type of motion. For example, for $Ca_s = 1.5$ and different initial orientations, the mean elastic membrane energy $E/G_s\ell^2$ converges in time towards a common value as shown in Figure 6.11. This equilibrium state is reached after a short transient for an initial angle $\zeta_0 = 60°$. The details of the motion of a capsule with $\zeta_0 = 60°$ at $Ca_s = 1.5$ are then shown in Figure 6.12. The capsule assumes what we call an *oscillating–swinging* motion, where the tip of the capsule oscillates both about the shear plane (Figure 6.12b) and within the shear plane about a mean inclination with respect to the flow direction (Figure 6.12a). The rotational motion is now taken over by the membrane as is apparent from the trajectory of point M_1^0 in the shear plane (Figure 6.12a). This behavior corresponds to values of $\zeta_{max} \geq 90°$, as shown in Figure 6.10a.

As Ca_s increases, the amplitude of the oscillations about the shear plane decreases. For

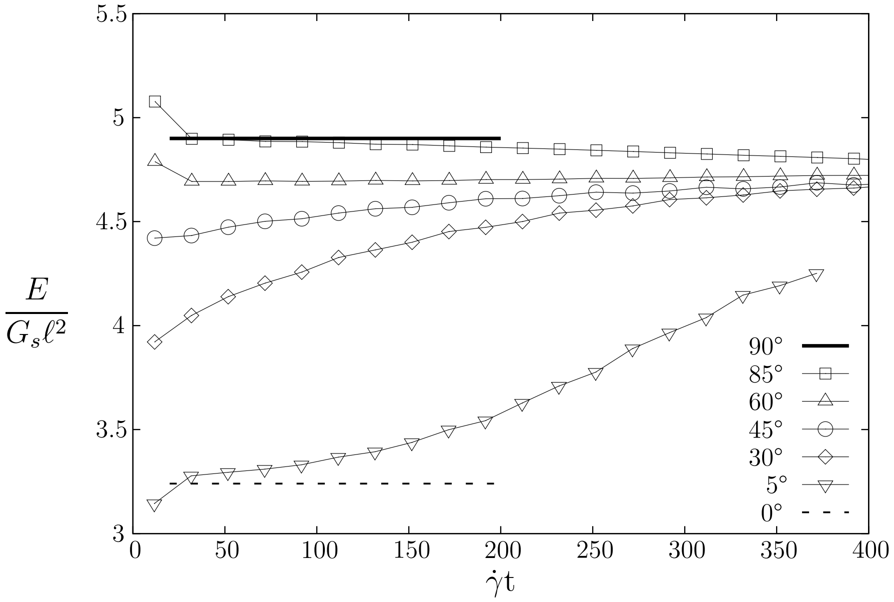

Figure 6.11: C2SK capsule at $Ca_s = 1.5$: effect of the initial orientation on the time evolution of the elastic energy stored in the membrane $E/G_s\ell^2$.

large values of the capillary number $Ca_s \geq 1.8$, the capsule positions its long axis in the shear plane ($\zeta_{max} = 90°$) for any initial orientation ζ_0: it undergoes the swinging regime described by Walter *et al.* (2011) and summarized in section 6.3.1. The convergence of the oscillating–swinging regime towards a pure swinging regime is also shown in Figure 6.10b: as Ca_s increases, the equilibrium elastic energy tends towards the values obtained in the swinging regime. The evolution of the capsule profile at equilibrium is therefore similar to the one shown in Figure 6.3b for $\zeta_0 = 90°$. The membrane tank–treads around the time–oscillating profile. But, even these oscillations decrease as Ca_s is increased: the capsule tends asymptotically towards a pure tank–treading motion at very large values of the capillary number.

6.3.6 Global effect of Ca_s

In conclusion, the motion and deformation of a prolate ellipsoidal capsule in shear flow depend in a complex way on the flow strength. There are two obvious equilibrium states for which the capsule keeps symmetry properties with respect to the shear plane and which correspond respectively to $\zeta_0 = 0°$ or $90°$. The mean equilibrium energy stored in the membrane E^∞ shown in Figure 6.10b indicates that the energy is larger when the capsule axis is in the shear plane ($\zeta_0 = 90°$) than when it is perpendicular to it ($\zeta_0 = 0°$). However, the energy criterion is not enough to govern the equilibrium state of the capsule even in Stokes flow. Indeed the capsule motion is the result of non–linear fluid–structure interactions. This may explain why there is a bifurcation from the rolling state towards

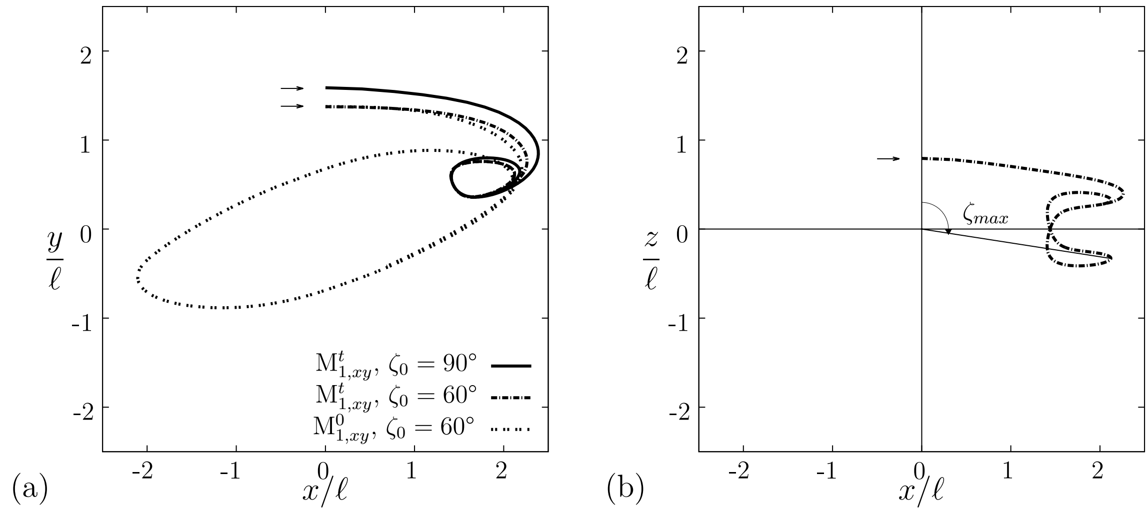

Figure 6.12: Motion of a C2SK capsule with $\zeta_0 = 60°$ at $Ca_s = 1.5$ up to the end of the first pseudo–period ($0 < \dot{\gamma}t < 29$): (a) trajectories of point $\mathrm{M}^t_{1,xy}$ (comparison with $\zeta_0 = 90°$) and of point $\mathrm{M}^0_{1,xy}$, the projection of point M^0_1 in the shear plane; (b) trajectory of point $\mathrm{M}^0_{1,xz}$ in the $xz-$plane. The arrows indicate the initial position at $\dot{\gamma}t = 0$. The horizontal line at $z = 0$ represents the shear plane.

the swinging state. During this transition, the capsule has first a quasi solid wobbling motion followed by a quasi fluid oscillating–swinging motion.

The question of the uniqueness of the equilibrium state then arises. In other words, is there an hysteresis effect? In order to give an answer to this question, we did the following experiment: starting from the oscillating–swinging equilibrium state found for $Ca_s = 1.5$, we have suddenly reduced the capillary number to $Ca_s = 0.9$. The resulting trajectory of the projection $\mathrm{M}^t_{1,xz}$ of the capsule tip in the $xz-$plane is shown in Figure 6.13. We note that the amplitude of the oscillations of the capsule about the shear plane ($x-$axis) increases with time until the capsule switches to the wobbling motion. It converges towards the same configuration as obtained for a capsule initially at $Ca_s = 0.9$ as shown in Figure 6.9b. If then we suddenly decrease Ca_s from 0.9 to 0.1, the capsule goes to the rolling regime described in section 6.3.3 (not shown). We thus conclude that the equilibrium states we find are unique.

6.4 Effect of membrane law and capsule aspect ratio

In order to assess the robustness of the results obtained with a SK law, we now consider a capsule with aspect ratio $a/b = 2$ and a strain–softening NH membrane. We find again that for low flow strength ($Ca_s \leq 0.5$), the stable mode of motion of the C2NH capsule is the rolling motion. In this regime, a capsule with a NH membrane is easier to deform than one with a SK membrane (Figure 6.14). Indeed for the same value of Ca_s, the capsule

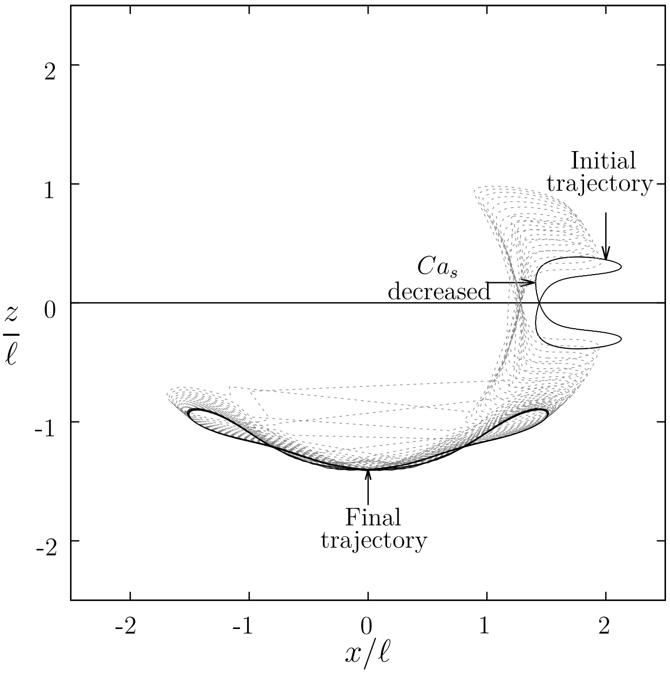

Figure 6.13: Time evolution of a capsule C2SK initially undergoing stable oscillating–swinging motion at $Ca_s = 1.5$, when the capillary number is suddenly changed to $Ca_s = 0.9$. The trajectory of the capsule tip $\mathrm{M}^t_{1,xz}$ in the $xz-$plane is followed in time.

deformation is larger for a NH membrane than for a SK one.

As shown in Figure 6.15a, for $Ca_s = 0.6$, the C2NH capsule has a wobbling motion followed by an oscillating–swinging motion for $Ca_s \geq 0.7$. However, for $Ca_s \geq 0.9$, the capsule does not seem to reach a steady trajectory. This is in agreement with the fact that there is no stable swinging regime in the shear plane for large values $Ca_s \geq 1$. Indeed, there is a critical flow strength for which the strain–softening elastic tension cannot balance the large viscous tension applied by the fluid (Barthès-Biesel, 2011).

The case of a capsule with a SK membrane and aspect ratio $a/b = 3$ is now considered. Note that since we consider equal volume capsules, the capsule dimensions are now $a/\ell = 2.08$ and $b/\ell = 0.693$. The capsule cross–section is thus smaller than it is for $a/b = 2$. The rolling motion is again found to be the stable regime for $Ca_s \leq 0.8$. It is then followed by a wobbling motion for $0.9 \leq Ca_s \leq 1.7$ and by an oscillating–swinging motion with decreasing oscillation about the shear plane as Ca_s increases (Figure 6.15b).

In conclusion we find the same qualitative motion (rolling followed by wobbling and eventually swinging with oscillations about the shear plane), irrespective of the capsule membrane law or aspect ratio. The main effect of these parameters is to change a little the values of Ca_s at transition. In particular, it seems that the main factor that triggers the transition from rolling to wobbling is the deformation of the membrane. Indeed, from Figure 6.14, we note that the last result of stable rolling motion before transition is

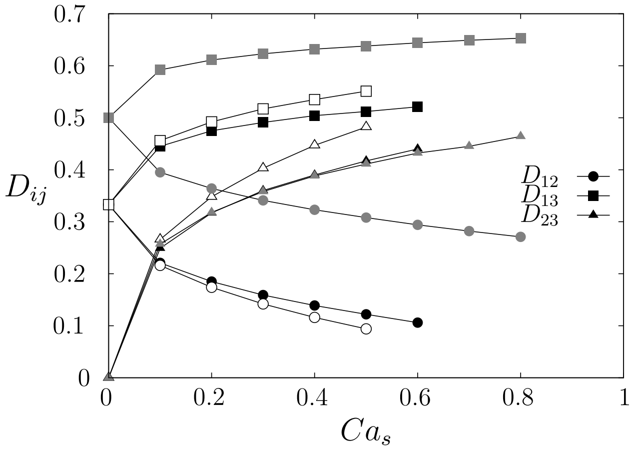

Figure 6.14: Influence of the capillary number Ca_s on the capsule deformation estimated by the Taylor parameters D_{ij} during the stable rolling regime $\zeta_0 = 0°$. Open symbols: C2NH; black closed symbols: C2SK; grey closed symbols: C3SK.

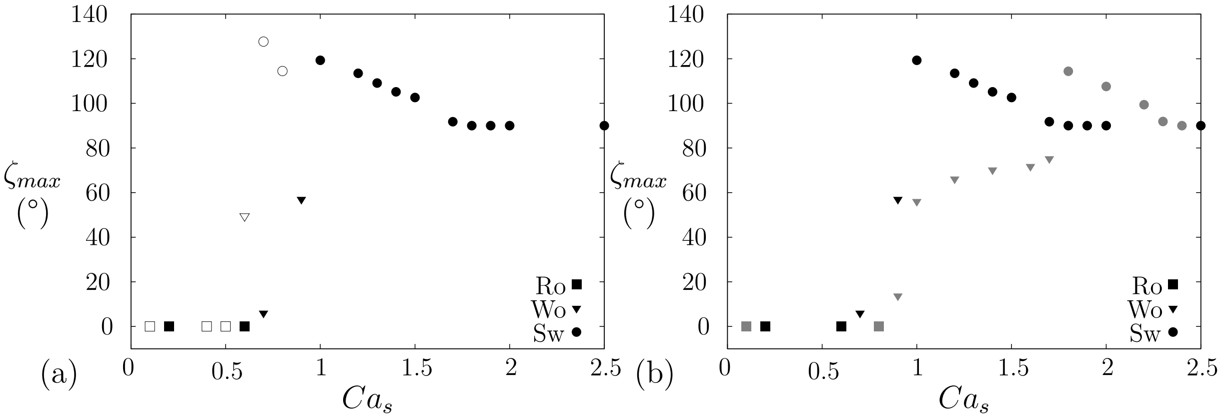

Figure 6.15: Influence (a) of the constitutive law and (b) of the aspect ratio on the maximum inclination ζ_{max} as a function of Ca_s. Ro: rolling; Wo: wobbling; Sw: oscillating–swinging tending to pure swinging; open symbols: C2NH; black closed symbols: C2SK; grey closed symbols: C3SK.

obtained for roughly the same values of the three deformation parameters

$$D_{23} = 0.45 \sim 0.47, \quad |D_{12} - D_{12}^0| = 0.23, \quad D_{13} - D_{13}^0 = 0.16 \sim 0.22.$$

This means that it corresponds to the same mean elastic energy in the membrane $E/G_s\ell^2 = 1 \sim 1.3$, which is rather small compared to the high levels of elastic energy reached in the swinging regime.

6.5 Discussion and conclusion

The study of the mechanical stability of the motion of a prolate ellipsoidal capsule under shear flow has provided new interesting results. We have found that for a prolate capsule in Stokes flow, the two obvious symmetric configurations where the capsule axis is either parallel or perpendicular to the shear plane do not always correspond to stable equilibrium states. Since in the Stokes regime, the dynamic time dependent term is removed from the Navier–Stokes equations, the only way to test the stability of an equilibrium solution is to perturb it. We have adopted this method and shown that for low flow strength, the capsule assumes a rolling motion with its axis parallel to the flow vorticity, whereas for high flow strength, the swinging motion in the shear plane is stable. We have not tried to determine with a high precision, the values of Ca_s for which transition occurs. The critical value is obtained within an interval of 0.1.

For example, in the case of a capsule with $a/b = 2$ and a SK ($C = 1$) membrane, we find that for moderate flow strength (up to $Ca_s = 0.6$), the stable equilibrium corresponds to the rolling regime: the prolate capsule orients its long axis parallel to the vorticity direction. For high flow strength ($Ca_s \geq 1.8$), the capsule, however, places its long axis in the shear plane and follows a swinging regime with oscillations decreasing with Ca_s. In the intermediate range ($0.7 \leq Ca_s \leq 0.9$), the capsule first exhibits a complex wobbling motion and precesses around the vorticity axis. Its long axis then makes a mean angle with the vorticity axis which increases with Ca_s. For $Ca_s > 1$, the capsule oscillates about the shear plane and assumes a swinging motion. The amplitude of the oscillations decreases with Ca_s.

Jeffery (1922) found that the final orientation of a rigid ellipsoidal particle suspended in an external flow was such that the viscous energy dissipation is minimum. Correspondingly, a prolate ellipsoid would have its long axis parallel to the vorticity. For small capillary numbers, the capsule behaves almost like a solid ellipsoid. It is thus not surprising that the stable equilibrium state, i.e. the rolling regime, corresponds to the Jeffery's regime. For $Ca_s > 0.6$, the capsule no longer converges towards the configuration that minimizes the viscous dissipation as can be surmised from Figures 6.8 and 6.11. The membrane deformation plays an important role and the fluid–structure interactions dictate the equilibrium configuration. We have corroborated these results by studying other prolate capsules with either a different membrane law or a different aspect ratio. We find that all these capsules have a stable rolling regime at low shear rate, from which they depart when a given level of deformation (or of elastic energy in the membrane) is reached. This allows us to surmise the role of the viscosity ratio λ between the internal and external fluids. Using a viscosity ratio $\lambda = 1$ simplifies significantly the computations which are then shorter. As we have studied the dynamic response of a capsule this is an appreciable advantage. For spherical capsules, it has been shown that $\lambda < 1$ leads to a moderate increase of the capsule deformation of order 20% for the same value of Ca_s (Foessel *et al.*, 2011). Thus we can expect a low internal viscosity capsule to quit the rolling regime for values of Ca_s lower than those found for $\lambda = 1$. Conversely as λ increases above unity, the internal viscosity effect is to decrease the capsule deformability. We can thus expect that the stability limit of the rolling regime will increase with the internal viscosity.

Experimentally, for a given capsule population, the capsule shape (size ratio a/b and characteristic length ℓ), internal viscosity μ and membrane elasticity moduli (G_s, K_s) are fixed. Thus the only way to increase Ca_s is through the shear rate $\dot{\gamma}$ and the external fluid viscosity (but then the viscosity ratio also changes while it is assumed to be unity in this study). Typical artificial capsules have a shear elastic modulus of the order of $G_s = 0.1$ to 1 N/m (Chang & Olbricht, 1993*b*; Chu *et al.*, 2011; Koleva & Rehage, 2012; Zhang & Salsac, 2012), while their size varies from $\ell = 30$ μm to 1 mm. With these values, we have to apply a viscous stress $\mu\dot{\gamma}$ of the order of 100 Pa to obtain a capillary number of $Ca_s = 0.1$. At the same time, we have to keep the flow Reynolds number $Re = \rho a^2 \dot{\gamma}/\mu$ small (where ρ is the fluid density). Experimental observations are best made at low values of the shear rate, typically $\dot{\gamma} < 10$ s^{-1} so that the experimental time t is not too short (see for example Abkarian *et al.* (2007)). Thus high values of the shear stress are difficult to achieve unless the external fluid viscosity is very large. We conclude that it is challenging to reach large values of Ca_s experimentally.

Furthermore, artificial capsules tend to break up for deformation levels of order 2–10% (Chang & Olbricht, 1993*b*; Koleva & Rehage, 2012) with a polymer membrane and of order 20–30% for a polymerized albumin membrane (Carin *et al.*, 2003). It follows that although interesting from the theoretical point of view, the high Ca_s behavior is not very likely to be observed. Thus, the most probable configuration that can be observed experimentally is the rolling regime.

Chapter 7

Equilibrium states of an oblate capsule in shear flow

In order to study the influence of the capsule aspect ratio on the stable equilibrium configurations, we now determine the stable equilibrium configuration of an oblate capsule. Firstly, we consider an oblate capsule with an aspect ratio of 0.5 and a strain-hardening membrane. We investigate the influence of the initial orientation, the capillary number Ca_s, and viscosity ratio λ between the internal and external fluids and evaluate the characteristic times that an oblate capsule needs to reach equilibrium. This study was submitted to the '*Journal of Fluid Mechanics*' with the title 'Stable equilibrium configurations of an oblate capsule in simple shear flow'. It was carried out F. Delahaye, D. Barthès-Biesel and A.-V. Salsac. The chapter is completed with additional results obtained on ellipsoidal capsules with various aspect ratio a/b. The results of simulations conducted on capsules having their revolution axis within the shear plane enable to provide a complete picture of the stable configuration states for a large range of capillary number Ca_s and aspect ratio a/b.

7.1 Introduction

Capsules, which consist of a thin deformable membrane around a liquid droplet, play the joint role of transporting and protecting an inner fluid content. The principle of microencapsulation is ubiquitous with many applications in industry. Besides its classical use in ink–jet printing, photography, cosmetic cream manufacturing, etc., it is at the source of innovative applications, many of them appearing in the field of biotechnologies (Ma & Su, 2013). For instance, contrast–enhanced ultrasound has become one of the most widespread imaging techniques thanks to the use of coated air microbubbles or of microcapsules filled with perfluorinated gases for echogenicity (Furlow, 2009). In pharmaceutics, drug and cell encapsulation is rapidly developing (Bhujbal *et al.*, 2014) and has led to new treatment techniques, such as targeted drug therapy. Similarly, encapsulation is used for the development of bioartificial organs (e.g. encapsulation of islets of Langerhans for diabetic patients (Clayton *et al.*, 1993) or of haemoglobin to create artificial blood (Chang, 2003)). Many instances of encapsulation may also be found in nature (e.g. seeds, eggs, cells). Red blood cells (RBC) are an example of natural capsules: their two–layer membrane composed of a lipid bilayer (outer layer) and a cytoskeleton protects a solution of hemoglobin (Mohandas & Gallagher, 2008).

The motion of spheroidal capsules or of biconcave red blood cells in simple shear flow with shear rate $\dot{\gamma}$ is quite complicated. It depends on the axis ratio a/b (a is half the revolution axis length), on the viscosity ratio λ between the internal and external liquids and on the relative flow strength, measured by the capillary number $Ca_s = \mu\dot{\gamma}\ell/G_s$, where μ is the suspending fluid viscosity, G_s the surface shear elastic modulus of the capsule membrane and ℓ the length scale defined as the radius of the sphere with the same volume as the capsule. Different behaviors have been identified. When the capsule revolution axis is in the shear plane, the particle can rotate like a quasi–solid particle (*tumbling motion*), or it can take a quasi–steady deformed shape where the long axis oscillates around a mean orientation in the shear plane, while the membrane rotates about the deformed shape (*swinging* or *tank–treading* motion, depending on the oscillation amplitude). Another equilibrium state is found when the particle revolution axis is perpendicular to the shear plane: the capsule takes a *rolling motion* and rotates like a (deformed) wheel under the flow vorticity. The transition from in–plane to rolling motion has received many names in the literature: wobbling, precessing, kayaking, oscillating swinging.

Experiments, carried out on single red blood cell, have shown that the cell deformability and dynamics are very different from those observed for a rigid particle or even a spherical capsule. At low Ca_s, a RBC has a tumbling motion which evolves into a swinging motion, as Ca_s increases (Abkarian *et al.*, 2007; Abkarian & Viallat, 2008; Fischer & Korzeniewski, 2013). However, this well established picture has recently been questioned by Dupire *et al.* (2012), who have observed that the tumbling motion became unstable so that the red blood cells took a rolling motion, before switching to tank–treading. Note that in most experiments the presence of a solid wall and/or a slight local non–linearity due to the parabolic nature of the flow field, may influence the resulting motion.

Motivated by these experimental observations, a number of numerical studies have investigated the dynamics of a spheroidal capsule placed in a simple shear flow. The first models considered a capsule with its revolution axis placed in the shear plane, where it remains under Stokes flow conditions (Ramanujan & Pozrikidis, 1998; Sui *et al.*, 2008; Bagchi & Kalluri, 2009; Walter *et al.*, 2011). It is found that the capsule has a tumbling motion at low Ca_s and a swinging motion at high Ca_s. At the tumbling–to–swinging transition, the capsule assumes a quasi–circular shape in the shear plane. The value of Ca_s at the transition depends on the capsule aspect ratio: transition occurs at higher Ca_s for prolate capsules than for oblate capsules. For a given shape, increasing the internal viscosity also shifts the transition to higher values of Ca_s.

The off–plane motion of a *prolate* capsule has been recently studied in simple shear flow in Stokes flow conditions by Dupont *et al.* (2013) or under low flow inertia (Reynolds number $Re = 0.2$) by Cordasco & Bagchi (2013) and Wang *et al.* (2013). Dupont *et al.* (2013) have considered flow strengths $0.1 \leq Ca_s \leq 2$. They have found that the low Ca_s tumbling motion in the shear plane is mechanically unstable: starting from any initial orientation, the capsule eventually places its revolution axis along the vorticity axis and takes a stable rolling motion. As Ca_s is increased, a prolate capsule tilts away from the vorticity axis and precesses around it. At still higher values of Ca_s, a stable swinging regime is observed, where the capsule longest axis tends towards the shear plane. Dupont *et al.* (2013) have shown that these stable equilibrium states did not depend on the initial orientation of the capsule, a result which is confirmed by Wang *et al.* (2013) for $Ca_s \geq 0.03$. The fact that Cordasco & Bagchi (2013) find that the motion depends on the initial capsule orientation may be due to too short computation times.

The question that arises is whether the results found for prolate capsules apply to oblate spheroidal capsules. Cordasco & Bagchi (2013) studied oblate ellipsoidal capsules for $0.05 \leq Ca_s \leq 0.6$, different axis ratios and no viscosity contrast ($\lambda = 1$). They conclude that an oblate spheroidal capsule always tends towards the shear plane where it takes a tumbling or swinging motion with oscillations about the shear plane (also called kayaking) depending on Ca_s. They also studied RBC dynamics for different viscosity contrasts. They find the same behavior as for oblate spheroids, when $\lambda \leq 1$. However, for larger values of the internal viscosity, they observe a tendency of the RBC towards a rolling motion: their conclusions are based on the trend of the evolution curves, as too short computational times are used in the simulations to observe the converged RBC regime. Wang *et al.* (2013) considered oblate capsules with axis ratio 2/3 for $0.003 \leq Ca_s \leq 0.3$ and $\lambda = 1$. They also find for $Ca_s \geq 0.03$ that the capsule tends towards the shear plane where it takes a tumbling or oscillating–swinging motion. In their study, the results depend on its initial orientation. The off-plane motion of an oblate capsule with a strain–softening membrane has finally been modeled by Omori *et al.* (2012) for two values of capillary number ($Ca_s = 0.3$ and 1.0), but they have failed to recognize a rolling motion for $Ca_s = 1$.

All those results indicate that the dynamics of prolate and oblate capsules are very different. If the dynamics of prolate spheroidal capsules are rather well understood, such is not the case for oblate ones, for which a comprehensive study has still to be performed. Indeed, there remain a number of pending questions:

- Does the final motion of an oblate capsule really depend on the initial orientation?
- What is the high flow strength motion of a capsule?

- How does the capsule internal viscosity affect the motion?
- How long does it take for a capsule to reach an equilibrium configuration?

The present work aims at investigating the dynamics of an oblate capsule subjected to a simple shear flow under Stokes flow conditions. Our objective is to find the stable equilibrium configurations and to study the influence of the capillary number and viscosity ratio, since experimentally the external viscosity is rarely matched with the viscosity of the internal fluid. In particular we shall show that the final equilibrium motion of an oblate capsule does not depend on its initial orientation, in contrast with previous conclusions. Another important objective is to determine the time required for an oblate capsule initially placed off the shear plane to reach its mechanical equilibrium state. Such information is crucial when setting up experiments to observe the behavior of oblate capsules. Specifically, it is important to make sure that the observed motion is indeed steady. Similarly, this information should also be useful to set up the proper computational times of models.

To solve the fluid–structure interaction problem, we use the numerical model developed by Walter *et al.* (2010) and Foessel *et al.* (2011), based on the coupling of a membrane finite element method for the capsule deformation with a boundary integral method for the internal and external flows. We briefly outline the problem and the numerical method in section 7.2. The equilibrium configurations of an oblate capsule initially positioned off the shear plane are studied in section 7.3 as well as the influence of the viscosity ratio between the internal and external flow. The characteristic times to reach equilibrium are evaluated in section 7.4 as a function of the viscosity ratio, before discussing all the results in section 7.5.

7.2 Method

7.2.1 Problem statement and numerical method

We consider a capsule with a very thin membrane, modelled as an isotropic hyperelastic surface S_t with surface shear modulus G_s, area dilatation modulus K_s and negligible bending resistance. In the reference undeformed state, the capsule is an oblate spheroid with aspect ratio $a/b = 0.5$, where $2a$ denotes the revolution axis length, and $2b$ the length of any two orthogonal long axes. The problem length scale $\ell = (ab^2)^{1/3}$ is defined as the radius of the sphere with the same volume as the capsule. For $a/b = 0.5$, we find $a/\ell = 0.63$ and $b/\ell = 1.26$.

We define the reference frame $\mathcal{F}'$ (O, $\underline{e}'_x$, $\underline{e}'_y$, $\underline{e}'_z$), where O is the capsule centre of mass and $\underline{e}'_x$, $\underline{e}'_y$, $\underline{e}'_z$ are the principal axes of the undeformed capsule. The revolution axis is

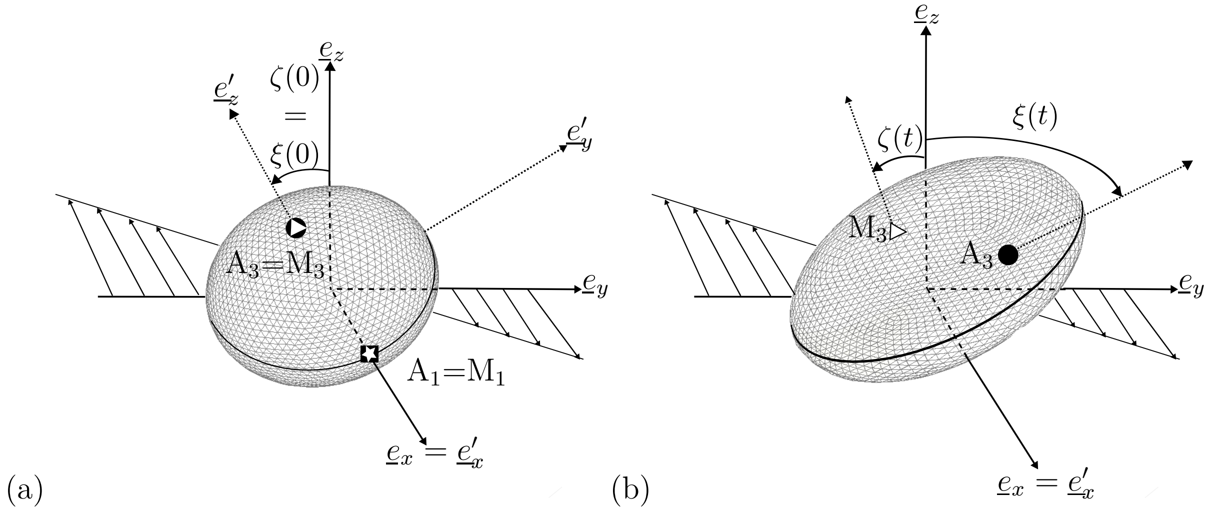

Figure 7.1: Reference (*a*) and deformed (*b*) configurations of an oblate capsule subjected to a simple shear flow. The initial capsule orientation is defined by the angle $\zeta(0)$ between the capsule revolution axis $\underline{e}'_z$ and the flow vorticity axis $\underline{e}_z$. The points $M_i(t)$ represent the tip of the capsule principal axes and the points $A_i(t)$ are the points initially located at the tip of the capsule principal axes.

initially along **e'**$_z$, so that the initial capsule profile is given by

$$\left(\frac{x'_s}{b}\right)^2 + \left(\frac{y'_s}{b}\right)^2 + \left(\frac{z'_s}{a}\right)^2 = 1, \tag{7.1}$$

where the coordinates (x'_s, y'_s, z'_s) correspond to the position of a material point on the membrane.

The capsule is suspended in an unbounded Newtonian incompressible fluid of viscosity μ. The inner fluid is also Newtonian and incompressible with viscosity $\lambda\mu$, where λ is the internal–to–external viscosity ratio. The density of the internal and surrounding fluids are equal, thus excluding gravity effects. The Reynolds number of the flow is assumed to be negligible, so that the internal and external flows are governed by the Stokes equations. The capsule is subjected to a simple shear flow with shear rate $\dot{\gamma}$ given by

$$\underline{v}^\infty = \dot{\gamma} y \underline{e}_x \tag{7.2}$$

in the laboratory reference frame $\mathcal{F}$ $(\mathrm{O}, \underline{e}_x, \underline{e}_y, \underline{e}_z)$.

At time $\dot{\gamma}t = 0$, the capsule orientation in space is defined by the angles between the basis vectors of the reference frames $\mathcal{F}'$ and $\mathcal{F}$. The capsule revolution axis $\underline{e}'_z$ makes an angle $\zeta(0)$ with the vorticity axis, such that $(\underline{e}'_z, \underline{e}_z) = (\underline{e}'_y, \underline{e}_y) = \zeta(0)$ and $(\underline{e}'_x, \underline{e}_x) = 0$ (Figure 7.1a). Thus $\zeta(0) = 0$ or $\pi/2$ corresponds to a capsule with its revolution axis parallel to the vorticity axis or to the shear plane, respectively.

The problem is solved numerically using the Boundary Integral – Finite Element method (BI–FE) (Foessel *et al.*, 2011). This method couples a boundary integral technique to compute the fluid flows (inside and outside the capsule) to a finite element method to compute the capsule membrane deformation. The method is summarized in this section, but more details are available in Walter *et al.* (2010), Barthès-Biesel *et al.* (2010) and Foessel *et al.* (2011).

The numerical procedure is based on a Lagrangian tracking of the position of the membrane material points of S_t. The capsule deformation and in–plane principal stretch ratios λ_{s1} and λ_{s2} may thus be computed from the position of the membrane points at each time. The capsule wall is assumed to be strain–hardening and to follow a Skalak law (Skalak *et al.*, 1973). The principal elastic tensions T_1 and T_2, which are forces per unit length of deformed membrane, are then given by

$$T_1 = \frac{G_s}{\lambda_{s1}\lambda_{s2}} \left[\lambda_{s1}^2(\lambda_{s1}^2 - 1) + C(\lambda_{s1}\lambda_{s2})^2 \left((\lambda_{s1}\lambda_{s2})^2 - 1\right)\right] \tag{7.3}$$

with a corresponding expression for T_2 obtained by permuting indices 1 and 2. The surface shear and area dilatation moduli are then related by $K_s = G_s(1 + 2C)$, where C is a constant such that $C > -1/2$.

The finite–element method is used to solve the equilibrium equation of the membrane

$$\underline{\nabla}_s \cdot \underline{T} + \underline{q} = \underline{0}, \tag{7.4}$$

and find the load $\underline{q}(\underline{x_s}, t)$ exerted by the fluids on the membrane at time t. In Equation (7.4), the symbol $\underline{\nabla}_s$ represents a surface gradient.

Knowing the viscous load $\underline{q}$, the velocity $\underline{v}(\underline{x}, t)$ of the membrane points is deduced from a boundary integral formulation for the three–dimensional motion of the internal and external fluids

$$\begin{aligned} \underline{v}(\underline{x_s}, t) &= \underline{v}^{\infty}(\underline{x_s}) - \frac{1}{8\pi\mu} \int_{S_t} \left(\frac{\mathbb{I}}{\| \underline{r} \|} + \frac{\underline{r} \otimes \underline{r}}{\| \underline{r} \|^3}\right) \cdot \underline{q}(\underline{y_s}, t)\, dS(\underline{y_s}) \\ &- \frac{1-\lambda}{8\pi} \int_{S_t} \left(\underline{v}(\underline{y_s}, t) - \underline{v}(\underline{x_s}, t)\right) \cdot \frac{\underline{r} \otimes \underline{r} \otimes \underline{r}}{\| \underline{r} \|^5} \cdot \underline{n}(\underline{y_s})\, dS(\underline{y_s}), \end{aligned} \tag{7.5}$$

where $\underline{v}^{\infty}$ is given by Equation (7.2), $\mathbb{I}$ is the identity tensor, $\underline{n}$ is the unit vector normal to S_t and $\underline{r} = \underline{x_s} - \underline{y_s}$ is the distance between the point $\underline{x_s}$, where the calculation is performed, and the point of integration $\underline{y_s}$. The new position of the membrane points at the next time step is found by using an explicit second–order Runge–Kutta method, to solve the kinematic condition, which relates the membrane velocity to the time derivative of the Lagrangian position of the membrane points

$$\underline{v}(\underline{x}_s, t) = \frac{\partial \underline{x}_s(\underline{X}_s, t)}{\partial t}, \qquad \underline{x}_s \in S_t \tag{7.6}$$

where $\underline{X}_s$ represents the position of a point in the reference configuration.

In general, the capsule motion and deformation are governed by:

- the capsule initial orientation $\zeta(0)$,
- the membrane constitutive law,
- the ratio of the area dilatation and shear moduli K_s/G_s,
- the capillary number $Ca_s = \mu\dot{\gamma}\ell/G_s$, which measures the ratio between the viscous and the elastic forces,
- the viscosity ratio λ.

We assume that the capsule membrane follows the Skalak law with $C = 1$ and study the influence of $\zeta(0)$, Ca_s and λ on the capsule dynamics.

7.2.2 Discretization, stability and convergence

One of the advantages of the BI–FE method is that all the problem unknowns are to be determined on the capsule surface and not in the entire domain volume. The capsule surface is meshed by subdividing sequentially the 20 triangular faces of an icosahedron inscribed in a sphere until the desired number of elements is reached. Nodes are then added at the middle of all the element edges and projected onto the sphere in order to generate second–order P_2 elements. This mesh is deformed into an ellipsoidal mesh with the desired axis ratio (Walter *et al.*, 2011). All the results are shown for a mesh with 2562 nodes and 1280 triangular curved elements.

The numerical method is stable when the time step satisfies the condition

$$\dot{\gamma} \triangle t < O(\frac{\Delta x Ca_s}{\ell}), \tag{7.7}$$

where Δx is the typical mesh size (Walter *et al.*, 2010). Here, $\Delta x = 0.075$. We use $\dot{\gamma} \triangle t = 5 \times 10^{-3}$ for $Ca_s \geq 0.5$ and decrease the time step proportionally for lower Ca_s.

To reach the steady state of a capsule initially off the plane, computational times of the order of $\dot{\gamma}t = 10^2 - 10^3$ are needed. In order to estimate the numerical error over such long computational times, we compute the relative error $\epsilon_V = |V - V_0|/V_0$ on the capsule volume V, where V_0 is the initial volume of the capsule. The error at $\dot{\gamma}t = 100$ is

- $\mathcal{O}(10^{-2})$ for $\lambda < 4$ and $Ca_s \leq 0.6$,
- $\mathcal{O}(10^{-3})$ for $\lambda < 4$ and $Ca_s > 0.6$ and for all values of Ca_s for $\lambda \geq 4$.

7.2.3 Result analysis

The capsule motion in space is complex. We characterize it by simultaneously studying the overall shape evolution (Eulerian description) and the motion of the membrane material points (Lagangian tracking).

The global geometry of the capsule is evaluated by means of the ellipsoid of inertia of the deformed shape, with principal axes denoted $L_i(t)$ $(i = 1, 2, 3)$ such that $L_1(t) > L_2(t) > L_3(t)$ at time t. The corresponding unit principal vectors in $\mathcal{F}$ are $\underline{v}_i(t)$ ($\underline{v}_1(0) = \underline{e}'_x$, $\underline{v}_2(0) = \underline{e}'_y$ and $\underline{v}_3(0) = \underline{e}'_z$). The capsule position in space is then determined from the angle $\zeta(t) = (\underline{v}_3(t), \underline{e}_z)$ between the capsule small axis and the vorticity direction (Figure 7.1b). We also follow the motion in time of the point $M_3(t)$, which corresponds to the intersection between the small axis direction $\underline{v}_3(t)$ and the membrane.

The membrane rotation is deduced from the motion in time of the points $A_i(t)$, which were initially located on the intersections between the $\underline{v}_i(0)$ directions and the membrane (Figure 7.1). We will for instance compare the motions of the points $A_3(t)$ and $M_3(t)$ in order to analyze eventual membrane rotation. We denote $\xi(t) = (\underline{OA}_3(t), \underline{e}_z)$ the angle between the $\underline{OA}_3(t)$ and the vorticity axis (Figure 7.1b). At time $\dot{\gamma}t = 0$, the points $A_3(0)$ and $M_3(0)$ are superimposed, so that $\xi(0) = \zeta(0)$.

7.3 Stable equilibrium configurations

7.3.1 Equilibrium configurations of a capsule with $\lambda = 1$

Obvious equilibrium positions

Two obvious equilibrium configurations exist for an oblate capsule placed in a shear flow under Stokes flow conditions: when the capsule revolution axis is initially in the shear plane or perpendicular to it.

When the capsule revolution axis is initially in the shear plane ($\zeta(0) = \xi(0) = 90°$, $A_3(0)$ and $M_3(0)$ in the shear plane), we have seen in the introduction that the capsule experiences tumbling at low Ca_s followed by a transition towards swinging for higher values of Ca_s. Figure 7.2 illustrates the characteristic dynamics of the capsule during half a period in both regimes (see Walter *et al.* (2011) for more details). In this case, the points $A_3(t)$ and $M_3(t)$ remain in the shear plane for all the values of Ca_s and time ($\zeta(t) = \xi(t) = 90°$).

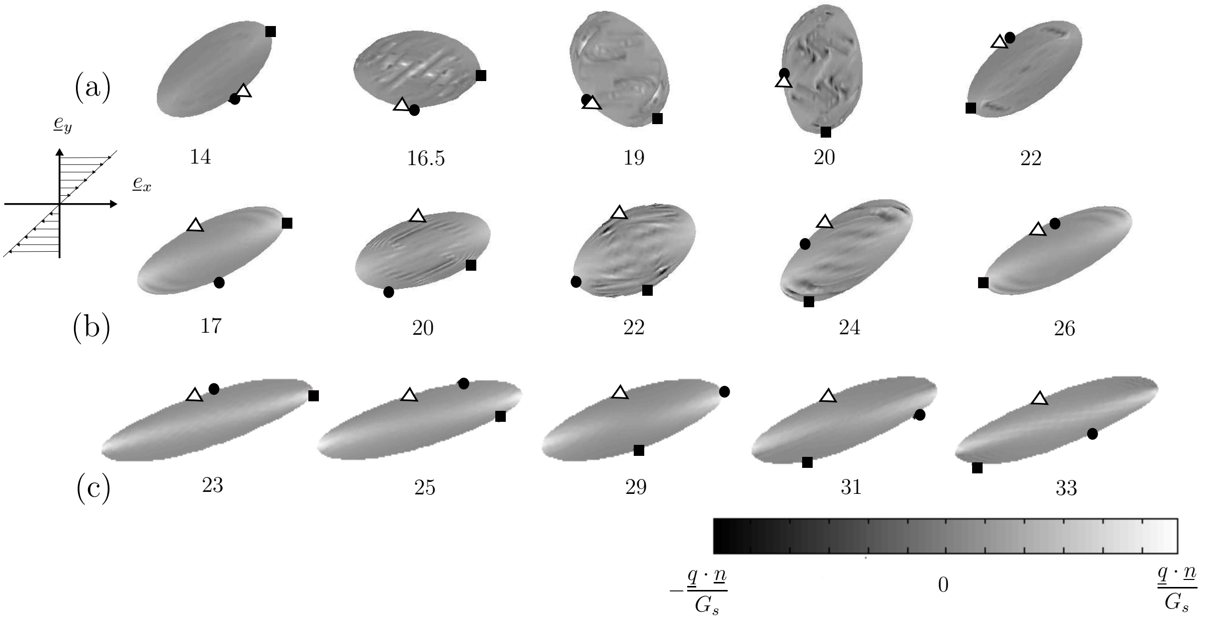

Figure 7.2: Capsule shape evolution over one half period at steady state when $\xi(0) = 90°$ ($\lambda = 1$). The grey scale corresponds to the normal component of the load $\underline{q} \cdot \underline{n}$ on the membrane, with maximum values depending on Ca_s. (*a*) $Ca_s = 0.01$: tumbling regime ($\max(\underline{q}\cdot\underline{n}/G_s) = 0.15$); (*b*) $Ca_s = 0.3$: swinging regime ($\max(\underline{q}\cdot\underline{n}/G_s) = 2$); (*c*) $Ca_s = 1.5$: quasi-steady tank-treading regime ($\max(\underline{q}\cdot\underline{n}/G_s) = 6$). The value of the non–dimensional time $\dot{\gamma}t$ is given below each shape. The points $A_1(t)$ (■) and $A_3(t)$ (●) are initially on the short and long axes respectively in the shear plane. The point $M_3(t)$ (△) represents the tip of the smallest capsule principal axis (see Figure 7.1).

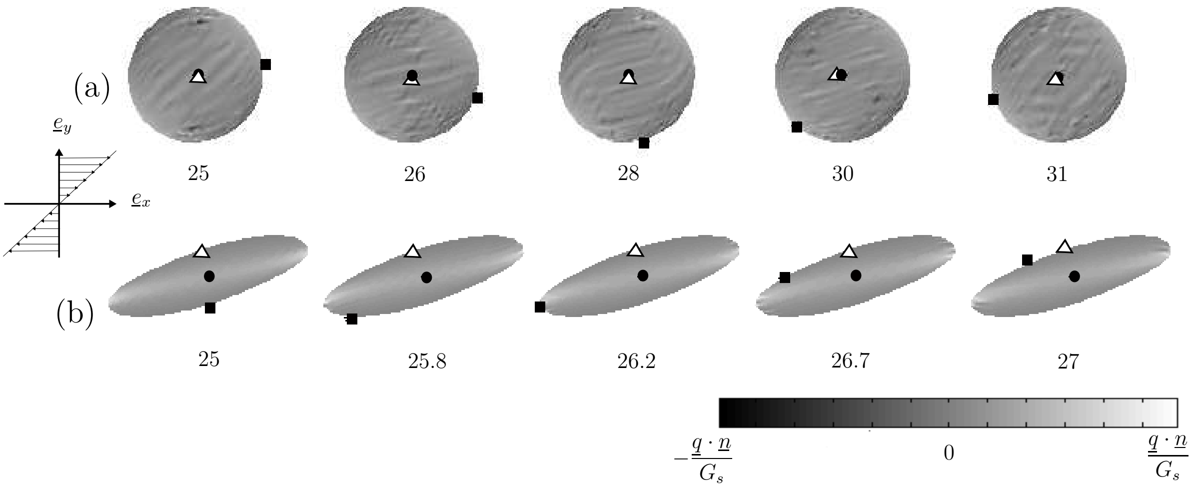

Figure 7.3: Capsule shape evolution over one half period at steady state when $\zeta(0) = 0°$ ($\lambda = 1$): capsule in rolling regime. (a) $Ca_s = 0.01$ ($\max(\underline{q} \cdot \underline{n}/G_s) = 0.1$); ($b$) $Ca_s = 1.5$ ($\max(\underline{q} \cdot \underline{n}/G_s) = 5$). Same legend as in Figure 7.2. The points $A_3(t)$ and $M_3(t)$ are superimposed in (a), whereas $A_3(t)$ is on the vorticity axis and $M_3(t)$ is in the shear plane in (b).

When the capsule revolution axis is initially along the vorticity axis ($\zeta(0) = \xi(0) = 0°$, $A_3(0)$ and $M_3(0)$ on the vorticity axis), the capsule cross–sections parallel to the shear plane are initially circular. They are deformed by the shear flow and the membrane rotates around the deformed shape. The capsule motion is called *rolling*, since the membrane rotates around the deformed cross–section like a (deformed) wheel. At low Ca_s (Figure 7.3a), the capsule cross–section is not much deformed so that the points M_3 and A_3 remain on the vorticity axis ($\zeta(t) = \xi(t) = 0°$). As the capillary number increases, the cross–section elongates in the straining direction (Figure 7.3b): the capsule small axis $\underline{v}_3$ and hence the point M_3 may eventually become located in the shear plane, while the point A_3 remains on the vorticity axis. In this case, the asymptotic values of the angles are $\zeta(t) = 90°$ and $\xi(t) = 0°$.

Note that for large Ca_s, the oscillation amplitude of the swinging regime observed when $\zeta(0) = 90°$ tends to zero so that the capsule experiences a quasi tank–treading motion (Figure 7.2c). This regime is visually the same as the rolling motion observed when $\zeta(0) = 0°$ at large Ca_s (Figure 7.3b). The only way to distinguish between the two regimes is by monitoring the position of the point A_3 and the angle $\xi(t)$. This shows that the best parameter to study the capsule motion is the angle $\xi(t)$. Experimentally, it can be achieved by attaching markers to the membrane, but it is difficult to perform. Resorting to numerical simulations is thus useful to distinguish between those regimes.

Stable equilibrium of an initially off–plane capsule

In Stokes flow, the mechanical stability of an equilibrium configuration can only be tested by perturbing the capsule orientation, which corresponds here to positioning the revolution axis with an initial orientation $\xi(0) = \zeta(0) \in]0^o, 90^o[$. We then follow the time evolution of the angles $\zeta(t)$ (to determine the overall capsule position) and $\xi(t)$ (to determine the type of capsule motion). Note that if $\xi(t) \to 90°$, the capsule tends towards the tumbling or the swinging regime (section 7.3.1). On the other hand, if $\xi(t) \to 0°$, the capsule stable configuration is the rolling motion. If $\xi(t)$ and $\zeta(t)$ tend towards any other value in $]0, 90°[$, the capsule takes at equilibrium a wobbling motion, where it precesses and oscillates about the vorticity axis.

We first investigate whether the initial orientation affects the final equilibrium configuration. We first consider a weak flow strength ($Ca_s = 0.01$) and three different initial orientations ($\zeta(0) = \xi(0) = 5°$, $45°$, $75°$). As shown in Figure 7.4a, the angles $\zeta(t)$ and $\xi(t)$ both tend to 90° independently of the initial orientation. The only effect of the initial position is the time it takes to reach equilibrium, which increases the further the capsule initially is from its final equilibrium position. For $Ca_s = 0.01$, the stable equilibrium regime is a quasi–solid tumbling motion (with no membrane rotation), which explains why the curves of $\zeta(t)$ and $\xi(t)$ are superimposed. For a larger flow strength $Ca_s = 0.3$, the angles $\zeta(t)$ and $\xi(t)$ both converge towards 90° but do not follow the same time–evolution during the transition phase (Figure 7.4b). During transient, the capsule takes a global oscillating swinging motion (evidenced by the oscillations of $\zeta(t)$), during which the membrane rotates to bring the point A_3 in the shear plane. This result is independent of the initial orientation (not shown).

When the capsule tends to position its small axis OM_3 and the point $A_3(t)$ in the shear plane, the resulting motion is identical to the one shown in Figure 7.2 when the capsule revolution axis is initially in the shear plane ($\zeta(0) = \xi(0) = 90°$). In conclusion, the tumbling and swinging motions are found to be the stable equilibrium configurations of an oblate capsule for low and medium–range capillary numbers such that $Ca_s < 0.9$.

However, for larger values $Ca_s \geq 0.9$, the principal short axis no longer remains within the shear plane: it exhibits an oscillation about the shear plane, which is superimposed onto the in–plane oscillation. The equilibrium state of the capsule thus evolves from a swinging to a wobbling (or oscillating–swinging) motion: the point $M_3(t)$ oscillates a little about the shear plane and the point $A_3(t)$ precesses around the vorticity axis with a constant mean inclination, as indicated in Figure 7.5. As Ca_s increases, the mean angle $\xi(t) = (OA_3(t), \underline{e}_z)$ decreases until the capsule changes drastically its motion and starts rolling. For $Ca_s \geq 1.5$, the capsule stable equilibrium configuration is rolling. It is illustrated in Figure 7.6a, which shows that for $Ca_s = 2$ the angle $\zeta(t)$ tends towards 90°

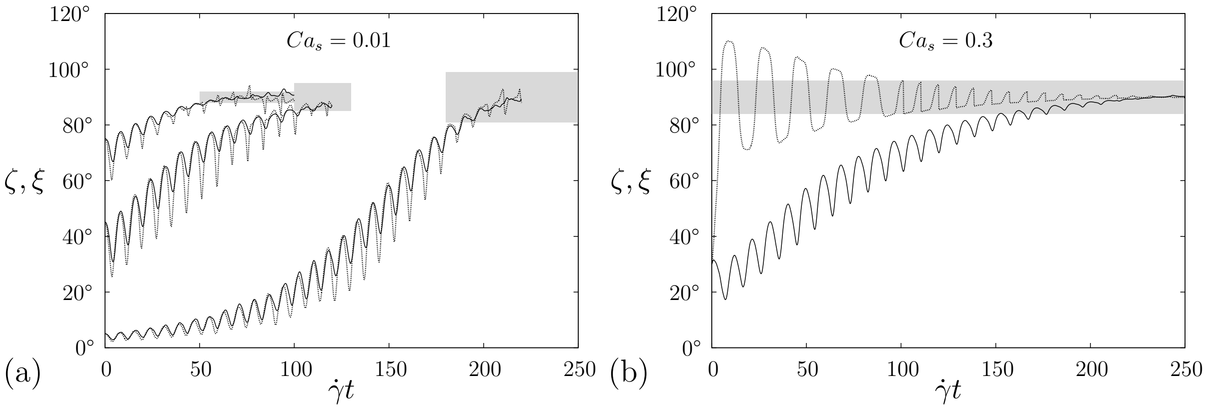

Figure 7.4: Transient evolution of the angles $\zeta(t)$ (dashed line) and $\xi(t)$ (full line) for different initial orientations ($\lambda = 1$). (a) Tumbling motion; (b) swinging motion. The grey zones represent the convergence criteria.

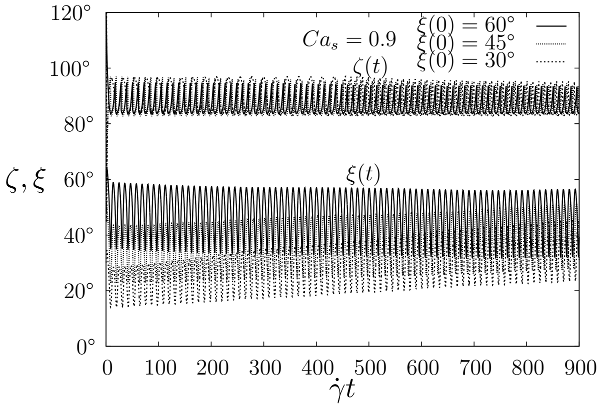

Figure 7.5: Wobbling motion for three initial orientations $\xi(0) = 30°$, $45°$ and $60°$ at $Ca_s = 0.9$ ($\lambda = 1$). The small axis oscillates a little about the shear plane, while $A_3(t)$ precesses and oscillates around the vorticity axis with an inclination which tends to $44° \pm 12°$ for all three initial orientations.

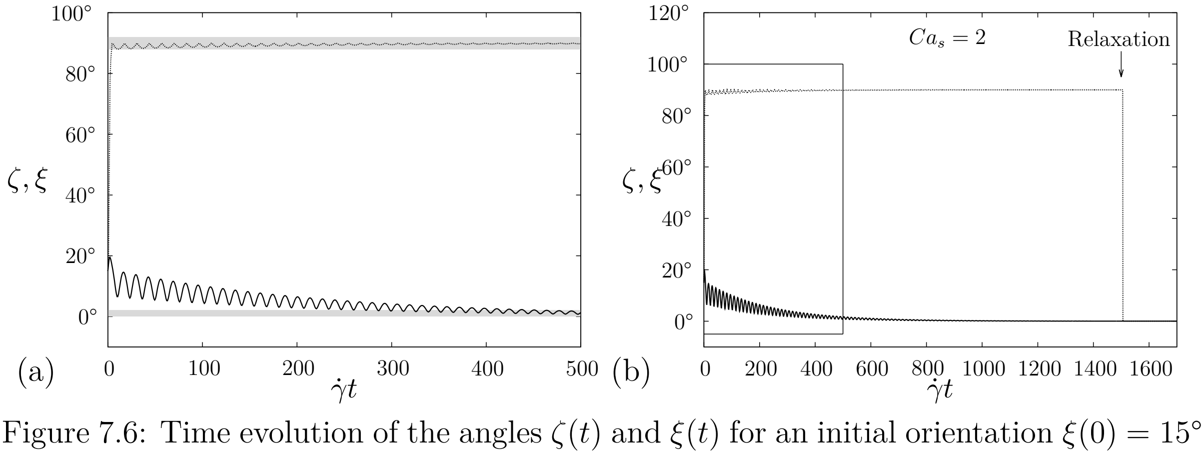

Figure 7.6: Time evolution of the angles $\zeta(t)$ and $\xi(t)$ for an initial orientation $\xi(0) = 15°$, at $Ca_s = 2$ ($\lambda = 1$). (a) Zoom on the initial time response ($\dot{\gamma}t \in [0, 500]$), which indicates that the capsule tends towards a rolling motion; (b) long time response followed by a relaxation phase ($\underline{v}^{\infty} = 0$ for $\dot{\gamma}t \geq 1500$), where both ξ and ζ go to zero. Same legend as in Figure 7.4.

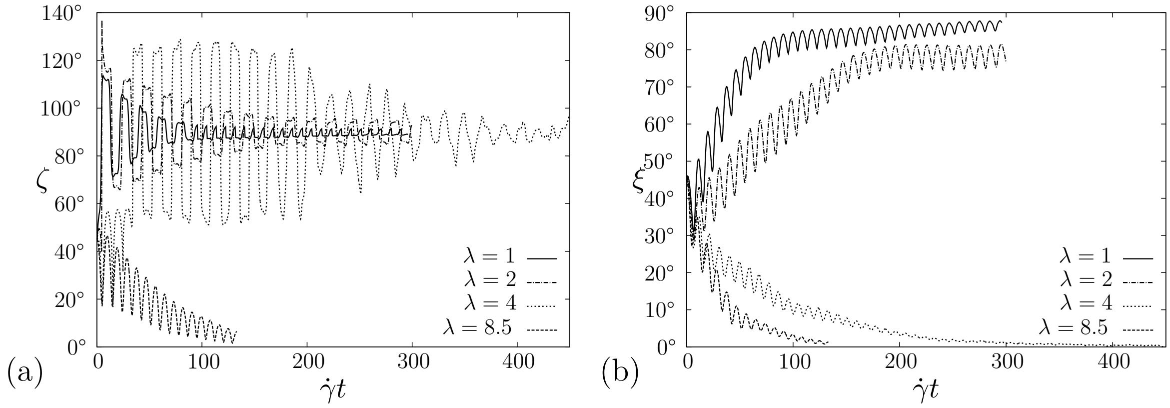

Figure 7.7: Time evolution of the angles (a) $\zeta(t)$ and (b) $\xi(t)$ for different viscosity ratios λ ($\zeta(0) = 45°$,$Ca_s = 0.2$).

whereas $\xi(t)$ converges towards 0°, the smallest axis being in the shear plane because of the large profile elongation. In order to verify that the capsule does have a rolling motion, we have run the following test: once the capsule has reached its equilibrium configuration, we set the far–stream velocity of the external flow at zero and follow the capsule re-orientation during relaxation. The second part of the graph of Figure 7.6b ($\dot{\gamma}t \geq 1500$) shows that the angle $\xi(t)$ remains equal to 0°, whereas $\zeta(t)$ decreases suddenly to 0°, when the flow is stopped. The capsule regains its oblate shape and has its revolution axis aligned with the vorticity axis. It indicates that, at equilibrium the capsule had previously assumed a rolling motion that is identical to the one observed when the short axis is initially aligned with the vorticity axis ($\zeta(0) = \xi(0) = 0°$), as shown in Figure 7.3b.

To summarize the cases for $\lambda = 1$, we have shown that, for $Ca_s < 0.9$, the situation is identical to the one considered by Walter *et al.* (2011), where the capsule revolution axis is initially positioned in the shear plane ($\zeta(0) = \xi(0) = 90°$). Correspondingly, the capsule assumes a quasi–solid tumbling motion for $Ca_s < 0.02$ and a swinging motion for $0.05 < Ca_s < 0.9$. The two regimes are separated by a transition motion characterized by the transient occurrence of a quasi–circular profile within the shear plane ($Ca_s \in [0.02, 0.05]$). For $0.9 \leq Ca_s \leq 1.5$, the capsule goes through a wobbling motion (also called oscillating precession), where its small axis oscillates about the shear plane while the point $A_3(t)$ precesses about the vorticity axis and gets nearer to it as Ca_s increases. Ultimately, for large values of Ca_s ($Ca_s \geq 1.5$), the capsule has a rolling motion. All these equilibrium states are independent of the initial orientation.

7.3.2 Influence of λ on the equilibrium configurations

We now study the influence of the viscosity ratio on the stable equilibrium configurations of the oblate capsule. We consider only viscosity contrasts larger than unity, as it was shown for initially spherical capsules that $\lambda < 1$ had little influence on the dynamics (Foessel *et al.*, 2011). As the mechanical equilibrium configuration is independent of the initial orientation when $\zeta(0) \in]0^{\circ}, 90^{\circ}[$, we position the capsule with an initial angle $\zeta(0) = 45^{\circ}$ and increase the viscosity of the internal fluid. Figure 7.7 shows the temporal evolution of the angles $\zeta(t)$ and $\xi(t)$ for $\lambda = 1$, 2, 4 and 8.5 in the case of a capillary number $Ca_s = 0.2$. For $\lambda = 1$, the capsule exhibits a swinging motion, as previously discussed. However, for $\lambda = 2$, the angle $\zeta(t)$ converges towards a value close to 90° while $\xi(t)$ oscillates about 77°: this indicates that a wobbling motion has set up. When the viscosity ratio is further increased ($\lambda = 4$), a transition to rolling occurs: the angle $\xi(t)$ tends to 0° while the capsule short axis exhibits dampened oscillations about the shear plane. For still higher values ($\lambda = 8.5$), the flow strength is not high enough to deform the capsule much: the smallest semi–diameter is on the vorticity axis ($\zeta \rightarrow 0^{\circ}$) and the profile in the shear plane is only slightly deformed. This shows that the viscosity ratio has a strong influence on the capsule equilibrium state for medium–range capillary numbers.

The combined effect of the viscosity ratio and capillary number is summarized in Figure 7.8. For $\lambda < 3$, the mechanical equilibrium configurations correspond to the ones observed for $\lambda = 1$. The viscosity ratio, however, influences the capillary number at which the tumbling–to–swinging and swinging–to–rolling transitions occur. The transition between tumbling and swinging takes place at higher Ca_s, since the increase in internal viscosity reduces the capsule deformability. For example, the transition is delayed from $0.02 \leq Ca_s \leq 0.05$ when $\lambda = 1$ to $0.06 \leq Ca_s \leq 0.09$ when $\lambda = 2$. On the contrary, the transition between swinging and rolling rather tends to occur for lower values of Ca_s, as λ increases. For example, at $Ca_s = 0.5$, the capsule converges towards the swinging regime at $\lambda = 1$ and towards the rolling regime at $\lambda = 2$.

The direct consequence of these two observations on the regime transitions is the disappearance of the swinging motion for $\lambda \sim 3$. For $\lambda \geq 4$, the stable mechanical equilibrium states are then only the tumbling and the rolling regimes. The capillary number of transition between tumbling and rolling further decreases with λ: at high λ, the rolling regime thus becomes the main mechanical equilibrium configuration that is likely to be observed (Figure 7.8).

It is of interest to compute the capsule deformation within the shear plane $D_{xy} = (L - B)/(L + B)$, where L and B are the longest and shortest semi–axes of the ellipsoid of inertia in the shear plane, respectively. The deformation D_{xy} is a quantity which is easily measured in the swinging or rolling regimes. We also provide the capsule semi-axis length L_z along the vorticity axis, as it enables to completely specify the geometry of the converged capsule shape together with D_{xy} and the constant volume constraint. Since both D_{xy} and L_z oscillate in the swinging regime, we give values that are averaged over

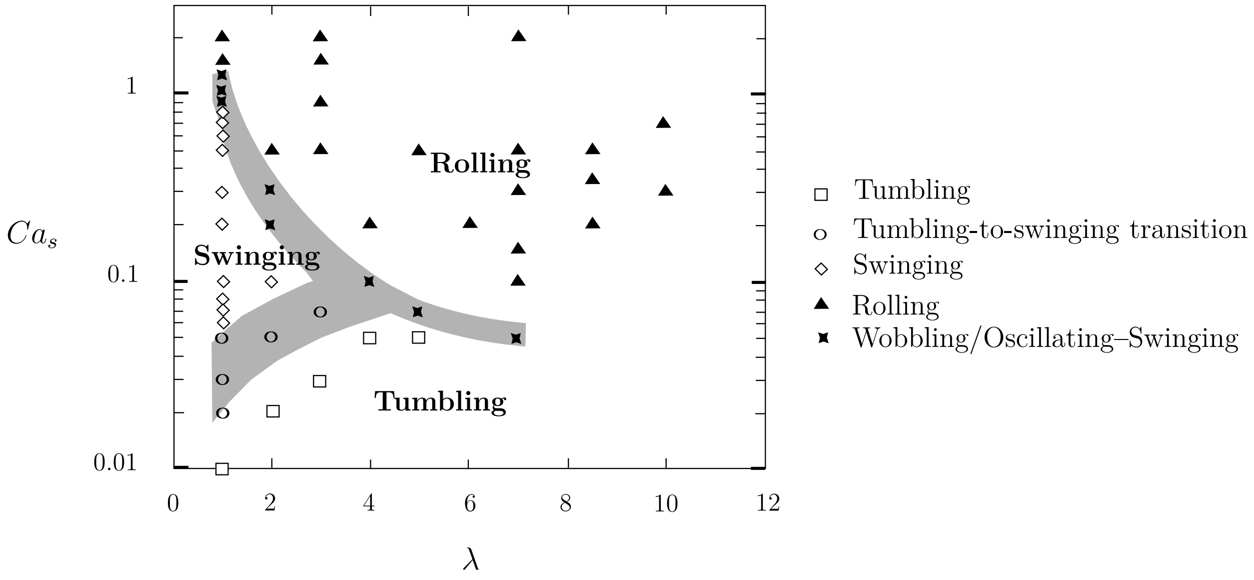

Figure 7.8: Sketch of the mechanical equilibrium configurations of an oblate capsule as a function of the capillary number Ca_s and viscosity ratio λ. The grey zones represent the tumbling–to–swinging and swinging–to–rolling transitions.

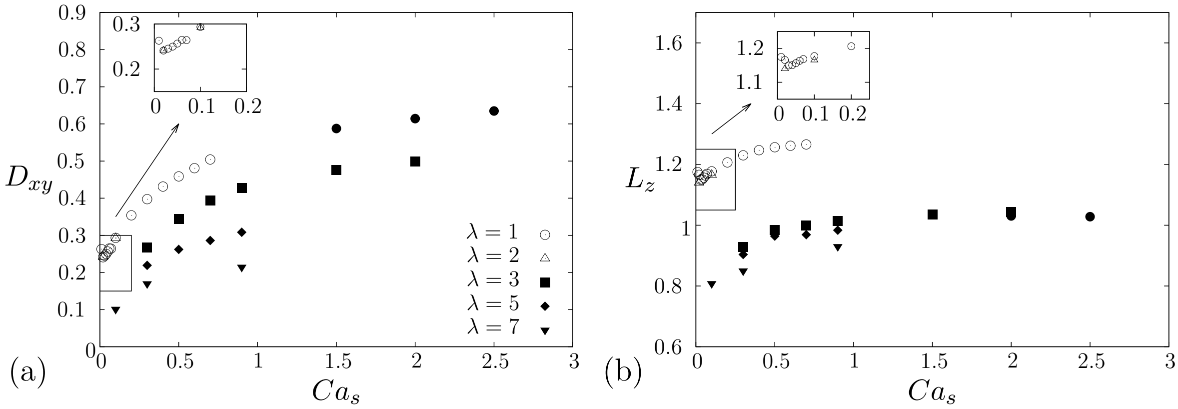

Figure 7.9: (a) Shear plane deformation and (b) semi–axis length along the vorticity axis. Open symbols: tumbling/swinging regime; full symbols: rolling regime.

ten periods. For $\lambda = 1$, we recover the results of Walter *et al.* (2011), which show a small decrease of D_{xy} and L_z during the tumbling–to–swinging transition, followed by a steady increase of both quantities with increasing Ca_s (Figure 7.9). A very similar behavior is found for $\lambda = 2$. For $Ca_s \geq 0.2$ and $\lambda \geq 3$, the rolling regime prevails, where D_{xy} steadily increases with Ca_s but decreases with λ, as expected. It should be noted that the deformation in the rolling regime is almost the same as the one which is found for a viscous spherical capsule (Foessel *et al.*, 2011). This seems to indicate that the shear plane deformed profile of an elastic capsule depends only on Ca_s and the viscosity ratio and is independent of the surface to volume ratio. Of course, this observation would need to be verified, but this is outside the scope of the present paper.

7.4 Time to reach the equilibrium configuration

All the previous results indicate that an oblate capsule placed off the shear plane requires a very long time τ of the order of $\dot{\gamma}\tau = 10^2 - 10^3$ to reach its mechanical equilibrium configuration. We have seen that the time τ depends on the initial orientation $\zeta(0)$, the capillary number Ca_s and the viscosity ratio λ. In this section, we study the convergence time of an oblate capsule. Such information can be useful to experimentalists for designing experimental protocols and to numericians for choosing adequately the computational time.

As is clearly apparent from Figures 7.4 and 7.6, the convergence time is difficult to determine with precision. We define an estimate of τ as the time it takes for a given angle ($\xi(t)$ or $\zeta(t)$) to be equal to 10% of the difference between its initial value and its value at equilibrium state. For example, based upon the time evolution of ζ, the convergence time τ_ζ would be such that:

$$|\zeta(\tau_\zeta) - \zeta_\infty| = 0.1|\zeta(0) - \zeta_\infty| \tag{7.8}$$

where ζ_∞ is the equilibrium value of ζ. The same definition applies to the convergence time τ_ξ based on ξ. The corresponding convergence areas are shown as grey zones in Figures 7.4 and 7.6. Note that their width depends on the difference between the initial and final orientations.

In the tumbling regime, the initial orientation influences significantly the convergence time as is clearly apparent in Figure 7.4a. However, in the swinging regime, we have checked that $\zeta(0)$ has little influence on either τ_ζ or τ_ξ. The same conclusion holds true for the rolling regime for $|\zeta(0) - \zeta_\infty| \leq 60^\circ$. We thus study an average off–plane inclination $|\zeta(0) - \zeta_\infty| = 45^\circ$ and show the combined effects of Ca_s and λ. In the wobbling regime, the time to reach equilibrium is fast for ζ, but very slow for ξ and depends significantly on the initial orientation of the capsule (Figure 7.5). We therefore do not try to determine it.

The convergence time depends significantly on whether it is based on $\zeta(t)$ or on $\xi(t)$ as is apparent in Figure 7.10a, where $\dot{\gamma}\tau$ is shown as a function of Ca_s for $\lambda = 1$. Indeed, in the swinging regime, the convergence time τ_ξ is roughly twice τ_ζ. We note that the convergence time increases with Ca_s in the swinging regime and decreases in the rolling regime. The effect of the viscosity ratio is that it significantly increases τ_ξ in the swinging regime as one could expect, since more energy is dissipated when the viscosity ratio increases. In the rolling regime, the response time decreases when the viscosity ratio increases because the capsule is less deformed and tends to behave like a rolling axisymmetric solid body. Note that experimentally, it is $\zeta(t)$ which is readily measured: to obtain $\xi(t)$, one would

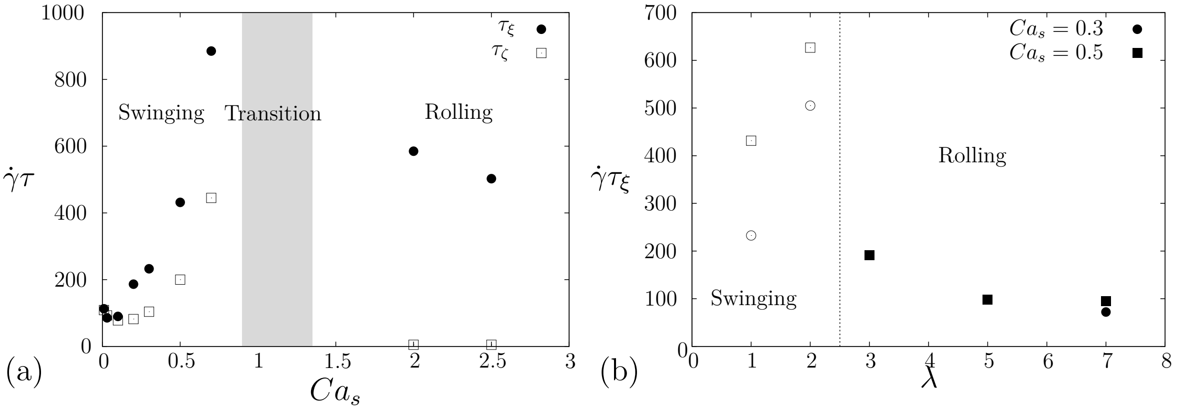

Figure 7.10: Convergence time for $\zeta(0) = \xi(0) = 45°$. (a) Effect of the capillary number for $\lambda = 1$; (b) Effect of the viscosity ratio for moderate Ca_s on the convergence time based on ξ (open symbols: swinging regime, full symbols: rolling regime). The grey zone and the vertical line represent the transition from in–plane to rolling motion.

need to attach a marker to the membrane and follow its motion over time. One must also be careful experimentally when an apparent steady inclination is obtained for ζ: it can be misleading, since the membrane will not be at equilibrium with the fluid until ξ has reached its final position.

7.5 Discussion and conclusion

The mechanical equilibrium configurations of an oblate capsule subjected to a simple shear flow have been determined numerically by initially positioning the capsule revolution axis off the shear plane and following the capsule dynamics. The study has been conducted for a capsule of aspect ratio $a/b = 0.5$ with a strain–hardening behavior of the Skalak law type (Skalak *et al.*, 1973) and different values of the viscosity contrast λ. We have been very careful to make sure that the equilibrium states were time–converged. We show that for the motion of the capsule to be unambiguously characterized, it is necessary to monitor two angles, which measure the general orientation $\zeta(t)$ of the deformed profile and the position $\xi(t)$ of the capsule initial apex.

Contrarily to previous results of the literature, we find that the equilibrium motion of an oblate capsule is independent of the initial position. For example at $\lambda = 1$ (an extensively studied case), the tumbling and the swinging regimes, obtained when the capsule axis is in the shear plane, are mechanically stable equilibrium configurations at low and moderate values of Ca_s ($Ca_s < 0.9$). When Ca_s increases, the capsule axis migrates away from the shear plane: a wobbling precession about the vorticity axis occurs for intermediate values of Ca_s until a stable rolling motion is reached where the capsule initial apex is located on the vorticity axis ($Ca_s \geq 1.5$). It is interesting to note that for a prolate capsule with $a/b = 2$ and $\lambda = 1$, the stable equilibrium states occur in reverse order as Ca_s increases: rolling, wobbling and swinging.

Cordasco & Bagchi (2013) also found that the capsule tends towards the shear plane, but they observe a kayaking (i.e. with oscillation about the shear plane) or a precession–to–kayaking motion, which depend on the initial orientation. This conclusion is due to too short computational times ($\dot{\gamma}t \leq 100$). Indeed, we also find such a kayaking motion (see Figure 7.4b), but it is transient and dies out with time. As for Wang *et al.* (2013), they find different motion modes which depend on the initial orientation. This may be due to small inertia effects, as the Reynolds number is small but finite in their study, whereas it is exactly zero in ours. Furthermore, they only considered moderate values of Ca_s and thus missed the rolling motion.

The new results provide detailed information on the influence of the internal–to-external viscosity ratio on the mechanical equilibrium configurations. We find that, for moderate value ($\lambda < 4$) the internal viscosity limits the range of Ca_s for which a swinging motion is possible. This can be easily understood, as high internal viscosity leads to high viscous energy dissipation during membrane rotation. In fact for large enough viscosity ($\lambda \geq 5$), the only in–plane motion is the quasi–solid tumbling motion. The other effect of large internal viscosity is to shift to low Ca_s values the transition from in–plane to rolling motion. A large internal viscosity leads to a significant tension jump across the interface and thus to membrane buckling, as reported by Foessel *et al.* (2011) and Yazdani & Bagchi (2013). The capsule deformability thus has a great influence on the mechanical equilibrium configuration, which depends on the fluid–structure interactions.

Dupire *et al.* (2012) have conducted an extensive study of the dynamics of human red blood cells in simple shear flow. In particular, they find that red blood cells converge towards a rolling regime when they flow in a Dextran solution ($\mu = 7.15$ mPa.s) under a shear rate between 10 s^{-1} and 15 s^{-1}. The characteristic length for a red blood cell is $\ell \sim 2.8\ \mu$m, based on a cell volume of order 100 μm^3 (Klöppel, 2012). The value of shear elastic modulus G_s depends on the constitutive law. Hochmuth & Waught (1987) estimated $G_s \simeq 4 - 5\ \mu$N/m for a strain–hardening law, such as the Skalak law. Using $G_s = 4\ \mu$N/m, the capillary number that corresponds to the rolling motion is then $Ca_s = 0.05 \sim 0.075$ at $\lambda \simeq 1$. This value is about $20 - 30$ times smaller than the one we predict for the on-start of rolling at $\lambda = 1$. However, a RBC has a significant membrane viscosity of order $\mu_s \sim 1 \times 10^{-7}$ Pa.s.m, leading to a dimensionless surface viscosity parameter $\eta = \mu_s/(\mu\ell) \sim 5$. The membrane viscosity effects add to those of the internal viscosity (Diaz *et al.*, 2001), so this may explain why the RBC rolls at low values of Ca_s.

Dupire *et al.* (2012) have also highlighted the influence of the membrane deformability on the stable equilibrium configuration. They observed that when the red blood cell membrane is stiffened, the cell no longer tends towards the rolling motion but towards the tumbling motion. This is consistent with the present results, since stiffening the cell membrane corresponds to increasing G_s and thus decreasing Ca_s.

We have also shown that a capsule initially placed off the shear plane takes a finite time to reach its stable equilibrium configuration depending on its initial orientation, flow strength and viscosity ratio. For a medium displacement from the shear plane ($\zeta(0) = 45°$), the non-dimensional convergence time varies between 50 and 400 at $\lambda = 1$ and $Ca_s \leq 0.5$. Consequently, it can sometimes be difficult to observe numerically or experimentally the mechanical equilibrium configuration. For example, for $\lambda = 1$ and $\dot{\gamma} = 1s^{-1}$ (respectively $10s^{-1}$), we find that a cell initially oriented at $\zeta(0) = 45°$ takes about 80 s (resp. 8 s) to reach tumbling (Figure 7.4a), 150 s (resp. 15 s) for swinging (Figure 7.4b) and 600 s (resp. 60 s) for rolling (Figure 7.6). As the typical window time to experimentally observe capsules or red blood cells is inferior to 1 minute, one must be careful to check that equilibrium conditions have indeed been reached.

7.6 Additional results: influence of the aspect ratio on the capsule dynamics

In this section, we summarize additional results obtained on the mechanical equilibrium configurations of prolate and oblate capsules in shear flow. We consider only the case of a capsule with a membrane devoid of bending resistance, which follows the Skalak law ($C = 1$). The results are presented in the form of phase diagrams as a function of the capillary number Ca_s and aspect ratio a/b. Firstly, we analyze the influence of the aspect ratio and viscosity ratio on the capsule regime, when the revolution axis is initially positioned in the shear plane. We then investigate the influence of the aspect ratio on the stable equilibrium configurations, when the revolution axis is initially off the shear plane at $\lambda = 1$.

7.6.1 Motions observed when $\zeta_0 = 90°$

The influence of the viscosity ratio and aspect ratio on the dynamics of an ellipsoidal capsule is presented in Figure 7.11 for a capsule having its revolution axis in the shear plane. The results are shown as a function of the capillary number Ca_s for three viscosity ratios $\lambda = 1, 0.5$ and 5. In each case, we recover the tumbling motion at low Ca_s and the swinging motion at high Ca_s (cf Ramanujan & Pozrikidis (1998), Sui *et al.* (2008) and Walter *et al.* (2011)). The viscosity ratio does not change qualitatively the capsule motion but has an influence on the value of the capillary number that corresponds to the transition between tumbling and swinging.

To define the transition between tumbling and swinging, we use the criterion introduced by Walter *et al.* (2011): the region of transition is characterized by a Taylor parameter

$$D_{12} = \frac{L_1 - L_2}{L_1 + L_2} < 0.05 \tag{7.9}$$

To unify the results, we denote L_1 and L_2 the lengths of the principle axes of the ellipsoid of inertia, which are located in the shear plane. L_1 and L_2 are chosen such as $L_1 \leq L_2$.

For a spherical capsule ($a/b = 1$), it is difficult visually to differentiate a tumbling motion and a tank–treading motion. In order to represent the transition between these two regimes, we use the relation introduced by Barthès-Biesel & Rallison (1981)

$$D_{12} = \frac{25}{12} Ca_s + \mathcal{O}(Ca_s^2). \tag{7.10}$$

and look for the value of D_{12} such as the Eq. (7.9) is satisfied.

For $\lambda = 0.5, 1$ and 5, the tumbling–to–swinging transition appears at higher Ca_s for prolate capsules ($a/b > 1$) than for oblate capsule since a much higher energy is necessary for an prolate capsule to reach the shape for which $D_{12} \approx 0$ (Walter *et al.*, 2011). It also explains why the transition has a "V" shape. In fact, the further the capsule shape departs from the sphere, the more difficult it is to deform its cross–section in the shear plane to have $D_{12} \approx 0$: more energy is thus needed.

Furthermore, the values of Ca_s, for which the tumbling–to–swinging transition appears, depends on the viscosity ratio. To determine the influence of the viscosity ratio, Figure 7.12 represents a schematic view of the transition found in Figure 7.11. The decrease of the viscosity ratio to $\lambda = 0.5$ does not change significantly the transition: it appears approximately at the same values of Ca_s (Figures 7.11a-b and 7.12). Now, if we increase the viscosity ratio λ to 5, the transition appears at higher Ca_s than at $\lambda = 1$ since more energy is needed to deform the capsule. The tumbling is thus stable on a larger range of Ca_s.

7.6.2 Stable equilibrium configurations

Figure 7.13 shows the influence of the capillary number Ca_s and aspect ratio a/b on the stable equilibrium configurations of ellipsoidal capsules initially positioned off the shear plane at $\lambda = 1$. Figure 7.13 shows that swinging and rolling are the two main regimes, which are observed in the range of values of Ca_s that was studied. We show that an oblate capsule adopts the tumbling motion at equilibrium at very low Ca_s ($Ca_s \approx 10^{-2}$), similarly

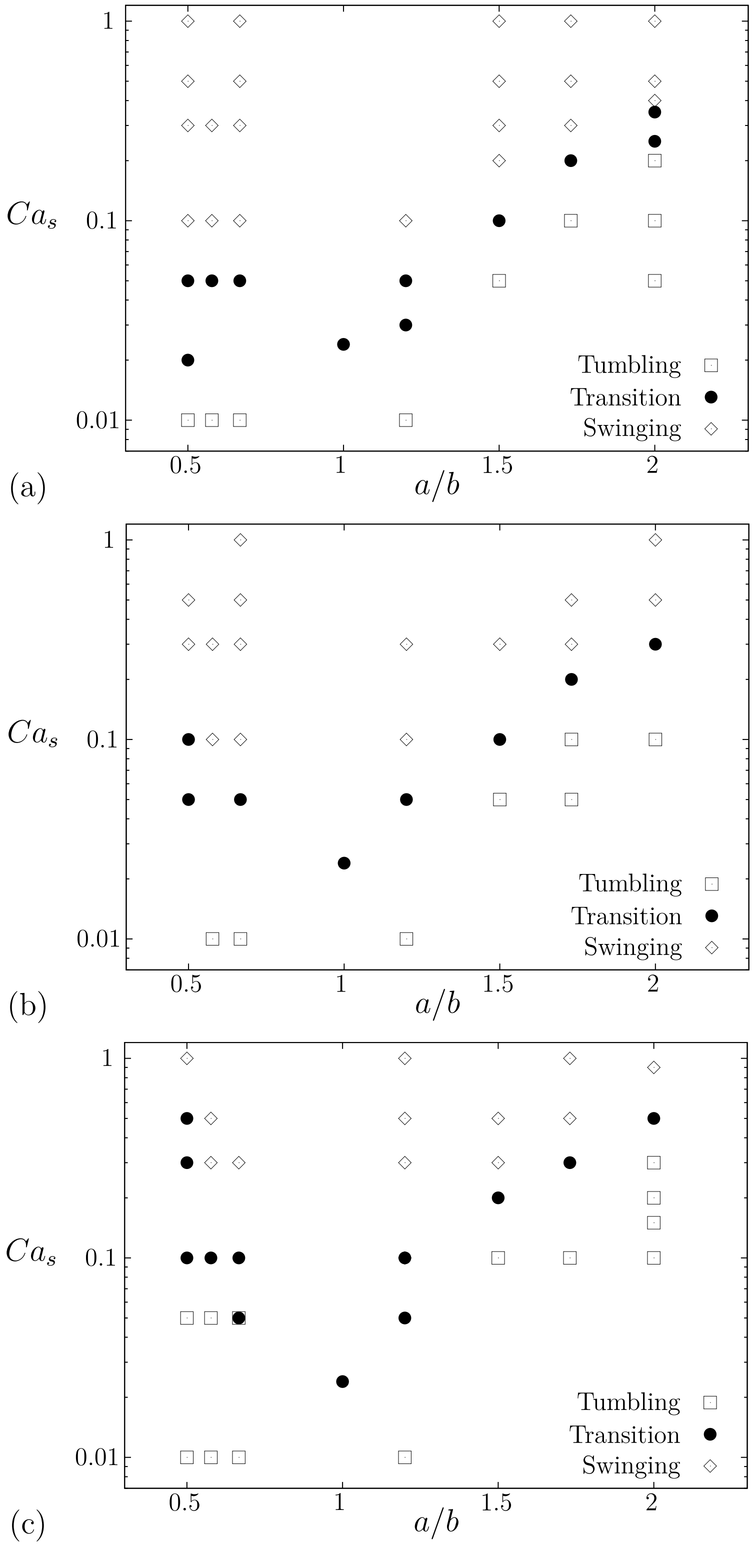

Figure 7.11: Ellipsoidal capsule with its revolution in the shear plane: phase diagram as a function of the aspect ratio a/b and the surface capillary number Ca_s for a viscosity ratio (*a*) $\lambda = 1$, (*b*) 0.5 and (*c*) 5.

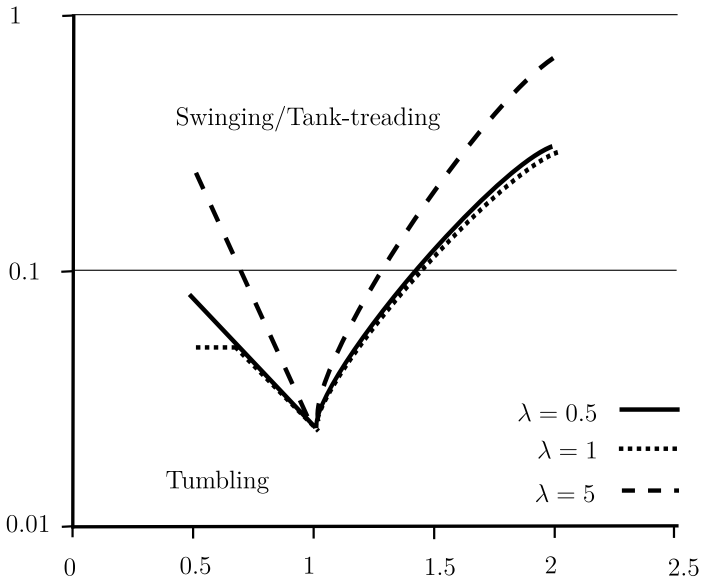

Figure 7.12: Ellipsoidal capsule with its revolution in the shear plane: schematic view of the transition tumbling/swinging for three viscosity ratios λ.

to Wang *et al.* (2013), but they found it at even lower values of Ca_s ($Ca_s \approx 5 \times 10^{-4}$).

It is interesting to note that the swinging and rolling regimes are reversed when Ca_s increases: an oblate capsule experiences a transition from swinging to rolling motion, which is the opposite for a prolate capsule.

Figure 7.13 also shows that the capillary number at the rolling–to–swinging transition (respectively swinging–to–rolling) increases when the aspect ratio increases (respectively decreases). As the transition is governed by the level of deformation, more energy is required to reach it, when the capsule is ellipsoidal with a large length difference between the revolution axis and the two orthogonal axes.

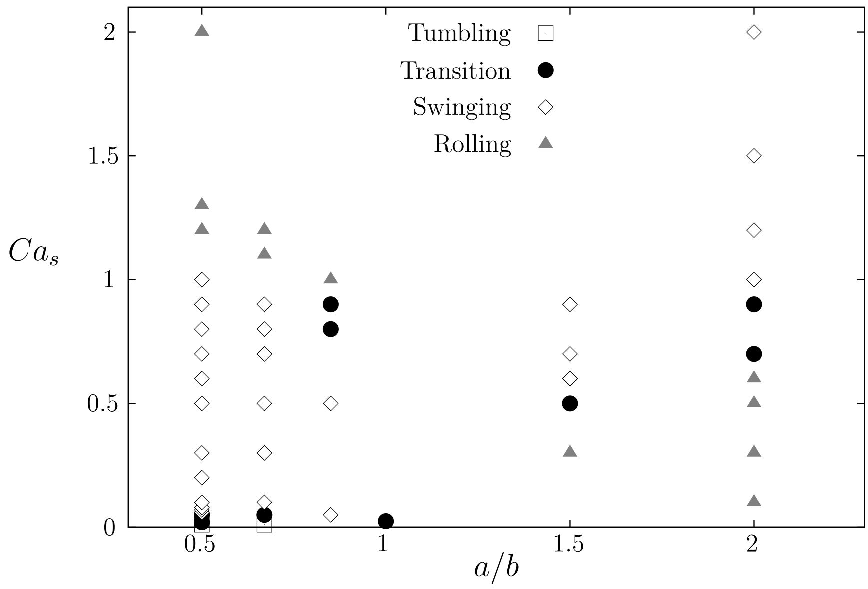

Figure 7.13: Stable equilibrium configurations for an ellipsoidal capsule initially off the shear plane: influence of the capillary number Ca_s and the aspect ratio a/b at $\lambda = 1$.

Chapter 8

Conclusions and perspectives

8.1 Conclusions

For the first time, we have enriched the numerical method developed by Walter *et al.* (2010) with a shell finite element method in order to study the influence of a small wall thickness on the capsule deformation. The fluid–structure problem of a capsule in an external flow is solved by coupling a shell finite element method for the capsule deformation with a boundary integral method for the internal and external flows. Using a shear–membrane–bending model, we implement, for the first time, a hyperelastic constitutive law (strain–hardening or strain–softening) for the membrane effects combined with the generalized Hooke's law for the bending effects to model the thin capsule wall behavior. Thanks to shell finite elements based on the Mixed Interpolation Tensorial Components technique, the numerical method is stable and free of locking, even when small values of wall thickness are considered.

The influence of a small value of bending resistance on the dynamics of an initially spherical capsule subjected to a simple shear flow or a planar hyperbolic flow is studied using this method for various constitutive laws. We show that, in this case, the main deformation mode is the stretching of the mid–surface. Membrane models are thus adequate to predict the elastic behavior and the deformation of spherical capsules subjected to a simple shear flow or a planar hyperbolic flow. However, when a capsule is not subjected to a shear flow such as in the case of a parabolic flow, bending resistance can reduce the capsule deformation compared to the one obtained with a membrane model.

Furthermore, if we are interested in the post–buckling behavior, a shell model is necessary since the wall bending resistance plays a role locally in the regions where buckling occurs. Its influence is studied in the low flow strength regime, for which wrinkling of the wall is observed to persist at steady state. We show that the wrinkle wavelength only depends on the bending number, which compares the relative importance of bending and shearing, and we provide the correlation law. These results on the dynamics of a capsule with bending resistance are interesting as they enable to determine values of bending resistance and shear modulus from experiments on capsules in a simple shear flow or a planar hyperbolic flow at low flow strength.

As the dynamics of a spherical capsule is different from the one of an ellipsoidal capsule, we have determined, for the first time, the stable equilibrium configurations of a prolate capsule subjected to a simple shear flow, using a membrane model. The stable equilibrium configurations of an oblate capsule have also been determined. We show that the stable equilibrium configurations are independent of the initial capsule orientation (if the capsule is not already in a equilibrium configuration) but depend on the surface capillary number, the viscosity ratio and the aspect ratio. We show that the tumbling and swinging regime, which were previously observed when the capsule revolution axis is initially positioned in the shear plane, do not correspond necessary to a stable equilibrium configuration. According to the capsule aspect ratio and the surface capillary number, we highlight that at equilibrium, the capsule converges towards the configuration observed when the capsule revolution axis is initially aligned with the vorticity axis. The capsule assumes also a rolling motion. In particularly, we show that when the surface capillary number increases, the stable equilibrium configurations are the reverse for an oblate capsule as compared to the ones of a prolate capsule. These results allow us to determine the time required for an oblate capsule initially placed off the shear plane to reach its stable equilibrium state. Such information is needed when setting up experiments to observe the behavior of oblate capsules such as red blood cells or for numerical modelers to choose the computational time adequately.

8.2 Perspectives

In this work, we have considered separately the effects on capsule dynamics of bending resistance and of non-sphericity. In the future, the combination of these effects could be studied. It will be interesting to continue the present research at the following aspects:

- **Dynamics of ellipsoidal capsules with bending resistance in shear flow.** We observe that an ellipsoidal capsule with a membrane devoid of bending resistance in shear flow is sometimes subjected to compressive tensions and that wrinkles appear. It would be interesting to study the influence of the bending resistance on the stable equilibrium configurations that we have determined with the membrane model. However, the use of the shell model might increase the convergence time. Some first simulations have shown a more complex dynamics than the one observed with the membrane model.

- **Dynamics of capsules with bending resistance flowing in a channel.** When an artificial capsule is deformed in a channel, the wall undergoes compressive tensions and wrinkles appear (Figure 8.1a). The localization of wrinkle formation can be predicted using the adapted membrane BI–FE method developed by Hu *et al.*

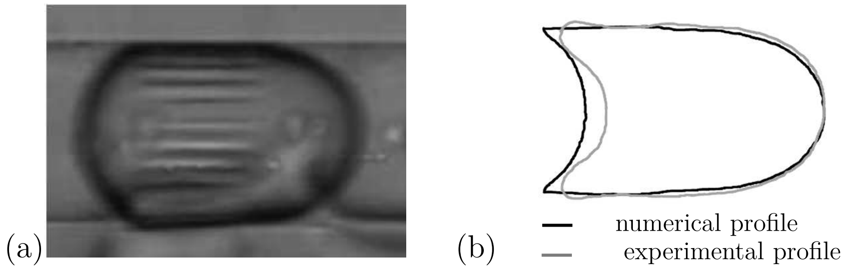

Figure 8.1: Capsule flowing in a channel: (*a*) wrinkle formation in a cylindrical channel (Chu, 2011), (*b*) comparison of profiles between experiments and numerical results for a capsule flowing in a square channel (UMR CNRS 7338).

(2012). The shell model could be used to study the post–buckling and in particular to determine the relation between wrinkle wavelength and wall thickness in a channel. Knowing this constitutive law, we will be able to determine the wall thickness. The wall bending will be found from the value of the wall thickness and the surface shear modulus will be deduced using the inverse analysis introduced by Hu *et al.* (2013) and explained in the section 1.3.3. This method is based on the comparison between experimental and numerical profiles of capsules flowing in a microfluidic channel to deduce the membrane mechanical properties of a population of artificial capsules. However, Figure 8.1b shows large differences between the experimental profile and the best matching numerical profile. In such case, the method fails to provide the capsule mechanical properties. This might be due to the fact that capsule shape cannot be correctly computed with a model devoid of bending resistance. In order to reduce the computational time, it will be interesting to first study the influence of the bending resistance on a capsule subjected to an unbounded parabolic flow. Some differences between the shell and membrane models might be observed since the stretching of the mid–surface is not the main deformation mode in such flow.

However, long computational times are already necessary to reach a steady state in these two cases when the wall bending resistance is neglected. The use of a thin shell model will increase conputational times. At this time, it seems difficult to carry out systematic studies with the shell model, as we have done with the membrane model. Such simulations are very expensive in time. To reduce computational times, it will be interesting to parallelize the numerical algorithm.

- **Experimental study on the dynamics of ellipsoidal capsule in shear flow.** Even if ellipsoidal capsules have interesting properties of mass transfer, there is no technique nowadays to produce ellipsoidal capsules with a wall–controlled given aspect ratio. If we are able to produce such capsule, it will be interesting to subject them to a simple shear flow, to compare experimental observations with the numerical results obtained in this thesis.

- **Dynamics of capsule with membrane viscosity.** Red blood cells have a significant membrane viscosity of order 1×10^{-7}. The differences between the numerical results and the experimental observations may be explained by the combined effect of the membrane viscosity and the internal viscosity. In order to identify the importance of the membrane viscosity, it will be interesting to take into account the membrane viscosity in the membrane model and carried out a study on its effect on the capsule dynamics.

Appendix A

Determination of the stability criterion

A.1 Thin shell model

The discrete solid problem (Eq. 3.18a,b) can be written under matrix form

$$\begin{bmatrix} K_{mm} & K_{mb} \\ K_{mb}^T & K_{bb} \end{bmatrix} \begin{bmatrix} u_s \\ \theta \end{bmatrix} = \begin{bmatrix} R \\ 0 \end{bmatrix} \tag{A.1}$$

where K_{mm}, K_{mb} and K_{bb} represent the membrane, membrane-bending and bending stiffness matrices respectively. R is similar to a reaction force. The two following equalities are deduced from the previous system

$$\begin{aligned} \{R\} &= [K_{mm}]\,\{u_s\} + [K_{mb}]\,\{\theta\} \\ \{\theta\} &= -[K_{mb}]^T\,[K_{bb}]^{-1} \end{aligned} \tag{A.2}$$

Thus,

$$\{R\} = \Big([K_{mm}] - [K_{mb}]\,[K_{bb}^{-1}]\,[K_{mb}]^T\Big)\ \{u_s\}\,. \tag{A.3}$$

As $\|[K_{mm}] - [K_{mb}]\,[K_{bb}]^{-1}\,[K_{mb}]^T\| \le [K_{mm}]$, the stability criterion defined previously by Walter *et al.* (2010) when the capsule wall is devoid of bending resistance, remains available: the introduction of the bending improves the numerical stability.

A.2 Membrane

When the capsule wall is modeled as a two–dimensional surface, the discrete form of the equilibrium equation (2.19) is

$$[K_s]\,\{u_s\} + [M_s]^T\{q\} = 0 \tag{A.4}$$

where $[K_s]$ and $[M_s]$ are the stiffness and mass matrix relative to the solid. All quantities relative to the solid and the fluid will be noted with the subscript "S" and "F" respectively.

The kinematical assumption (Eq. 2.59) is written in the discrete form

$$[M_s]\;\{\dot{u}_s\} = [M_f]\;\{\dot{u}_f\} \tag{A.5}$$

where the notation $\dot{u}$ represents the time derivative of the vector $\{u\}$.

When the internal and external fluids have the same viscosity ($\lambda = 1$), the expression of the velocity (Eq. 2.74) deduced from the boundary integral formulation can be written

$$[M_f]\;\{\dot{u}_f\} = [K_f]^{-1}\{q\} \tag{A.6}$$

Using the equality (A.4, A.5), the equation (A.6) becomes

$$\begin{aligned} \{q\} &= [K_f]\,[M_f]\;\{\dot{u}_f\} \\ &= [K_f]\,[M_s]\;\{\dot{u}_s\} \end{aligned} \tag{A.7}$$

By substituting the expression of $\{q\}$ in the equation (A.4), we find

$$[K_s]\,\{u_s\} = -\left([M_s]^T[K_f]\,[M_s]\right)\;\{\dot{u}_s\}\,. \tag{A.8}$$

This expression can be rewritten as

$$\frac{\{u_s^{n+1}\} - \{u_s^n\}}{\{u_s^{n+1}\}} = \frac{[K_s]\Delta t}{[M_s]^T[K_f]\,[M_s]} \tag{A.9}$$

to find an expression of the time step Δt.

We can then estimate the approximative size of the mass and stiffness matrices $[M_s]$, $[K_f]$ and $[K_f]$

$$\begin{aligned} [M_s] &\sim 1 \\ [K_f] &\sim \frac{\mu}{\Delta x} \\ [K_s] &\sim \frac{G_s}{(\Delta x)^2}. \end{aligned} \tag{A.10}$$

Thus,

$$\frac{[K_s]\Delta t}{[M_s]^T[K_f]\,[M_s]} \sim \frac{G_s}{(\Delta x)^2} \times \frac{\Delta x}{\mu} \times \Delta t = \frac{\dot{\gamma}\ell}{\Delta x\, Ca_s}\Delta t \tag{A.11}$$

Finally, the stability condition of the membrane numerical algorithm verifies

$$\dot{\gamma}\Delta t < \mathcal{O}\left(\frac{\Delta x\, Ca_s}{\ell}\right). \tag{A.12}$$

Bibliography

Abkarian, M., Faivre, M. & Viallat, A. 2007 Swinging of red blood cells under shear flow. *Phys. Rev. Lett.* **98**, 188302.

Abkarian, M., Lartigue, C. & Viallat, A. 2001 Motion of phospholipidic vesicles along an inclined plane: sliding and rolling. *Phys. Rev. E* **63**, 041906.

Abkarian, M. & Viallat, A. 2008 Vesicles and red blood cells in shear flow. *Soft Matter* **4**, 653 – 657.

Akchiche, M. 1987 Étude expérimentale du mouvement et de la déformation d'une capsule sous l'effet de l'écoulement d'un fluide visqueux. Application au globule rouge. PhD thesis, Université de Technologie de Compiègne.

Alexopoulos, L. G., Haider, M. A., Vail, T. P. & Guilak, F. 2003 Alterations in the mechanical properties of the human chondrocyte pericellular matrix with osteoarthritis. *J. Biochem. Eng.* **125**, 323 – 333.

Andry, M.-C., Edwards-Lévy, F. & Lévy, M.-C. 1996 Free amino group content of serum albumin microcapsules. III. A study at low pH values. *Int. J. Pharm.* **128**, 197 – 202.

Anna, S. L., Bontoux, N. & Stone, H. A. 2003 Formation of dispersions using 'flow focusing' in microchannels. *Appl. Phys. Lett.* **82**, 364 – 366.

Aoki, T., Ohashi, T., Matsumoto, T. & Sato, M. 1997 The pipette aspiration applied to the local stiffness measurement of soft tissues. *Annu. Biomed. Eng.* **25**, 581 – 587.

Bagchi, P. 2007 Mesoscale simulation of blood flow in small vessels. *Biophys. J .* **92**, 1858 – 1877.

Bagchi, P. & Kalluri, R. M. 2009 Dynamics of nonspherical capsules in shear flow. *Phys. Rev. E* **80** (1), 016307.

Barthès-Biesel, D. 1980 Motion of a spherical microcapsule freely suspended in a linear shear flow. *J. Fluid Mech.* **100**, 831 – 853.

Barthès-Biesel, D. 1991 Role of interfacial properties on the motion and deformation of capsules in shear flow. *Physica A* **172**, 103 – 124.

Barthès-Biesel, D. 2011 Modeling the motion of capsules in flow. *Curr. Opin. Colloid In.* **16**, 3 – 12.

Barthès-Biesel, D., Diaz, A. & Dhenin, E. 2002 Effect of constitutive laws for two dimensional membranes on flow-induced capsule deformation **460**, 211 – 222.

Barthès-Biesel, D. & Rallison, J. M. 1981 The time–dependent deformation of a capsule freely suspended in a linear shear flow. *J. Fluid Mech.* **113**, 251 – 267.

Barthès-Biesel, D., Walter, J. & Salsac, A.-V. 2010 *Computational hydrodynamics of capsules and biological cells*, chap. Flow-induced deformation of artificial capsules, pp. 35–70. Taylor & Francis.

Bathe, K. J. & Dvorkin, E. N. 1986 A formulation of general shell elements – the use of mixed interpolation of tensorial components. *Int. J. Num. Meth. Engng* **22**, 697 – 722.

Batoz, J.-L. & Dhatt, G. 1992 *Modélisation des structures par éléments finis: Coques*. Hermès.

Bhujbal, S. V., de Vos, P. & Niclou, S. P. 2014 Drug and cell encapsulation: Alternative delivery options for the treatment of malignant brain tumors. *Adv. Drug Deliv. Rev.* **67 – 68**, 142 – 153.

Bonnet, M., Frangi, A. & Rey, C. 2014 *The finite element method in solid mechanics*. P. Roncoroni.

Bouchemal, K., Briançon, S., Perrier, E., Fessi, H., Bonnet, I. & Zydowicz, N. 2004 Synthesis and characterization of polyurethane and poly(ether urethane) nanocapsules using a new technique of interfacial polycondensation combined to spontaneous emulsification. *Int. J. Pharm.* **269**, 89 – 100.

Bucalem, M. L. & Bathe, K. J. 1993 Higher–order MITC general shell elements. *Int. J. Num. Meth. Engng* **36**, 3729 – 3754.

Carin, M., Barthès-Biesel, D., Edwards-Lévy, F., Postel, C. & Andrei, D. C. 2003 Compression of biocompatible liquid-filled HSA–alginate capsules: Determination of the membrane mechanical properties. *Biotechnol. Bioeng.* **82**, 207 – 212.

Cerda, E. & Mahadevan, L. 2003 Geometry and physics of wrinkling. *Phys. Rev. Lett.* **90** (7), 074302.

Chamoret, D. 2002 Modélisation du contact: nouvelles approches numériques. PhD thesis, Ecole Centrale de Lyon.

Chang, K. S. & Olbricht, W. L. 1993*a* Experimental studies of the deformation and breakup of a synthetic capsule in extensional flow. *J. Fluid Mech.* **250**, 587 – 608.

Chang, K. S. & Olbricht, W. L. 1993*b* Experimental studies of the deformation and breakup of a synthetic capsule in steady and unsteady simple shear flow. *J. Fluid Mech.* **250**, 609 – 633.

Chang, T. M. S. 2003 Future generations of red blood cell substitutes. *J. Intern. Med.* **253**, 527 – 535.

Chang, T. M. S., Macintosh, F. C. & Mason, S. G. 1966 Semipermeable aqueous microcapsules: I. Preparation and properties. *Can. J. Physiol. Pharm.* **44**, 115 – 128.

Chapelle, D. & Bathe, K. J. 2011 *The Finite Element Analysis of Shells – Fundamentals (Computational Fluid and Solid Mechanics). Second Edition.*

Chu, T. X. 2011 Fabrication et caractérisation de populations de microcapsules avec une technique microfluidique. PhD thesis, Université de Technologie de Compiègne.

Chu, T. X., Salsac, A.-V., Barthès-Biesel, D., Griscom, L., Edwards-Lévy, F. & Leclerc, E. 2013 Fabrication and in-situ characterization of microcapsules in a microfluidic system. *Microfluid Nanofluid* **14**, 309 – 317.

Chu, T. X., Salsac, A.-V., Leclerc, E., Barthès-Biesel, D., Wurtz, H. & Edwards-Lévy, F. 2011 Comparison between measurements of elasticity and free amino group content of ovalbumin microcapsule membranes: Discrimination of the cross–linking degree. *J. Colloid Interf. Sci.* **355** (1), 81 – 88.

Clayton, H. A., James, R. F. L. & London, N. J. M. 1993 Inslet microencapsulation: a review. *Acta Diabetol.* **30**, 181 – 189.

Cordasco, D. & Bagchi, P. 2013 Orbital drift of capsules and red blood cells in shear flow. *Phys. Fluids* **25**, 091902.

Coupier, G., Kaoui, B., Podgorski, T. & Misbah, C. 2008 Noninertial lateral migration of vesicles in bounded Poiseuille flow. *Phys. Fluids* **20**, 111702.

de Loubens, C., Deschamps, J., Georgelin, M., Charrier, A., Edward-Lévy, F. & Leonetti, M. 2014 Mechanical characterization of cross–linked serum albumin microcapsules. *Soft Matter* **10**, 4561 – 4568.

Diaz, A., Barthès-Biesel, D. & Pelekasis, N. 2001 Effect of membrane viscosity on the dynamic response of an axisymmetric capsule. *Phys. Fluids* **13** (12), 3835 – 3838.

Diaz, A., Pelekasis, N. A. & Barthès-Biesel, D. 2000 Transient response of a capsule subjected to varying flow conditions : effect of internal fluid viscosity and membrane elasticity. *Phys. Fluids* **12**, 948– 957.

Dimitrakopoulos, P. 2014 Effects of membrane hardness and scaling analysis for capsules in planar extensional flows. *J. Fluid Mech.* **745**, 487 – 508.

Doddi, S. K. & Bagchi, P. 2008*a* Effect of inertia on the hydrodynamic interaction between two liquid capsules in simple shear flow. *Int. J. Multiphase Flow* **34**, 375 – 392.

Doddi, S. K. & Bagchi, P. 2008*b* Lateral migration of a capsule in a plane Poiseuille flow in a channel. *Int. J. Multiphase Flow* **34** (10), 966 – 986.

Dodson, W. R. & Dimitrakopoulos, P. 2008 Spindles, cusps, and bifurcation for capsules in Stokes flow. *Phys. Rev. Lett.* **101** (20), 208102.

Dodson, W. R. & Dimitrakopoulos, P. 2014 Properties of the spindle–to–cusp transition in extensional capsule dynamics. *EPL* **106**, 48003.

Dupire, J., Socol, M. & Viallat, A. 2012 Full dynamics of a red blood cell in shear flow. *Proc. Natl. Acad. Sci. USA* **109 (51)**, 20808 – 20813.

Dupont, C., Salsac, A.-V. & Barthès-Biesel, D. 2013 Off–plane motion of a prolate capsule in shear flow. *J. Fluid Mech.* **721**, 180 – 198.

Dvorkin, E. N. & Bathe, K. J. 1984 A continuum mechanics based four–node shell element for general nonlinear analysis. *Eng. Comput.* **1**, 77 – 88.

Edwards-Lévy, F., Andry, M.-C. & Lévy, M.-C. 1993 Determination of free amino group content of serum albumin microcapsules using trinitrobenzenesulfonic acid: effect of variations in polycondensation pH. *Int. J. Pharm.* **96**, 85 – 90.

Edwards-Lévy, F., Andry, M.-C. & Lévy, M.-C. 1994 Determination of free amino group content of serum albumin microcapsules: II. effect of variations in reaction time and in terephthaloyl chloride concentration. *Int. J. Pharm.* **103** (3), 253 – 257.

Eggleton, C. D. & Popel, A. S. 1998 Large deformation of red blood cell ghosts in a simple shear flow. *Phys. Fluids* **10**, 1834 – 1845.

Evans, E. & Rawicz, W. 1990 Entropy–driven tension and bending elasticity in condensed–fluid membranes. *Phys. Rev. Lett.* **64**, 2094 – 2097.

Finken, R. & Seifert, U. 2006 Wrinkling of microcapsules in shear flow. *J. Phys.: Condens. Matter* **18** (15), L185 – L191.

Fischer, T. & Korzeniewski, R. 2013 Threshold shear stress for the transition between tumbling and tank-treading of red blood cells in shear flow: dependence on the viscosity of the suspending medium. *J. Fluid Mech.* **736**, 351 – 365.

Foessel, E., Walter, J., Salsac, A.-V. & Barthès-Biesel, D. 2011 Influence of internal viscosity on the large deformation and buckling of a spherical capsule in a simple shear flow. *J. Fluid Mech.* **672**, 477 – 486.

Furlow, B. 2009 Contrast-enhanced ultrasound. *Rad Tech.* **80**, 547S – 561S.

Ganán-Calvo, A. M. & Gordillo, J. M. 2001 Perfectly monodisperse microbubbling by capillary flow focusing. *Phys. Rev. Lett.* **87**, 2745011 – 2745014.

Garstecki, P., Fuerstman, M. J., Stonec, H. A. & Whitesides, G. M. 2006 Formation of droplets and bubbles in a microfluidic T–junction-scaling and mechanism of break–up. *Lab. Chip.* **6**, 437 – 446.

Gautier, A., Carpentier, B., Dufresne, M., Dinh, Q. Vu, Paulier, P. & Legallais, C. 2011 Impact of alginate type and bead diameter on mass transferts and the metabolic activities on encapsulated c3a cells in bioactificial liver applications. *Eur. Cell. Mater.* **21**, 94 – 106.

Ghirardi, P., Catenazzo, G., Mantero, O., Merotti, G. C. & Marzo, A. 1977 Bioavailability of digoxin in a new soluble pharmaceutical formulation in capsules. *J. Pharm. Sci.* **66**, 267 – 269.

Gimeno, M. 1996 An overview of the latest development of microencapsulation for agricultural products. *J. Environ. Sci. Heal. B* **31**, 407 – 420.

Hang, W.-X., Chang, C. B. & Sung, H. J. 2012 Three–dimensional simulation of elastic capsules in shear flow by the penalty immersed boundary method. *J. Comput. Phys.* **231**, 3340 – 3364.

Hay, K. L. & Bull, B. S. 2009 Statistical clues to postoperative blood loss: Moving averages applied to medical data. *Blood Cells Mol. Dis.* **43** (3), 250 – 255.

Heinrich, V. & Rawicz, W. 2005 Automated, high–resolution micropipet apsiration reveals new insight into the physical properties of fluid membranes. *Langmuir* **21**, 1962 – 1971.

Hochmuth, R. M. 2000 Micropipette aspiration of living cells (review). *J. Biomech.* **33**, 15 – 22.

Hochmuth, R. M. & Waught, R. E. 1987 Erythrocyte membrane elasticity and viscosity. *Annu. Rev. Physiol.* **49**, 209 – 219.

Hu, X.-Q., Salsac, A.-V. & Barthès-Biesel, D. 2012 Flow of a spherical capsule in a pore with circular or square cross–section. *J. Fluid Mech.* **705**, 176 – 194.

Hu, X.-Q., Sévénié, B., Salsac, A.-V., Leclerc, E. & Barthès-Biesel, D. 2013 Characterization of membrane properties of capsules flowing in a square–section microfluidic channel: effects of the membrane constitutive law. *Phys. Rev. E.* **87**, 063008.

Huang, K.-S., Liu, M.-K, Wu, C.-H, Yen, Y.-T. & Lin, Y.-C. 2007 Calcium alginate microcapsule generation on a microfluidic system fabricated using the optical disk process. *J. Micromech. Microeng.* **17**, 1428 – 1434.

Janssen, L. J. J. M. & Nijenhuis, K. Te 1992 Encapsulation by interfacial polycondensation. I. The capsule production and a model for wall growth. *J. Membr. Sci.* **65** (1), 59 – 68.

Jeffery, G. B. 1922 The motion of ellipsoidal particles immersed in a viscous fluid. *P. Roy. Soc. A – Math. Phy.* **102**, 161 – 179.

Kessler, S., Finken, R. & Seifert, U. 2008 Swinging and tumbling of elastic capsules in shear flow. *J. Fluid Mech.* **605**, 207 – 226.

Klöppel, T. 2012 A finite element model for the human red blood cell. PhD thesis, Technische Universität München.

Klöppel, T. & Wall, W. A. 2011 A novel two-layer, coupled finite element approach for modeling the nonlinear elastic and viscoelastic behavior of human erythrocytes. *Biomech. Model Mechanobiol.* **10**, 445 – 459.

Koleva, I. & Rehage, H. 2012 Deformation and orientation dynamics of polysiloxane microcapsules in linear shear flow. *Soft Matter* **8**, 3681 – 3693.

Kwok, R. & Evans, E. 1981 Thermoelasticity of large lecithin bilayer vesicles. *Biophys. J.* **35**, 657 – 632.

Lac, E. & Barthès-Biesel, D. 2005 Deformation of a capsule in simple shear flow: effect of membrane prestress. *Phys. Fluids* **17**, 0721051 – 0721058.

Lac, E., Barthès-Biesel, D., Pelakasis, A. & Tsamopoulos, J. 2004 Spherical capsules in three–dimensional unbounded Stokes flows: effect of the membrane constitutive law and onset of buckling. *J. Fluid Mech.* **516**, 303 – 334.

Ladyzhenskaya, O. A. 1969 *The mathematical theory of viscous incompressible flow*, 2nd edn. Gordon and Breach.

Lam, P. L. & Gambari, R. 2014 Advanced progress of microencapsulation technologies: In vivo and in vitro models for studing oral and transdermal drug deliveries. *J. Control. Release* **178**, 25 – 45.

Le, D. V. 2010 Effect of bending stiffness on the deformation of liquid capsule enclosed by thin shells in shear flow. *Phys. Rev. E* **82**, 016318.

Le, D. V. & Tan, Z. 2010 Large deformation of liquid capsules enclosed by thin shells immersed in the fluid. *J. Comput. Phys.* **229**, 4097 – 4116.

Le, D. V., White, J., Peraire, J., Lim, K. M. & Khoo, B. C. 2009 An implicit immersed boundary method for three–dimensional capsules. *J. Comput. Phys.* **228**, 8427 – 8445.

Le Tallec, P. 2009 *Modélisation et calcul des milieux continus.*.

Lee, P.-S. 2004 On triangular finite elements for general shell structures. PhD thesis, Massachusetts Institute of Technology.

Lee, P.-S. & Bathe, K.-J. 2004 Development of MITC isotropic triangular shell finite elements. *Comput. Struct.* **82** (11-12), 945 – 962.

Lefebvre, Y. & Barthès-Biesel, D. 2007 Motion of a capsule in a cylindrical tube: effect of membrane pre–stress. *J. Fluid Mech.* **589**, 157 – 181.

Lefebvre, Y., Leclerc, E., Barthès-Biesel, D., Walter, J. & Edwards-Lévy, F. 2008 Flow of artificial microcapsules in microfluidic channels: A method for determining the elastic properties of the membrane. *Phys. Fluids* **20**, 123102 – 123110.

Lévy, M.-C., Andry, M.-C., Lefebvre, S. & Manfait, M. 1995 Fourier transform infrared spectroscopic studies of cross–linked human serum albumin microcapsules. 3 Influence of terephthaloyl chloride concentration on spectra and correlation with microcapsule morphology and size. *J. Pharm. Sci.* **84** (2), 161 – 165.

Lévy, M.-C., Lefebvre, S., Andry, M.-C., Rahmouni, M. & Manfait, M. 1994 Fourier–transform infrared spectroscopic studies of cross–linked human serum albumin microcapsules. 2. Influence of reaction time on spectra and correlation with microcapsule morphology and size. *J. Pharm. Sci.* **83** (3), 419 – 422.

Lévy, M.-C., Lefèbvre, S., Rahmouni, M., Andry, M.-C. & Manfait, M. 1991 Fourier transform infrared spectroscopic studies of human serum albumin microcapsules prepared by interfacial cross–linking with terephthaloychloride: influence of polycondensation pH on spectra and relation with microcapsule morphology and size. *J. Pharm. Sci.* **80**, 578 – 585.

Li, S., Lewis, J. E., Stewart, N. M., Qian, L. & Boyter, H. 2008 Effect of finishing methods on washing durability of microencapsulated aroma finishing. *J. Text. I.* **99**, 177 – 183.

Li, X. & Sarkar, K. 2008 Front tracking simulation of deformation and buckling instability of a liquid capsule enclosed by an elastic membrane. *J. Comput. Phys.* **227**, 4998 – 5018.

Li, X. Z., Barthès-Biesel, D. & Helmy, A. 1988 Large deformations and burst of a capsule freely suspended in an elongational flow **187**, 179 – 196.

Liu, L., Yang, J.-P, Ju, X.-J., Xie, R., Yang, L., Liang, B. & Chu, L.-Y. 2009 Microfluidic preparation of monodisperse ethyl cellulose hollow microcapsules with non–toxic solvent. *J. Colloid Interf. Sci.* **336 (1)**, 100 – 106.

Liu, X., Gao, C., Shen, J. & Möhawald, H. 2005 Multilayer microcapsules as anti–cancer drug delivery vehicle: Deposition, sustained release, and in vivo bioactivity. *Macromol. Biosci.* **5**, 1209 – 1219.

Ma, G. & Su, Z.-G 2013 *Microspheres and Microcapsules in Biotechnology: Design, Preparation and Applications*. Pan Stanford Publishing.

Mohandas, N. & Gallagher, P. G. 2008 Red cell membrane: past, present and future. *Blood* **112 (10)**, 3939 – 3948.

Nazzaro, F., Orlando, P., Fratianni, F. & Coppola, R. 2012 Microencapsulation in food science and biotechnology. *Curr. Opin. Biotech.* **23**, 182 – 186.

Ocepek, B., Boh, B., Sumiga, B. & Tavcer, P. F. 2012 Printing of antimicrobial microcapsules on textiles. *Color. Technol.* **128 (2)**, 95 – 102.

Omori, T., Imai, Y., Yamaguchi, T. & Ishikawa, T. 2012 Reorientation of a non-spherical capsule in creeping shear flow. *PRL* **108**, 138102(5).

Orive, G., Santos, E., Pedraz, J. L. & Hernández, R. M. 2014 Application of cell encapsulation for controlled delivery of biological therapeutics. *Adv. Drug Deliv. Rev.* **67-68**, 3 – 14.

Pandey, R., Zahoor, A., Sharma, S. & Khuller, G. K. 2003 Nanoparticle encapsulated antitubercular drugs as a potential oral druf delivery system against murine tuberculosis. *Tuberculosis* **83**, 373 – 378.

Pariot, N., Edwards-Lévy, F., Andry, M.-C. & Lévy., M.-C. 2002 Cross–linked β-cyclodextrin microcapsules. II. Retarding effect on drug release through semi-permeable membranes. *Int. J. Pharm.* **232**, 175 – 181.

Peng, Z., Asaro, R. J. & Zhu, Q. 2011 Multiscale modelling of erythrocytes in stokes flow. *J. Fluid Mech.* **686**, 299 – 337.

Peskin, C.S. 2002 The immersed boundary method. *Acta Numer.* **11**, 479 – 517.

Pozrikidis, C. 1990 The axisymmetric deformation of a red blood cell in uniaxial straining Stokes flow. *J. Fluid Mech.* **216**, 231 – 254.

Pozrikidis, C. 1992 *Boundary Integral and Singularity Methods for Linearized Viscous Flow.* Cambridge Univiversity Press.

Pozrikidis, C. 1995 Finite deformation of liquid capsules enclosed by elastic membranes in simple shear flow. *J. Fluid Mech.* **297**, 123 – 152.

Pozrikidis, C. 2001 Effect of membrane bending stiffness on the deformation of capsules in simple shear flow. *J. Fluid Mech.* **440**, 269 – 291.

Rachik, M., Barthès-Biesel, D., Carin, M. & Edwards-Lévy, F. 2006 Identification of the elastic properties of an artificial capsule membrane with the compression test: Effect of thickness. *J. Colloid Interf. Sci.* **301**, 217 – 226.

Ramanujan, S. & Pozrikidis, C. 1998 Deformation of liquid capsules enclosed by elastic membranes in simple shear flow: Large deformations and the effect of capsule viscosity. *J. Fluid Mech.* **361**, 117 – 143.

Schneeweiss, I. & Rehage, H. 2005 Non–spherical capsules for the food industry. *Chem. Ing. Tech.* **77 (3)**, 236 – 239.

Secomb, T.W., Styp-Rekowska, B. & Pries, A. 2007 Two–dimensional simulation of red blood cell deformation and lateral migration in microvessels. *Annu. Biomed. Eng.* **35**, 755 – 765.

She, F. Y., Qi, D. M., nd J.Z. Shao, Z. J. Chen & Yang, L. 2012 Preparation of organic pigment microcapsules and its application in pigment printing of silk fabric. *Adv. Mat. Res.* **441**, 145 – 149.

Skalak, R., Tozeren, A., Zarda, R. P. & Chien, S. 1973 Strain energy function of red blood cell membranes. *Biophys. J .* **13**, 245 – 264.

Skotheim, J. M. & Secomb, T. W. 2007 Red blood cells and other nonspherical capsules in shear flow: Oscillatory dynamics and the tank–treading–to–tumbling transition. *Phys. Rev. Lett.* **98** (7), 078301.

Suarez, I. P. 2006 Robustesse des éléments finis triangulaires de coque. PhD thesis, Université Pierre et Marie Curie.

Sui, Y., Chen, X. B., Chew, Y. T., Roy, P. & Low, H. T. 2010 Numerical simulation of capsule deformation in simple shear flow. *Comput. Fluids* **39** (2), 242 – 250.

Sui, Y., Low, H. T., Chew, Y. T. & Roy, P. 2008 Tank–treading, swinging, and tumbling of liquid–filled elastic capsules in shear flow. *Phys. Rev. E* **77** (1), 016310.

T. Vandamme, D. Poncelet & Subra-Paternault, P. 2007 *Microencapsulation.* Des sciences aux technologies.

Taylor, G. I. 1934 The formation of emulsions in definable fields of flow. *Proc. R. Soc. Lond. A* **146**, 501 – 523.

Thorsen, T., Roberts, R. W., Arnold, F. H. & Quake, S. R. 2001 Dynamic pattern formation in a vesicle–generating microfluidic device. *Phys. Rev. Lett.* **86**, 4163 – 4166.

Trimarchi, D. 2012 Analysis of downwind sail structures using non-linear shell finite elements: wrinkle development and flui interaction effects. PhD thesis, University of Southampton.

TRIMARCHI, D., VIDRASCU, M., TAUNTON, D., TURNOCK, S. R. & CHAPELLE, D. 2013 Wrinkle development analysis in thin sail-like structures using mitc shell finite elements. *Finite Elem Anal Des* **64**, 48 – 64.

VALOT, P., BABA, M., NEDELEC, J.-M. & SINTES-ZYDOWICZ, N. 2009 Effects of process parameters on the properties of biocompatible Ibuprofen–loaded microcapsule. *Int. J. Pharm.* **369**, 53 – 63.

WALTER, A., REHAGE, H. & LEONHARD, H. 2000 Shear–induced deformation of polyamid microcapsules. *Colloid Polymer Sci.* **278**, 169 – 175.

WALTER, A., REHAGE, H. & LEONHARD, H. 2001 Shear induced deformation of microcapsules: shape oscillations and membrane folding. *Colloid Surface A* **183 – 185**, 123 – 132.

WALTER, J. 2009 Couplage intégrales de frontières – éléments finis: application aux capsules sphériques et ellipsoïdales en écoulement. PhD thesis, Université de Technologie de Compiègne.

WALTER, J., SALSAC, A.-V. & BARTHÈS-BIESEL, D. 2011 Ellipsoidal capsules in simple shear flow: prolate versus oblate initial shapes. *J. Fluid Mech.* **676**, 318 – 347.

WALTER, J., SALSAC, A.-V., BARTHÈS-BIESEL, D. & LE TALLEC, P. 2010 Coupling of finite element and boundary integral methods for a capsule in a Stokes flow. *Int. J. Num. Meth. Engng* **83**, 829 – 850.

WANG, Z., SUI, Y., SPELT, P. D. M. & WANG, W. 2013 Three–dimensional dynamics of oblate and prolate capsules in shear flow. *Phys. Rev. E* **88**, 053021.

XIANG, Z. Y., LU, Y. C., ZOU, Y., GONG, X. C. & LUO, G. S. 2008 Preparation of microcapsules containing ionic liquids with a new solvent extraction system. *React. Funct. Polym.* **68 (8)**, 1260 – 1265.

YANG, Z., PENG, Z., LI, J., LI, S., KONG, L., LI, P. & WANG, Q. 2014 Development and evaluation of novel flavour microcapsules containing vanilla oil using complex coacervation approach. *Food Chem.* **145**, 272 – 277.

YAZDANI, A. & BAGCHI, P. 2013 Influence of membrane viscosity on capsule dynamics in shear flow. *J. Fluid Mech.* **718**, 569 – 595.

YEH, C.-H., ZHAO, Q., LEE, S.-J. & LIN, Y.-C 2009 Using a T–junction microdluidic chip for monodisperse calcium alginate mircoparticles and encapsulation of nanoparticles. *Sensor. Actuat. A–Phys.* **151**, 231 – 236.

Zhang, H., Tumarkin, E., Peerani, R., Nie, Z., Sullan, R.M.A., Walker, G.C. & Kumacheva, E. 2006 Microfluidic production of biopolymer microcapsules with controlled morphology. *J. Am. Chem. Soc.* **128**, 12205 – 12210.

Zhang, L. & Salsac, A.-V. 2012 Can sonication enhance release from liquid–core capsules with a hydrogel membrane? *J. Colloid Interf. Sci.* **368**, 648 – 654.

Zheng, J., Yie, X., Dai, Z., ans S. Liu, Y. Wang & Yan, X. 2009 Novel iron–polysaccharide multilayered microcapsules for controlled insulin release. *Acta Biomater.* **5**, 1499 – 1507.

Zuidam, N. J. & Shimoni, E. 2010 *Encapsulation Technologies for Active Food Ingredients and Food Processing*. Springer.